

## Skin-Interfaced Wearable Sweat Sensors for Precision Medicine

Published as part of the Chemical Reviews virtual special issue "Wearable Devices".

Jihong Min,<sup>‡</sup> Jiaobing Tu,<sup>‡</sup> Changhao Xu,<sup>‡</sup> Heather Lukas,<sup>‡</sup> Soyoung Shin, Yiran Yang, Samuel A. Solomon, Daniel Mukasa, and Wei Gao\*Cite This: *Chem. Rev.* 2023, 123, 5049–5138

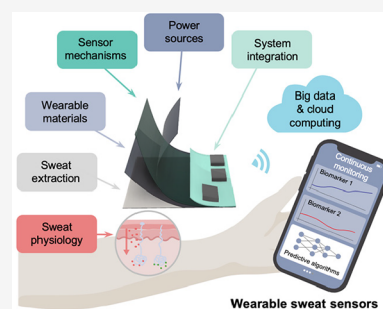
Read Online

ACCESS |

Metrics &amp; More

Article Recommendations

**ABSTRACT:** Wearable sensors hold great potential in empowering personalized health monitoring, predictive analytics, and timely intervention toward personalized healthcare. Advances in flexible electronics, materials science, and electrochemistry have spurred the development of wearable sweat sensors that enable the continuous and noninvasive screening of analytes indicative of health status. Existing major challenges in wearable sensors include: improving the sweat extraction and sweat sensing capabilities, improving the form factor of the wearable device for minimal discomfort and reliable measurements when worn, and understanding the clinical value of sweat analytes toward biomarker discovery. This review provides a comprehensive review of wearable sweat sensors and outlines state-of-the-art technologies and research that strive to bridge these gaps. The physiology of sweat, materials, biosensing mechanisms and advances, and approaches for sweat induction and sampling are introduced. Additionally, design considerations for the system-level development of wearable sweat sensing devices, spanning from strategies for prolonged sweat extraction to efficient powering of wearables, are discussed. Furthermore, the applications, data analytics, commercialization efforts, challenges, and prospects of wearable sweat sensors for precision medicine are discussed.



## CONTENTS

1. Introduction	5050	4.6. Wearable Sweat Rate Sensor	5068
2. Physiology of Sweat	5051	4.7. Wearable Sweat Sensors Based on Piezo-electrics and Other Methods	5069
2.1. Structure and Mechanisms	5051	4.8. The Emerging Sweat Sensors Based on Bioaffinity Recognition	5070
2.2. Sweat Stimulation	5053	4.8.1. Antibody-Based Sensors	5070
2.3. Sweat Secretion and Electrolyte Reabsorption	5053	4.8.2. Nucleic Acid-Based Sensors	5073
2.4. Biomarkers in Sweat	5055	4.8.3. MIP-Based Sensors	5074
2.4.1. Analyte Transport and Partitioning	5055	4.8.4. Biosensor Design Considerations	5075
2.4.2. Sweat Composition Analysis	5055	5. Sweat Extraction and Sampling	5075
2.5. Sweat Physiology Outlook	5057	5.1. Sweat Induction	5075
3. Essential Material Properties for Wearable Sensors	5057	5.1.1. Thermally-Induced, Exercise-Induced, and Natural Sweat	5075
3.1. Biocompatibility	5057	5.1.2. Iontophoresis-Induced Sweat	5076
3.2. Permeability	5058	5.1.3. Sweat Composition by Different Induction Methods	5078
3.3. Conductivity	5058	5.2. Sweat Sampling	5078
3.4. Transparency	5058	5.2.1. Absorbent-Based Sweat Sampling	5078
3.5. Adhesion Property	5059	5.2.2. Pressure Driven Microfluidics	5078
3.6. Scalability	5059		
4. Biosensor Mechanisms	5059		
4.1. Electrochemical Potentiometric Sensors	5059		
4.2. Electrochemical Amperometric Sensors	5061		
4.3. Electrochemical Direct Oxidation	5063		
4.4. Wearable Sweat Sensors Based on Transistors	5065		
4.5. Wearable Optical Sweat Sensor	5065		

Received: November 22, 2022

Published: March 27, 2023



5.2.3. Sweat Sampling with Material- and Structure-Enhanced Fluid Transport	5081
5.3. Integrated Platforms for Sweat Induction and Sampling	5082
5.4. Discussion	5083
6. Powering Wearable Sweat Sensors	5084
6.1. Wearable Energy Harvesting	5084
6.1.1. Harvesting Biochemical Energy from Sweat	5084
6.1.2. Harvesting Kinetic Energy from the Body	5086
6.1.3. Harvesting Solar Energy from the Environment	5087
6.1.4. Hybrid Energy Harvesting	5089
6.1.5. Wireless Energy Harvesting	5091
6.2. Wearable Energy Storage	5091
6.2.1. Wearable Batteries	5091
6.2.2. Wearable Supercapacitors	5093
7. System-Level Integration	5094
7.1. Analog Interface	5094
7.1.1. Iontophoretic Sweat Stimulation	5094
7.1.2. Sweat Analysis	5094
7.2. Signal Processing and Wireless Communications	5095
7.3. Power Management	5095
7.4. Electronic Design Considerations	5095
7.4.1. Degree of Integration	5096
7.4.2. Degree of Conformability	5097
8. Applications of Wearable Sweat Sensors	5097
8.1. Fitness Monitoring	5097
8.2. Cystic Fibrosis Diagnosis	5100
8.3. Dietary and Nutrition Monitoring	5101
8.4. Stress and Mental Health Monitoring	5103
8.5. Therapeutic Drug Monitoring	5104
8.6. Substance Abuse Monitoring	5105
8.7. Chronic Diseases Management	5107
9. Data Processing for Wearable Sweat Sensors	5107
9.1. Multimodal Sensors	5107
9.1.1. Multiplexed Data Acquisition	5107
9.1.2. Sensor Crosstalk and Calibration	5109
9.2. Machine Learning-Based Data Analysis	5110
9.2.1. Curse of Dimensionality	5110
9.2.2. Feature Selection	5111
9.2.3. Model Selection	5111
9.2.4. Machine Learning Inspired Designs	5112
9.2.5. Machine Learning Discussions	5112
9.3. Data Privacy	5112
9.3.1. Medical Data Security	5112
9.3.2. Future of Data Privacy	5113
10. Path to Commercialization	5113
10.1. Product Life Cycle	5113
10.2. Emerging Market Landscape	5115
11. Challenges and Future Outlook	5116
Author Information	5117
Corresponding Author	5117
Authors	5117
Author Contributions	5118
Notes	5118
Biographies	5118
Acknowledgments	5118
References	5118

## 1. INTRODUCTION

Wearable sensors hold the promise of providing noninvasive and continuous insight into the biochemical landscape of our body.<sup>1–7</sup> From their simple origin as pedometers, wearable sensors have evolved tremendously into the more complex field of health monitoring. Fueled by increasing urbanization, improved lifestyle, and increasing awareness toward health and safety, the wearable sensor industry has witnessed an exponential growth in the demand for technologies that offer continuous health monitoring in the past decade.<sup>8</sup> Current state-of-the-art commercial wearable devices primarily focus on monitoring biophysical signals (temperature, heart rate) that indicate the physical manifestations of an underlying health state or condition which constrain the application of these devices within well-being services. Owing to the complexity and multidimensional nature of various diseases, deeper, multiplexed information acquired at the molecular level is needed before wearable sensors can be adopted for disease monitoring. From smart watches to e-skins, innovations in wearable sweat sensors promise to address this technological gap by expanding the biometrics accessible noninvasively through the skin.

Sweat contains a wealth of biochemical information that can be noninvasively and readily accessed on-demand or even continuously.<sup>3,9–11</sup> Compared with the complexities and discomforts associated in the sampling of other biofluids like blood, interstitial fluid, tear, saliva, and urine, sweat sampling can be conveniently and unobtrusively achieved by placing a sensor patch on accessible locations of the skin. Molecular biomarkers unveiled by wearable sweat sensors through continuous and noninvasive monitoring can provide a more detailed understanding of the biochemical processes that govern our health, enabling precision medicine through personalized monitoring of an individual's fitness and health conditions, as well as disease diagnosis and prognosis. Furthermore, the large amounts of biochemical profiles collected by sweat sensors from patients and healthy populations during the daily activities can be processed through predictive algorithms to realize personalized therapeutics and preventative care. At the same time, large data sets collected at the population-level can improve real-time epidemiological surveillance and enhance the precision of public health responses.

Advances in sensor technologies, materials science, and electronics lead to the advent of the first fully integrated multiplexed wearable sweat sensor in 2016.<sup>12</sup> Since then, numerous wearable sweat sensing systems have been developed, typically consisting of a flexible sweat sensor array for conformal contact, a flexible printed circuit board (FPCB) with rigid electronic components for signal processing and wireless communication, and a power source such as a lithium-ion battery to power the electronics. However, for the widespread commercial adoption of wearable sweat sensors, several challenges need to be addressed.

Rigid or thick elements in sweat-sensing systems often impede the device from achieving a stable, conformal, and breathable interface with the skin, potentially leading to motion-induced artifacts, discomfort, and skin irritations. Furthermore, effective sweat sampling often requires airtight contact with the skin which can be achieved by straps on wristwatches and headbands, or by novel deformable adhesives. Breakthroughs in elastic wearable materials could

gradually replace rigid and bulky parts of wearable sweat sensing systems with lightweight and deformable counterparts to seamlessly interface the skin, evolving from semirigid wristband sensors to e-textile sensors or e-skin sensors.

Next, the continuity and reliability of sweat sensor data are fundamental for achieving continuous health monitoring. Effective sweat sampling is the first step toward achieving continuous and accurate biomarker analysis. Early sweat sampling methods for analyzing biomarkers in sweat were often confounded by discrepancies due to skin contamination, sweat evaporation, sweat stimulation methods, and sweat rate effects. In addition, sweat stimulation was primarily achieved physically through exercise or thermal stress, leading to large variations in sweat rate and limiting sweat collection to very specific scenarios. Chemical sweat stimulation methods, as well as efficient sweat collection materials and microfluidic designs, can minimize fouling of sweat samples and extend the use of sweat sensors to sedentary and everyday scenarios. Ultimately, highly precise, specific, and stable sweat sensors for detecting a wide range of biomarkers need to be developed or improved upon. These sensors should also be supported by calibration sensors that simultaneously analyze variables that can potentially influence sensor readings or sweat content, such as skin temperature, sweat electrolyte balance, and sweat rate. Lastly, the vast amount of continuous data collected by sweat sensors can be aggregated through big-data and cloud computing techniques to better comprehend the meaning of the biomarker levels in terms of personal health status.

This review provides a comprehensive overview on the field of wearable sweat sensors from various perspectives including sweat physiology, materials science, sensing mechanism, power sources, system integration, and data analytics (Figure 1). In

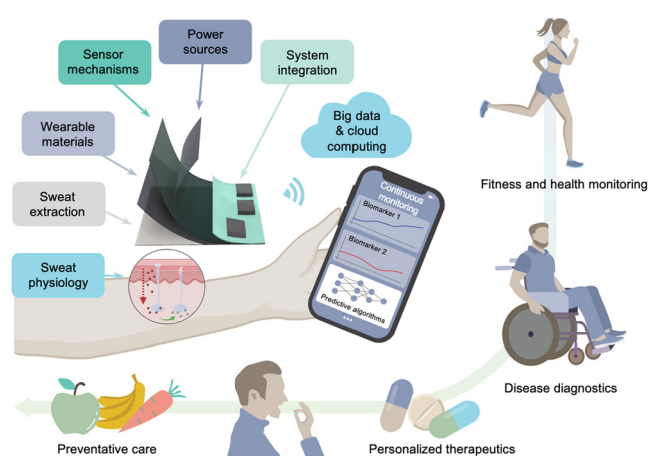


**Figure 1.** Overview of skin-interfaced wearable sweat sensors for personalized and precision healthcare. Created with BioRender.com.

addition to introducing the latest wearable sweat sensor devices reported in the literature, we provide an in-depth summary of the various engineering aspects that are considered when designing a device. Starting off by overviewing sweat physiology in terms of sweat gland structure, sweat secretion mechanisms, and sweat composition, we then highlight the essential material properties needed for wearable sweat sensors. We then go on to discuss various sweat biomarker detection mechanisms (not limited to electrochemical) and methods for sweat extraction and sampling. Next, we describe energy harvesting and energy storage methods for powering these

wearables, as well as system-level integration strategies for integrating sensors, electronic circuitry, and power sources into a complete wearable device. Furthermore, we outline the various applications of wearable sweat sensors in terms of fitness monitoring, disease diagnostics, and precision medicine. Finally, we discuss data postprocessing for wearable sweat sensors and their path to commercialization.

## 2. PHYSIOLOGY OF SWEAT

Sweat is produced from glands located deep within the skin, the body's largest organ by surface area. The skin has a stratified structure including the stratum corneum, epidermis, dermis, and hypodermis. The dermis is the major component of the skin containing blood vessels, nerve endings, and the base of sweat glands, sebaceous glands, and hair follicles (Figure 2a). The average eccrine sweat gland density is 200/cm<sup>2</sup>, but this varies between individuals and across the body with the highest density among the palms and soles (~400/cm<sup>2</sup>).<sup>13,14</sup> The total number of eccrine sweat glands is on the order of 1.6–5 million.<sup>13</sup>

Sweat plays a very important role in maintaining the body's core temperature, providing a means of thermoregulation. Should body core temperatures rise above 40 °C without modulation, there is a risk of protein denaturation, cell death, and subsequent organ failure.<sup>13</sup> Beyond thermal regulation, sweat also participates in skin homeostasis. Moisturizing factors in sweat, such as lactate and urea, maintain the plasticity and barrier integrity of the stratum corneum. Secretion of antimicrobial compounds such as dermcidin, lactoferrin, lysozymes, and immunoglobulin E (IgE) antibodies contributes to the skin's first line of defense against infection.<sup>15</sup> The loss of sweat glands after severe damage as in the case of burn victims presents new challenges in regenerative wound healing and demands further research into sweat gland physiology.

Eccrine sweat glands secrete a highly filtered, aqueous fluid composed of electrolytes, metabolites, and additional molecules. Apocrine sweat glands secrete a viscous fluid containing lipids, proteins, steroids, and ions, by exocytosis in the apocrine gland coil.<sup>16</sup> Volatile organic compounds from apocrine secretions act as pheromones.<sup>13</sup> Apocrine and eccrine sweat glands are differentially stimulated. The apocrine sweat gland responds strongly to emotional stimuli and sympathomimetic drugs via adrenergic innervation, but does not respond to cholinergic or thermal stimulation like the eccrine sweat gland.<sup>15,17</sup> The apoecrine sweat gland shares properties of both eccrine and apocrine glands; it may develop during puberty in the axillae region from existing eccrine sweat glands. The gland retains an eccrine-like sweat duct but has an apocrine-like secretory tubule. Apoecrine sweat ultimately resembles aqueous eccrine sweat and arises from an intermediate type of stimulation.<sup>18</sup> This review focuses on eccrine sweat as eccrine sweat glands are the most abundant and active source of sweat.

In this section, we present the physiology of eccrine sweat from stimulated innervation to sweat secretion. We describe sweat gland development and structure. Additionally, we discuss molecule partitioning into sweat and give an overview of accessible biomarkers in sweat.

### 2.1. Structure and Mechanisms

The eccrine sweat tubule is a conduit for sweat and electrolyte exchange 4–8 mm in length. At the base, the secretory coil is

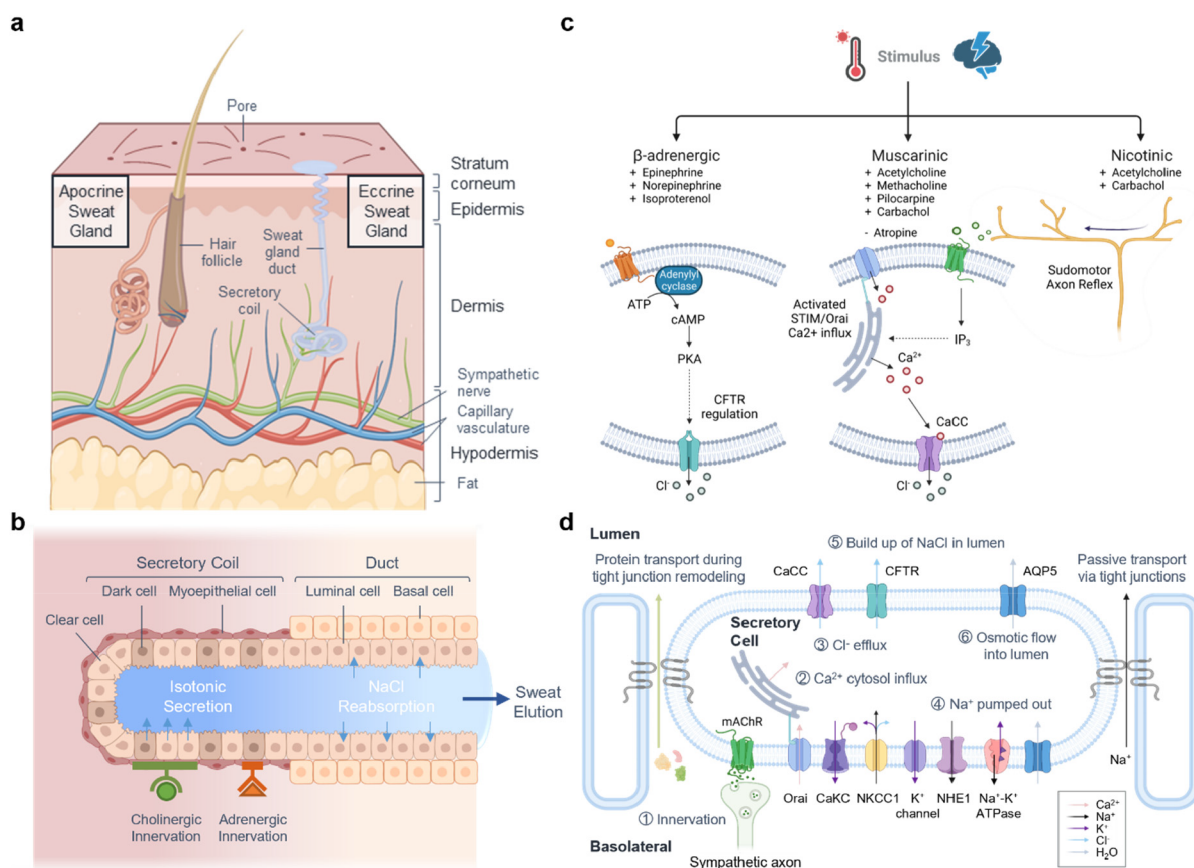


**Figure 2.** Physiology of sweat glands and eccrine sweat secretion. **a**, Structure of the skin, including apocrine and eccrine sweat glands. **b**, The eccrine sweat gland can be broken down into two primary components: the secretory coil and the sweat duct where isotonic secretion and reabsorption occur, respectively, to produce a hypotonic aqueous fluid. **c**, Sweat is stimulated primarily through  $\beta$ -adrenergic and muscarinic innervation.  $\beta$ -adrenergic and muscarinic signaling pathways use cAMP and  $\text{Ca}^{2+}$  as second messengers, respectively, to activate chloride channels. Activation of nicotinic receptors may amplify the sweating response beyond the localized region via the sudomotor axon reflex. **d**, Several membrane channels are involved in the secretion of electrolytes and the subsequent osmotic flow into the lumen. Created with [BioRender.com](https://www.biorender.com/).

500–700  $\mu\text{m}$  in size with a lumen inner diameter of 30–40  $\mu\text{m}$  and a coil outer diameter of 60–120  $\mu\text{m}$ .<sup>13</sup> The secretory coil is interwoven with capillaries for vascular exchange and sudomotor nerve fibers for autonomic modulation.<sup>14,19</sup> The secretory tubule straightens into the dermal duct with an inner diameter of 10–20  $\mu\text{m}$  and outer diameter of 50–80  $\mu\text{m}$  composed of two to three layers of epithelial cells.<sup>13</sup> The sweat duct is straight from the dermis to the epidermis, and then transitions to a helical structure in the epidermis that terminates in the stratum corneum. The number of turns of the helical duct varies from 4 to 6 and varies proportionally to the stratum corneum thickness, yet the pitch angle remains constant across sweat glands.<sup>20</sup> The helical structure makes the sweat duct act as a helical antenna resulting in resonance behavior. Sweat duct dimensions, density, distribution, and the dielectric properties of the stratum corneum all determine the resonant frequency and subsequent skin-THz wave interactions. The duct length varies from 150 to 600  $\mu\text{m}$  and varies proportionally to the stratum corneum thickness.<sup>20</sup> The sweat duct widens into the acrosyringium, a pore on the outer surface. The acrosyringium is composed of epithelial cells with no clear distinction or border to the epidermis. The lumen has a diameter of 20–60  $\mu\text{m}$  and may also contain cornified cells.<sup>13</sup>

Humans are born with almost all their sweat glands, with gland development occurring mostly during the first two trimesters. This is one explanation for higher observed duct

densities in children than adults.<sup>20</sup> The sweat gland develops from a group of multipotent  $\text{K14}^+$  progenitors, descendants of epidermal stem cells. It grows downward as a straight duct, stratifying in the lower half to proliferative  $\text{K14}^{\text{low}}/\text{K18}^+$  suprabasal progenitors. The  $\text{K14}^{\text{low}}/\text{K18}^+$  suprabasal progenitors develop into luminal cells, while the remaining  $\text{K14}^+$  progenitors give way to myoepithelial cells.<sup>21</sup> Although sweat glands have limited turnover and proliferation capabilities, there is some promise of regeneration. Stem cells associated with secretory luminal and myoepithelial cells were found to promote epidermis and sweat gland regeneration when amplified and seeded in the wound bed.<sup>22</sup> Additionally, the use of three-dimensional (3D) bioprinting matrices has been studied for sweat gland morphogenesis with tissue-level self-organization.<sup>23</sup>

The secretory coil and duct define the two major steps of sweat generation: isotonic secretion and salt reabsorption (Figure 2b). Ductal cells facilitate transcellular reabsorption with mitochondria-rich basal cells contributing to uptake. The secretory coil is made up of basal myoepithelial cells and luminal clear and dark cells, named for their appearance in eosin, toluidine blue, and methylene blue stains.<sup>13</sup> Myoepithelial cells strengthen the structure of the secretory coil and create a microenvironment for gland stem cell differentiation.<sup>24</sup> Clear cells contain many mitochondria suggesting that they facilitate most of the active sweat secretion and osmotic flow.<sup>13</sup>

Dark cells are granular, containing many vesicles. Dark cells are more involved in the secretion of proteins, including periodic acid-Schiff (PAS)-positive diastase-resistant glycoproteins, dermicidin, and sialomucin.<sup>24</sup> The interdependent relationship between clear and dark cells requires further investigation.

Sweat secretion is stimulated by adrenergic and cholinergic innervation (Figure 2c). The sudomotor response involves several adenosine triphosphate (ATP)-dependent steps, and is suppressed by ouabain and metabolic inhibitors.<sup>14</sup> When the secretory cell is stimulated, a signaling cascade occurs involving  $\text{Ca}^{2+}$  or cyclic adenosine monophosphate (cAMP) as second messengers to trigger the efflux of  $\text{Cl}^-$  into the lumen of the secretory coil.  $\text{Na}^+$  is pumped out at the basolateral membrane and diffuses down its electrochemical gradient into the lumen. The buildup of electrolytes in the lumen renders it hypertonic with respect to the cytosol; this osmotic gradient drives the primary sweat solution out of the cell and into the secretory lumen (Figure 2d). Advective mass transport drives fluid up the eccrine sweat duct. Along the sweat duct, luminal cells reabsorb ions to produce a hypotonic sweat solution. We describe this process in further detail below.

## 2.2. Sweat Stimulation

Thermoregulatory sweating is an autonomic response to signals from thermoreceptors in the preoptic-anterior hypothalamus area. Upon an increase in core temperature, thermoreceptors send through efferent pathways to postganglionic sympathetic neurons in the dermis.<sup>14</sup> Cholinergic nerve fibers around the secretory coil release acetylcholine, thus activating muscarinic receptors on the membrane of the eccrine secretory cell. Activation of muscarinic G-protein-coupled receptors (GPCRs) increases intracellular inositol trisphosphate ( $\text{IP}_3$ ).  $\text{IP}_3$  binds to receptors on the endoplasmic reticulum (ER) membrane to release  $\text{Ca}^{2+}$  into the cytosol.<sup>25</sup> Stromal interaction molecule protein, stromal interaction molecule 1 (STIM1), monitors the ER  $\text{Ca}^{2+}$  levels, and when  $\text{Ca}^{2+}$  stores are depleted STIM1 induces store-operated  $\text{Ca}^{2+}$  entry by binding to and activating Orai, a  $\text{Ca}^{2+}$  channel on the plasma membrane.<sup>25</sup> This influx of  $\text{Ca}^{2+}$  mediates the exchange of electrolytes resulting in sweat secretion.

Sweating is also adrenergically stimulated under the “fight or flight” response. The physical reaction to stress, anxiety, fear, and pain occurs mostly in the palms, soles, and axillary region and may have the selective advantage of increasing palmoplantar friction for fleeing.<sup>13</sup> “Emotional” sweating is controlled by the limbic system, and efferent signals are sent to adrenergic nerve fibers in the sweat secretory coil. Release of epinephrine and norepinephrine in signaling stimulates  $\alpha$ - and  $\beta$ -adrenoreceptors in sweat secretory cells. A synthetic sympathomimetic drug, isoproterenol, selectively stimulates  $\beta$ -adrenoreceptors and has been used to further differentiate the two pathways.  $\beta$ -Adrenergic stimulation is the dominant pathway in emotional sweating. The magnitude of stimulated sweat secretion (measured by secretory rate) is 4:2:1 for cholinergic,  $\beta$ -adrenergic, and  $\alpha$ -adrenergic pathways, respectively.<sup>26</sup>  $\alpha$ -Adrenergic stimulation results in  $\text{Ca}^{2+}$  influx similar to cholinergic pathways.  $\beta$ -Adrenergic GPCRs activate adenylyl cyclase and increase the intracellular concentration of cAMP. cAMP activates protein kinase A (PKA), which in turn mediates  $\text{Cl}^-$  secretion by opening the cystic fibrosis transmembrane conductance regulator (CFTR).<sup>27,28</sup> In the case of cystic fibrosis, CFTR is defective or absent, resulting in blocked CFTR  $\text{Cl}^-$  secretion during  $\beta$ -adrenergic stimulation

and inhibited  $\text{Cl}^-$  reabsorption. A “ratiometric” sweat rate test comparing adrenergic and cholinergic sweat rates may be used to assess CFTR functional activity.<sup>29</sup>

Sweat may be generated at the periphery of a stimulated region via the sudomotor axon reflex (Figure 2c). Nicotinic agonists interact with receptors on postganglionic sudomotor terminals at the base of the sweat gland, causing antidromic axonal conduction toward a branch point followed by orthograde conduction down the branching fibers. Acetylcholine is then released at the nerve terminals and binds to muscarinic receptors on the eccrine sweat gland, resulting in sweat secretion similar to the direct iontophoretic response.<sup>14,30</sup> The spatial extension of this sweating could be millimeters beyond the periphery of the stimulation region.<sup>31</sup> The sudomotor axon reflex may be used to assess autonomic nervous system disorders, such as diabetic neuropathy.<sup>14,32</sup> The sudomotor axon reflex may also be used to separate drug-induced sweat stimulation and sweat sampling regions to prevent cross-contamination.<sup>30</sup> The sudomotor axon response has a longer latency than the direct cholinergic response by about 5 s, which accounts for axonal conduction and neuroglandular transmission. The sudomotor axon response and direct response produce similar sweat volumes in the presence of nicotinic agonists. In contrast to the direct stimulated sweat response, which continues over an hour after cessation of the stimulus, the sudomotor axon response returns to baseline 3–5 min after stimulus cessation.<sup>33</sup>

The sweat rate is modulated in part by nonuniform, localized activation. Under mental stress, sweat production of adjacent sweat glands varied strongly.<sup>34</sup> The cumulative sweating response controlled by the sympathetic nerve is discretized into active and inactive sweat glands.<sup>34</sup> The sweat rate in healthy individuals ranges from 0.2 to 1  $\mu\text{L}/\text{cm}^2/\text{min}$ .<sup>35,36</sup> At an average sweat gland density of 200/ $\text{cm}^2$ , this equals 1–5 nL/gland/min. The sweat rate is affected by local skin temperature.<sup>13</sup> Sweat stimulated pharmacologically may also further increase the sweat rate to approximately 10 nL/gland/min.<sup>37</sup> Sweat rate decay and cessation occur in part due to the subcutaneous elimination of the sweat stimulant (e.g., acetylcholinesterase).<sup>14,38</sup> Interindividual variations in sweat rate are likely due to differences in the function and responsiveness of the sweat gland.<sup>39</sup> Many factors may influence the sweat response including gender, physical fitness, menstrual cycle, and circadian rhythm.<sup>13</sup> Intraindividual regional variations in observed sweat rate may be associated with variations in sweat gland density and distribution.<sup>20,39</sup> For example, the forehead has a high density of sweat glands and has the highest tested sweat rate region during both active and passive thermal sweating.<sup>39,40</sup>

## 2.3. Sweat Secretion and Electrolyte Reabsorption

Upon stimulation,  $\text{Ca}^{2+}$  and cAMP act as intracellular messengers for sweat secretion.  $\text{Ca}^{2+}$  activates transmembrane  $\text{K}^+$  and  $\text{Cl}^-$  channels. TMEM16A and bestrophin 2 are  $\text{Ca}^{2+}$ -activated chloride channels (CaCCs) located on the apical membrane of secretory gland cells. Bestrophin 2 is expressed only in dark cells, yet it is necessary for sweat generation.<sup>41</sup> CFTR is the active  $\text{Cl}^-$  channel in cAMP-mediated  $\beta$ -adrenergic sweat secretion. PKA-independent CFTR activation via calmodulin-mediated  $\text{Ca}^{2+}$  signaling results in cross-talk between cAMP and  $\text{Ca}^{2+}$  signaling for CFTR regulation.<sup>42</sup> It is possible CFTR may be involved in both sweat secretion pathways.

Table 1. Composition of Sweat

Biomarkers		Sweat concentration (mM)	Blood concentration (mM)	Molecular weight (Da)	References	
Electrolytes	Sodium	10–100	135–150	23	40, 336, 681, 682	
	Chloride	10–100	97–107	35	40, 348, 683	
	Potassium	1–20	3.5–5	39	40, 684, 685	
	Ammonium	0.5–8	0.01–0.4	18	64, 686	
Metabolites	Lactate	5–60	0.5–25	90	40, 687–694	
	Glucose	0.01–0.3	3.3–17.3	180	65, 695, 696	
	Urea	2–40	1.8–7.1	60	72–74, 693, 695	
	Uric acid	0.02–0.1	0.1–0.5	168	72–76	
	Creatinine	0.01–0.03	0.065–0.12	113	72, 73, 362	
	Minerals	Calcium	0.2–2	2.2–2.7	30	77–80
Magnesium		0.02–0.4	0.7–0.95	24	77–80	
Iron		0.0001–0.03	0.006–0.027	56	77–80	
Zinc		0.0001–0.02	0.01–0.017	65	77–80	
Nutrients	Amino acids	Tyrosine	0.2–0.4	0.055–0.3	181	57, 85–87
		Tryptophan	0.055–0.08	0.02–0.091	204	57, 85–87
		BCAAs <sup>a</sup>	0.2–1	0.2–1.2	117–131	57, 85–87
Hormones	Vitamin C	0.01–50 × 10 <sup>-3</sup>	2.8–200 × 10 <sup>-3</sup>	176	83, 84	
	Cortisol	0.1–20 × 10 <sup>-3</sup>	0.07–690 × 10 <sup>-3</sup>	362	91–93	
	Testosterone	0.8–1.6 × 10 <sup>-6</sup>	0.5–35 × 10 <sup>-6</sup>	288	697	
	Dehydroepiandrosterone	6.9–455 × 10 <sup>-6</sup>	0.35–11.91 × 10 <sup>-3</sup>	288	697	
Proteins	Neuropeptide Y	1.9–6.8 × 10 <sup>-10</sup>	1.4–6.1 × 10 <sup>-10</sup>	4272	96	
	C-reactive protein	4.2–250 × 10 <sup>-9</sup>	7–29 × 10 <sup>-6</sup>	120,000		
	Cytokines	Interleukin 6	3.7–6.9 × 10 <sup>-10</sup>	2.4–5.6 × 10 <sup>-10</sup>	21,000	96, 100
		Interleukin 8	1.8–7.2 × 10 <sup>-10</sup>	1.5–6.5 × 10 <sup>-10</sup>	8452	100, 101
Substances	Ethanol	2.5–22.5	2–22.5	46	698	
	Acetaminophen	<50 × 10 <sup>-3</sup>	66–132 × 10 <sup>-3</sup>	151	567	
	Levodopa	<2.5 × 10 <sup>-3</sup>	<5 × 10 <sup>-3</sup>	197	699	

<sup>a</sup>BCAAs: branched-chain amino acids.

As Cl<sup>-</sup> diffuses into the lumen at the apical membrane, Cl<sup>-</sup> enters the cell via basolateral Na-K-Cl cotransporter 1 (NKCC1), a Na<sup>+</sup>-K<sup>+</sup>-2Cl<sup>-</sup> electroneutral cotransporter. Excess accumulated Na<sup>+</sup> is then actively pumped out via Na<sup>+</sup>/H<sup>+</sup> exchanger 1 (NHE1) and Na<sup>+</sup>-K<sup>+</sup> ATPase.<sup>25</sup> Na<sup>+</sup> is passively transported paracellularly down the electrochemical gradient established in the lumen. A buildup of electrolytes in the lumen of the secretory coil results in an osmotic gradient driving transcellular fluid flow via aquaporin 5 (AQP5) and paracellular flow from the interstitial fluid (ISF).<sup>19,24</sup> As a result, the aqueous fluid in the secretory coil becomes isotonic with respect to ISF, blood, and cytosol.

Continued sweat secretion drives flow up the sweat duct, where reabsorption of electrolytes results in a hypotonic final sweat secretion. CFTR is necessary for Cl<sup>-</sup> reabsorption. Unlike in the secretory coil, CFTR in the sweat duct is constitutively active. CFTR activity is complexly regulated by intracellular cAMP, ATP, and K<sup>+</sup> levels. CFTR conduction of Cl<sup>-</sup> is transcellular, but CFTR is present at a greater surface density on the apical membrane.<sup>27</sup> In contrast to the secretory coil, Na<sup>+</sup> transport in the duct is transcellular rather than paracellular. Na<sup>+</sup> is reabsorbed passively by the epithelial sodium channel (ENaC) at the apical membrane and actively pumped at the basolateral membrane by Na<sup>+</sup>/K<sup>+</sup> ATPase.<sup>13</sup> ENaC and CFTR interact with each other in complex ways.<sup>27,43</sup> Na<sup>+</sup> reabsorption is reduced by increases in luminal Ca<sup>2+</sup>.<sup>44</sup> ENaC is regulated by Ca<sup>2+</sup> in other reabsorption cells,<sup>45</sup> suggesting that inhibition of ENaC by increases in Ca<sup>2+</sup> reduces the membrane permeability and passive Na<sup>+</sup> flux at the apical luminal cell membrane. As sweat rate increases, Na<sup>+</sup>

reabsorption increases; however, the Na<sup>+</sup> secretion rate increases relatively more, resulting in higher salt concentrations at higher sweat rates.<sup>46</sup>

Bicarbonate (HCO<sub>3</sub><sup>-</sup>) is involved in both sweat secretion and reabsorption, yet the mechanisms remain unclear. HCO<sub>3</sub><sup>-</sup> exchange is mediated by both CFTR and Bestrophin 2 channels.<sup>24,27</sup> Various carbonic anhydrase isoforms also regulate HCO<sub>3</sub><sup>-</sup> by reversibly converting CO<sub>2</sub> to HCO<sub>3</sub><sup>-</sup>. Carbonic anhydrase II (CA2) operates intracellularly in secretory coil clear cells and ductal cells.<sup>13,25</sup> Carbonic anhydrase XII (CA12) is a transmembrane protein also broadly expressed in the sweat gland. Defective CA12 results in excessive Na secretion in sweat.<sup>24</sup> HCO<sub>3</sub><sup>-</sup> plays an important role in regulating the acid–base chemistry of sweat secretion both intracellularly and extracellularly. Cytosolic pH affects ion channel activity. For example, ENaC becomes inhibited at acidic cytosolic pH in ductal cells.<sup>24</sup> pH-sensitive phosphatases occur in the intercellular canaliculi of secretory cells. HCO<sub>3</sub><sup>-</sup> may also be secreted in coordination with acidic proteins, such as sialomucin, to neutralize the pH in the lumen.<sup>24</sup> Final sweat pH can range from roughly 5 to 7 and is positively correlated with sweat rate. Sweat pH in the secretory coil has a neutral pH, like ISF; but pH decreases as it moves through the sweat duct. This suggests that ductal HCO<sub>3</sub><sup>-</sup> reabsorption at low sweat rates contributes to the acidification of sweat.<sup>47</sup> Fluctuations in sweat pH represent a challenge in sweat sensing, both because pH may affect partitioning of detected molecules and also because pH may directly affect biosensor performance.

Acclimatization to thermal (and physical) stimuli markedly affects sweat generation. Physically fit individuals have higher glandular functions and sweat rates per gland after methacholine stimulation.<sup>48</sup> Over a multiweek exercise series, acclimatization due to increased fitness resulted in a reduced lactic acid concentration in sweat.<sup>49</sup> Additionally, thermal acclimatization increases the Na<sup>+</sup> reabsorption capacity of the human eccrine sweat gland.<sup>35</sup>

## 2.4. Biomarkers in Sweat

Sweat is an information-rich biofluid containing many molecules that can serve as biomarkers. Sweat is composed of various electrolytes, metabolites, hormones, proteins, and peptides (Table 1). Sweat samples may be analyzed using metrics such as biomarker concentrations, biomarker flux, sweat rate, sweat pH, and ionic strength to provide important information as they correlate to health. In some cases, biomarker flux may represent a better metric of analysis since it accounts for the dynamic water flux, which may affect concentration measurements. Biomarker flux may be calculated using the product of sweat rate and biomarker concentration.<sup>50</sup> Recent reports have shown promising correlations between the levels of a number of sweat and blood analytes,<sup>19</sup> indicating the great potential of using sweat as an alternative source for personalized healthcare. Since sweat is readily available for noninvasive sampling, sweat is an attractive biofluid for point-of-care (POC), at-home, and continuous diagnostics. Moreover, new biomarker discovery for precision medicine can be greatly facilitated by the continuous, large sets of data collected through noninvasive sweat analysis in daily activities.<sup>51</sup>

**2.4.1. Analyte Transport and Partitioning.** Prior to electrolyte reabsorption in the sweat duct, initial sweat secretion is isotonic and resembles filtered ISF. Passive sweat secretion may result in reduced concentrations 10- to 1000-fold lower than in ISF and blood plasma. However, blood-to-sweat correlations vary based on the analyte and its subsequent partitioning. Analyte partitioning occurs primarily via transcellular and paracellular transport. Small, uncharged analytes readily enter sweat transcellularly via diffusion through the plasma membrane of capillary endothelial cells.<sup>19</sup> Large, hydrophilic molecules enter sweat paracellularly via diffusion and advective transport through the intercellular canaliculi between adjacent cells.

Transcellular transport of small, lipophilic molecules results in strong blood–sweat correlations as these molecules freely diffuse across the selectively permeable cell membrane. This is likely the dominant transport mechanism for several classes of analytes, including steroid hormones (i.e., cortisol<sup>52</sup>), ethanol,<sup>53</sup> and many therapeutic and abused drugs (e.g., nicotine, fentanyl). Partitioning is limited by the least permeable state. This results in plasma correlations that hold only for the unbound fractions of the analyte as is the case with cortisol.<sup>19</sup> For instance, ionization may impede the molecule from transcellular transport. The pH of sweat may become an important consideration for weak acids and weak bases due to the possibility of ion trapping. In the case of ammonia (NH<sub>3</sub>), which has a pK<sub>a</sub> of 9.3, NH<sub>3</sub> diffuses readily into the secretory lumen but under acidic sweat conditions (as in the case of exercise), NH<sub>3</sub> protonates to become ammonium (NH<sub>4</sub><sup>+</sup>). In the protonated form, transcellular exchange is impeded and NH<sub>4</sub><sup>+</sup> accumulates in the lumen of the sweat gland. This phenomenon results in amplified sweat concentrations.<sup>52</sup> Since primary sweat pH is 7.2 to 7.3 in the secretory coil,<sup>47</sup> this

phenomenon is likely to mostly impact reabsorption in the sweat duct. While ion trapping is a common topic of research in subcellular pharmacokinetics, the role of ion trapping in sweat partitioning warrants further consideration.

The intercellular canaliculi forms a >10 nm gap for paracellular molecular transport, but tight junctions adjoining secretory cells act as a roadblock.<sup>19</sup> Tight junctions are formed by over 40 different proteins, with the claudin family of transmembrane proteins defining the structure and selective permeability of the tight junction.<sup>19</sup> Paracellular sweat partitioning is likely to occur during tight-junction remodeling allowing for ISF molecules in the canaliculi to make their way into the lumen. Tight junctions may be modulated using calcium chelators. For example, citrate addition leads to a > 10x increased flux of glucose to sweat from ISF.<sup>50</sup> Although paracellular sweat partitioning may result in significant dilution from blood plasma protein levels, this nonspecific channel for proteins from the ISF may still result in correlated blood plasma ratios for trend analysis.

The observed lag time between blood and sweat measurements is on the order of ones to tens of minutes. The secretory coil is highly vascularized, minimizing the lag in circulating blood changes.<sup>19</sup> In the simplified case of transcellular transport, the rate of diffusion determines the time to enter the lumen of the sweat duct. Once in the lumen, advective transport by osmotic fluid flow (i.e., sweat rate) determines the time from analyte secretion to analyte elution. When the correlation of blood alcohol and sweat alcohol content was measured continuously, the lag time for signal onset ranged 2.3–11.4 min and 19.32–34.44 min for the overall curve.<sup>53</sup> The relative contributions of sweat flow rates and analyte partitioning mechanisms on the sensor response remains obscure. For sweat generation or refreshing to be the rate-limiting step, the sweat collection designs should be further optimized. Further work is required to better define the variation in lag of different analyte partitioning. However, real-time sensing is contextual; the measurement of an analyte whose concentration changes slowly relative to the lag in transport and sensing is effectively a real-time measurement.

**2.4.2. Sweat Composition Analysis.** Sweat has been surveyed broadly using liquid chromatography (LC) or gas chromatography (GC), mass spectrometry (MS), and nuclear magnetic resonance (NMR) techniques. NMR requires minimal sample preparation but achieves a lower sensitivity. MS is often preceded by chromatographic techniques to enhance detection quality.<sup>16</sup> A high coverage LC-MS technique based on chemical isotope labeling was used to identify over 2707 unique metabolites across 54 sweat samples.<sup>54</sup> Subsequently, 83 metabolites were identified with high confidence. With such a diverse data set, LC-MS may be used to characterize the sweat submetabolome and draw statistically significant observations based on gender and activity duration.<sup>54</sup> LC-MS and GC-MS represent the gold standard of trace concentration sweat biomarker identification and quantification. The disadvantage of these techniques is that they require expensive equipment along with complex protocols that require thorough validation for use in metabolite identification and quantification.

Regional variations in sweat composition have been studied using a variety of assays, recently including NMR and multiplexed immunoassays.<sup>55,56</sup> In general, there are minimal variations in sweat composition when sampling from different body locations. No significant difference was observed for

sweat cytokine composition at different arm locations, and metabolic profiles are generally conserved across the body.<sup>55,56</sup> Sweat from the upper chest, upper back, arms, and forehead exhibited similar NMR spectra.<sup>55</sup> Sweat from the lower back, axillary, and inguinal regions contained a higher fat content, but this may be due to sweat mixing with sebum since these areas also contain a high density of sebaceous glands. Forehead sweat exhibited high levels of lactate, pyruvate, glycerol, and serine relative to the arm sweat. Serine content was also high on the hands and feet.<sup>55</sup> Since serine is active in skin regeneration, this is indicative that these regions may undergo more epithelial turnover. The hands appear to have a lower content of natural moisturizing factors, such as glycerol and urea.<sup>55,57</sup> For electrolytes, regional sodium chloride concentrations are well-correlated with whole-body sweat concentrations, with the exception of forehead sweat possibly due to the effects of a significantly higher sweat rate. The forearm, thigh, and calf were all highly correlated and are potential single-site sweat collection areas.  $\text{HCO}_3^-$  concentration was high at the forearm despite the average sweat rate.  $\text{K}^+$  and lactate concentrations were higher at the extremities (foot, hand, and forearm).<sup>40</sup>

**Electrolytes.**  $\text{Na}^+$  and  $\text{Cl}^-$ , the most copious electrolytes found in sweat, are partitioned into sweat via active mechanisms that are tied to the osmotic secretion of water. Therefore,  $\text{Na}^+$  and  $\text{Cl}^-$  serve as potent biomarkers of electrolyte balance and hydration status for cystic fibrosis diagnostics and fitness monitoring applications. According to the  $\text{Na}^+\text{-K}^+\text{-2Cl}^-$  cotransport model as outlined previously, a series of cascading effects instigated by the stimulation of cholinergic nerve endings surrounding the sweat gland induce the influx of  $\text{NaCl}$  into the secretory coil lumen, which then causes the osmotic influx of water.<sup>47,58,59</sup> In this primary sweat,  $\text{Na}^+$  levels are isotonic and  $\text{Cl}^-$  levels are slightly hypertonic to plasma. However, as this fluid gets pumped through the duct,  $\text{Na}^+$  and  $\text{Cl}^-$  ions are reabsorbed through ENaC and CFTR to prevent rapid electrolyte loss. Despite wide ranging concentrations, resulting sweat  $\text{Na}^+$  and  $\text{Cl}^-$  levels are often hypotonic to plasma levels. Additionally, as reabsorption of these ions occurs at steady rates, increased sweat rates correlate with increased  $\text{Na}^+$  and  $\text{Cl}^-$  levels in final sweat.

$\text{K}^+$  is another electrolyte secreted via the  $\text{Na}^+\text{-K}^+\text{-2Cl}^-$  cotransport model that is relevant to the function of nerve and muscle cells.<sup>47</sup> While understanding of the exact partitioning mechanism of  $\text{K}^+$  requires further investigation, studies have shown that  $\text{K}^+$  levels of primary sweat in the secretory coil are isotonic to plasma levels but increase to hypertonic levels in final sweat exiting the duct.<sup>60,61</sup> Furthermore,  $\text{K}^+$  concentrations seem to not have a strong correlation with sweat rate.<sup>40,62</sup>

$\text{NH}_4^+$ , an electrolyte found in sweat with metabolic origins, is of interest for tracking liver and kidney function, as well as exercise intensity.<sup>63</sup> As described previously,  $\text{NH}_3$  is a small and uncharged polar molecule with a  $\text{pK}_a$  of 9.3 (weakly basic), allowing for passive diffusion into the sweat gland lumen where weakly acidic conditions result in increased protonation to ammonium. Due to its charge, the ammonium ion gets entrapped in the lumen of the sweat gland, yielding sweat ammonium levels to be 20–50 times higher than plasma ammonium levels.<sup>64</sup> Furthermore, sweat ammonium levels have been reported to decrease with increased sweat pH and sweat rates.<sup>52</sup>

**Metabolites.** Blood glucose monitoring is critical for managing diabetes, and sweat glucose has the potential to serve as a noninvasive surrogate. Some studies have shown positive correlations between sweat and blood glucose levels, and while the exact partitioning mechanism is still being studied, the primary source of sweat glucose is likely to be from blood through paracellular transport.<sup>50,65,66</sup> The rather large size and polarity of glucose likely limit its passage through the tight junctions of the sweat gland, resulting in sweat glucose levels being  $\sim 100$  times lower than blood glucose levels.

Lactate is a metabolite found in sweat that has been extensively studied as a potential biomarker for muscle exertion and fatigue. While the transport mechanism of lactate from plasma to sweat is obscure and the correlation between lactate levels in sweat and plasma is weak, sweat lactate is also produced from sweat gland metabolism and can still be reflective of whole-body exertion. Sweat lactate levels are typically higher than blood lactate levels and decrease with increased sweat rates, potentially due to dilution.

Along with ammonia, urea, uric acid, and creatinine are nitrogenous compounds produced from protein metabolism that indicate renal function. As a small polar molecule that can passively diffuse through the sweat gland through paracellular transport, sweat urea has been speculated to primarily originate from the blood.<sup>47,67</sup> However, reported sweat urea concentrations are often significantly higher than blood urea concentrations (up to 50 times), potentially indicative of additional sources of urea in sweat. A popular hypothesis is that there is a finite pool of urea in the epidermis that gets depleted during profuse sweating, supported by studies showing that sweat urea levels trend toward blood urea levels with increased sweating.<sup>68</sup> Additionally, studies indicate the potential for active mechanisms of urea excretion through sweat as an alternative method for excreting excess metabolic wastes.<sup>69–71</sup> Uric acid and creatinine are slightly larger molecules that are found in sweat at micromolar levels and around 5 times lower than in blood.<sup>72–76</sup> While the partitioning mechanism of these metabolites has not been studied in detail, a positive correlation between sweat and serum uric acid levels has been reported.<sup>75</sup>

**Minerals.** Trace minerals such as  $\text{Ca}^{2+}$ ,  $\text{Mg}^{2+}$ ,  $\text{Fe}^{2+}$ , and  $\text{Zn}^{2+}$  are often found in sweat at concentrations similar to or slightly lower than blood concentrations.<sup>77–80</sup> Due to their small size and hydrophilicity, these trace minerals have the potential to be secreted through sweat via paracellular mechanisms in their free and ionized states. However, approximately 30–45% of plasma  $\text{Mg}^{2+}$ , 50% of plasma  $\text{Ca}^{2+}$ , 70% of plasma  $\text{Zn}^{2+}$ , and above 95% of plasma  $\text{Fe}^{2+}$  are bound to proteins or complexed with anions, likely impeding passive diffusion into the sweat glands.<sup>81,82</sup>

**Nutrients.** Water-soluble vitamins such as ascorbic acid and thiamine, which are large and polar molecules, have been reported in sweat at concentrations significantly lower than in blood.<sup>83,84</sup> On the other hand, amino acids, which are the building blocks of protein in our bodies, are often found in sweat at concentrations similar to or sometimes even higher than in blood.<sup>57,85–87</sup> The levels of amino acids in sweat are likely attributed to partitioning from plasma, as well as production of natural moisturizing factors (NMF) and hydrolysis of the epidermal protein filaggrin in the stratum corneum.<sup>88</sup> As such, studies have shown that sweat amino acid concentrations decline with increased sweat rates.<sup>89</sup> Positive correlations between sweat and serum levels, as well as

Table 2. Materials and Properties for Wearable Sweat Sensors

Materials class	Biocompatibility	Permeability	Conductivity	Transparency	Adhesion property	Fabrication	References
Natural materials (textile, paper)	Excellent	Excellent	Poor	Good	Poor	Weaving	105, 106, 129, 244, 246, 700–702
Inorganic materials (liquid metals, Au, Ag, graphene, CNTs <sup>a</sup> , etc.)	Poor	Poor	Excellent	Poor	Poor	Deposition, lithography, inkjet printing, 3D printing, screen printing, self-assembly	112, 117, 121, 122, 703–706
Polymers (PDMS <sup>b</sup> , SEBS <sup>c</sup> , polyimide, etc.)	Good	Poor	Good	Excellent	Excellent	Mold casting, laser engraving, spin coating, lithography	707–710, 133
Hydrogels (alginate, gelatin, PVA <sup>d</sup> , etc.)	Excellent	Excellent	Good	Excellent	Excellent	Mold casting, 3D printing, spin coating, lithography	132, 711–716

<sup>a</sup>CNT, carbon nanotubes. <sup>b</sup>PDMS, polydimethylsiloxane. <sup>c</sup>SEBS, styrene-ethylene-butylene-styrene. <sup>d</sup>PVA, poly(vinyl alcohol).

increases in sweat concentrations after supplement intake, have been reported for nutrients such as ascorbic acid and branch-chain amino acids (BCAAs).<sup>83,87</sup>

**Hormones.** Hormones are chemicals that carry signals throughout our bodies for regulating physiological processes and behavior. Cortisol is a primary glucocorticoid hormone produced by the adrenal glands to regulate the body's stress response. As a large lipid-soluble molecule that can diffuse through lipid bilayer membranes via intracellular passive transport, unbound cortisol is found in various body fluids.<sup>90</sup> However, over 90% of endogenous cortisol in blood is bound to carrier proteins that hinder intracellular passive transport.<sup>91–93</sup> While significantly lower in concentration than serum cortisol levels, cortisol levels in sweat and saliva have been reported to correlate with unbound cortisol in serum.<sup>93,94</sup>

Neuropeptide Y (NPY) is one of the most abundant peptides in the central nervous system and acts as a hormone that has close ties with stress, appetite, and depression.<sup>95</sup> When the levels of various cytokines and neuropeptides were compared between women with and without major depressive disorder (MDD), elevated sweat NPY levels were observed in patient subjects.<sup>96</sup> In addition, a good correlation was found between NPY levels in sweat and blood.<sup>96</sup>

**Proteins.** Proteins are macro molecules (>5 kDa) constructed by numerous amino acids. In sweat, proteins with protective functions for maintaining the epidermal barrier integrity (dermicidin, apolipoprotein D, clusterin, prolactin-includible protein, and serum albumin) make up 91% of the secreted proteins.<sup>97–99</sup> Trace-level proteins such as c-reactive protein (CRP) and cytokines are of particular interest as they modulate the body's inflammation and immune response. While CRP levels in sweat have been reported to be significantly lower than in blood, many cytokines have been reported to be in sweat at concentrations similar to or higher than in blood.<sup>96,100,101</sup> While the exact partitioning mechanism of cytokines into sweat is uncertain, promising correlations between sweat and blood cytokine levels have been widely reported.<sup>96,100</sup> Considering their large size, it is likely that most of the cytokines found in sweat are produced locally by the eccrine gland. However, their production is often due to a systemic response throughout the body, and therefore sweat cytokine levels can still be reflective of systemic levels.

**Substances.** Exogenous substances including toxins and drugs are often metabolized by enzymes and excreted via urine and sweat. When alcohol is ingested, 90% of the ethanol is broken down sequentially into acetaldehyde, acetate, and acetyl coenzyme A (CoA); a portion of the remaining ethanol is excreted through sweat. As ethanol is both soluble in water and lipids, it can passively diffuse through most membranes in

the body, leading to strong correlations between sweat and blood ethanol levels.

### 2.5. Sweat Physiology Outlook

There is much yet to learn about sweat gland physiology. Human sweat duct density and distribution have been investigated using ductal pore counting, colorimetry, and plastic impression techniques.<sup>20</sup> The advent of optical coherence tomography has allowed for noninvasive morphological visualization.<sup>20,34</sup> 3D sweat gland tissue models are being developed to better understand sweat physiology for pathology and tissue regeneration.<sup>15</sup> These models will contextualize sweat measurements and correlated analyte concentrations by revealing interdependent pathways. Improved sweat gland models may help in developing algorithms for calibration.

The development of continuous, compact, on-body collection-to-analysis sweat sensing platforms will further improve the quality and quantity of data for sweat characterization. Real-time multiplexed sweat measurements will also contribute to our understanding of the physiological sweat response. Tissue level sweat pH regulation remains a hurdle for pH-dependent sensing platforms. Understanding the acid–base controls in the sweat gland may aid in designing on-body stimulation and collection platforms at predictable sweat pH. Elucidating the factors that contribute to dynamic sweat concentrations and analyte partitioning is necessary to relate noninvasive sweat measurements to system-level changes both in time and concentration. Increasing our understanding of the physiology of the sweat gland and surrounding skin tissue may also better explain variations in localized sweat measurements from systemic trends. Data from biological models and wearable sweat sensors will complement each other for growth in both fields.

## 3. ESSENTIAL MATERIAL PROPERTIES FOR WEARABLE SENSORS

On-body applications and unique operating conditions in complex biofluids require wearable sweat sensors to have certain essential material properties. Functional materials in wearables typically include four classes:<sup>4</sup> natural materials such as textiles and papers, inorganic conducting materials as well as nanomaterials including metallic and carbon-based composites, stretchable polymers, and stretchable hydrogels (Table 2). In this section, we summarize and review essential material properties requisite for wearable sweat sensing applications.

### 3.1. Biocompatibility

Biocompatibility is defined as the ability of a material to perform with an appropriate host response in a specific

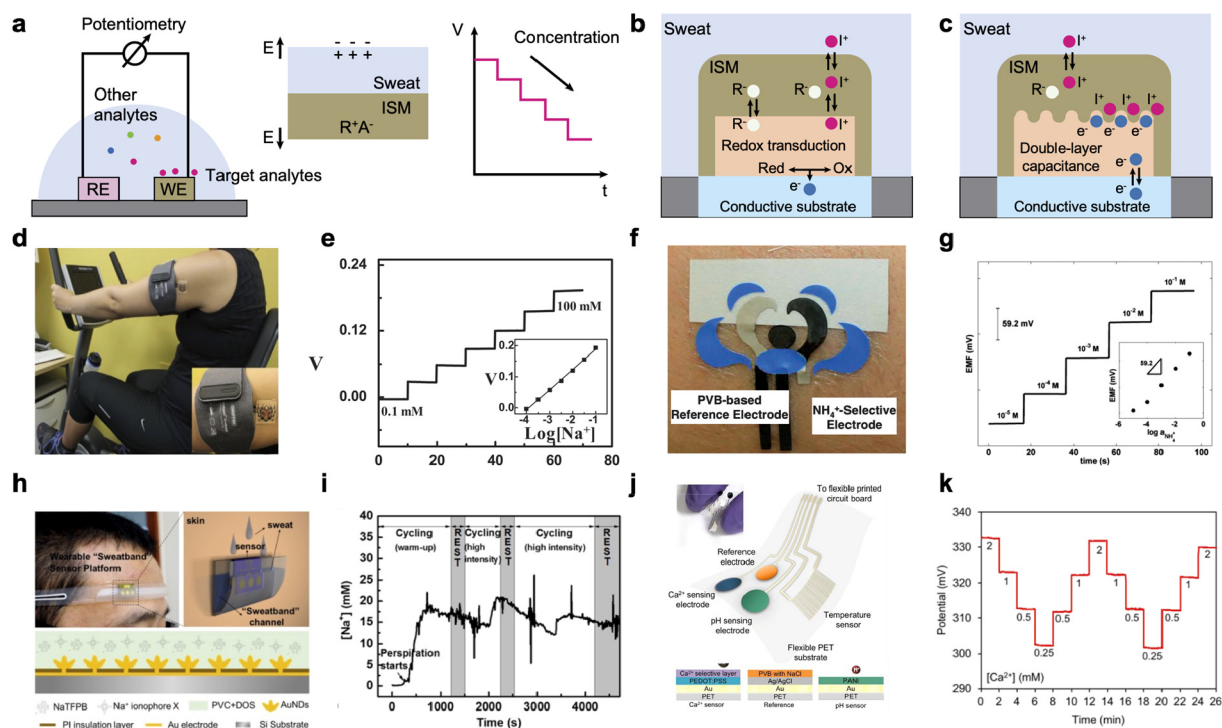


**Figure 3.** Electrochemical potentiometric sweat sensors. **a**, Schematic of potentiometry operating mechanism and sensor configurations. **b**, Schematic showing the redox capacitance-based ISEs using electroactive materials as ion-to-electron transducers. **c**, Schematic showing the double-layer capacitance-based ISEs using nanomaterials as ion-to-electron transducers. **d**, An epidermal potentiometric sodium sensor on a subject performing exercise activities. **e**, Sensor response to varying sodium concentrations over 0.1–100 mM range. **d,e**, Reproduced with permission from ref 152. Copyright 2014 Elsevier. **f**, An epidermal potentiometric ammonium sensor with a PVB-based reference electrode. **g**, Sensor response to varying sodium concentrations over 0.1–100 mM range. **f,g**, Reproduced with permission from ref 153. Copyright 2013 Royal Society of Chemistry. **h**, A wearable sweat sensor platform based on gold nanodendrite array. **i**, Real-time on-body sodium data using the sweatband sensor over a period of repetitive indoor cycling. **h,i**, Reproduced with permission from ref 154. Copyright 2017 American Chemical Society. **j**, A fully integrated wearable wristband that could detect  $\text{Ca}^{2+}$  and pH at the same time. **k**, A representative sensitivity and repeatability performance test of  $\text{Ca}^{2+}$  sensors. **j,k**, Reproduced with permission from ref 147. Copyright 2016 American Chemical Society.

application.<sup>102</sup> Biocompatibility is one of the key considerations for wearable sensors, as nontoxic materials as well as resistance to biofouling and corrosion are prerequisite before on-body human experiments. A number of biomaterials have been studied, including metals (titanium, gold, stainless steel and alloys), ceramics, polymers, and composite materials.<sup>103</sup> For wearables, natural materials such as cellulose and fabrics are optimal for long-term wearing,<sup>104–106</sup> while a number of synthesized inert materials have demonstrated similar properties.<sup>7,107</sup> Depending on their applications, transient bioresorbable materials have also been developed to meet disposable use.<sup>108,109</sup>

### 3.2. Permeability

Permeability of a material is an advantage for long-term wear as it allows the exchange of heat, air, and moisture, which affects thermal comfort and wetness discomfort.<sup>110</sup> Most early pioneering examples of wearables were focused on transitioning rigid wafer-based materials into flexible ones, which usually applied polyimide (PI) or polydimethylsiloxane (PDMS) as the substrate, and thus were not gas or sweat permeable.<sup>111</sup> Subsequent research introduced a number of gas and sweat permeable material substrates, including textiles and fabrics,<sup>105,106</sup> as well as tattoo-like electrodes without substrates;<sup>112</sup> however, the permeability to sweat also causes measuring inaccuracies of sweat biomarkers. To meet the recent demands of sweat monitoring, materials that are comfortable, gas permeable, and sweat impermeable have

been further developed, often using structurally engineered nanomeshes with tiny pores for gas exchange.<sup>113,114</sup>

### 3.3. Conductivity

Conductive materials are the foundation for wearable sensors and devices. An ideal conductive material aims to retain stable electrical performance against strain and sweat interference. One example is to use liquid metals and ionic liquids,<sup>115–118</sup> as they can best offer conductivity and stretchability in their intrinsic fluidic nature. However, liquid metals need to be encapsulated in channels and typically require complex designs for integrated electronics. Therefore, a number of conductive polymers and hydrogels have been introduced that balance cost and stretchability.<sup>119,120</sup> In order to improve the conductivity, nanomaterials including both nanoparticles and nanowires are often adopted.<sup>121,122</sup>

### 3.4. Transparency

Considering the wearing comfort and daily user compliance, transparent materials have gained rising interest. One design strategy is to use ultrathin materials, and build the wearable sensors into tattoo-like patches for both physiological and biochemical monitoring.<sup>123,124</sup> Another approach is to apply intrinsically transparent nanomaterials such as nanomesh and nanowire networks,<sup>125–127</sup> and transparent polymers and hydrogels such as PDMS.<sup>128</sup>

### 3.5. Adhesion Property

A strong adhesion to skin can improve signal reliability. However, excessive adhesion may also make removing the wearable patch difficult after use and may even cause skin irritation. For ultrathin and ultralight electrode tattoo patches, they can be applied onto human skin by surface tension.<sup>112,129</sup> For more complicated wearable devices with electronics, external adhesives are usually introduced, such as using bandages or medical adhesives.<sup>130,131</sup> However, these adhesive methods usually require additional cleaning as adhesive residue is often leftover on the skin after the patch is removed. Several recent studies have focused on adhesive dry electrodes,<sup>132,133</sup> which aim to achieve a robust and reversible adhesion on sweaty skin.

### 3.6. Scalability

Fabrication cost and scalability is one of the key considerations when it comes to practical use. To decrease the cost of conventional cleanroom lithography,<sup>123</sup> a number of fabrication methods have been carried out, including transfer printing,<sup>134</sup> electrospinning,<sup>112</sup> roll-to-roll gravure printing,<sup>135</sup> laser engraving,<sup>75</sup> 3D printing,<sup>136</sup> inkjet printing,<sup>137</sup> and screen printing.<sup>138</sup>

Overall, the application of on-body wearable sensors requires building materials to be biocompatible, conductive for electrical interconnects, comfortable for daily wearing, and scalable for mass fabrication. In addition to these requirements that are general to wearable sensing, wearable sweat sensors demand special attention to materials that can achieve strong adhesion with sweaty skin, high stability in the sweat matrix, and selective permeability of gas and sweat.

## 4. BIOSENSOR MECHANISMS

Novel sweat sensing platforms based on various detection methods have raised enormous attention for noninvasive and real-time biomarker detection *in situ* for personalized healthcare.<sup>1–3,9</sup> These sensors are required to be miniaturized for on-body wearing and label-free for direct measurements.<sup>4,5</sup> Not only are they required to have robust performance in complex and dynamic chemical environments, but also to have a sufficient detection limit and a wide linear range to detect biomarkers at physiologically relevant ranges. Most wearable sweat sensors are based on electrochemical, optical, and bioaffinity detection mechanisms. In the following sections, we describe in detail the major categories and their sensing mechanisms.

### 4.1. Electrochemical Potentiometric Sensors

Wearable potentiometric sensors measure the passive open-circuit potential between the working electrode and reference electrode (Figure 3a). Such electrochemical sensors consist of a sensing electrode that is modified with a target-sensitive component and a reference electrode that maintains a stable potential in different solutions such as sweat. Most wearable potentiometric sensors are based on ion-selective electrodes (ISEs), which use a nondestructive measurement that converts ionic signals to electric potentials. The measured potential signal follows the well-known Nernst equation<sup>139</sup>

$$E = E_0 + \frac{RT}{nF} \ln a_i$$

where  $E$  is cell potential,  $E_0$  is standard potential when  $a_i = 1$ ,  $R$  is the universal gas constant,  $T$  is absolute temperature,  $n$  is the

number of electrons involved,  $F$  is the Faraday constant, and  $a_i$  is ionic activity quotient in aqueous and solid membrane phases. From the Nernst equation, the theoretical potential response limit of ISEs is around 59.2 mV at 25 °C per decade change of target analyte concentration. Due to its low-cost, simple operation, and reliable and continuous measurement, ISEs have been widely applied for the detection of trace-level metals,<sup>140,141</sup> drugs,<sup>142,143</sup> and organics.<sup>144</sup> Conventional ISEs are based on liquid contact, which is unfavorable for miniaturized designs and wearable usage. Solid-contact ISEs, on the other hand, have enabled the continuous detection of ions such as  $\text{Na}^+$ ,  $\text{K}^+$ ,  $\text{H}^+$ ,  $\text{Ca}^{2+}$ , using potentiometric sensors in biofluids,<sup>12,145–148</sup> as well as heavy metal pollutants.<sup>149</sup>

The typical structure of an ISE consists of a sandwiched structure including an electron-conductive electrode substrate, an ion-to-electron transduction layer, and an ion-selective membrane (ISM) layer. A variety of solid-contact ISE materials have been studied as ion-to-electron transducers, mainly into two categories:<sup>150</sup> redox capacitance using electroactive materials, and double-layer capacitance using nanomaterials (Figure 3b,c). ISMs typically contain an ionophore, lipophilic anionic sites, and a polymer matrix with its plasticizer. The polymer matrix is ion-permeable and enables strong mechanical stability to protect the ionophore and anionic sites from leaching and damage during operation. While primary ions could migrate into and out of the ISM, the ionophore binds to specific target ions across the solution/membrane interface. Due to such permselectivity, only the target ions can be transduced to the electrode substrate. Lipophilic anionic sites, also known as ion-exchangers, facilitate a charge neutral state of the ISM in order to attract ion movement. Meanwhile, the reference electrode is usually based on Ag/AgCl with saturated  $\text{Cl}^-$  ions in a polymer matrix to keep a stable reference potential.<sup>151</sup>

Conducting polymers are the most studied candidates for the ion-to-electron transduction layer due to their high redox capacitance and their electrical and ionic conductivity. As shown in Figure 3b, conducting polymers, including polyaniline (PANI), polypyrrole (PPY), poly(3,4-ethylenedioxythiophene) (PEDOT), and poly(3-octylthiophene) (POT), can serve as the transducer by reversible doping–dedoping cycles of  $\text{Ox} + e^- \rightleftharpoons \text{Red}$ , where PANI, PPY, and PEDOT are stable in fully oxidized forms and POT is stable in the nonoxidized form.<sup>155</sup> In wearable applications, however, only PEDOT and PANI have been widely used, as PPY is sensitive to side reactions in complex media at different potentials,<sup>155</sup> and POT is vulnerable owing to its gradual dissolution and severe drift.<sup>156</sup> PANI and PEDOT can be conveniently deposited onto the conductive substrate with controlled thickness through electropolymerization using electrochemical scans. PANI can serve as a standalone pH sensor as it also demonstrates protonation–deprotonation capability to  $\text{H}^+$  in solutions.<sup>157</sup> PEDOT is known to have low sensitivity to  $\text{O}_2$  and pH,<sup>158</sup> which is highly suitable for wearable sweat sensors. In addition to conducting polymers, some other electroactive materials have also been reported, including self-assembled monolayers (SAMs),<sup>159–162</sup> ion exchange resins,<sup>163,164</sup> and metallic redox couples.<sup>165–167</sup>

Nanomaterials with a large surface area, on the other hand, can directly convert ion charges to electronic signals through double-layer capacitance mechanism (Figure 3c). Nanomaterials pose a high contact area with ISM, and therefore, a large double-layer capacitance is formed at the interface where

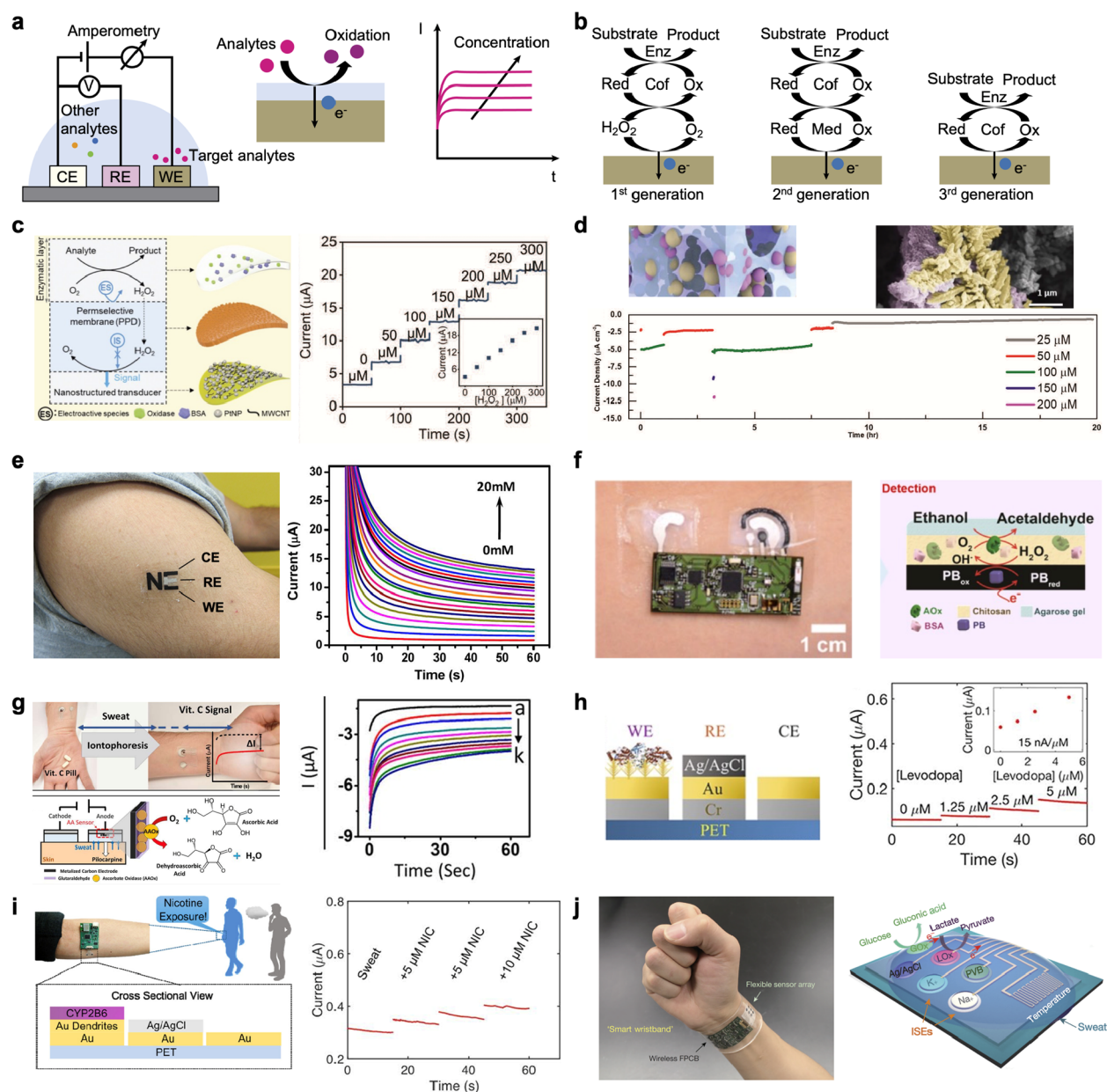


**Figure 4.** Electrochemical amperometric sweat sensors. **a**, Schematic of amperometry operating mechanism and sensor configurations. **b**, Schematic showing the 3 generations of amperometric enzymatic sensors. **c**, A 1st generation wearable mediator-free enzymatic sensor with capability to detect glucose, lactate, and choline. Reproduced with permission from ref 187. Copyright 2019 Wiley. **d**, A 2nd generation wearable glucose sensor with porous membrane that enables long-term glucose monitoring for up to 20 h. Reproduced with permission from ref 188. Copyright 2019 Wiley. **e**, A wearable lactate tattoo sensor was built for lactate sensing in human perspiration during exercise. Reproduced with permission from ref 189. Copyright 2013 American Chemical Society. **f**, A wearable alcohol sensor for noninvasive alcohol monitoring in iontophoresis-induced sweat. Reproduced with permission from ref 190. Copyright 2016 American Chemical Society. **g**, A flexible tattoo patch for vitamin C detection to keep track of nutrients level in the body and guide dietary interventions. Reproduced with permission from ref 191. Copyright 2020 American Chemical Society. **h**, A wearable sweat band for noninvasive levodopa drug monitoring for Parkinson's disease. Reproduced with permission from ref 192. Copyright 2019 American Chemical Society. **i**, A wearable sweat band using nicotine-oxidizing enzyme, cytochrome P450 2B6 for noninvasive nicotine detection. Reproduced with permission from ref 193. Copyright 2020 American Chemical Society. **j**, A fully integrated wearable wristband that could detect metabolites and electrolytes at the same time. Reproduced with permission from ref 12. Copyright 2016 Springer Nature.

electrons at the nanomaterials side and ions at the ISM side attract each other through Coulomb interaction. In order to enhance the ion-to-electron transduction efficiency, a lot of nanomaterials of different dimensions have been proposed in order to maximize the interface contact area, including spherical carbon fullerene,<sup>168,169</sup> carbon nanotubes (CNTs),<sup>170–172</sup> graphene,<sup>173–175</sup> metallic nanopar-

ticles,<sup>176–178</sup> metal–organic frameworks (MOFs), and so on.<sup>179</sup>

With recent development in personalized healthcare and digital medicine, monitoring the electrolyte balance in biofluids such as sweat has attracted growing interest. Na<sup>+</sup> detection is one of the most distinguished wearable applications, as sodium plays a key role in electrolyte balance and dehydration prevention. Figure 3d shows an example of an epidermal

potentiometric sodium sensor, which was fabricated with screen-printed carbon electrodes followed by tattoo transfer.<sup>152</sup> A near-Nernstian response to varying sodium concentrations over 0.1–100 mM range was observed (Figure 3e), with a rapid response to dynamics within 10 s. On-body testing of the sensor during exercise was performed with the capability to monitor sweat sodium dynamics continuously. Similarly, an ammonium sensor was developed by applying an ammonium-selective ISM based on the nonactin ionophore,<sup>153</sup> with a polyvinyl butyral (PVB)-based reference electrode (Figure 3f). The obtained potentiometric sensor showed a wide range between 0.1 and 100 mM, which is within the physiological levels of ammonium in sweat, as shown in Figure 3g.

To increase the ion-to-electron transduction efficiency and facilitate miniaturized wearable design, gold nanodendrite arrays were introduced as an alternative solid-contact that achieved high performance through double-layer capacitance. As shown in Figure 3h, a wearable gold nanodendrite array-based sensor platform was carried out, with a much larger surface area of around 7.23 cm<sup>2</sup> compared with 1.85 cm<sup>2</sup> of unmodified bare electrodes.<sup>154</sup> The sensor was fabricated on a microwell patterned chip and exhibited a three-dimensional branched structure to increase interface contact and hydrophobicity. The highly enhanced surface area guaranteed fast response to exercise and rest dynamics (Figure 3i).

With individual sensors detecting one specific analyte at a time, multiplexed screening of several target electrolytes in an integrated platform could enable a more complete health profile to meet the needs of clinical applications. One such multiplexed system shown in Figure 3j exhibits a fully integrated wearable wristband that could detect Ca<sup>2+</sup> and pH at the same time.<sup>147</sup> Measurement of ionized calcium was challenging due to its dependence on pH, with an increase in calcium concentration when pH decreases (Figure 3k). With dual-channel, simultaneous measurements, real-time quantitative sweat analysis was enabled and provided insight about Ca<sup>2+</sup> and pH homeostasis in human body.

The sensitivity of the potentiometric sensors is guided by Nernst equation where the potential changes logarithmically with target concentration. Despite significant progress in wearable potentiometric sensors, many limitations remain unaddressed to meet the practical clinical wearable applications. The stability of ISE potential depends on the chemical stability and reversible transitions. One failure mechanism is due to chemical leaching of the ionophore and ion-exchangers in the ISM over long-term operation, which may cause the readings to drift over time.<sup>180,181</sup> This is mainly determined by the polymeric ISM diffusion properties. Another failure mechanism is due to water formation at the ISM/conductive substrate interface. The uptake and diffusion of water in the polymeric ISM is the main reason for the water layer formation,<sup>173–175</sup> in which water acts as a reservoir with changing compositions and forms a dynamic interface potential affecting the accuracy of readings. Research has found that a thin water layer as small as 100 Å could harm sensor readings, selectivity, and drift rate.<sup>182,183</sup> With further water formation, the adhesion between the ISM and substrate is weakened and may cause the ISM to delaminate.<sup>184</sup> Therefore, it is crucial that a highly hydrophobic and low water absorptive material is selected for the ISM matrix, and that an efficient mechanical adhesion between the substrate and ISM can be obtained, so that a well-protected ion-to-electron transduction layer is formed against water for robust and long-term operations.

Another challenge for wearable ISE commercialization is the unpredictable E<sup>0</sup> deviation between electrodes, which requires ISEs to be calibrated every time before use. Conducting polymers exist in wide-ranging redox states with different doping levels during deposition.<sup>185</sup> Nanomaterial thickness and local microscopic morphology could also cause enormous variations between sensor batches, especially with differences in experimental protocols. A universal approach to preparing reproducible and consistent ISEs with minimal calibration is needed to achieve the ultimate goal of calibration-free and maintenance-free sensors for user-friendly applications.

## 4.2. Electrochemical Amperometric Sensors

Wearable amperometric sensors measure current signals of redox reactions during the target substrate to product process at a constant applied potential. Such electrochemical sensors typically consist of a 3-electrode configuration, in which a working electrode is immobilized with a target-sensitive component, a counter electrode that forms a closed circuitry, and a reference electrode with a stable potential (Figure 4a). The most common amperometric sensors are enzymatic sensors, in which the highly target selective and sensitive enzymes are immobilized onto the electrode surface in a hydrophilic porous matrix. For an ideal amperometric sensor, the current density is linearly proportional to the target concentration, allowing for immediate quantification for analytes.

Enzymatic sensors consist of three generations depending on the direct/indirect detection and electron transfer mechanism (Figure 4b). A first generation enzymatic sensor is developed by monitoring hydrogen peroxide (H<sub>2</sub>O<sub>2</sub>) in the enzymatic reaction at the electrode surface. Most enzymatic sensors utilize oxidases, such as glucose oxidase (GOx) complexed with coenzyme flavin adenine dinucleotide (FAD), or glucose dehydrogenase (GDH), in conjunction with cofactors (e.g., flavin adenine dinucleotide (FAD) and pyrroloquinoline quinone (PQQ)), which are widely adopted for enzymatic glucose sensors.<sup>186</sup> GOx oxidizes glucose into gluconic acid in the presence of water and oxygen, and H<sub>2</sub>O<sub>2</sub> is further oxidized, during which electron transfer is accomplished through cofactor FAD. As shown in Figure 4c, enzymatic sensors, composed of a coupled platinum nanoparticle/multiwall carbon nanotube layer and a permselective membrane layer, can be used to detect glucose, lactate, and choline could be detected with high sensitivity and selectivity.<sup>187</sup> First generation enzymatic sensing is an indirect monitoring method and the oxidase reaction relies on the use of oxygen as an electron acceptor. Once the oxygen concentration fluctuates in the solution, error readings can occur.

To eliminate oxygen dependence, second generation enzymatic sensors replace oxygen with a synthesized mediator as the electron acceptor, shuttling electrons from glucose oxidase to the electrode. A representative mediator is Prussian blue (PB), which is widely adopted due to its high electrocatalytic activity for H<sub>2</sub>O<sub>2</sub> reduction in the presence of O<sub>2</sub> relative to conventional electrodes (e.g., platinum), and its low redox potential at around 0 V.<sup>194</sup> An example second generation wearable glucose sensor was based on an all-printed temporary tattoo with a reverse iontophoretic module integrated for extraction of interstitial glucose.<sup>124</sup> As a proof of concept, the patch could monitor variations in glycemic levels before and after food consumption. However, PB-based

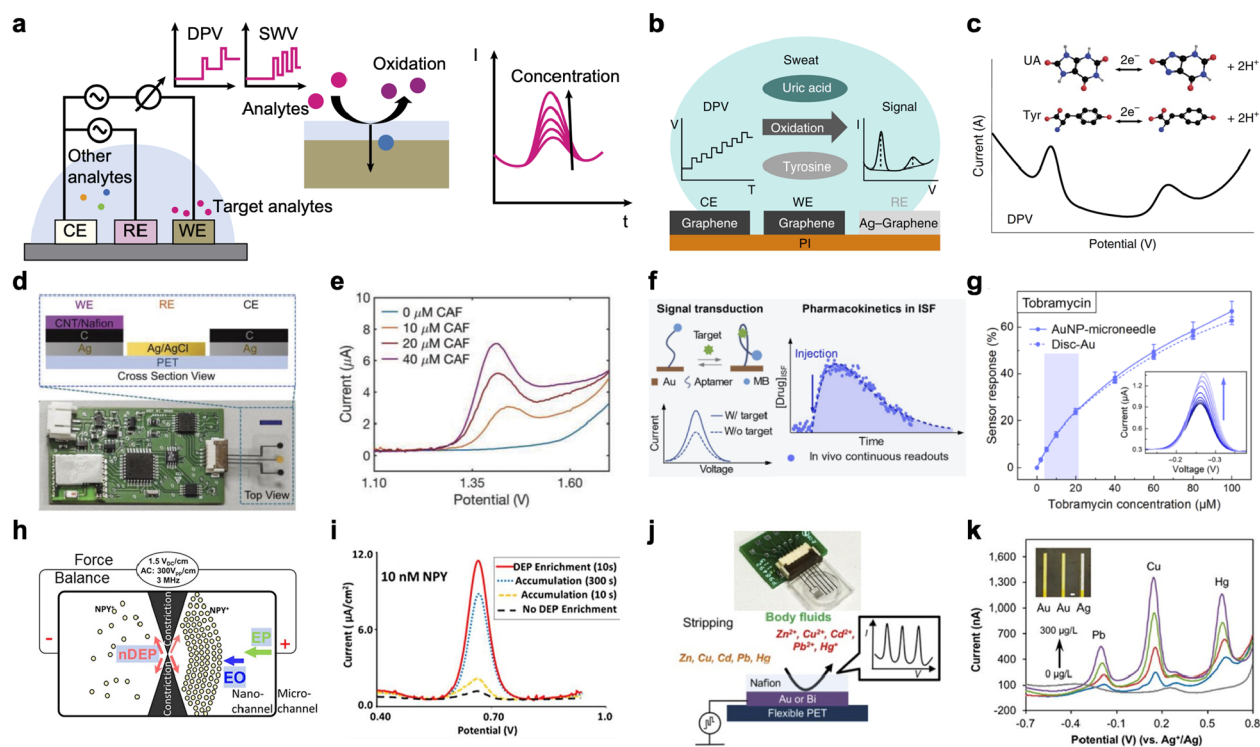


**Figure 5.** Electrochemical sweat sensors using direct oxidation. **a**, Schematic of differential pulse voltammetry (DPV)/square wave voltammetry (SWV) operating mechanism and sensor configurations. **b**, Detection of uric acid and tyrosine in sweat based on a laser-engraved sensor. **c**, Quantitative analysis of uric acid and tyrosine is based on oxidation peak height in DPV curve. **b,c**, Reproduced with permission from ref 75. Copyright 2019 Springer Nature. **d**, Detection of sweat caffeine levels using a wearable sweatband after drug intake. Scale bar, 5 mm. **e**, Characterization of a caffeine sensor with a linear response between peak height and caffeine concentrations with a high sensitivity. **d,e**, Reproduced with permission from ref 206. Copyright 2018 Wiley. **f**, Monitoring of circulating drugs' pharmacokinetics using an aptamer immobilized sweat sensor. **g**, Detection of antibiotics dynamics such as tobramycin and vancomycin that do not have natural recognition elements. **f,g**, Reproduced with permission from ref 205. Copyright 2022 The American Association for the Advancement of Science. **h**, Electrokinetic preconcentration of the neuropeptide Y using negative dielectrophoretic (nDEP) trapping. **i**, Electrochemical detection of neuropeptide Y and Orexin A at picomolar levels from subnanoliter solution samples with dielectrophoresis preconcentration. **h,i**, Reproduced with permission from ref 210. Copyright 2014 American Chemical Society. **j**, Detection of heavy metals from body fluids such as sweat using electrochemical square wave anodic stripping voltammetry. **k**, Simultaneous detection of Pb, Au, and Hg on a Au working microelectrode. **j,k**, Reproduced with permission from ref 211. Copyright 2016 American Chemical Society.

enzymatic sensors have poor operation stability,<sup>187,188</sup> making sensor readings unreliable and unverifiable over time. One follow-up study improved the stability by introducing a porous membrane with effective enzyme immobilization (Figure 4d).<sup>188</sup> The porous membrane exhibited a robust adhesion to nanodendritic solid contacts, which facilitated PB maintenance and prevented enzyme outflow. Together with synthesized nanostructured electrodes, the wearable glucose sensor demonstrated long-term glucose monitoring for up to 20 h. The third generation enzymatic sensors are mediator-free and enable direct electron transfer between enzyme and electrodes, which reduces the influence of mediator deterioration. This is usually realized by using nanomaterials such as carbon nanotubes (CNTs)<sup>195,196</sup> and MOFs.<sup>197</sup>

A number of wearable enzymatic sensors have been built for different wearable applications. For example, a wearable lactate tattoo sensor was built for lactate sensing in human perspiration during exercise (Figure 4e).<sup>189</sup> The sensor was applied to human subjects for real-time continuous monitoring of sweat lactate dynamics during cycling exercise, during which the sensors demonstrated flexibility against mechanical deformation.

Wearable amperometric sensors can be used not only for monitoring natural metabolites within sweat, but also for

monitoring food and drug intake by tuning the corresponding enzyme. For example, a wearable alcohol sensor was developed for noninvasive alcohol monitoring in iontophoresis-induced sweat (Figure 4f).<sup>190</sup> On-body human studies demonstrated the capability of differentiating ethanol level increase before and after alcohol consumption, which could be used to prevent drunk driving. Similarly, nutrient intake monitoring such as vitamin C could be enabled to keep track of nutrient levels in the body and guide dietary interventions.<sup>191,83</sup> As shown in Figure 4g, a flexible tattoo patch was modified with ascorbate oxidase and applied onto several human subjects' wrists.<sup>191</sup> Dynamic rise and fall of sweat vitamin C concentrations were observed consistently among different subjects taking varying amounts of both commercial vitamin C pills and vitamin C-rich fruit juices, indicating the potential for personalized nutrition solutions. Besides nutrient intake, wearable enzymatic sensors could be used for drug intake as well. Figure 4h demonstrates noninvasive levodopa monitoring, which is the standard medication clinically prescribed for Parkinson's disease treatment.<sup>192</sup> Optimization of levodopa dosage plays a key role in Parkinson's symptom management and mitigating side effects, yet the drug dosage is highly dependent on patient conditions. To monitor the low-concentration of levodopa, a nanodendritic platform was fabricated to increase sensitivity to

as low as  $1.25\ \mu\text{M}$ .<sup>192</sup> On-body studies exhibited an increase of levodopa levels after the subjects consumed levodopa-containing fava beans, which suggests the potential for routinely monitoring levodopa dosage and drug misuse prevention.

Wearable amperometric sensors can also be adopted to monitor potential environmental hazards. As demonstrated in Figure 4i, nicotine detection can be achieved using a wearable sweat band.<sup>193</sup> A nicotine-oxidizing enzyme, cytochrome P450 2B6, was immobilized onto a nanodendritic surface using a self-assembled monolayer of 11-mercaptopundecanoic acid. Both smokers and nonsmoker subjects were tested, showing elevated sweat nicotine levels for subjects with cigarette smoke inhalation. Such a platform can be used for smoke exposure assessment and modified for other potential hazards.

It is worth noting that wearable amperometric sensors can be combined with the aforementioned wearable potentiometric sensors to monitor metabolites and electrolytes at the same time. As shown in Figure 4j, a fully integrated wearable sensor array that monitors glucose, lactate,  $\text{Na}^+$ , and  $\text{K}^+$  could be assembled for multiplexed *in situ* perspiration analysis on a single platform.<sup>12</sup> A customized FPCB was developed for signal transduction, processing and wireless transmission. Temporal metabolite and electrolyte profiles can be obtained simultaneously with human subjects engaged in physical activities, which represents a milestone in the development of personalized health monitoring.

Amperometric sensors can measure analytes in a wide range of concentrations (ranging from  $\mu\text{M}$  to tens of mM), and their sensitivities usually depend on electrode size and sensor structure. When analyzing targets below  $\mu\text{M}$  levels, amperometric sensors typically suffer from low signal-to-background noise ratios. In addition, the sensitivity of the enzymatic sensors can be influenced by the matrix pH and operation temperature. To date, several approaches have been carried out to increase sensitivity and stability of wearable amperometric sensors. To increase sensitivity, nanomaterials including gold nanodendrites,<sup>192,193</sup> gold nanomesh,<sup>198</sup> gold fibers,<sup>199</sup> Pt nanospheres modified carbon textile,<sup>200</sup> MXenes,<sup>201</sup> and so on were carried out to increase sensor surface area. Another research focus is to improve the stability and long-term operations in sweat. Wearable enzymatic sensors may fail due to the poor stability of mediators, including PB, in complex solutions.<sup>187,188</sup> As a side reaction, PB can react to the hydroxide ions and therefore is soluble in neutral sweat, which causes the sensor to malfunction over time.<sup>202</sup> It is also known that biofouling and electrode surface inactivation may limit the practical use of affinity-based wearable amperometric sensors in complex biofluids. Some recent studies have been carried out to introduce antifouling coatings for working electrodes,<sup>203,204</sup> which prevents nonspecific interactions and preserves original mediators. However, introducing additional coatings may also sacrifice sensitivity, which is unfavorable for low-concentration analytes. There is a high demand for more research on stabilizing mediators and antifouling functional materials.

### 4.3. Electrochemical Direct Oxidation

In addition to chronopotentiometry and chronoamperometry, a number of electrochemical techniques, including square wave voltammetry (SWV),<sup>205</sup> differential pulse voltammetry (DPV),<sup>206</sup> fast-scan cyclic voltammetry (FSCV),<sup>207</sup> and linear sweep voltammetry (LSV),<sup>87</sup> have been developed to realize

direct target detection and bypass the need of target-sensitive components such as ionophores and enzymes. SWV and DPV are among the most common approaches for detecting electroactive materials. Similar to amperometric configurations, DPV/SWV-based sensing involves a 3-electrode system, including a working electrode with high material stability and high surface area, a counter electrode that forms a closed circuitry, and a reference electrode with a stable potential (Figure 5a). A time-dependent staircase excitation waveform of pulsed step voltammetry was applied between the working and counter electrodes to increase the ratio between the faradaic and nonfaradaic currents, and the current response is recorded before and at the end of the pulsed voltage. Reduction occurs at the working electrode surface when the potential is lower than the redox potential, and at potentials higher than the redox potential, oxidation occurs.<sup>208</sup> During redox reactions, electroactive materials lose or gain electrons accordingly, resulting in current response with a limit of detection down to nanomols.<sup>209</sup>

DPV and SWV methods have been widely applied to monitor electroactive molecules in sweat.<sup>75,87,205,206</sup> For example, uric acid and tyrosine in sweat, which are risk factors for cardiovascular disease and metabolic disorders,<sup>212,213</sup> can be detected at low concentrations on a laser-engraved sensor with DPV (Figure 5b).<sup>75</sup> Quantitative analysis is based on the oxidation peak height in the DPV curve, as shown in Figure 5c. Detection of uric acid and tyrosine was evaluated on physically trained and untrained subjects under exercise and after a protein-rich diet, as well as gout patients, which provides a paradigm for noninvasive electroactive metabolites monitoring. Additionally, when the electrode is functionalized with molecularly imprinted polymers and redox-active nanoparticles, trace-levels of multiple metabolites and nutrients, including all essential amino acids and vitamins could be analyzed.<sup>87</sup>

Apart from metabolite monitoring, DPV and SWV measurements can be used for drug intake detection as well. For example, sweat caffeine levels can be monitored using roll-to-roll printed CNTs/Nafion modified carbon electrodes as shown in Figure 5d.<sup>206</sup> The caffeine sensor demonstrated a linear response between voltammogram peak height and caffeine concentrations with a high sensitivity (Figure 5e). An elevated caffeine concentration in sweat was observed after caffeine consumption. Similarly, when the electrode was further immobilized with drug-specific aptamers, real-time measurements of the circulating drugs' pharmacokinetics could be realized, as shown in Figure 5f.<sup>205</sup> Efficient transduction of the target–aptamer binding was converted into current readouts using SWV, which could then be used to predict the drug's pharmacokinetic characteristics. Therapeutic monitoring of antibiotic dynamics (e.g., tobramycin, vancomycin), which do not have natural recognition elements, was enabled (Figure 5g), which could improve antibiotics-based treatments.

To increase the limit of detection of direct oxidation techniques, electrochemical preconcentration techniques have been implemented to detect neurotransmitters and neuromodulators. For example, Figure 5h demonstrates an electrokinetic preconcentration of the NPY and Orexin A within small volume samples.<sup>210</sup> Both NPY and Orexin A have extremely low concentrations at picomolar levels within sweat.<sup>96</sup> By integrating negative dielectrophoretic enrichment or by electrochemical adsorptive accumulation, million-fold enrichment of target biomarkers was first accumulated onto

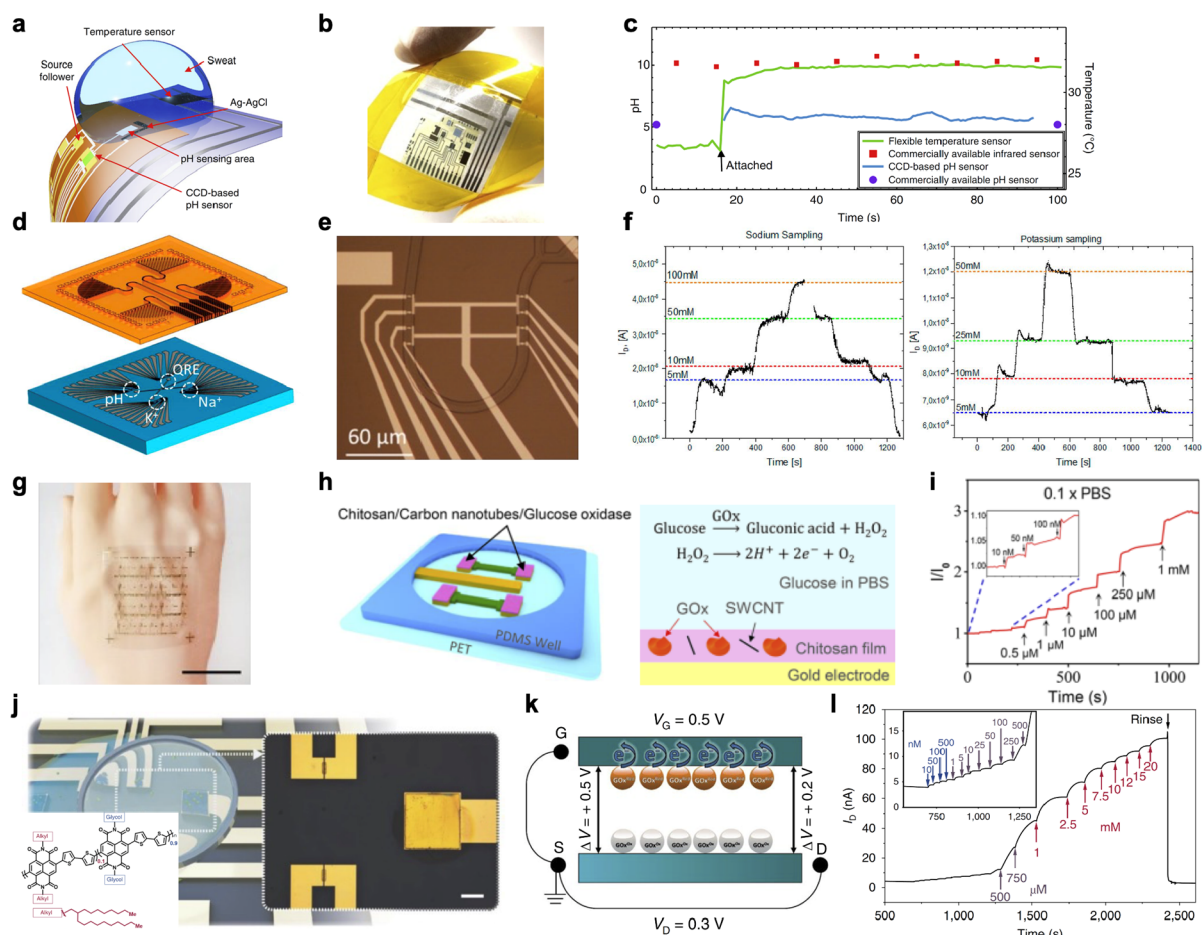


**Figure 6.** Wearable sweat sensors based on transistors. **a**, A transistor-based inorganic pH chemical sensor with ultrahigh sensitivity beyond Nernst limit. **b**, Optical image of the pH transistor using flexible polyimide as substrate. **c**, pH monitoring with a sensitivity of around 240 millivolts per pH unit. **a–c**, Reproduced with permission from ref 219. Copyright 2018 Springer Nature. **d**, A lab-on-skin system with microfluidics on top of an ISE-functionalized FET chip. **e**, Optical image of the microfluidics system, which aligned on the top gate of the FET array. **f**, Real-time measurement of  $\text{Na}^+$  and  $\text{K}^+$  ions with steep variations of the drain current using ion-selective FET. Scale bar, 3 cm. **d–f**, Reproduced with permission from ref 220. Copyright 2018 American Chemical Society. **g**, A wearable  $\text{In}_2\text{O}_3$  nanoribbon transistor with a fully integrated on-chip gate for glucose detection in sweat. **h**, The sensor source and drain electrode were immobilized with GOx, using sweat as the liquid gate dielectric. **i**, A wide detection range from nM level to mM level and a detection limit down to 10 nM was obtained using nanoribbon FET. **g–i**, Reproduced with permission from ref 221. Copyright 2018 American Chemical Society. **j**, Schematic of the organic electrochemical transistor to detect glucose and power generation from biofluids. Scale bar, 200  $\mu\text{m}$ . **k**, Schematic of enzymatic reaction transferring electrons to the channel when gate voltage is smaller than source-drain bias. **l**, Real-time response of the mediator-free enzyme-coupled organic FET to successively added glucose in biofluids. **j–l**, Reproduced with permission from ref 222. Copyright 2019 Springer Nature.

patterned graphene-modified electrodes, followed by electrochemical detection of NPY and Orexin A at picomolar levels from subnanoliter solution samples (Figure 5i). Under the precisely controlled trapping force of dielectrophoresis, such methods successfully avoided interferences from high levels of dopamine and ascorbic acid within biological matrices, allowing for comparable detection sensitivities to immunoassays.<sup>210</sup>

In addition to detecting electroactive molecules, electrochemical direct oxidation methods can be applied to detect heavy metals. Heavy metals are known to harm different body organs and cause both acute and chronic toxic effects.<sup>214</sup> Although major ions such as  $\text{Na}^+$ ,  $\text{K}^+$ , and  $\text{Ca}^{2+}$  can be monitored using potentiometric ISEs as aforementioned, trace-levels of heavy ions on the order of  $\mu\text{g}/\text{L}$  are below the detection limit and do not have a universal ionophore for simultaneous measurement. Therefore, a preconcentration technique was developed to detect heavy metals in sweat. As

shown in Figure 5j, using an electrochemical square wave anodic stripping voltammetry (SWASV), simultaneous measurement of Zn, Cd, Pb, Cu, and Hg ions can be achieved on Au and Bi microelectrodes.<sup>211</sup> Heavy metal ions in solution were first reduced and accumulated onto the electrode surface, followed by anodic stripping analysis, during which distinct peaks at different oxidation potentials were observed (Figure 5k).

For direct oxidation methods, these electrochemical sensors could detect ultralow concentrations of analytes (down to nM) as DPV and SWV minimize the background charging current and realize highly sensitive electrochemical target analysis. Note that when coupled with electrochemical preconcentration techniques, they can achieve even lower detection limits down to sub-nM or pM levels. Despite the significant development in detecting low concentrations of electroactive analytes in sweat, several challenges exist for continuous wearable monitoring practice. One limitation is that DPV and

many direct oxidation methods require lengthy scanning cycles to obtain reliable, quantitative results. Therefore, such methods are not as efficient and continuous compared with potentiometric and amperometric ones. Another limitation is that DPV electrodes may experience analyte adsorption and biofouling after several scanning cycles,<sup>215–217</sup> making them not suitable for long-term wearable monitoring. The other problem for wearable sweat sensor applications is the coexistence of many interfering analytes in complex biofluids. Many analytes, such as tryptophan and tyrosine exist at similar redox potentials with overlapping peaks.<sup>87</sup> Thus, the selectivity of such voltammetric biosensors could be limited for specific applications and it is crucial to develop peak-separation algorithms or novel electrochemical techniques when dealing with sweat analysis.

#### 4.4. Wearable Sweat Sensors Based on Transistors

The emergence of flexible field-effect transistors (FETs) has sparked recent platform development for wearable sensors due to their signal amplification function and multiple material choices for different applications.<sup>218</sup> A typical transistor consists of a source, drain, gate, and semiconducting channel with a dielectric layer. Generally, the source-drain current of the transistor is controlled by the applied gate voltage, and when the electrode surface is functionalized with target-sensitive components, the channel conductance will change and generate current signals. In order to amplify the sensitivity and increase detection limit of conventional potentiometric and amperometric sensors, transistors with active sensing electrodes have been implemented.

Figure 6a exhibits a FET-based inorganic pH chemical sensor with ultrahigh sensitivity by using a flexible charge-coupled device based on accumulation cycles of electron charge transfer.<sup>219</sup> While conventional charge-coupled devices are based on rigid silicon chips, such pH sensors use InGaZnO for the channel and flexible PI as the substrate to make it flexible for wearable applications (Figure 6b). The FET operates by an electron transfer sequence controlled first by the input control gate voltage and then by the transfer gate voltage. With 100 cycles of accumulation, the pH sensor achieved a sensitivity of around 240 mV per pH unit, which is around four times larger than the Nernst limit of conventional potentiometric pH ones (Figure 6c).

Since FETs can be conveniently fabricated in arrays owing to their uniform structures using microfabrication, detecting multiple analytes is possible with flexible FETs. As shown in Figure 6d, a 3D-integrated complementary metal-oxide semiconductor (CMOS)-compatible microfluidic platform functionalized with ion-selective FET arrays was built.<sup>220</sup> With the top gate functionalized with selective polymer ISM, the platform was able to track pH, Na<sup>+</sup>, and K<sup>+</sup> at the surface of the skin in real-time. Sweat from human skin was collected passively by capillary action in the microfluidic channel (Figure 6e). Upon switching flow with varying salt dilutions, real-time measurement of Na<sup>+</sup> and K<sup>+</sup> ions could be obtained with steep variations of the drain current, as demonstrated in Figure 6f.

To date, a number of enzyme-based FETs have proven effective in the continuous monitoring of metabolites including glucose, lactate, uric acid and cholesterol.<sup>223–225</sup> For example, Figure 6g demonstrated a wearable In<sub>2</sub>O<sub>3</sub> nanoribbon transistor with a fully integrated on-chip gate for glucose detection in sweat.<sup>221</sup> Using aqueous electrolyte as the liquid gate dielectric, both source and drain electrode were immobilized with GOx, chitosan and single-walled CNTs

using inkjet printing, as shown in Figure 6h. Conductance increased when electrode surface detected H<sup>+</sup> generation during glucose oxidation, and the sensor achieved a wide detection range from nM level to mM level and a detection limit down to 10 nM (Figure 6i).

Organic FETs, in particular, mark a milestone in the development of wearable sweat sensor field owing to their low-cost, lightweight, and intrinsic soft nature.<sup>226</sup> Organic electrochemical FETs are usually thin-film transistors, in which a thin layer of organic semiconductors was deposited on flexible substrate instead of rigid inorganic ones such as silicon. These organic materials can be simply deposited using spin-coating,<sup>227,228</sup> bottom-up growth,<sup>229</sup> vacuum deposition,<sup>230</sup> and with diverse material choices, achieving specific detection functionalities has been the aim of recent research.<sup>218</sup> As shown in Figure 6j, a hydrophilic n-type organic FET was built to detect glucose and power generation from biofluids.<sup>222</sup> An electron-transporting material named NDI-T2 copolymer P-90 was used, which operated in the accumulation mode with a positive voltage at the gate electrode, increasing the channel current to switch on the transistor. When glucose is enzymatically oxidized and the gate voltage is smaller than the source-drain bias, the enzymatic reaction will transfer electrons to the channel (Figure 6k). The real-time response in biofluids of the mediator-free enzyme-coupled organic FET to successively added glucose was observed with a detection range of 6 orders of magnitude (Figure 6l). When paired with a polymeric cathode, the n-type polymer could be further used as a self-bipowered sensor to power the transistor. Similarly, an organic FET-based lactate sensor was built by incorporating an ionogel as a solid-state electrolyte.<sup>231</sup> Based on the aforementioned conducting polymer poly(3,4-ethylenedioxythiophene):poly(styrenesulfonate) (PEDOT:PSS), lactate oxidase (LOx) and ferrocene mediator were immobilized in the ionogel layer on top of the channel. During enzymatic reaction, the ferrocene mediator carries electrons to the gate voltage and causes a decrease in gate potential, which increases the gate current concomitantly.

With significant improvements in versatility of wearable FET-based sensors, there are still some challenges to address, including improving the sensor's mechanical stability against bending effects to reduce signal distortion, and improving the electrical protection against the liquid operating environment. An intrinsic trade-off among sensitivity, stability, operating range, and operating voltage also occurs to detect trace-levels of analytes.<sup>232</sup>

Despite raising interest in organic chemical materials for organic FETs, moreover, they suffer from low electron mobility and therefore inferior electrical performance because of their semicrystalline characteristics and chain disorder.<sup>233</sup> Fabrication of these organic polymers is also less consistent compared with conventional semiconductor fabrication, which makes organic FETs more vulnerable to experimental setup and material defects. More fundamental research on developing novel organic materials and fabrication techniques is needed to increase the yield of organic FETs for scalable and reproducible sensor performance.

#### 4.5. Wearable Optical Sweat Sensor

Apart from electrochemical sensors, wearable optical sensors have been widely used for metabolite and electrolyte monitoring. Optical sensors typically detect biomarkers by monitoring absorbance (colorimetric), emission (fluorescence

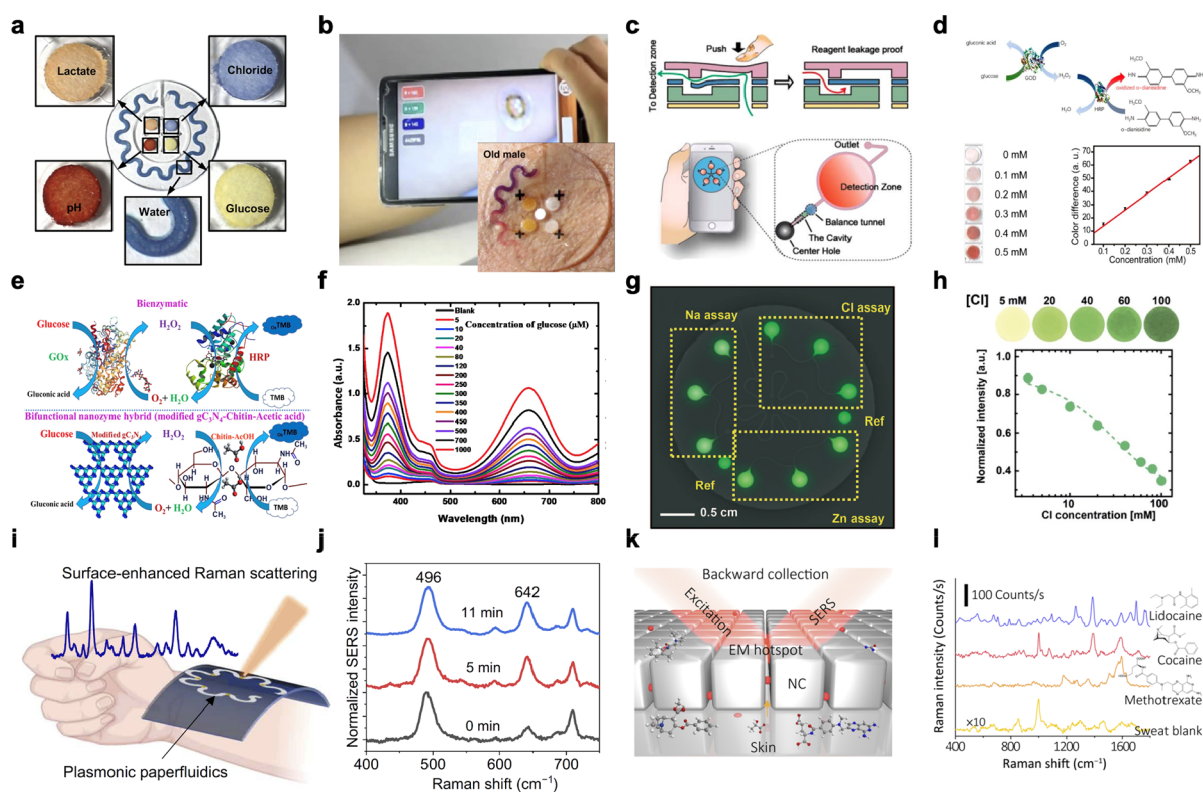


**Figure 7.** Wearable optical sweat sensors. **a**, An integrated platform that contains colorimetric assay arrays and sweat microfluidics that detects glucose, lactate,  $\text{H}^+$  and  $\text{Na}^+$ . **b**, A smart phone app for image capture and RGB analysis to read the concentration quantitatively. **a,b**, Reproduced with permission from ref 239. Copyright 2016 The American Association for the Advancement of Science. **c**, A microfluidics design of a colorimetric sensor array that consists of a check valve to prevent backflow. **d**, Chromogenic reaction of colorimetric glucose sensor and colorimetric response various glucose concentrations from 0.1 to 0.5 mM. **c,d**, Reproduced with permission from ref 240. Copyright 2019 American Chemical Society. **e**, Chemically modified carbon nitride-chitin-acetic acid hybrid that displayed glucose oxidase-like activity. **f**, Ultraviolet–visible (UV–vis) absorption of chromogenic indicator 3,30,5,5-tetramethylbenzidine in chemically modified nanozyme with varying glucose concentration (0–1000  $\mu\text{M}$ ). **e,f**, Reproduced with permission from ref 243. Copyright 2020 Elsevier. **g**, A soft microfluidic system prefilled with fluorescent probes for sweat chloride, sodium and zinc detection. **h**, Fluorescent probe response to analyte concentration under visible light illumination. **g,h**, Reproduced with permission from ref 245. Copyright 2018 Royal Society of Chemistry. **i**, A wearable plasmonic paper-based microfluidic system for sweat rate and metabolite detection. **j**, Quantitative measurement of uric acid based on surface-enhanced Raman spectroscopy (SERS) spectrum. **i,j**, Reproduced with permission from ref 246. Copyright 2022 The American Association for the Advancement of Science. **k**, SERS sensing of plasmonic metafilm based on ordered silver nanocube superlattice as the sensing component. **l**, Detection of a wide range of drugs within the human sweat sample using SERS. **k,l**, Reproduced with permission from ref 247. Copyright 2021 The American Association for the Advancement of Science.

or luminescence), or scattering (plasmonics).<sup>234</sup> These optical sensors are usually coupled with microfluidics for constant sweat refreshment, and often utilize colorimetric assays to make sensing patches free of electronics that are low-cost and can be easily disposed of after use.

In wearable colorimetric sensors, chromogenic reagents change color through biochemical or hydrolytic reactions upon exposure to target analytes. Depending on the stimulus mechanism, the color-changing process of chromogenic reagents can be classified as electrochromism (for electron transduction in an enzymatic reaction), ionochromism (for target ion detection), or halochromism (for pH sensing).<sup>234</sup> The rise of wearable colorimetric sensors has made it possible for continuous human health monitoring under long-distance outdoor conditions.<sup>235–238</sup> For example, Figure 7a demonstrates an integrated platform that contains colorimetric assay arrays and sweat microfluidics.<sup>239</sup> Embedded colorimetric assays including glucose, lactate,  $\text{H}^+$ , and  $\text{Na}^+$  were placed in a set of reservoirs, and these colorimetric reagents changed color upon target interaction, with color change correlated to analyte concentration. To meet the need of quantitative analysis

applications, an NFC electronics module was integrated, with a smart phone app for image capture and RGB color analysis to read the marker concentration (Figure 7b). Similarly, a series of five microfluidic channels each assembled with colorimetric glucose agents was developed, using a check valve to avoid reagent backflow (Figure 7c).<sup>240</sup> Such glucose sensors could perform five measurements in parallel to minimize colorimetric reading errors, and could achieve a linear detection range of 0.1–0.5 mM for sweat glucose with a limit of detection of 0.03 mM (Figure 7d).

Inspired by natural enzymes, nanozymes, defined as various functional nanomaterials that mimic the enzymatic function, have been introduced.<sup>241</sup> These enzyme-mimicking nanomaterials are typically low-cost, high stability, and can be tuned for versatile applications. Due to the inexpensive materials and simple mass-fabrication methods, nanozymes are particularly attractive to wearable and disposable colorimetric sensors. To overcome their key problem of low catalytic activity and poor specificity, many nanomaterials were intentionally designed with similar structures of natural enzyme;<sup>242</sup> for instance, mimicking glucose oxidase to catalyze glucose oxidation

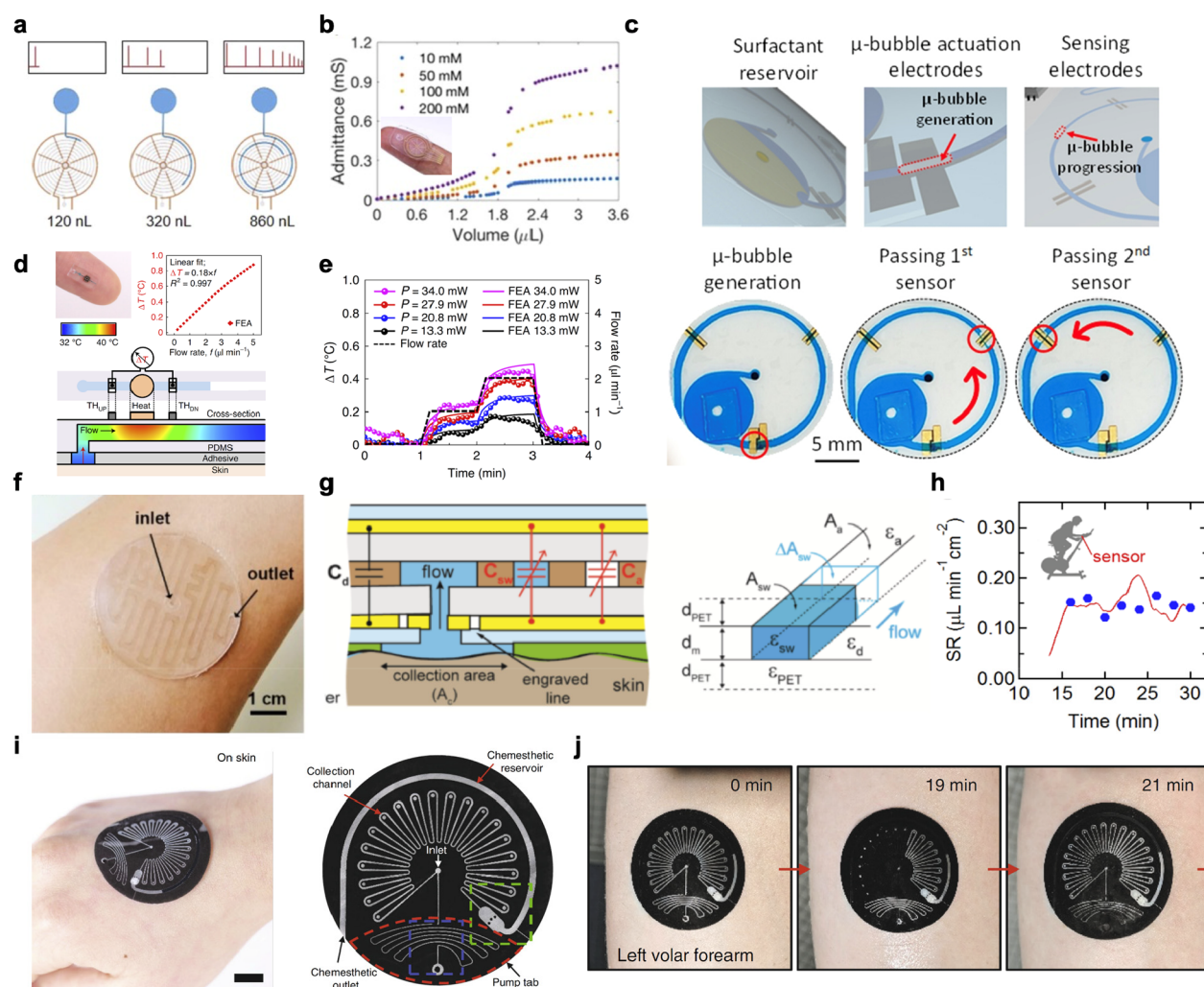


**Figure 8.** Wearable sweat rate sensor. **a**, An impedance sensor embedded in sweat microfluidics to monitor resting thermoregulatory sweat. **b**, Dependence of impedance on varying salt concentrations. **a,b**, Reproduced with permission from ref 253 under CC BY 4.0. Copyright 2021 Nyein et al. **c**, Sweat rate monitoring based on digitized microbubble detection mechanism by calculating microliter-scale bubbles generated by electrolysis. Reproduced with permission from ref 254. Copyright 2022 Royal Society of Chemistry. **d**, A thermal sweat flow sensing module based on a short and straight fluid channel with a flow sensor. **e**, Detection of sweat rate by temperature difference with varying flow rate under different heater power. **d,e**, Reproduced with permission from ref 255. Copyright 2021 Springer Nature. **f**, Capacitance-based sweat rate sensors. **g**, Measurement mechanism by capacitance difference of the microfluidic area between those filled with sweat from that of air. **h**, On-body trial with the capacitance sensor being measured using an LCR meter continuously. **f–h**, Reproduced with permission from ref 256. Copyright 2020 American Chemical Society. **i**, A resettable visual sweat rate sensor with functionalities of collecting sweat, purging collected sweat, and chemesthetic ejection. Scale bar, 1 cm. **j**, Optical image showing the sweat collection system being reset by the user after rehydration. **i,j**, Reproduced with permission from ref 257 under CC BY 4.0. Copyright 2019 Reeder et al.

process.<sup>243,244</sup> Figure 7e shows chemically modified carbon nitride-chitin-acetic acid hybrid that displayed intrinsic peroxidase-like activity.<sup>243</sup> The chemically modified graphitic carbon nitride could oxidize glucose and generate hydrogen peroxide, while chitin and acetic acid could further decompose hydrogen peroxide. The sensitive colorimetric nanozyme could detect hydrogen peroxide with a limit of detection to 0.052  $\mu\text{M}$ , as well as detect glucose with a limit of detection to 0.055  $\mu\text{M}$  for semiquantitative analysis, as shown in Figure 7f.

A complementary approach for wearable optical sensors is fluorometric imaging.<sup>245,248</sup> In wearable fluorescent sensors, a light source is required for analyte detection. When fluorophores are excited at certain wavelengths, they will re-emit light with an increase in wavelength. Fluorophores are typically combined with a target-sensitive biomolecule, which change structure upon binding with an analyte, causing a shift

in the fluorescent signal. Figure 7g exhibits a soft microfluidic system prefilled with fluorescent probes for sweat  $\text{Cl}^-$ ,  $\text{Na}^+$ , and  $\text{Zn}^{2+}$  detection.<sup>245</sup> Chemical probes were embedded in a series of chambers under light excitation light, and a smartphone imaging module was paired for quantitative measurement of fluorescence intensity, which is nearly linear to analyte concentration under visible light illumination (Figure 7h). Human subjects wearing fluorometric sensors demonstrated measurement of sweat  $\text{Cl}^-$ ,  $\text{Na}^+$ , and  $\text{Zn}^{2+}$  along with estimated sweat loss.

Several other wearable optical sensors have adopted plasmonic detection using external equipment such as surface-enhanced Raman spectroscopy (SERS).<sup>247,249,246</sup> In SERS, a nanoscale roughened metallic surface and a laser source is required. Laser excitation of the nanosurface will excite highly localized surface plasmons. When a target

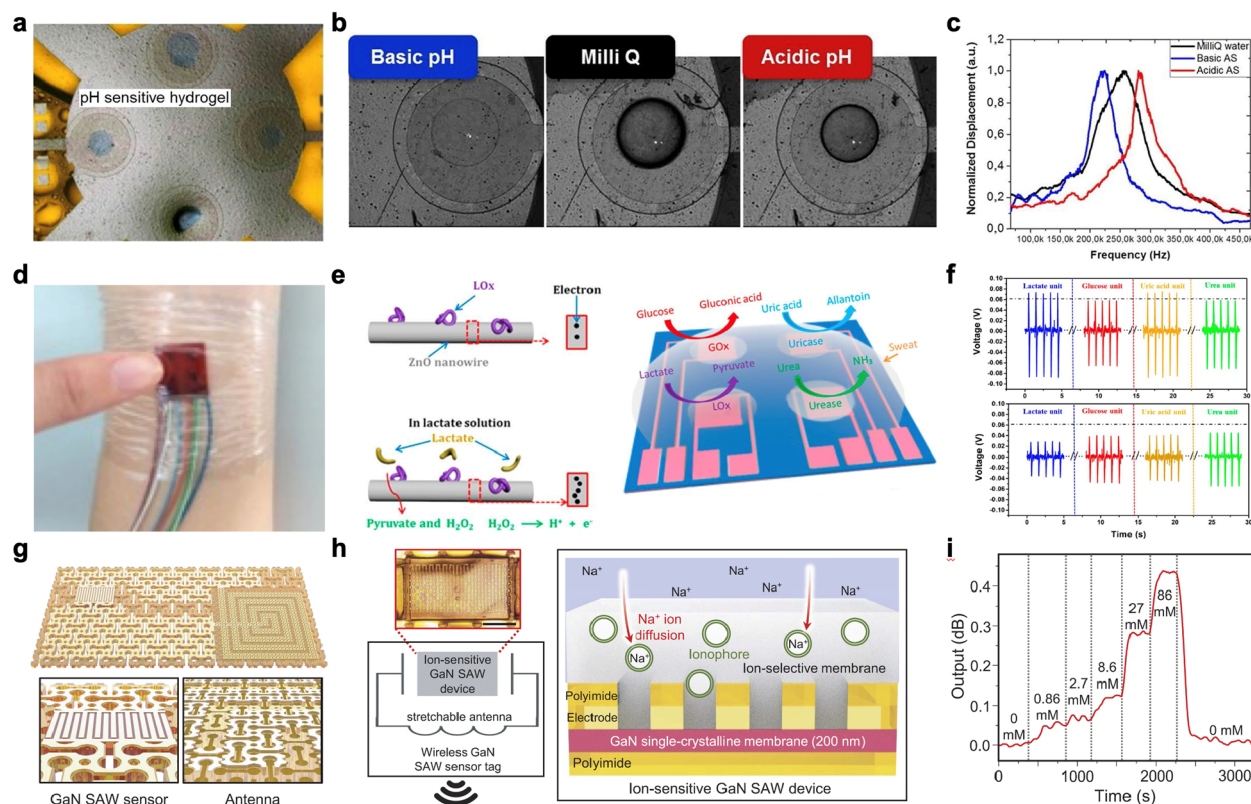


**Figure 9.** Wearable sweat sensor based on piezoelectric and other methods. **a**, A piezoelectric sweat pH sensor based on pH sensitive hydrogels. **b**, Optical images of a pH-sensitive hydrogel in acidic, neutral, and basic solutions. **c**, Resonant frequency shift of piezoelectric membrane in response to pH. **a–c**, Reproduced with permission from ref 258 under CC BY 4.0. Copyright 2020 Scarpa et al. **d**, Optical image of a piezoelectric patch for multimodal metabolites monitoring. **e**, Mechanism of coupling effect between the surface enzymatic reaction and piezoelectric characteristic of ZnO nanowire. **f**, Multimodal signals including glucose, lactate, uric acid and urea could be obtained using the piezoelectric sensor. **d–f**, Reproduced with permission from ref 259. Copyright 2017 American Chemical Society. **g**, A chip-less wireless sensor system using surface acoustic wave sensors for sweat ion sensing. Scale bar, 200  $\mu\text{m}$ . **h**, Sensing mechanism of ISM-coated surface acoustic wave sensors. **i**, Dynamic response of surface acoustic wave sensors to different sweat ion concentrations. **g–i**, Reproduced with permission from ref 260. Copyright 2022 The American Association for the Advancement of Science.

molecule is absorbed on the metal surface, an enhancement in Raman signal can be observed. As demonstrated in Figure 7i, a wearable plasmonic paper-based microfluidic system was built for sweat rate and metabolite detection.<sup>246</sup> The label-free paper patch was then analyzed using SERS to identify multiple analytes. Owing to the powerful SERS spectrum, quantitative measurement of uric acid was enabled as shown in Figure 7j. Similarly, trace amounts of drugs can be detected using a wearable plasmonic-metamaterial sensor.<sup>247</sup> A thin hydrogel layer loaded with sweat stimulation drugs was mounted on one of the two spiral fractal mesh electrodes, while a plasmonic metamaterial composed of an ordered silver nanocube superlattice as the sensing component was mounted in a through-hole cut in the hydrogel layer (Figure 7k). SERS spectra could detect a wide range of drugs within the human sweat sample as demonstrated in Figure 7l, with a detection range from  $10^{-5}$  M to  $10^{-1}$  M.

One critical drawback for wearable colorimetric sensors is that the color changes associated with certain assays are irreversible,<sup>7</sup> which makes it difficult to distinguish dynamics of sweat analytes. A potential solution is to use passive capillary bursting valves, which separate measurements in time and spatially into a series of reaction chambers for successive colorimetric analysis.<sup>250,251</sup> Another challenge is the quantitative accuracy, as taking images for concentration calibration

can be easily distorted by environmental lights and settings. On the other hand, wearable fluorescent sensors require an additional light source as well as optical accessories to acquire fluorescence, posing a high power demand during long-term wear. Fluorescence-based sensors can also suffer from influences from ambient light such as sunlight, and require light-tight enclosures to retrieve accurate fluorescence signals. For wearable plasmonic sensors, detection of the analytes depends on external SERS equipment, which is not suitable for daily wearing under casual activity and subsequent continuous long-term monitoring.

#### 4.6. Wearable Sweat Rate Sensor

With the rapid development of wearable sweat sensors with real-time health assessment capabilities, quantifying sweat flux has become an important research focus to meet the calibration needs for personalized medicine. For instance, metabolite concentrations can decrease with an increased sweat rate due to dilution. Wearable sweat rate sensors have thus been integrated with biochemical sensors to form a more complete health profile.

A common approach for monitoring sweat rate is impedance-based measurement.<sup>252,253</sup> Figure 8a features an example of an impedance sensor embedded in sweat microfluidics to monitor resting thermoregulatory sweat.<sup>253</sup> Sweat enters the sensing microfluidics through hydrophilic

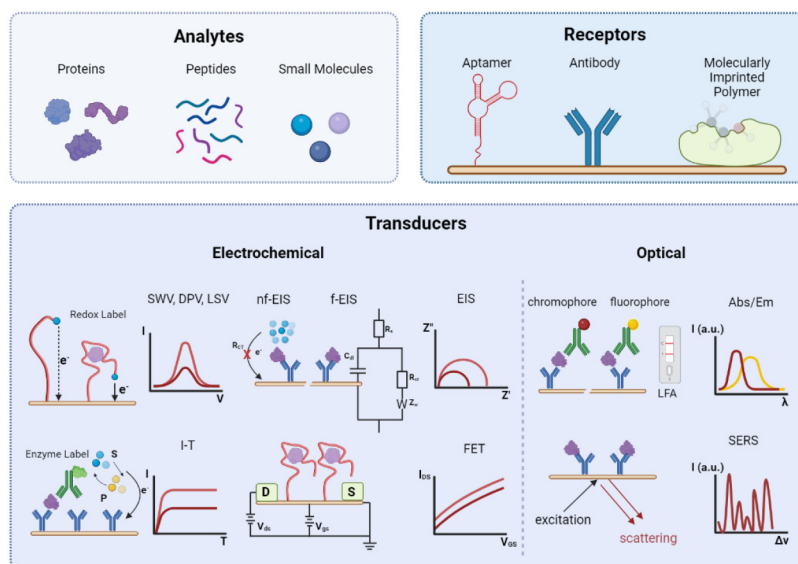


**Figure 10.** Major components of a bioaffinity sensor. Bioaffinity detects analytes including proteins, nucleic acids, and small molecules. A bioaffinity sensor recognizes an analyte via affinity interactions with a receptor (aptamer, antibody, or molecularly imprinted polymer) and converts the interactions into measurable signals via a transducer. Transducers employed for epidermal sweat sensing are either electrochemical or optical. SWV, square wave voltammetry; DPV, differential pulse voltammetry; LSV, linear sweep voltammetry; I, current; V, potential;  $R_{CT}$ , charge transfer resistance;  $C_{dl}$ , double layer capacitance;  $R_s$ , solution resistance;  $Z_w$ , Warburg element;  $Z'$ , real impedance;  $Z''$ , imaginary impedance; nf-EIS, nonfaradaic electrochemical impedance spectroscopy. f-EIS, faradaic impedance spectroscopy; S, substrate; P, product; I-T, chronoamperometry; D, drain; S, source;  $V_{ds}$ , drain-source voltage;  $V_{gs}$ , gate-source voltage; FET, field effect transistor; Abs, absorbance; Em, emission; I (a.u.), intensity;  $\lambda$ , wavelength; LFA, lateral flow assay;  $\Delta\nu$ , Raman shift. Created with [BioRender.com](https://www.biorender.com).

fillers for rapid sweat uptake, and then goes through the spiral channel. An admittance pulse is spiked and measured each time the sweat contacts one of the radial electrodes, and by counting spikes and adjacent time intervals, the sweat volume and sweat rate can be estimated. The impedance and sweat rate calculation also depends on salt concentrations in sweat; at higher NaCl concentrations, a smaller impedance occurs (Figure 8b). Recent research monitored sweat rate based on a digitized microbubble detection mechanism.<sup>254</sup> As shown in Figure 8c, microliter-scale bubbles were generated by electrolysis intermittently, and their velocity was measured using impedimetric sensing by measuring the passage time across two impedance sensing electrode pairs.

In another method, a thermal flow sensing module was built using a short and straight fluid channel with a flow sensor (Figure 8d).<sup>255</sup> The simple fluid channel was built without the need for complex microfluidic networks, and also avoiding electronic contact with sweat. The flow sensor consisted of a thermal actuator and precision thermistors, of which temperature upstream and downstream relative to the flow direction was recorded. Upon activation of the thermal actuator, the generated heat was transported with the flow of sweat, creating a temperature difference at upstream and downstream sites, which could then be calculated and converted to flow rate. As shown in Figure 8e, with varying flow rate under different heater power, the temperature difference could be detected proportionally.

Several other sweat rate sensors are based on capacitance, which consists of two conducting parallel plates, plastic insulating layers, and a central microfluidic channel formed by laser cutting a plastic film (Figure 8f).<sup>256</sup> The capacitance difference of the microfluidic area between regions filled with sweat versus air can be converted to sweat flow, as demonstrated in Figure 8g. During an on-body trial, the

capacitance sensor was measured using an LCR meter continuously, and the measured sweat rate coincided with values from a conventional sweat collection device (Figure 8h).

Sweat rate monitoring can also be done visually without the need of active components or power sources. As shown in Figure 8i, a system of pinch valves and suction pumps can be used to reset the sweat rate sensing patch.<sup>257</sup> The epifluidic sweat system was fabricated using soft lithography, with capabilities to visualize sweat flow in the channel and to manually purge collected sweat, as exhibited in Figure 8j. Once sweat loss reaches the critical value of 25  $\mu\text{L}$ , an effervescent chemical pump is activated, releasing chemesthetic agents to create a sensory alert feedback.

#### 4.7. Wearable Sweat Sensors Based on Piezoelectrics and Other Methods

Several other techniques have been developed as alternative methods for the detection of sweat analytes. One example used piezoelectric materials for sweat pH monitoring by transducing the physicochemical changes of pH responsive hydrogels with piezoelectric aluminum nitride (AlN) membranes (Figure 9a).<sup>258</sup> The hydrogel is made of a poly(ethylene glycol)-diacrylate macromer with 2-carboxyethyl acrylate, and its carboxylic group is protonated in acidic conditions and deprotonated in a basic environment, resulting in the polymeric chains to shrink or swell accordingly (Figure 9b). Upon deformation of the hydrogel, the resonant frequency shift is recorded in the piezoelectric AlN membranes, which has a responsivity of about 12 kHz per pH unit change in artificial sweat (Figure 9c).

Figure 9d gives another example of adopting piezoelectric materials for multimodal metabolite detection.<sup>259</sup> The wearable e-skin is composed of piezo-biosensing units of enzyme/ZnO nanoarrays, and piezoelectric impulse of the piezo-biosensing units serves as both the power supply and

biosensor at the same time. As shown in Figure 9e, the sensing capability arises from the coupling effect between the surface enzymatic reaction and piezoelectric characteristic of the ZnO nanowire. Multimodal signals for glucose, lactate, uric acid, and urea could be obtained (Figure 9f).

Another significant development is sensing ion concentrations using surface acoustic wave sensors.<sup>260</sup> As shown in Figure 9g, a chip-less wireless sensor system was built based on freestanding ultrathin single crystalline piezoelectric gallium nitride (GaN) membranes. The GaN membrane was coated with ISM to sense viscosity and mass changes of the ISM upon target ions binding to ionophores (Figure 9h). The resonant peak shifts in the surface acoustic wave sensor can be used to wirelessly detect sweat ionic concentration dynamics (Figure 9i).

#### 4.8. The Emerging Sweat Sensors Based on Bioaffinity Recognition

Although numerous wearable sweat sensors based on various signal transduction mechanisms have been reported as discussed in Sections 4.1–4.7, existing wearable sweat biosensors that can perform continuous biosensing are primarily based on a few target recognition mechanisms such as enzymatic reactions, ion-selective recognition, or direct oxidation. Given the low concentrations of disease relevant biomarkers in sweat (nM or lower), the performance of ion-selective and enzymatic sensors may be limited in interrogating trace-level targets like hormones and proteins. In this regard, the design of ultrasensitive bioaffinity sensors which are specific to various disease biomarkers is a cornerstone of the development of wearable sweat biosensors for noninvasive health and disease monitoring.<sup>261</sup> It should be noted that most reported bioaffinity sweat sensors are currently limited to point-of-care one-time use and cannot perform continuous *in situ* monitoring.

Bioaffinity sensors typically consist of a bioreceptor layer for specific molecule recognition, and a signal transducer which converts the recognition event between a target and a receptor into a measurable signal (Figure 10). General classes of bioreceptors employed for wearable sweat biosensor construction include antibodies, receptor proteins, nucleic acids, and biomimetic materials like molecularly imprinted polymers (MIPs).<sup>262</sup> The intrinsic properties of the bioreceptors, in essence, determine several operational characteristics of a biosensor, including selectivity, sensitivity, stability, and reversibility.

The architecture and design of transduction interfaces govern the physical characteristics (size, portability, type of instrumentation), costs, as well as the limit of detection for the target. In recent years, affinity-based formats have been coupled with various types of transducer interfaces such as electrochemical,<sup>263</sup> optical,<sup>264</sup> and piezoelectric<sup>265</sup> sensors. Electrochemical sensors are versatile tools that can be easily integrated with epidermal systems with high innate sensitivity, scalability, and low instrumentation costs. Electrochemical impedance spectroscopy (EIS) probes the impedance of an electrode–solution interface by applying a small amplitude (typically 5–10 mV peak-to-peak) sinusoidal perturbation while registering the current response. In nonfaradaic EIS, the binding event between biomarkers and receptors immobilized on the transducer interface leads to a change in the double layer capacitance ( $C_{dl}$ ) in the Randles circuit and consequently the impedance ( $Z$ ) of the system due to the dielectric

properties of the biomarkers based on the Gouy–Chapman–Stern model.<sup>266</sup> In contrast, faradaic EIS requires the presence of redox active species. The association of biomarkers presents an electrostatic and/or steric barrier to the redox probes at the interface and modulates the charge transfer resistance ( $R_{ct}$ ) and the impedance of the system. Other techniques that monitor the faradaic response of targets with direct electrochemical properties or the faradaic response of electrochemical tracers include amperometry and voltammetry (square wave voltammetry, differential pulse voltammetry and cyclic voltammetry). Bioreceptors, especially aptamers, have also been integrated with various FETs on the skin.<sup>218</sup> The modulation of charge distribution at the semiconducting interface (gate electrodes) upon target binding translates into a measurable change in the current that flows between the source and drain electrodes. Surface charged species distribution and electrolyte concentration in the detection media play an important role in the transduction mechanisms of most electrochemical sensors. Unlike conventional biofluids like serum and saliva, sweat electrolyte and pH content vary hugely with different subjects and different collection methods. Therefore, the influence of such variations should be carefully addressed in the design and implementation of electrochemical sensors for *in situ* sweat analysis.

Optical transduction mechanisms can be further categorized into colorimetry, fluorescence, chemiluminescence, and plasmonic.<sup>267</sup> The simplest format of a colorimetric bioaffinity sensor used for wearable sweat analysis is the lateral flow assay (LFA).<sup>268</sup> The association of biomarkers with bioreceptor-immobilized metal nanoparticles leads to a visible change in the absorbance wavelength and/or intensity due to the aggregation or accumulation of nanoparticles within the test-zone. Plasmonic affinity sensors require the excitation of noble metal films or nanoparticles with incident laser and measure the change of surface plasmon resonance (SPR) or the modulation of SERS from the interface in response to target binding.<sup>269</sup> Smartphone-enabled optical wearable sensing and signal processing technologies are less influenced by electrolyte content of sweat samples as compared with electrochemical biosensors; however, these technologies need to account for variation in ambient lighting as mentioned previously.<sup>270</sup>

Often, many targets of interest do not possess optical or electrochemical properties that can be directly detected by a transducer. As a result, the addition of a signaling tracer that either competes with the analyte (competitive format) or binds to a secondary binding site on the target where a target is “sandwiched” between a surface immobilized receptor and receptor-based tracer (sandwich format) is necessary to produce a measurable signal.<sup>271</sup> Enzymatic tracers are sometimes incorporated in a sensing format to amplify the signals of a system and achieve a lower detection limit.<sup>272</sup> As some formats are complex and multistep, epidermal microfluidic modules that can be programmed to manipulate reagents may be necessary to achieve miniaturization and automation.<sup>273</sup> Together, the features of bioreceptors, transducers and sensing formats determine the operational characteristics of a wearable sweat biosensor.

**4.8.1. Antibody-Based Sensors.** Antibodies are the most widely used bioreceptors in bioaffinity sensors due to their superior affinity and specificity to targets, versatility, and commercial availability. Depending on whether an electrochemical or optical tracer is used, antibody-based sensors are classified into labeled (with tracers) and label-free immuno-

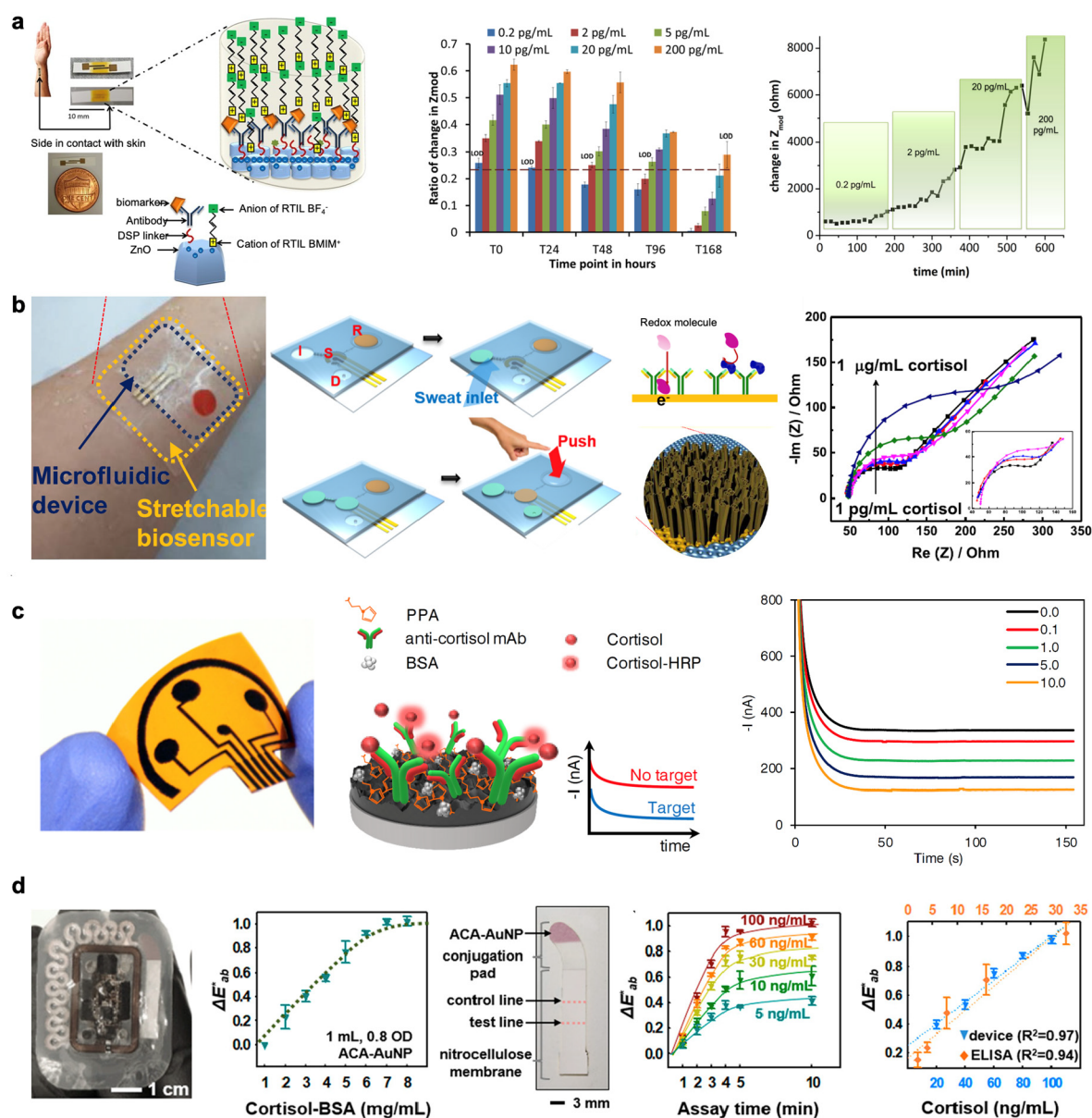


**Figure 11.** Wearable immunosensors. **a**, Nonfaradaic impedance sensor mediated with room temperature ionic liquid (RTIL) to enhance the stability of sweat cortisol detection. Reproduced with permission from ref 276 under CC BY 4.0. Copyright 2017 Munje et al. **b**, Microfluidic faradaic impedance sensor whose detection is initiated by manually pushing redox molecules in the reagent chamber to the detection chamber. Reproduced with permission from ref 284. Copyright 2020 Elsevier. **c**, Amperometric cortisol sensor on flexible laser-engraved graphene substrate. Reproduced with permission from ref 93. Copyright 2020 Elsevier. **d**, Colorimetric detection of cortisol based on a lateral flow strip embedded in a soft, microfluidic patch. Reproduced with permission from ref 292 under CC BY 4.0. Copyright 2020 Proceedings of the National Academy of Sciences.

sensors. In label-free immunosensors, the association of an antigen with an antibody is directly transduced into electrical or optical signals.<sup>274</sup> Nonfaradaic EIS is the most commonly used technique in constructing label-free sweat immunosensors. A nonfaradaic EIS sensor was developed for ethyl glucuronide (EtG), a metabolite of ethanol, in spiked human sweat.<sup>275</sup> Impedance across two coplanar gold or zinc oxide (ZnO) electrodes functionalized with monoclonal anti-EtG antibodies was measured. The paper reports a working range of 0.001–100 μg/L on both glass and PI substrates and demonstrates that ZnO electrodes have better detection sensitivity than gold electrodes. Based on a similar concept, the same group reported a non-Faradaic EIS sensor using room temperature ionic liquid (RTIL) with nanoporous ZnO

electrodes on flexible polymer membranes to enhance the stability of the bioreceptor (antibodies) for the detection of interleukin 6 (IL-6) and cortisol in spiked human sweat (Figure 11a).<sup>276</sup> The IL-6 sensors demonstrated distinguishable signals above the specific signal threshold after 168 h of storage and a 10-h continuous detection from 0.2 to 200 pg/mL IL-6 in spiked human sweat. A printed two-electrode system functionalized with anti-CRP antibodies or anti-IL-1β was fabricated for nonfaradaic EIS detection.<sup>277</sup> In addition to cortisol, CRP, and IL-1β, the same device was modified with other antibodies for the detection of IL-6, IL-8, IL-10, tumor necrosis factor α (TNF-α), IL-31, interferon γ (IFN-γ), dehydroepiandrosterone (DHEA), and NPY in collected eccrine sweat.<sup>278–283</sup>

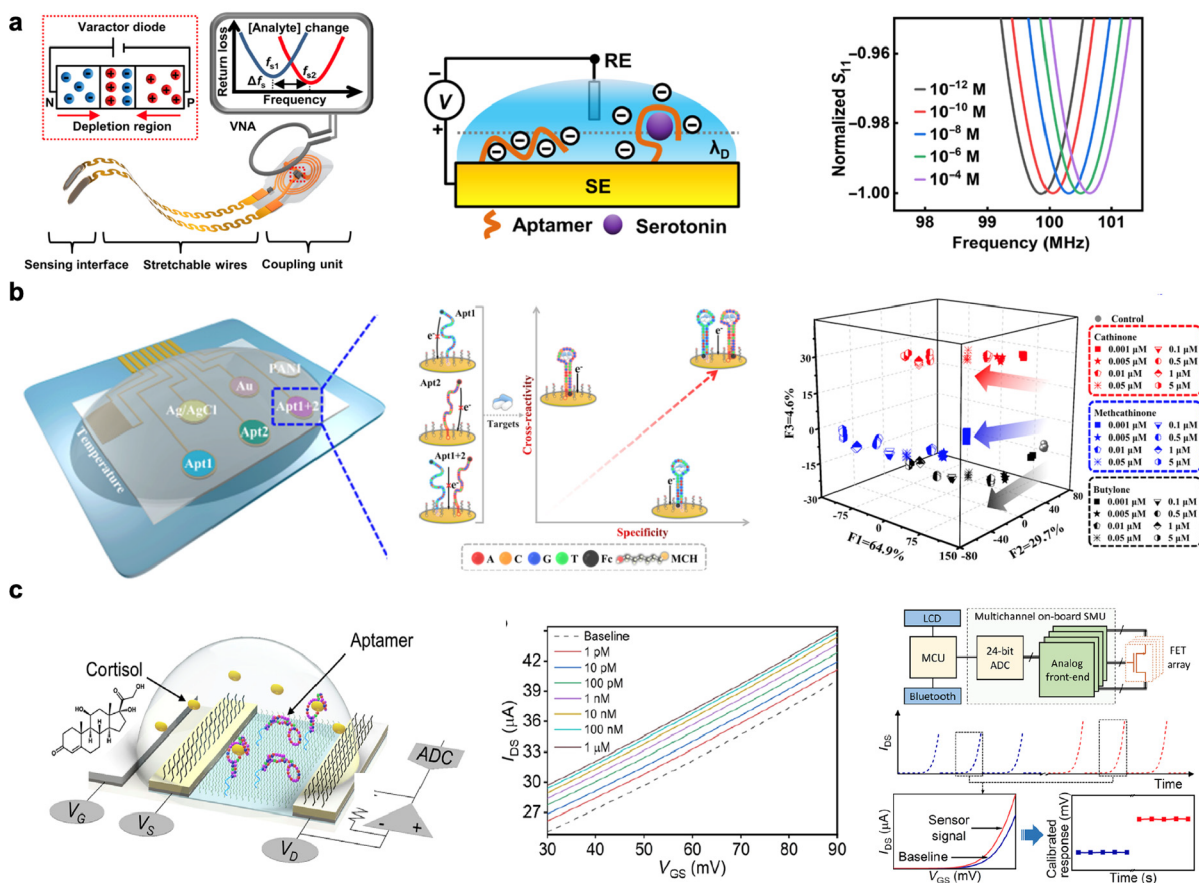


**Figure 12.** Wearable aptasensors. **a**, A wearable tuning circuit-inspired wireless aptasensor on gold electrode for serotonin detection in biofluids. Reproduced with permission from ref 301. Copyright 2022 The American Association for the Advancement of Science. **b**, Multiplexed aptamer array based on two different methylene labeled aptamer array for common drugs of abuse detection in artificial sweat. Reproduced with permission from ref 302. Copyright 2022 American Chemical Society. **c**, Field effect transistor-based aptasensor thin  $\text{In}_2\text{O}_3$  for the detection of sweat cortisol. Reproduced with permission from ref 91. Copyright 2022 The American Association for the Advancement of Science.

Although the need for redox species in faradaic EIS immunosensors complicates their execution on the skin as compared with nonfaradaic EIS sensors, this bottleneck has been addressed with a stretchable microfluidic module that delivers a predeposited redox mediator solution, potassium ferricyanide, to the antibody immobilized 3D nanostructured gold working electrode while washing away the unbound cortisol and sweat (Figure 11b).<sup>284</sup> Charge transfer resistance ( $R_{ct}$ ) in the presence of redox mediator increases with increasing concentration of cortisol from 1 pg/mL to 1  $\mu\text{g}/\text{mL}$ . An ATi3C2Tx MXene-loaded laser-induced graphene (LIG) sensor was reported for noninvasive POC detection of cortisol. The introduction of MXene improves the sensitivity of the LIG electrode after transfer onto PDMS.  $R_{ct}$  of the sensor increases by approximately 1000  $\Omega$  from 10 pM to 100 nM cortisol.<sup>285</sup> On a similar basis, a thread-based immunosensor was developed by immobilizing anticortisol on a L-cysteine-gold nanoparticle-MXene modified electrode via EDC/NHS coupling.<sup>286</sup> The change in charge transfer resistance caused by cortisol binding was monitored by amperometry in the presence of potassium ferricyanide and the sensor reported a linearity of 5–180 ng/mL for sweat cortisol detection. In addition to increasing the charge transfer resistance of redox species in solution, antigen association to immobilized antibodies may also hinder the kinetics of electron transfer between redox species immobilized below the antibody layer

and electrolytes in the solution. Conductive carbon yarn (CCY) deposited with a redox active  $\text{Fe}_2\text{O}_3$  nanostructure was functionalized with anticortisol antibodies for cortisol detection.<sup>287</sup> Using cyclic voltammetry (CV), the magnitude of the redox peak current decreases with increasing cortisol due to the insulating behavior of cortisol binding. The sensor exhibited a working range of 1 fg/mL to 1  $\mu\text{g}/\text{mL}$ . The same group reported a ZnO nanorod integrated CCY for cortisol detection.<sup>288</sup> The charge transfer resistance of potassium ferricyanide was monitored using CV and DPV. Changes in oxidation peak current as a function of cortisol concentration were found to be linear between 1 fg/mL to 1  $\mu\text{g}/\text{mL}$ . A screen-printed carbon electrode with electrodeposited gold nanoparticles (AuNPs) was functionalized using thiol-poly(ethylene glycol) (PEG)-carboxylic acid for subsequent anticortisol immobilization.<sup>289</sup> DPV in the presence of ferrocenyl methanol was applied to the electrode after cortisol binding and the change in charge transfer resistance was recorded.

Immunosensors are also frequently coupled with direct signals for labeled detection of antigens. The addition of signal labels is believed to amplify analytical signals.<sup>290</sup> Common labels used for immunosensors include enzymes (peroxidase, alkaline phosphatase, luciferase), fluorescent labels (fluorescein, rhodamine, Cy5), and redox molecules (methylene blue, ferrocene, thionine). However, the requirement of label

addition and washing steps impedes labeled immunosensors' practical implementation on the skin. For example, a flexible, wireless sweat cortisol immunosensor was constructed on laser-engraved graphene electrodes by electropolymerization of carboxyl-rich pyrrole derivative and antibody immobilization with ethyl (dimethylamino propyl) carbodiimide/*N*-hydroxysuccinimide (EDC/NHS) chemistry (Figure 11c).<sup>93</sup> Sweat cortisol competes with horseradish peroxidase (HRP) labeled cortisol for binding with the immobilized antibody. The concentration of cortisol has an inverse relation to the cathodic current generated by the enzymatic reduction of hydrogen peroxide in the presence of the mediator, hydroquinone. The sensor was only designed as a POC system as it requires an additional washing and substrate adding step off-body at the bench. HRP-labeled antigen has also been used as an optical tag for sweat biomarker detection. Labeled competitive immunosensors on capillary arrays were modified with various drug antibodies and drug-HRP (methadone, methamphetamine, amphetamine, and tetrahydrocannabinol).<sup>291</sup> Drugs in artificial sweat were detected by adding chemiluminescent substrate to the array and recording the chemiluminescence image with a CMOS camera. However, the form factors of this technology (rigid capillary array, bulky CMOS camera) make it difficult to integrate with epidermal systems. A skin-interfaced soft microfluidic system was combined with a lateral flow immunoassay for sweat collection and cortisol analysis (Figure 11d).<sup>292</sup> Colorimetric measurements of sweat cortisol were carried out by capturing the images with a smartphone and correcting for ambient lighting conditions after 5 min of incubation on the skin.

Despite the cost of production, stability issues, and potential batch-to-batch variation, antibodies are still a staple component of current biosensing technologies due to their exceptional sensitivity and selectivity for biomarkers. Future research into the production of nanobodies, a more compact and heat-stable alternative, could potentially resolve issues associated with the storage and implementation of the current generation of immunosensors.<sup>293</sup> The production of nonanimal derived antibodies may also provide greater versatility and reproducibility, while also reducing relevant ethical concerns.<sup>294,295</sup> Although such opportunities exist for antibody manufacturers and researchers, significant effort is needed to produce and investigate the performance of these alternatives before their eventual integration in epidermal sweat sensing systems.

**4.8.2. Nucleic Acid-Based Sensors.** Aptamers are a new class of bioreceptors produced by *in vitro* selection of single-stranded nucleotides with desired binding affinities. To date, various aptamers are produced to bind a broad spectrum of targets like metal ions, small molecules, proteins and whole cells via their 3D stem and/or loop structures.<sup>296</sup> Compared with antibodies, advantages of aptamers include facile and low-cost preparation, low batch-to-batch variability, nonimmunogenic properties, easy modification with functional groups, and stability.<sup>297,298</sup> The unique properties of aptamers make them compatible with many sensing modalities for POC applications.

For example, cortisol aptamers were immobilized with a 5'-terminal thiol group to ZnO nanoporous electrodes that had been previously reported for a cortisol immunosensor using nonfaradaic EIS.<sup>299</sup> Instead of measuring impedance, the authors performed chronoamperometry by applying a step potential input of 0.35 V (0.35 to  $-0.35$ ) for 60 s. The steady-state current change revealed the change in the nonfaradaic

capacitive double layer with increasing cortisol concentration. The same group also reported a platform for simultaneous detection of cortisol and NPY using aptasensors on porous gold electrodes.<sup>300</sup> Nonfaradaic EIS was used to monitor the dose response of both targets and the platform reported detection ranges of 1–256 ng/mL of cortisol and 1–256 pg/mL of NPY. Based on the concept of nonfaradaic impedance, a tuning circuit-inspired wireless serotonin aptasensor was developed on gold electrodes (Figure 12a).<sup>301</sup> Binding of serotonin to the aptamer induces a conformational change which modulates the surface potential within the electrical double layer. The sensing interface is coupled with a pair of varactor diodes and a coil to form an inductor-capacitor (LC) resonance circuit. Therefore, the change in surface potential of the aptasensor serves as a reverse bias that drives the varactors for battery-free wireless signal transduction. Further validation of this sensing system with other relevant trace-level sweat biomarkers is necessary to demonstrate its feasibility in wearable sweat sensing.

The ease of aptamer chemical modification has also inspired various tracer labeled sensing formats. For instance, cortisol aptamers modified with a thiol end and a methylene-blue redox molecule on the opposite side were immobilized on gold electrodes for cortisol sensing (Figure 12b).<sup>302</sup> Upon binding, the aptamers undergo conformation changes by folding. Therefore, the distance between the redox molecule and the electrode surface decreases, leading to an increase in the electron transfer rate and redox peak current measured by SWV. A similar concept was implemented to construct an integrated aptasensor array for drugs.<sup>302</sup> Two aptamer sequences (Apt1 and Apt2) which demonstrate different binding affinities to bioamine drugs were modified with a methylene blue signal reporter. Gold electrode sensor arrays were either modified with one or both aptamers (Apt1 or Apt2; Apt1 + Apt2). After variable feature extraction from the electrochemical signals of the aptasensor array, 16 drug analytes present distinct fingerprints that can be identified in both artificial and human sweat samples.

FET is another popular transducer system that has been interfaced with aptamers for sweat biomolecule sensing. A newly identified cortisol aptamer sequence was immobilized on a flexible thin  $\text{In}_2\text{O}_3$  FET (Figure 12c).<sup>91</sup> The conformational change of the aptamer strand after target association leads to the rearrangement of the negatively charged aptamer backbone that modulates the surface charge of the FET, which translates into quantitative changes in gate voltage ( $V_{\text{GS}}$ ) and source drain current ( $I_{\text{DS}}$ ). An integrated system with an on-board multichannel source measurement unit was developed for on-body applications. Similarly, cortisol aptamers were immobilized on electrospun conducting polyacrylonitrile (PAN) nanofibers deposited with carboxylated PEDOT in a liquid-ion gated FET system on PET.<sup>303</sup> The aptasensor showed high selectivity and sensitivity (LOD = 10 pM) for cortisol detection in human sweat. Although FETs boast high sensitivity and label-free detection mechanisms, their application in real body fluids is limited by the high ionic strength of biofluids, which lowers the signals and deteriorates FET biosensors' sensitivity. The compact structure of aptamers enables target capturing and aptamer folding within the electrical double layer, allowing electrical signal generation.

Aptamers can also be coupled with optical transducers for the POC detection of sweat biomarkers. For instance, an aptamer-based LFA strip was designed for sweat cortisol

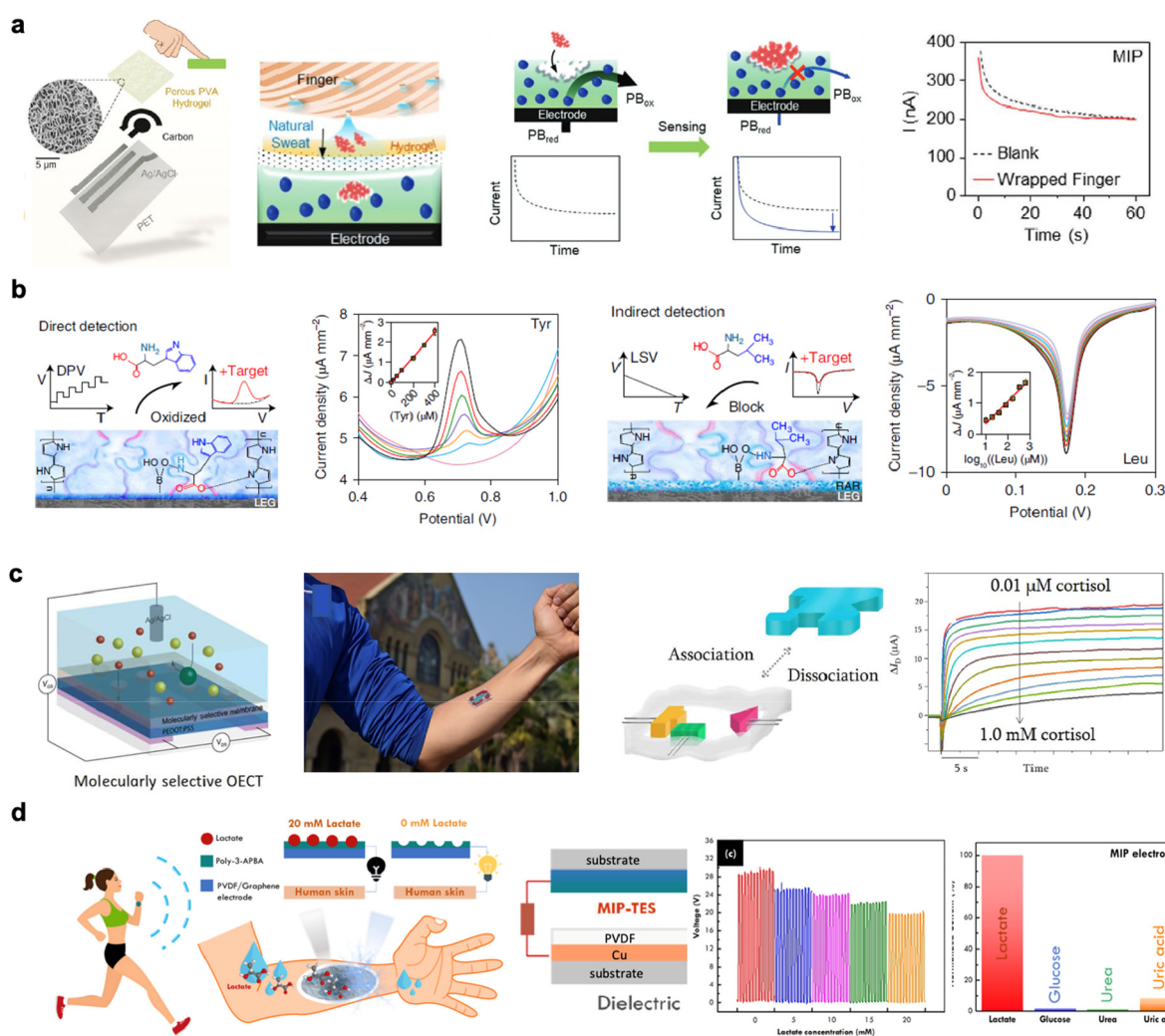


**Figure 13.** Wearable MIP-based sensors. **a**, Touch-based amperometric MIP sensor for cortisol. Reproduced with permission from ref 311. Copyright 2021 Wiley. **b**, Wearable electrochemical MIP sensor for the detection of electroactive (tyrosine) and nonelectroactive (leucine) targets. Reproduced with permission from ref 87. Copyright 2022 Springer Nature. **c**, Organic electrochemical transistor integrated with a molecularly selective membrane for sweat cortisol detection. Reproduced with permission from ref 312. Copyright 2018 The American Association for the Advancement of Science. **d**, MIP-based self-powered triboelectric sensor for the label-free detection of lactate. Reproduced with permission from ref 313. Copyright 2022 Elsevier.

detection.<sup>304</sup> Cortisol aptamers were physically adsorbed to AuNPs. Upon cortisol binding, the aptamers dissociate from the AuNP, allowing free AuNPs to be captured by the cysteamine immobilized test zone resulting in visual detection of cortisol higher than 1 ng/mL.

Although many believe that aptamers are stable and cheaper alternatives to antibodies, it should be noted that nucleic acids are still susceptible to endogenous nucleases in *in vivo* applications.<sup>305</sup> In addition, mass production of nucleic acids is still costly. The enzymatic stability issue could potentially be addressed by replacing DNAs (DNAs)/ribonucleic acids (RNAs) with peptide nucleic acid (PNA) and xeno nucleic acids (XNA).<sup>306,307</sup> Despite increasing research on the design and selection of sensitive and selective aptamers against various targets, only a limited number of targets have been extensively investigated (e.g., thrombin, cortisol, serotonin) with few aptamer sequences demonstrating reversible target binding suitable for continuous monitoring applications.

**4.8.3. MIP-Based Sensors.** MIPs are synthetic biomimetic bioreceptors whose affinities are generated by self-assembling

monomers with templates through covalent or noncovalent interactions and subsequent polymerization to form a cast-like shell.<sup>308</sup> The removal of templates from the polymer generates binding sites for selective recognition of targets. MIPs are a cheap, mass-producible, robust alternative to conventional bioreceptors like antibodies, enzymes, and aptamers. As MIPs generally do not possess signaling or catalytic properties, the design of signaling mechanisms which respond to the interaction between MIPs and templates are essential for the construction of MIP-based sensors.

In electrochemical MIP sensors, recognition events typically trigger a change in the dielectric properties of the electrode interface and signals are registered in the presence of electroactive species. For example a flexible electrochemical platform was constructed for sweat urea detection using potassium ferricyanide as redox mediators.<sup>309</sup> Binding of urea with recognition sites on urea-imprinted PEDOT on a CNT network and a gold nanotube (AuNT) network hinders the electron transfer of the potassium ferricyanide probe, translating into a measurable change in the DPV signal. The MIP

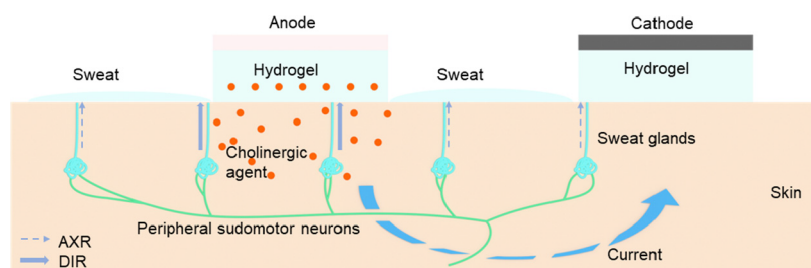


**Figure 14.** Scheme of iontophoresis-based sweat induction. AXR: Axon-reflex mediated sweating. DIR: direct stimulated sweating.

sensor demonstrates good linear response and selectivity toward physiologically relevant urea levels. The same group reported a flexible electrochemiluminescence (ECL) sensor by imprinting urea and lactate on Ru(II)-polyethylenimine (PEI)@SiO<sub>2</sub> immobilized AuNTs networks.<sup>310</sup> The porous MIP membrane provides electron transfer paths for the electrochemical oxidation of Ru(II)-PEI@SiO<sub>2</sub> and its ECL emission. As the pores, which are also the binding sites, are occupied by target molecules, the electron transfer channels are gradually blocked, leading to reduced ECL signals. The ECL platform demonstrated on-body sampling and detection of sweat urea and lactate with high stability. Similarly, a lactate sensor based on MIP-coated Ag nanowires (AgNWs) on a screen-printed electrode was demonstrated in sweat. The oxidation current of Ag decreased as lactate molecules occupied the imprinted cavities on the MIP.<sup>311</sup> PB was embedded with cortisol-imprinted electropolymerized PPY MIP as a redox reporter on screen-printed carbon electrodes (Figure 13a). The electrodes are coated with a porous poly(vinyl alcohol) (PVA) hydrogel to allow diffusion of cortisol from the accumulated finger sweat to the MIP electrode upon touch. Binding to the cortisol template impedes the electron transfer process of the embedded PB. Using amperometry, the oxidation current of PB decreases as a function of increasing cortisol concentration.<sup>311</sup> To allow for continuous sensing, *in situ* regeneration of the electropolymerized MIP is typically performed with amperometry (Figure 13b).<sup>87</sup> A generic strategy for electroactive species involves electropolymerizing the template on laser-engraved graphene electrodes and conducting detection with DPV. To detect nonelectroactive targets, the MIP membrane is prepared on top of an electrodeposited PB layer and binding events are monitored by LSV. A broad range of small molecule targets can be sensed using these techniques, including amino acids, metabolites, and nutrients.

A MIP-based, wearable PEDOT:PSS-based organic electrochemical transistor (OECT) was developed for noninvasive cortisol sensing (Figure 13c).<sup>312</sup> MIP particles were entrapped in an inert plasticized poly(vinyl chloride) matrix to form the molecularly selective membrane (MSM). Binding of cortisol to the MSM modulates the ion transport to the PEDOT:PSS channel, which modulates the drain current. Hence, the OECT transducer allows the detection of nonelectroactive targets without the need for a redox reporter. A MIP-based self-powered triboelectric sensor also demonstrated label-free detection of a nonelectroactive target, lactate (Figure 13d).<sup>313</sup> Lactate binding to the lactate-imprinted MIP on polyvinylidene fluoride (PVDF)/graphene electrode lowers the energy barrier and electric potential of the triboelectric nanogenerator (TENG).

MIP sensors have demonstrated immense potential in the development of wearable and continuous epidermal biosensing

technologies. However, several challenges will need to be addressed before the broad adoption and integration of MIPs as artificial bioreceptors for on-body biomarker detection. Current research into MIPs primarily focuses on the detection of small molecules, and the sensitive recognition of larger molecules like proteins has been rarely explored. Nonspecific binding of targets with similar structures and functional groups is a common challenge faced by all MIPs.<sup>262</sup> This is even harder to address for large molecules due to the heterogeneous nature of interactions at the binding sites.<sup>314</sup>

**4.8.4. Biosensor Design Considerations.** There are countless biosensor configurations with the selection and combination of different bioreceptors and signal transducers. Understanding the unique advantages and disadvantages of different bioreceptors and transducers and thoughtful selection is a critical step to the successful implementation of bioaffinity sensing technologies for wearable sweat analysis. It is challenging to simultaneously achieve the best sensitivity, selectivity, reproducibility, reusability, and stability: antibody- and nucleic acid-based sensors can achieve high sensitivity and selectivity, but their *in situ* regeneration is extremely challenging; certain aptamer- and MIP-based sensors may have limited sensitivity but can operate *in situ* continuously. Therefore, it is crucial to identify and achieve certain critical biosensor characteristics and inevitably compromise on others based on different application scenarios. For instance, if molecules with similar structural and functional groups exist at similar concentrations as a target analyte, it is important to select receptors with better selectivity such as antibodies and aptamers. On the other hand, if the reusability of a sensor is critical for more frequent or continuous sampling, MIPs or certain aptamers that have limited sensitivity but can be regenerated could be a better candidate. Hence, understanding the nature of the specific target and its analogs in sweat and the intended application scenario such as sampling frequency is important for designing sweat biosensors.

## 5. SWEAT EXTRACTION AND SAMPLING

The accessibility of sweat as a biofluid has shown great potential for noninvasive wearable health monitoring. Various methods of sweat stimulation were introduced over the past decades in different settings, and sampling of the induced sweat was heavily investigated with novel prototypes. In this section, we will summarize the common sweat induction methods and recent innovations in sweat sampling.

### 5.1. Sweat Induction

**5.1.1. Thermally-Induced, Exercise-Induced, and Natural Sweat.** Sweat can be induced in various manners, such as thermal stimulation, exercise, natural secretion, and iontophoresis. For thermal stimulation, subjects are placed in a heated environment (e.g., sauna bathing) to induce thermal

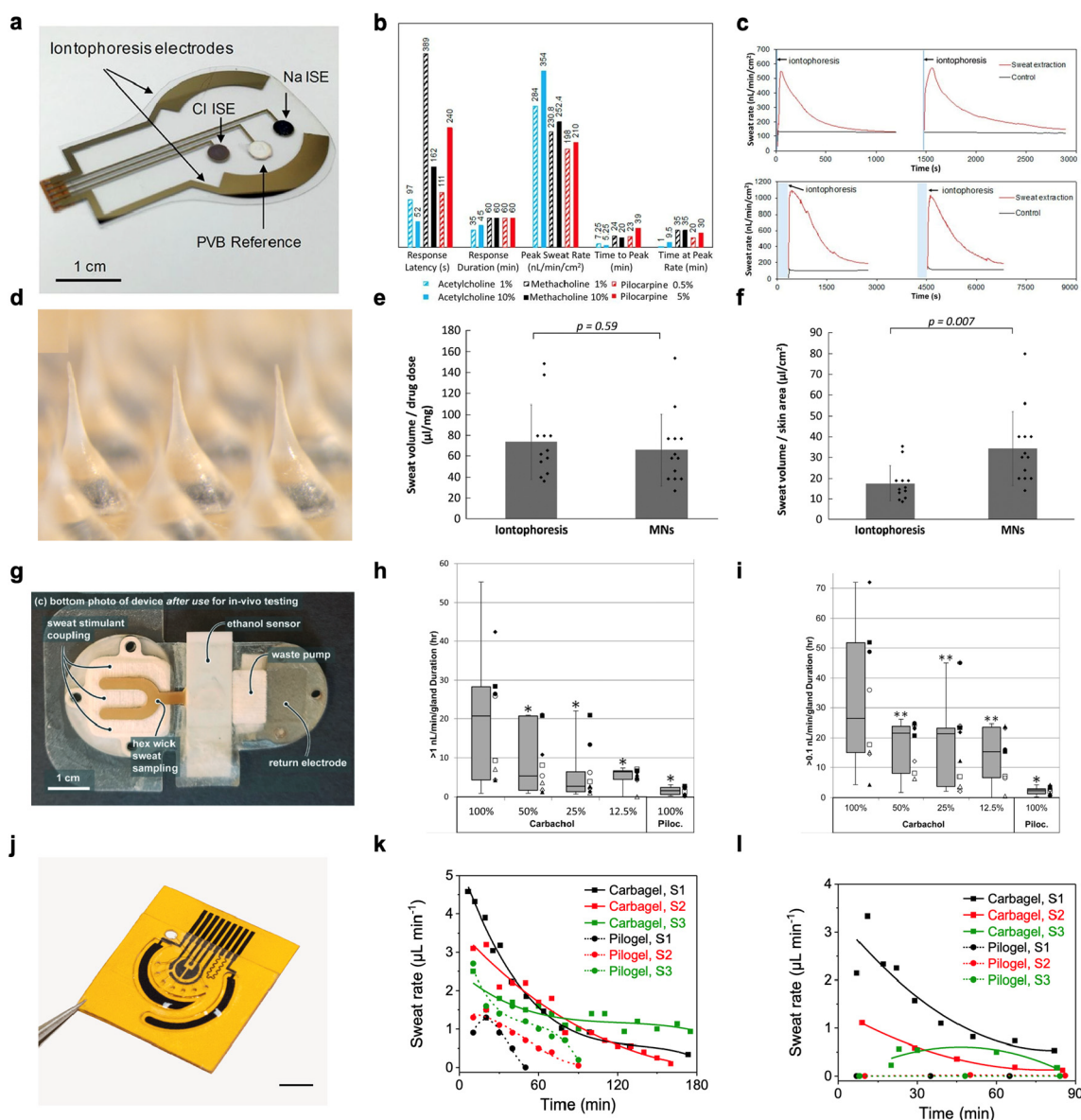


**Figure 15.** Iontophoresis-based sweat induction. **a–c**, An iontophoresis patch (**a**) and sweating responses to different cholinergic agents (**b,c**). Reproduced with permission from ref 326. Copyright 2017 Proceedings of the National Academy of Sciences. **d–f**, A microneedle-based iontophoresis device (**d**) and *in vivo* sweat responses of the device (**e,f**). Reproduced with permission from ref 327 under CC BY 4.0. Copyright 2021 Wiley. **g**, A carbachol-based iontophoresis sensing device. Reproduced with permission from ref 53. Copyright 2018 Royal Society of Chemistry. **h,i**, High sweat rate (**h**) and low sweat rate (**i**) duration of carbachol and pilocarpine iontophoresis stimulation, respectively. Reproduced with permission from ref 37. Copyright 2018 Elsevier. **j**, A flexible laser-engraved iontophoresis sensing patch. Scale bar, 5 mm. **k,l**, Localized sweat rates measured from the stimulated (**k**) and surrounding (**l**) skin areas after a 5 min iontophoresis with pilocarpine and carbachol. **j–l**, Reproduced with permission from ref 87. Copyright 2022 Springer Nature.

sweat at a skin temperature of 40–41 °C, with a full-body sweat production of 0.6–1 kg/h.<sup>315–317</sup> Exercise-induced sweat is prevalent in many studies; however, the sweat rate could fluctuate with respect to variations in exercise type and intensity. Some common exercises include treadmill running and stationary biking, where the exercise intensity could be controlled and recorded. As thermal and exercise induction could impose constraints on subjects' physical conditions and testing environment, there is an increasing trend in using naturally occurring sweat for downstream sensing.<sup>318–323</sup> The naturally secreted sweat, also called “background sweat”, occurs during regular routines and entails relatively low sweat rates around 10 times lower than that of exercise sweat.<sup>321</sup>

**5.1.2. Iontophoresis-Induced Sweat.** Iontophoresis is a procedure where a small current delivers a cholinergic drug loaded in hydrogel into the skin. Two pieces of hydrogels are attached to the skin; the anode hydrogel contains a cholinergic agent while the cathode hydrogel contains electrolytes to facilitate current flow (Figure 14). As the cholinergic agent stimulates the muscarinic 3 (M3) receptors on sweat glands, a direct sweat response is elicited. Depending on nicotinic receptor specificity, the iontophoretic drug may induce peripheral sudomotor axon reflex sweating.<sup>30</sup>

**Sweating Response by Different Cholinergic Agents.** Different cholinergic agonists could be used to induce sweating, and the sweating response varies in duration and area, which is determined by the receptor activity and

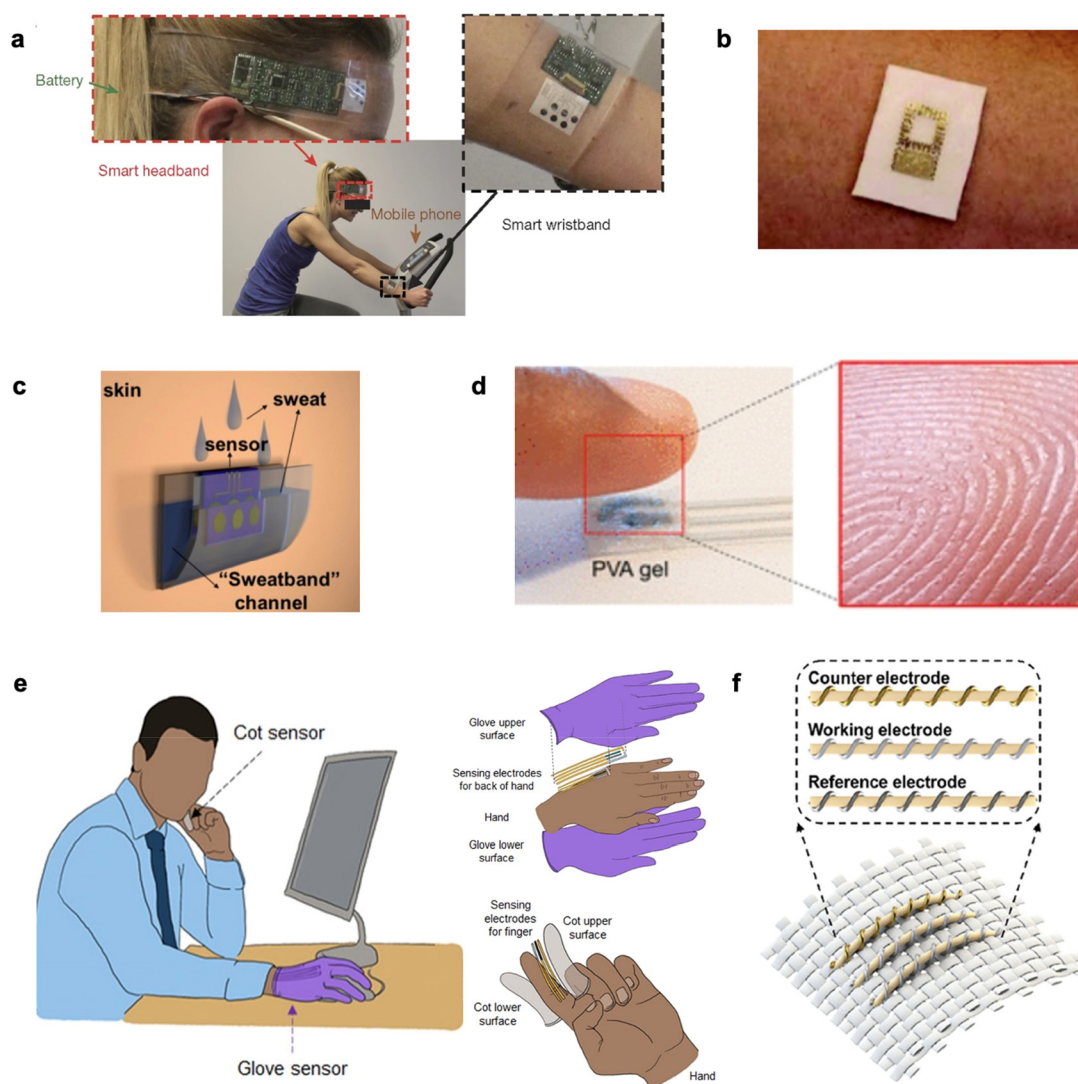


**Figure 16.** Sweat sampling without microfluidic systems. **a**, Rayon pad to direct exercise sweat to sensors in a fully integrated sweat band. Reproduced with permission from ref 12. Copyright 2016 Springer Nature. **b**, Absorbent sponge for sweat wicking from the skin to sweat sensing by the gold electrodes patterned facing outward. Reproduced with permission from ref 346. Copyright 2014 Wiley. **c**, Silicone headband with a channel for gravity-facilitated sweat flow through the chip. Reproduced with permission from ref 154. Copyright 2017 American Chemical Society. **d**, Touched-based hydrogel for sweat capture from a fingertip. Reproduced with permission from ref 323. Copyright 2021 American Chemical Society. **e**, Nitrile glove-based and cot-based system for natural sweat analysis. Reproduced with permission from ref 321. Copyright 2020 The American Association for the Advancement of Science. **f**, Fiber-based platform for sweat capture from the skin. Reproduced with permission from ref 199. Copyright 2019 American Chemical Society.

susceptibility to acetylcholinesterase (AChE) hydrolysis. Acetylcholine and methacholine are hydrolyzed by AChE and thus have a shorter sweating duration. On the other hand, the nicotinic activity of the cholinergic agents affects the indirect axon-reflex sweating and thus the area of the sweat response. For example, the  $\beta$ -methyl group of bethanechol limited the nicotinic activity and thus the sweating response is highly localized and mostly direct sweating underneath the placement of the iontophoresis gel. Detailed studies and summaries of the receptor activities and sweating response can be found in previous literature.<sup>33,37,324,325</sup>

**Wearable Platforms for Sweat Iontophoresis.** Over the past decade, various iontophoresis devices have been developed for wearable sweat induction. The commercially available Macroduct system is Food and Drug Administration (FDA)-approved for iontophoresis-based sweat induction for cystic fibrosis diagnosis and uses pilocarpine as the cholinergic

agonist. After initial current ramping, a constant current is administered through the pilocarpine gel discs strapped onto the arm. The device automatically ramps down the current and shuts down after 5 min. Although the device provides customizable options with the straps for stimulation at different locations on extremities and across different age groups (babies to adults), the system remains bulky and unsuitable for regular wear. Similar systems could be achieved for initial prototype testing with an iontophoresis device and custom lab-made hydrogels loaded with selected cholinergic agonists.<sup>37</sup> To improve wearability, a flexible wristband containing iontophoresis electrodes and housing an FPCB was developed (Figure 15a).<sup>326</sup> The sweating response to iontophoresis gels loaded with different cholinergic agonists (acetylcholine, methacholine, and pilocarpine) was characterized in terms of response latency, sweating duration, peak sweat rate, time to peak and time at peak rate (Figure 15b).

Moreover, periodic iontophoresis of different acetylcholine loads was performed and higher sweat rate with longer sweat duration was observed for the 10% acetylcholine gel compared to the 1% acetylcholine gel (Figure 15c). In addition to the gel-based wearable systems,<sup>190,254,328–331</sup> a pilocarpine-loaded microneedle patch was recently developed for sweat testing.<sup>327</sup> With an array of 100 microneedles at a length of 600  $\mu\text{m}$ , the iontophoresis patch is much smaller and thinner than a regular commercial iontophoresis gel (Figure 15d). In an equine model, the microneedle patch produces a much higher sweating volume per unit area and unit dose compared to the pilocarpine hydrogel (Figure 15e,f). While the previous studies focused on local sweating, the first use of carbachol for sweat extraction was integrated into a band-aid-shaped system with an external iontophoresis device (Figure 15g).<sup>53,332,333</sup> With the custom-made carbachol gels compared with pilocarpine gels, the group also studied the sweating duration at high sweat rates (Figure 15h) and at low sweat rates (Figure 15i) over a long time frame (over 10 h). More recently, a flexible laser-engraved iontophoresis patch with a much smaller form factor was developed with small carbachol gels cast onto laser-engraved graphene electrodes, and on-demand sweat induction was achieved by integrated FPCB (Figure 15j).<sup>87</sup> The sweat rates at the stimulated area and the surrounding skin areas were characterized after a 5 min iontophoresis with pilocarpine and carbachol (Figure 15k,l). In addition to novel form factors, variation in the current profile for enhanced sweat volume was studied and a sinusoidal pulsed current profile was suggested for use in patients with sweat problems.<sup>334</sup>

**5.1.3. Sweat Composition by Different Induction Methods.** The composition of sweat may vary across sweat induction methods. First, the pH of sweat tends to be higher in iontophoresis-induced sweat compared to thermogenic sweat.<sup>335</sup> High sweat rates and low ductal  $\text{HCO}_3^-$  reabsorption may contribute to this higher pH.  $\text{Ca}^{2+}$  and  $\text{Mg}^{2+}$  levels were observed to be higher in sweat obtained from the sauna than in sweat obtained from exercise.<sup>336</sup> Recent metabolomic studies also revealed variations in lipid profiles<sup>337</sup> and metabolites<sup>319</sup> among iontophoresis-induced, exercise-induced, and natural sweat, including notable variations in L-alanine, pyruvate, L-aspartate, BCAAs, asparagine, lysine, and fumarate concentrations.<sup>319</sup> The stability of metabolites in sweat also plays a critical role in the quantitation process; sweat metabolite stability was shown to last for 90 min at simulated body temperature.<sup>338</sup> For natural sweat at a much slower sweat rate, it is suggested that quantitation results may be compromised due to metabolic quenching of enzymatic reactions and metabolite stability, an issue especially relevant for untargeted metabolomics analysis.<sup>339</sup> For targeted metabolomics analysis, such as drug tests, controlled stability studies should be done to achieve repeatable quantitation within the applicable detection range.<sup>340</sup> Moreover, tissue-dependent factors (e.g., keratin amount and thickness of stratum corneum) affect the iontophoresis response between individuals and at different body locations, potentially also impacting the sweat composition.<sup>339</sup>

## 5.2. Sweat Sampling

**5.2.1. Absorbent-Based Sweat Sampling.** Upon sweat induction, proper sweat collection is required such that low volumes of sweat produced are efficiently harvested for analysis.<sup>341</sup> Historically, sweat was sampled without a transporting mechanism (i.e., microfluidic system). Several

materials have been used for sweat collection with no microfluidic system, which can wick (e.g., rayon,<sup>12,326,342–344</sup> paper,<sup>345</sup> textile,<sup>199</sup> absorbent pad or sponge,<sup>346–349</sup> hydrogel<sup>311,322,323,350,351</sup>) or capture (e.g., glove<sup>321</sup> and sweatband<sup>154</sup>) the sweat directly on the sensing system. A 1.5 cm  $\times$  2 cm  $\times$  50  $\mu\text{m}$  sized rayon pad was used to collect up to 10  $\mu\text{L}$  of sweat for sweat sensing (Figure 16a):<sup>12</sup> the rayon efficiently captures small sample volumes by confining fluid transport to the wicking nanogrooves of the rayon fiber.<sup>343,352</sup> To obtain consistent real-time on-body results, newly secreted sweat was absorbed onto the pad, refilling and replacing old sweat that is transported along the rayon fiber by capillary motion. In addition to rayon, hydrophilic, functional, soft, and porous substrates could serve as useful for sweat collection on the skin (Figure 16b).<sup>346</sup> Suitable materials for selection include cellulose paper, cellulose sponge, poly(vinyl alcohol) sponge, hydrophilic polyurethane foam dressing, and silicone foam dressing. In addition to the porous sponge format, a silicone-based and commercially available sweatband was incorporated into a sweat sampling platform to guide sweat sampling during active movement (i.e., exercise) by means of gravity-driven sweat collection channels that load the sensor and pool sweat in a reservoir (Figure 16c).<sup>154</sup> A nitrile glove-based sweat sampler was used to passively collect hundreds of microliters of sweat within 30 min (Figure 16e).<sup>321</sup> Additionally, elastic textiles can be utilized to collect sweat and soak the interwoven sensing fibers (Figure 16f).<sup>199</sup>

Hydrogels are biocompatible and do not require active sweat stimulation, enabling their use in various touch sensor pads.<sup>311,322,323,350,351</sup> Hydrogels decrease the resistance of sweat secretion at the skin since the hydrophilicity of hydrogels reduces the Laplace pressure barrier: the hydrogel acts as a reservoir for sweat, transports sweat away from the skin surface and thus prevents local accumulation that builds the pressure barrier.<sup>322</sup> With a finger touch, the sensor directly extracts and collects the sweat and monitors the targeted biomarker without any additional stimulation.<sup>322</sup> Hydrogel pads, however, do not reflect the actual biomarker concentration but rather the concentration within the hydrogel, which is limited by diffusion during contact.<sup>350,351</sup> A porous PVA hydrogel membrane-based cortisol and glucose biosensor was introduced to resolve the previous issues (Figure 16d).<sup>323</sup> Created with a water-soluble sucrose template, the porous hydrogel structure offers higher permeability and lower impedance relative to nonporous systems, shortening the sweat sampling time and thus reducing sensing lag. Under natural perspiration, the sweat-absorbing PVA porous hydrogel membrane pulls the sweat droplets from the fingertip in contact by capillary pressure.<sup>323</sup>

**5.2.2. Pressure Driven Microfluidics.** Although direct sweat sampling using absorbent materials is simple and easy to implement, there are limitations to be resolved.<sup>353</sup> Direct sweat sampling limits the capability of the biosensor due to mixing and carry-over between new sweat and old sweat, resulting in contaminating sweat samples. For instance, with the bulk rayon material (e.g., regenerated cellulose), it is hard to rapidly capture a change in the analyte concentration.<sup>352,354,355</sup> Without a system for continuous sweat flow to refresh the sensing sample and control of sample evaporation and volume, the biosensor may yield less reliable continuous readings and should serve as a single-use only device. Microfluidics enables a continuous sweat flow through microfluidic channels and encapsulated sensing chambers or reservoirs and therefore

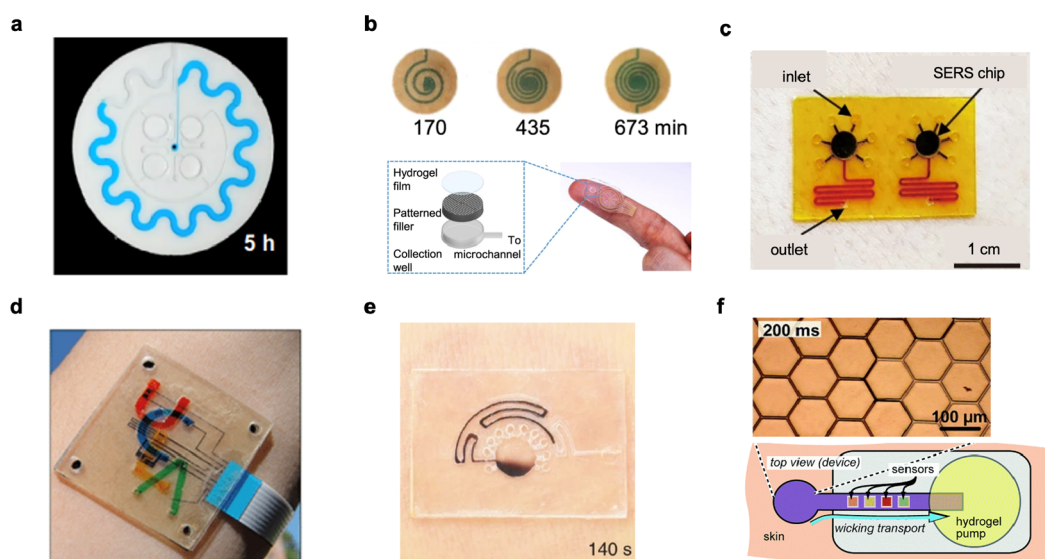


**Figure 17.** Sweat sampling with pressure driven microfluidics. **a**, PDMS-based sweat harvesting system. Reproduced with permission from ref 239. Copyright 2016 The American Association for the Advancement of Science. **b**, PDMS microfluidic with hydrophilic fillers for natural sweat collection and transport. Reproduced with permission from ref 253 under CC BY 4.0. Copyright 2021 Nyein et al. **c**, PDMS-based wearable SERS microfluidic platform. Reproduced with permission from 249 under CC BY 4.0. Copyright 2022 He et al. **d**, Laser-patterned 3D microfluidic system. Reproduced with permission from ref 357. Copyright 2019 Royal Society of Chemistry. **e**, Laser-engraved microfluidic patch with fast sweat refreshing. Reproduced with permission from ref 75. Copyright 2019 Springer Nature. **f**, Hex-wick for fast and low-volume sweat sampling. Reproduced with permission from ref 352. Copyright 2018 Royal Society of Chemistry.

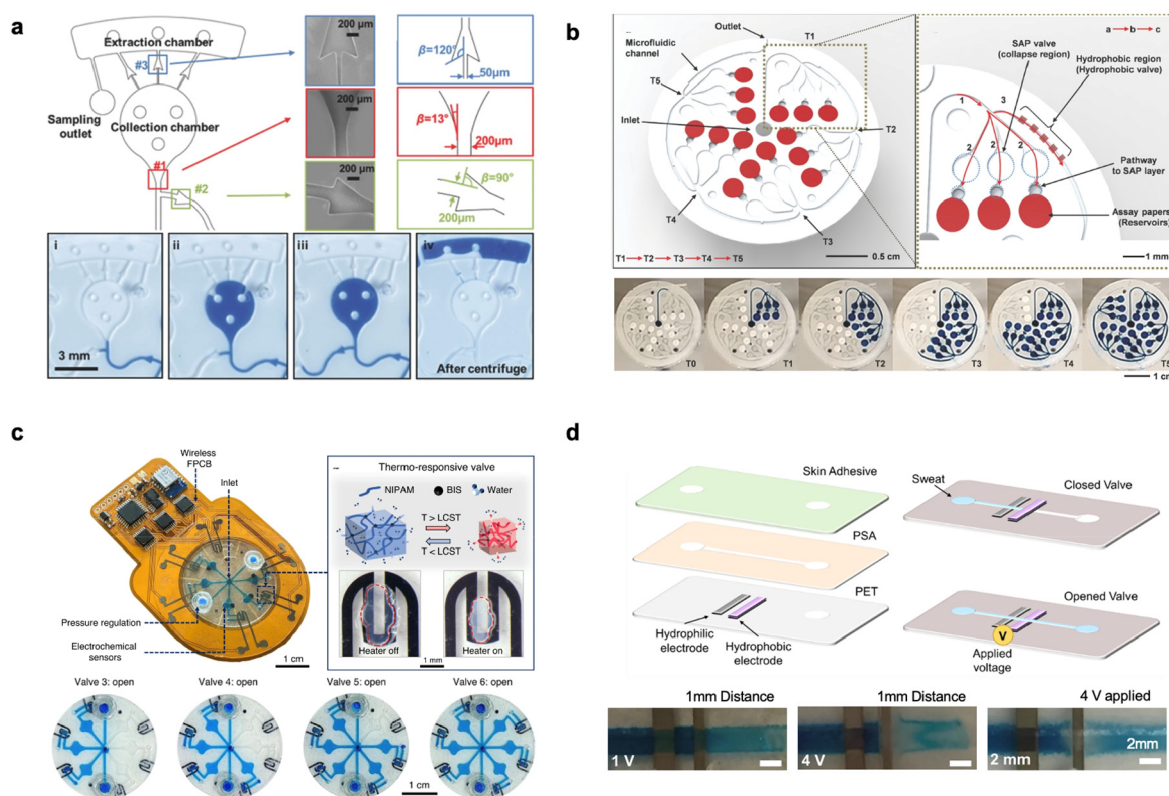


**Figure 18.** Sweat sampling with fluid actuation. **a**, Passive actuation based on capillary bursting valves. Reproduced with permission from ref 251. Copyright 2017 Wiley. **b–d**, Active actuation based on super absorbent polymer (SAP) (**b**), thermal-responsive hydrogel (PNIPAM) (**c**), and electrowetting valves (**d**). **b**, Reproduced with permission from ref 364. Copyright 2018 Wiley. **c**, Reproduced with permission from ref 365 under CC BY 4.0. Copyright 2020 Lin et al. **d**, Reproduced with permission from ref 366. Copyright 2021 Springer Nature.

resolves the limits.<sup>75,353</sup> With the use of microfluidics, microliter sampling volumes can be collected at the sensor

surface to generate the same quality of response compared to bulk solution analysis.<sup>75,87</sup>

Conventional microfluidics uses PDMS as the building-block material and directs the flow of secreted sweat via capillary action.<sup>239,252</sup> The combination of soft microfluidics (PDMS) with flexible plastic substrates (polyethylene terephthalate (PET)) has been introduced to ensure continuous and long-term sensing with a well-sealed detection chamber, which harvests sweat to decrease evaporation and contamination of sweat samples.<sup>252</sup> A soft-epidermal microfluidic system using PDMS was invented to capture and transport sweat to microchannels and reservoirs (Figure 17a).<sup>239</sup> In this design, the geometry of the channel was tailored to reach high structural stability, low vapor permeability, and minimal backpressure to prevent backflow.<sup>239</sup> To facilitate faster sweat sampling, patterned hydrophilic filler (SU8) with thin hydrogel film was applied in the sweat collecting reservoir to enhance rapid uptake at low secretion rates and reduce filling lag before the sweat flows through the PDMS channels to arrive at the sensing area (Figure 17b).<sup>253</sup> Flexible microfluidic nanoplasmonic sensors were developed with PDMS and a nonpermeable SERS substrate for the microfluidic system (Figure 17c).<sup>249</sup>

In addition to PDMS-based systems, other materials have been used to develop pressure-drive microfluidics.<sup>75,352,356,357</sup> Layers of thin-film polymers were integrated into a microfluidic chip by roll-to-roll processing and the chip featured hydrophobic polymeric materials to transport the sweat sample under natural gland pressure.<sup>358</sup> In addition to roll-to-roll processing, laser ablation and engraving were applied on adhesives and polymeric films (e.g., poly(methyl methacrylate) (PMMA), PET) to create microfluidics that achieved rapid sweat sampling.<sup>75,87</sup> With proper layer designs, the laser-engraved microfluidics could be flexible, and complex in 3D structure with minimal dead volume (Figure 17d).<sup>357</sup> In addition to having a flexible and complex structure, laser-engraved microfluidics offers good sweat refreshing and could potentially provide an estimate of the sweat rate (Figure 17e).<sup>75</sup> For low volume sampling, a hexagonal network of gold-coated open microchannels was developed to achieve rapid wicking transport and reduce dead volume against the skin surface and analyte exchange (Figure 17f).<sup>352</sup> In another design, hydrophilic plastic films and adhesives were processed by cutting plotter and subsequent lamination to achieve fast elimination of sweat from the skin and wicking of sweat into channels.<sup>356</sup>

While pressure-driven microfluidics resolve problems in sweating mixing and contamination, the conventional PDMS material is susceptible to the adsorption of small hydrophobic molecules over time and the systems have limited control of sweat flow rate and sweat flow direction.<sup>359,360</sup> In this section, various fluid activation methods for sweat sensing are discussed.

**Passive Fluid Actuation.** A classic example of passive fluid actuation is the capillary bursting valves (CBVs). CBVs passively control the direction of sweat flow by creating valves of different bursting pressures determined by the channel geometry (Figure 18a).<sup>251</sup> The varied CBVs provide paths of different pressure resistance, and sweat travels through the less resistance. As sweat enters the sampling device from the skin, it goes through channels and a series of microreservoirs and fills sequentially.<sup>237,251,361–363</sup> The CBV can also be used for direction control in multireagent reaction scenarios (e.g., immunoassay), where storage of the sweat inside the reservoir is required for the incubation process.<sup>284</sup>

In addition to channel geometry, the surface hydrophilicity could also be tuned to achieve passive fluid control, as shown in the hydrophobic valves at the junction of fluid chamber and channel. In one study, the innate hydrophobicity of PDMS was preserved at the hydrophobic valve while hydrophilic treatment was performed on the channel surface. When sweat enters the device, the advancing front of sweat in the hydrophilic channel becomes blocked by the hydrophobic valve and forced to flow into the chamber. As the chamber becomes fully filled, the sweat flow overcomes the bursting pressure of the hydrophobic valve and goes through the channel. Upon judicious design and placement of the hydrophobic valves, channels and chambers, sequential filling of the chambers could be achieved with little mixing effects.<sup>367</sup>

Besides the one-time use valving system demonstrated above, a reusable Tesla valve system was developed with optimized geometry from conventional designs.<sup>368</sup> The Tesla valves improve the diodicity (one-direction flow characteristic), accelerating forward flow while limiting reverse flow. For sweat sampling at low Reynolds number, an adapted geometry of the Tesla valve was constructed minimize reflux at the inlet and evaporation at the outlet of sweat sampling.<sup>369</sup>

**Active Fluid Actuation.** While passive fluid valves work by posing a pressure barrier which is overcome by sweat flow, active valve systems could stop the flow in response to certain stimuli. In one embodiment, superabsorbent polymer (SAP) was implemented as an active valve for sweat sampling and isolation (Figure 18b).<sup>364</sup> Once the sweat flows through the SAP and fills the reservoir, the SAP swells and block the sweat flow into/out of the reservoir. Once the reservoirs are full, close the sweat flow by swelling. Coupled with hydrophobic valves, the system allows for sequential filling of multiple reservoirs over time.<sup>364</sup> Another example is a resettable strain-actuated elastomeric pinch valves (EPV) and elastomeric suction pumps (ESP) that open the valve for fluid flow into a negative pressure volume upon user-activated pull on the device.<sup>257</sup> The EPV is a narrow pinch valve that stays close as default due to van der Waals forces between the parallel PDMS surface; upon the manual pull of the device, a strain-induced deformation of the EPV occurs and the valve becomes open for fluid flow. The ESP relies on a serpentine microchannel with a variable volume upon lateral extension of the serpentine. While the manual pull opens the EPV, the strain also deforms the serpentine channel and created an increase in the volume, thus creating a negative pressure for fluid suction through the EPV into the serpentine channels and then to the exit. When the pull is released, the EPV returns to the default close state and the serpentine channels shrink to the initial state volume.

Another example of active fluid actuation is microheater-controlled thermos-responsive hydrogel valves. Poly(*N*-isopropylacrylamide) (PNIPAM) hydrogel was selected as it deforms significantly when the local temperature crosses past its lower critical solution temperature (LCST) (Figure 18c).<sup>365</sup> When the local temperature rises from below to above the LCST, the hydrogel shrinks to open the valve for fluid flow; when the local temperature drops to below the LCST, the hydrogel expands and the valve is closed.<sup>370</sup> A circuit-controlled micropatterned heater was employed in this design to control the local temperature and thus the valve.

In addition to thermal activation, electrowetting has been employed to construct valves for sweat sampling. An electrowetting valve consists of two parallel conductive electrodes across a microfluidic channel. The surface of the

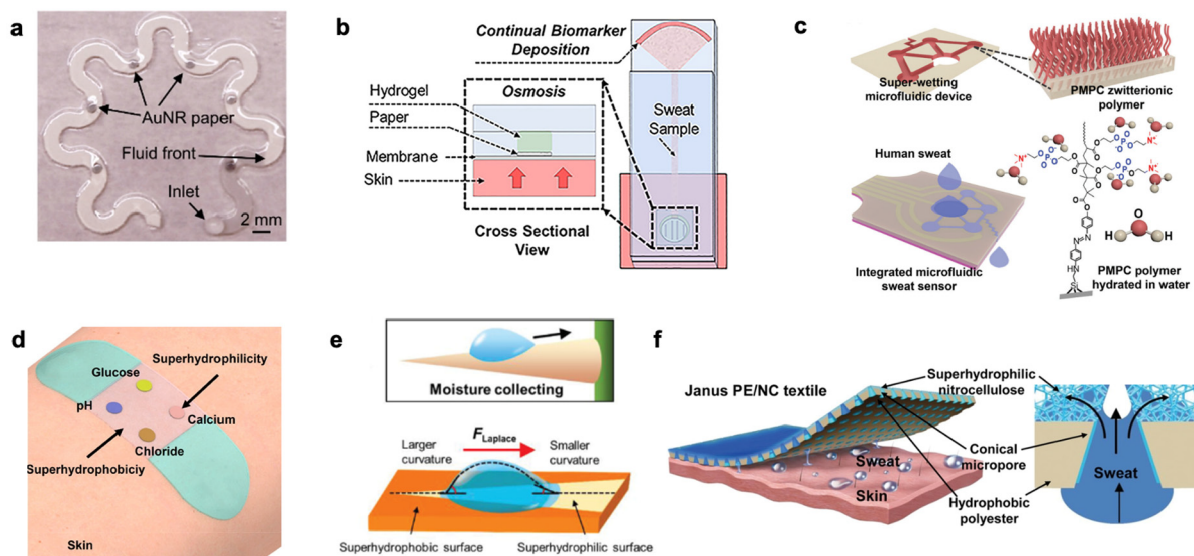


**Figure 19.** Sweat sampling with material-enhanced fluid transport. a–c, Sweat transport improved with paper (a), hydrogel (b), and Zwitterionic polymer grafting (c). a, Reproduced with permission from ref 246. Copyright 2022 The American Association for the Advancement of Science. b, Reproduced with permission from ref 374. Copyright 2021 American Chemical Society. c, Reproduced with permission from ref 385. Copyright 2021 Wiley. d, Sweat collection by patterned superhydrophobic-superhydrophilic band. Reproduced with permission from ref 236. Copyright 2019 American Chemical Society. e, Cactus-spine-inspired directional sweat sampling. Reproduced with permission from ref 386. Copyright 2021 Wiley. f, Janus textile for directional sweat transport across layers. Reproduced with permission from ref 387. Copyright 2019 Wiley.

electrode downstream is coated with a film of hydrophobic insulator material; as the electrolyte solution (i.e., sweat) flows through, the fluid front is blocked by the downstream hydrophobic electrode.<sup>371,372</sup> When a low voltage is applied to the electrode pair, the interfacial surface energy of the hydrophobic surface is reduced, and the electro-wetting-on-dielectric actuation occurs to open the valve for fluid flow. For sweat sampling application, the conventional electro-wetting valve design<sup>373</sup> was adapted with a hydrophilic electrode upstream to wick the fluid (Figure 18d).<sup>366</sup> Moreover, the optimized electro-wetting valve was designed with the optimal spacing and hydrophobic coating to enable fast actuation and at a low potential to prevent hydrolysis. With multiple electro-wetting valves, sequential filling of the designated reservoirs is achieved.

**5.2.3. Sweat Sampling with Material- and Structure-Enhanced Fluid Transport.** While conventional plastic films or silicones (e.g., PDMS) provide excellent designs for fluid sampling, these materials usually monolithically attach to skin and lacks breathability for long-term wear. When positioned with channel direction vertical to sea level, there could be gravitational force that affects the sweat fluid flow inside the channel. To address the limitations, various alternative materials have been introduced.

**Paper/Hydrogel-Based Fluid Transports.** Paper-based microfluidics<sup>246,374–381</sup> provides superior breathability thanks to the fibrous network. Without the need of external pumping, paper-based microfluidics enables fluid flow with capillary force and eliminates air bubbles with its air-permeability. With judicious placement of filter paper inside the channels and chambers, sequential filling of chambers was achieved with excellent wicking performance and minimum backflow.<sup>381</sup> In another embodiment, the paper was placed along the serpentine microfluidic channel to route the sweat flow for flow rate quantitation and biomarker analysis; the clear contrast between wet and dry paper provides a visible estimate

of the sweat loss, which could be further modeled based on the Lucas–Washburn equation (Figure 19a).<sup>246,382</sup> The paper can also be integrated with hydrogels to combine osmotic pumping and capillary wicking into the same sampling scheme.<sup>374–376</sup> A hydrogel with a highly concentrated osmolyte solution creates a chemical gradient that drives osmosis and helps direct sweat into the system and sweat gets wicked along the paper strip to the pie-shaped evaporation pad (Figure 19b).<sup>374</sup> The capillary action continues to drive fluid flow for long-term use as the sweat evaporates from the paper pad. However, the fluid flow degrades gradually when the hydrogel osmolarity changes over time.<sup>383,384</sup> Many paper-based microfluidics have direct contact with skin and could be susceptible to contamination during sweat sampling.

**Materials to Improve Hydrophilicity-Based Fluid Transport.** PDMS is inherently hydrophobic, but its surface hydrophilicity may be tuned by either plasma treatment, surface coating,<sup>388,389</sup> mixing of hydrophilic polymer,<sup>390,391</sup> or surface microstructure.<sup>392–394</sup> However, phase separation of PDMS and the hydrophilic polymer<sup>395</sup> results in poor long-term stability,<sup>396</sup> and cost issues<sup>397</sup> are remaining for those treated PDMSs. A superhydrophilic zwitterionic polymer surface was designed to increase the duration of hydrophilicity and wettability of PDMS and address those problems (Figure 19c).<sup>385</sup> Zwitterionic polymers (poly(2-methacryloyloxyethyl phosphorylcholine) and poly(sulfobetaine methacrylate)) contain both positive and negative charge in the same functional monomer and become significantly hydrated in an aqueous solution.<sup>398</sup> With the zwitterionic polymer grafted onto hydrophobic PDMS substrate, the wettability was significantly improved and the sweat transport can overcome gravity.<sup>385</sup> Similarly, surface modification was performed to tune the hydrophilicity and hydrophobicity for efficient sweat sampling.<sup>236,399</sup> With superhydrophobic silica on top of the PET film with masked O<sub>2</sub> plasma treatment for hydrophilicity modification, a superhydrophobic sweat band with super-

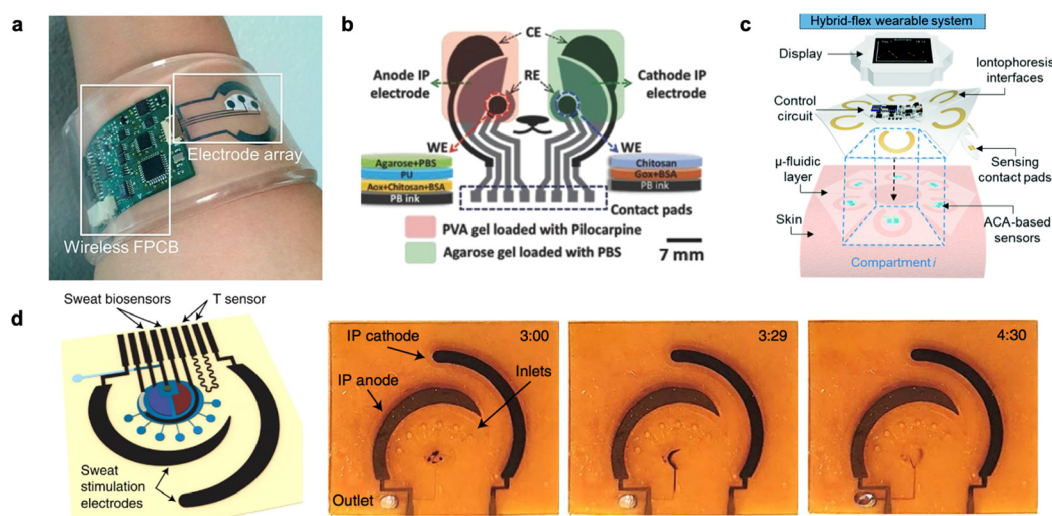


**Figure 20.** Sweat sampling with induction. **a**, Iontophoresis with rayon-based sweat sampling. Reproduced with permission from ref 326. Copyright 2017 Proceedings of the National Academy of Sciences. **b,c**, Pilocarpine-iontophoresis induction with tattoo-based sensing platform (**b**) and multicompartment laser-patterned microfluidic systems (**c**). **b**, Reproduced with permission from ref 331 under CC BY 4.0. Copyright 2018 Wiley. **c**, Reproduced with permission from ref 405. Copyright 2020 Royal Society of Chemistry. **d**, Carbachol-iontophoresis with laser-engraved microfluidics. Reproduced with permission from ref 87. Copyright 2022 Springer Nature.

hydrophilic microwells was developed; with the high contrast of the hydrophobic–hydrophilic property around the microwell, the sweat collected forms as droplets for colorimetric detection (Figure 19d).<sup>236</sup> Similarly, hydrophobic PDMS-coated cotton with a hydrophilic Modal thread as a microreservoir and a microchannel was implemented for sweat sampling and sensing.<sup>400</sup> In another work inspired by cactus spines, the superhydrophilic coating was patterned as a wedge inside a rectangular superhydrophobic bound: a laplace pressure gradient was therefore created to enable directional sweat transport while accelerating the circulation rate of sweat and reducing sensing lag time (Figure 19e).<sup>386</sup>

Besides factors that affect water contact angle, there are scenarios when low water permeability is desired for proper function in sweat sensing. For aquatic athletes, poly(styrene-isoprene-styrene) (SIS) was selected for sweat collection underwater.<sup>235</sup> SIS possesses low water permeability, resistance to water transport, flexibility, and high elasticity.

**Janus Textile-Based Fluid Transports.** While some capillary-based sweat sampling could enable fast sweat wicking against gravity, a Janus layer could achieve similar directional transport from one side to the other and against gravity. A Janus material refers to a material with asymmetric properties on each side;<sup>235</sup> in our discussion, it refers to an interface with asymmetric wettability (one side superhydrophobic while the other hydrophilic). With proper thickness and pore size of both hydrophobic and hydrophilic layers, the water can penetrate from the hydrophobic to the hydrophilic side but cannot penetrate in the opposite direction. A modified commercial Janus system for sweat sensing was developed with polyester (PE) for a hydrophobic and nitrocellulose (NC) membrane for a superhydrophilic layer with conical micropores that guide sweat flow unidirectionally (Figure 19f).<sup>387</sup> With a conical shape, the micropores prevent undesirable stickiness and cold sensations from sweat. Various Janus systems were also employed in sweat sampling as a fiber network<sup>401</sup> and treated silk;<sup>402</sup> Janus membranes are also useful for eliminating sweat from the sensing area.<sup>403</sup>

### 5.3. Integrated Platforms for Sweat Induction and Sampling

As iontophoresis provides a feasible means for wearable sweat sensing in sedentary individuals, various platforms integrating iontophoresis with sweat sampling were developed in recent years. An iontophoresis-integrated wearable sensor was developed to ensure a sweat flow rate with long sensing time while using a water-absorbent thin rayon pad to wick sweat (Figure 20a).<sup>326</sup> Tattoo-based biosensors integrated with pilocarpine-iontophoresis were also proposed (Figure 20b).<sup>190,331,404</sup> A porous cryogel instead of a hydrogel was selected for a drug-loaded anode material to provide better permeability for drug release. Recently, a multicompartment iontophoresis device was developed to allow for on-demand pilocarpine iontophoresis at different time points of the day with laser-patterned microfluidics for fluid sampling (Figure 20c).<sup>331,405</sup>

Sample contamination from skin and a cholinergic agonist (e.g., pilocarpine) occurred in the previous designs. To address the challenges, sweat sensors with integrated carbachol-iontophoresis and microfluidics for sweat sampling were developed to enable sampling outside the stimulation area to reduce mixing of the agonist with sweat.<sup>37,53</sup> Hex-wick structures allow for fast collection of low volume sample and fast transport to the sensing area and further downstream to the waste pump.<sup>53</sup> A hydrophilic thin film of fumed-silica was implemented as the fluid coupling between the hex-wick and sensor surface to promote rapid rewetting.<sup>53</sup> Recently, a laser-engraved sensor with integrated carbachol-iontophoresis was reported (Figure 20d).<sup>87</sup> The inlets of the laser-engraved microfluidic system were placed away from the stimulation area to sample sudomotor axon reflex sweat, which is less contaminated with the carbachol agonist. Moreover, with the optimized inlet–outlet geometry, the sweat refreshing is fast upon a short iontophoresis session at a low iontophoresis current.

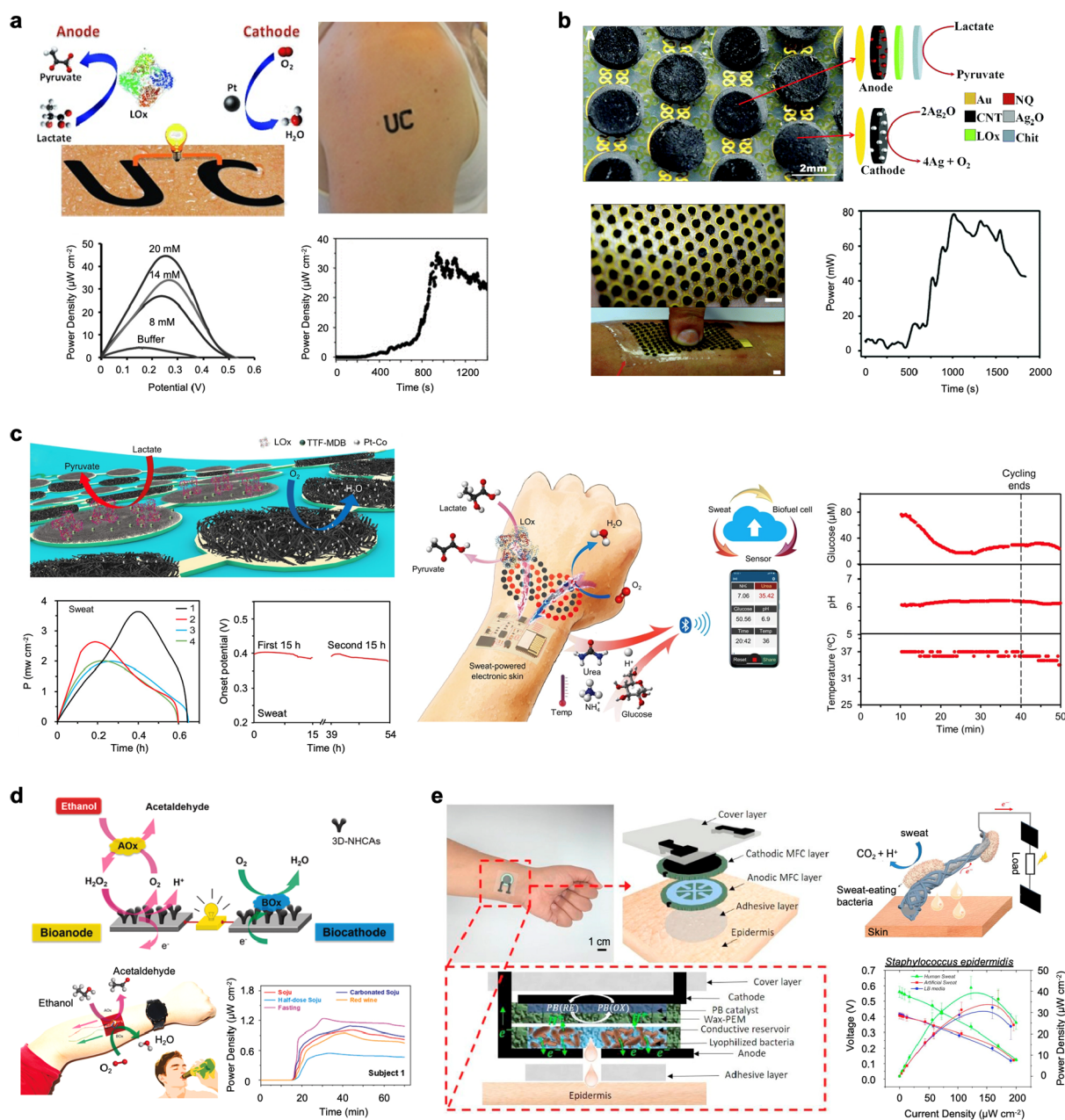


**Figure 21.** Biofuel cells for harvesting chemical energy from sweat. **a**, Epidermal tattoo-based biofuel cell for harvesting energy from sweat lactate. Reproduced with permission from ref 415. Copyright 2013 Wiley. **b**, Island-bridge-based lactate biofuel cell for enhanced performance under strain. Scale bar, 5 mm. Reproduced with permission from ref 419. Copyright 2017 Royal Society of Chemistry. **c**, A fully perspiration-powered electronic skin (PPES) for battery-free and wireless multiplexed sweat sensing. Reproduced with permission from ref 410. Copyright 2020 The American Association for the Advancement of Science. **d**, Ethanol biofuel cell for harvesting energy from sweat after alcohol consumption. Reproduced with permission from ref 413. Copyright 2021 Elsevier. **e**, Microbial fuel cell-based skin-interfaced microfluidic system for harvesting energy from bacteria in sweat. Reproduced with permission from ref 421. Copyright 2020 Elsevier.

#### 5.4. Discussion

The access to sweat has attracted intense research interest. Different sweat induction methods have been studied and varied sweat rates have been observed. Heat- and exercise-induced sweating could yield high sweat rates but impose constraints on individuals' fitness and sampling environment; natural sweat, on the other hand, offers convenient sampling but limits continuous monitoring due to low volumes. To achieve sweat induction in sedentary individuals, iontophoresis has been used as a nonstrenuous means to induce sweat with cholinergic agonists. A desired sweating response can be

achieved with a careful selection and dosing of the agonist and can be induced on-demand and on-body with recently invented devices.

As sweat arrives to the surface of the skin, harvesting and sampling of the sweat is critical to achieve reliable sensing downstream. Wicking materials are utilized to collect sweat directly and route sweat to sensors with great convenience and adaptability to different devices, but mixing of sweat and contaminants could become an issue. Microfluidic systems address these issues, using reservoirs that sweat can be stored in and continuously transferred to via microfluidic channels. Although microfluidics system under natural gland pressure

and capillary force enables continuous monitoring and reduces contamination issues, it does not allow to control sweat flow rate nor the direction of sweat flow. Furthermore, lag time issue occurs due to large amount of sweat required to be stored before transferring. Passive and active fluid actuation methods (i.e., valve systems) allow to control the flow of sweat. Superhydrophobic-superhydrophilic materials resolve lag time issues with faster and directional sweat transport. Yet, there are limitations such as valve controls require complicated construction or external control to actuate.

To achieve efficient sweat sensing, evaluation of the suitable sweat induction and sampling schemes should be considered. As an optimal sweat induction method is selected, feasible sweat sampling materials and methods could be narrowed down depending on the desired sweat refreshing rate, the sensor response time and detection time frame (one-time detection vs hours). With continued advances in micro/nanotechnology and increased understanding of sweat physiology, it can be expected that improvements in sweat induction and sampling devices could be achieved in the future.

## 6. POWERING WEARABLE SWEAT SENSORS

Current wearable devices in the market are primarily powered by bulky rechargeable lithium-ion batteries that need to be charged by a universal serial bus (USB) cable or through inductive coupling every couple of days. In the short run, companies are looking for innovations to extend the battery life of wearable devices and minimize the inconveniences of frequent charging. While the increase of battery power density is slow, rapid improvements in low-power electronics and wireless communication protocols have contributed significantly to extend the battery life of wearables, and the convenience of wireless charging options has also appealed to customers. On the other hand, charging of wearable devices can be eliminated by developing wearable energy harvesting systems that can harvest energy from human sweat, human motion, or the environment. In the long term, it is also critical to devise powering systems that are biocompatible and sustainable. Currently lithium batteries are rigid and bulky, limiting wearability to applications such as wrist watches that people are already accustomed to. Furthermore, lithium batteries often contain toxic heavy metals and flammable electrolytes that can cause potential safety hazards and disposal burdens.<sup>406</sup> Wearable powering systems composed of energy harvesting modules and energy storage modules that are flexible, stretchable, washable, and sustainable are highly sought after. These innovations will not only serve as a convenience to everyday users of wearable sensors, but also can be life changing in emergency or military scenarios where traditional device charging is not possible.

### 6.1. Wearable Energy Harvesting

An abundance of energy is present within our bodies and environment. Biochemical energy from sweat biofuels, kinetic energy from our body heat or motions, as well as solar energy from the sun or artificial light can be scavenged and converted into electrical energy to power wearables.<sup>407–409</sup> For wearable sensing applications, it is essential to develop compact and conformal energy harvesting modules that can be comfortably worn while scavenging power sufficient for electronic data acquisition and wireless communication. Recently, a variety of energy harvesting modules such as biofuel cells (BFCs), photovoltaic (PV) cells, TENGs, and magnetoelastic nano-

generators (MEGs) have been reported for powering wearable sweat sensors.

#### 6.1.1. Harvesting Biochemical Energy from Sweat.

Biofuel cells utilize catalysts such as enzymes and microbes to generate bioelectricity from redox-active fuels in biofluids such as lactate and glucose. For powering sweat sensors, biofuel cells harvesting energy from sweat metabolites is a natural match, and lactate is the most popularly used fuel due to its high concentration in sweat. Lactate biofuel cells consist of an anode immobilized with an LOx enzyme and a redox mediator such as ferrocene or quinone derivatives to facilitate the oxidation of lactate into pyruvate, with a complementary cathode consisting of a platinum (Pt) alloy or bilirubin oxidase (BOx) for facilitating the oxygen-reduction reaction. While lactate biofuel cells have reported the highest power density generating up to  $3.5 \text{ mW cm}^{-2}$  from natural sweat,<sup>410</sup> biofuel cells utilizing alternate fuels such as glucose, fructose, and ethanol have also been reported with promising applications.<sup>411–414</sup>

The first reported wearable sweat lactate BFC was based on a temporary transfer tattoo (Figure 21a).<sup>415</sup> The screen-printed carbon anode was modified with a tetrathiafulvalene (TTF)/CNT composite layer to mediate electron transfer at a low oxidation potential, followed by an LOx/albumin layer to catalyze the selective oxidation of lactate, and a chitosan/glutaraldehyde layer to secure the electrode materials. The screen-printed carbon cathode was modified with a Pt black layer, to facilitate the oxygen reduction reaction (ORR), and a Nafion protection film. The tattoo-based BFC could output up to  $44 \mu\text{W cm}^{-2}$  in a buffer containing 20 mM lactate, and up to  $70 \mu\text{W cm}^{-2}$  from sweat during an on-body cycling study.

Such screen-printing methods have also been applied for fabricating textile-based lactate biofuel cells.<sup>416,417</sup> Lactate biofuel cells printed on a detachable care label were integrated into various garments including headbands and wristbands, outputting up to  $100 \mu\text{W cm}^{-2}$  with 15 mM lactate.<sup>416</sup> While the care label could not be stretched, it could go through repeated deformations without losing significant power. To achieve stretchable textile-based BFCs, stretchable CNT inks and  $\text{Ag}_2\text{O}/\text{Ag}$  inks were developed respectively for the BFC anode and cathode.<sup>417</sup> Such inks were screen printed as serpentine structures on a polyurethane (PU) and Ecoflex modified stretchable textile such as a sock. The stretchable textile BFC could output up to  $250 \mu\text{W cm}^{-2}$  with 20 mM lactate and maintain a stable power output after 100 cycles of 100% stretching. In addition, a self-contained laser-induced graphene-based wearable BFC-in-a-tube was recently reported for energy generation from untreated human sweat to power a wearable digital watch.<sup>418</sup>

BFCs capable of outputting milliwatt levels of power are highly desired for Bluetooth-based wireless sensing applications. "Island-bridge" configuration epidermal BFCs have been reported with high power output, stretchability, and durability.<sup>419,420</sup> An electronic-skin biofuel cell (E-BFC) with lithographically patterned serpentine interconnects and screen-printed 3D CNT island electrodes was designed to output nearly  $1.2 \text{ mW cm}^{-2}$  with 20 mM lactate, while maintaining a higher power output after 100 cycles of 50% stretching (Figure 21b).<sup>419</sup> The high power output is attributed to the high active surface area of the LOx modified 3D carbon nanotube-naphthoquinone (CNT-NQ) pellets and 3D  $\text{Ag}_2\text{O}$ -CNT pellets fixed on the Au islands as bioanodes and biocathodes, respectively. Furthermore, the serpentine interconnects enable

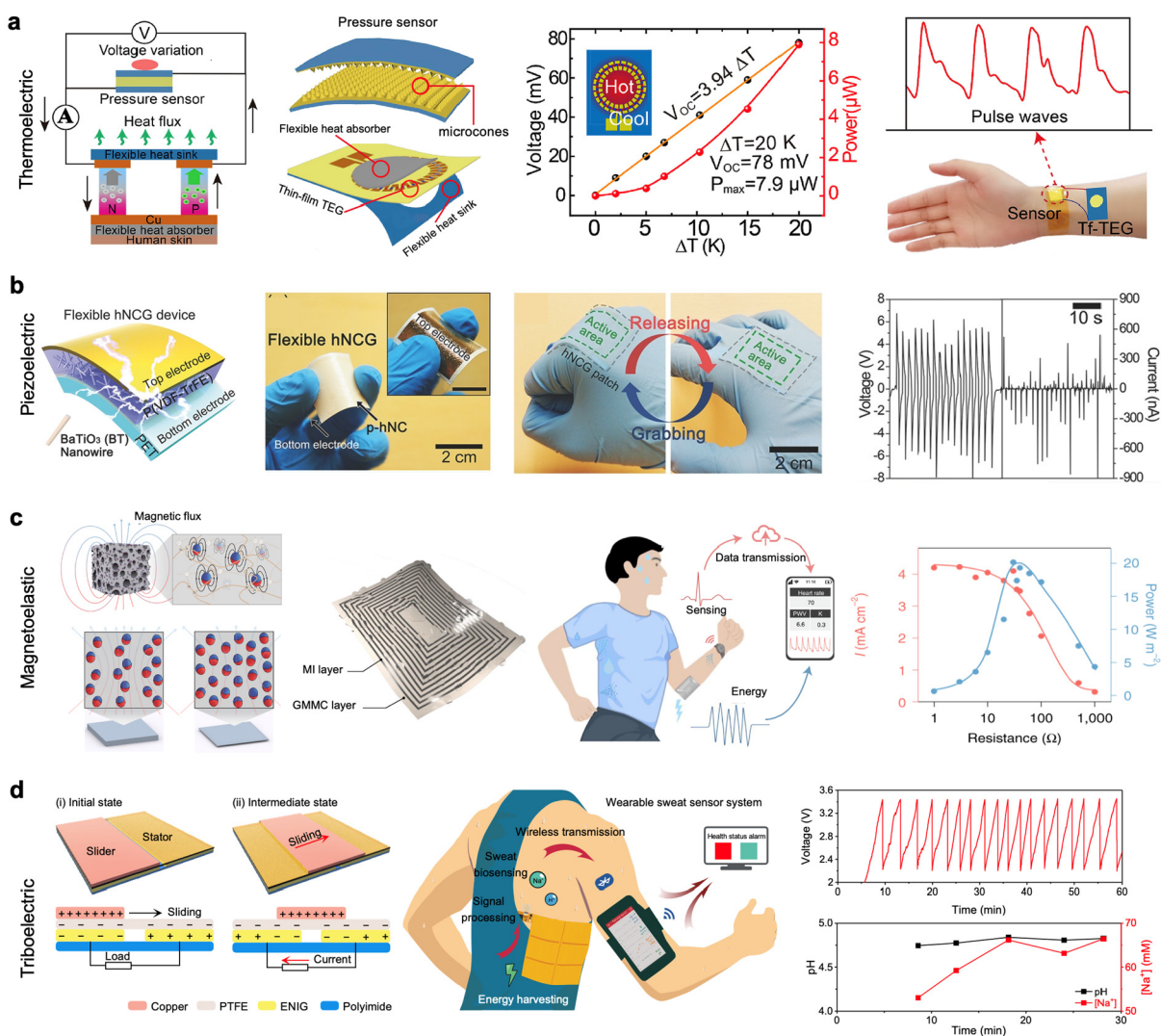


**Figure 22.** Nanogenerators for harvesting physical energy from the body. **a–d**, Skin-interfaced wearable devices for harvesting energy via the thermoelectric effect (**a**), the piezoelectric effect (**b**), the magnetoelastic effect (**c**), and the triboelectric effect (**d**). **a**, Reproduced with permission from ref 427. Copyright 2020 Elsevier. **b**, Reproduced with permission from ref 428. Copyright 2018 Wiley. **c**, Reproduced with permission from 429. Copyright 2021 Springer Nature. **d**, Reproduced with permission from ref 430. Copyright 2020 The American Association for the Advancement of Science.

repeated stretching of the device while imposing negligible strain on the active island electrodes. The E-BFC generated up to  $1 \text{ mW cm}^{-2}$  during active exercise on a human subject and was able to power a BLE radio.

In addition to high power output, long-term stability and system integration are key aspects of designing BFC-powered wearable sweat sensors. A fully perspiration-powered electronic skin (PPES) was designed by integrating a high-performance lactate BFC and a wireless multiplexed metabolic sensor system onto an ultrathin PI substrate (Figure 21c).<sup>410</sup> The BFC bioanode was prepared by modifying an Au electrode array with hierarchical Ni (h-Ni) microstructures, reduced graphene oxide (rGO) films, Meldola's blue-tetrathiafulvalene-modified carbon nanotubes (MDB-TTF-CNT), and LOx, whereas the BFC biocathode was prepared by modifying an Au electrode array with MDB-modified CNTs and cobalt-doped Pt nanoparticles. The lactate BFC could output up to  $2 \text{ mW cm}^{-2}$  with  $20 \text{ mM}$  lactate, and up to  $3.5 \text{ mW cm}^{-2}$  in real human sweat, which is the highest reported power density so far in the literature. Furthermore, the BFC displayed a very

stable performance over 60 h of continuous operation. Such an impressive power density and stability is attributed to the monolithic integration of 0D to 3D nanomaterials, which enables a dramatic increase in surface area and promotes facile electron transfer as well as low overpotential lactate oxidation. The battery-free PPES was able to harvest energy from exercise-induced sweat to power the continuous monitoring of sweat biomarkers (such as glucose, pH, urea, ammonium, and skin temperature) and transmission of data via BLE advertisements.

Alternate enzymatic biofuel cells harvesting energy from metabolites such as glucose, fructose, and ethanol have also shown promise.<sup>411,413,414,422</sup> As an example, an ethanol BFC was developed to harvest energy from sweat following the consumption of alcohol (Figure 21d).<sup>413</sup> The three-dimensional coraloid nitrogen-doped hierarchical-microporous carbon aerogels (3D-NHCAs), alcohol oxidase (AOx), and terephthalaldehyde (TPA) modified bioanode catalyze the oxidation of ethanol into acetaldehyde, while the 3D-NHCAs, BOx, and TPA modified biocathode reduces oxygen into water.

Due to the low concentration of ethanol present in sweat, the ethanol BFC generates a peak power density of  $1.01 \mu\text{W cm}^{-2}$ . However, as the peak power generated is correlated to the ethanol levels in sweat, the epidermal ethanol BFC could potentially serve as a self-powered sensor as demonstrated in devices utilizing glucose and lactate BFCs as self-powered sweat sensors.

Microbes can also be utilized to harvest energy from sweat in several ways.<sup>421,423–426</sup> One method is to develop microbial fuel cells that harvest energy by garnering the electrons produced during cellular respiration. A major advantage of using microbes as opposed to enzymes as catalysts for generating electricity is that bacteria offer significantly longer shelf life and operation. For wearable on-skin application, several sweat-eating bacteria that exist on the skin were assessed for their bioelectrogenesis capability, then integrated into a skin-interfaced microfluidic system (Figure 21e).<sup>421</sup> Devices utilizing lyophilized *S. epidermidis* were able to produce an average maximum power density of  $41.74 \mu\text{W cm}^{-2}$ . For extended long-term operational capabilities, *B. subtilis*, a skin-habitant microbe that can enter and revive from dormancy depending on the availability of sweat was utilized in developing long-functioning wearable microbial fuel cells.<sup>423,425</sup> The device could maintain a power density of  $24 \mu\text{W cm}^{-2}$  even after 48 h of operation. Aside from fuel cell-based energy harvesting,  $40 \mu\text{m}$  thick microbial biofilm sheets were also engineered to harvest hydroelectricity from sweat evaporating on the skin surface.<sup>426</sup> The device could continuously output  $\sim 1 \mu\text{W cm}^{-2}$  while not relying on cell viability.

As such, biofuel cells can be fabricated from biocompatible and sustainable materials to harvest biochemical energy directly from the surface of the skin. Enzymatic biofuel cells based on lactate can generate milliwatt levels of power from natural sweat, which is sufficient to power multiplexed wireless wearable sensor systems. On the other hand, sweat energy harvesters based on microbes have the potential to improve durability and shelf life.

**6.1.2. Harvesting Kinetic Energy from the Body.** Our bodies convert chemical potential energy into thermal and mechanical energy to maintain body temperature and achieve locomotion. The kinetic energy produced by our bodies can be readily harvested by wearable generators. Thermoelectric generators (TEGs) and pyroelectric nanogenerators (PYNGs) have been developed to convert body heat into electrical energy, whereas piezoelectric nanogenerators (PENGs), MEGs, and TENGs have been reported to convert body motion into electrical energy.

The first commercial energy harvesting wearable electronic device was powered by body heat. In 1998, taking advantage of the Seebeck effect, Seiko developed an electronic wristwatch that used thermoelectric generators to harvest energy from the temperature differential between the skin and the environment. This device could produce  $\sim 25 \mu\text{W}$  over a  $1.5 \text{ }^\circ\text{C}$  temperature differential. Since then, various wearable TEGs have been developed to increase power output and improve wearability.<sup>427,431–437</sup> Bismuth telluride-based alloys are popular candidates for TEGs owing to their high Seebeck coefficients and low thermal conductivities. For increased biocompatibility, bismuth telluride-based legs have been fabricated on flexible and stretchable substrates.<sup>427,431,432,434,436,437</sup> Flexible heat sinks have also been incorporated for increasing temperature differential and power.<sup>427,434,436</sup> A super absorbent polymer-

based flexible heat sink was paired with a flexible TEG module to generate up to  $38 \mu\text{W cm}^{-2}$  for the first 10 min during sedentary wearable use, capable of powering a wearable electrocardiogram (ECG) sensor.<sup>434</sup> For enhanced skin conformability, a thin-film TEG was constructed with a heat-absorbing insulation film and a flexible hydrogel heat sink to maximize the temperature gradient between the skin and the environment (Figure 22a).<sup>427</sup> Despite its 2D structure, the thin-film TEG could be applied on the skin to supply sufficient power in the  $\mu\text{W}$  range for self-powered pulse monitoring. On the other hand, bismuth telluride-based alloys can be rigid and brittle. For improved robustness and deformability, alternate materials have also been explored for developing fiber-based TEGs,<sup>438,439</sup> thin-film TEGs,<sup>427,435</sup> and organic TEGs.<sup>440</sup>

Back in 1880, Pierre and Jacques Curie discovered that an external mechanical force applied on a semiconductor crystal can break central symmetry and cause charge separation that leads to a piezoelectric potential. For piezoelectric energy harvesting in wearable applications, it is important to identify natural human movements that can exert the most mechanical force on the piezoelectric nanogenerator. The first account of a wearable piezoelectric energy harvesting device in 2001 took advantage of two mechanic forces exerted on the shoe during walking: the heel-strike force was absorbed by a prestressed semiflexible piezoelectric lead zirconate titanate (PZT) harvester and the sole bending force was harnessed by flexible multilaminar PVDF harvester.<sup>441</sup> Mounted under the insole of the shoe, the rather bulky PZT and PVDF harvesters could output 8.4 mW at a 1.1 Hz walking pace and 1.3 mW at a 0.8 Hz walking pace. Further inspired by the development of a ZnO nanowire array-based PENG in 2006,<sup>442</sup> various wearable PENGs scavenging energy mostly from the heel strike force or joint bending force were developed to improve performance and wearability.<sup>443,444</sup> As heel strike-based PENGs do not require extreme flexibility, inorganic piezoelectric materials like PZT with high piezoelectric coefficients are ideal. However, bulk inorganic piezoelectric materials can be stiff and brittle. As harvesters relying on muscle contraction-based joint bending require high deformability, inorganic piezoelectric materials can be discretized into nanostructures such as nanorods,<sup>445</sup> nanowires,<sup>446</sup> or thin films.<sup>447</sup> Another popular approach to achieve high flexibility or stretchability is to use organic piezoelectric materials. While piezopolymers are highly deformable, their electrical properties are an area for improvement. To achieve highly efficient and flexible piezopolymer-based PENGs, lead-free perovskite  $\text{BaTiO}_3$  nanowires were incorporated into a poly(vinylidene fluoride-co-trifluoroethylene) (P(VDF-TrFE)) piezoelectric nanocomposite (Figure 22b).<sup>428</sup> The nanocomposite nanogenerator could harvest up to 14 V and  $4 \mu\text{A}$  during simulated bending, and up to 8 V and 900 nA during repeated grabbing and releasing hand motions when placed under a glove.  $\text{BaTiO}_3$  nanowires and the PVC polymer were also aligned into piezoelectric fibers that were to be woven into a fabric with cotton threads.<sup>448</sup> This stretchable textile PENG could be worn as an elbow pad to generate up to 1.9 V and 24 nA during arm bending.

Mechanical force can also change the magnetic property of a material as characterized by the magnetoelastic effect or Villari effect. However, this effect is generally observed in rigid alloys that are too stiff to comply on the skin for wearable devices. In 2021, a soft wearable MEG that can generate  $2.02 \text{ mW cm}^{-2}$  with continuous hand tapping was developed on the discovery

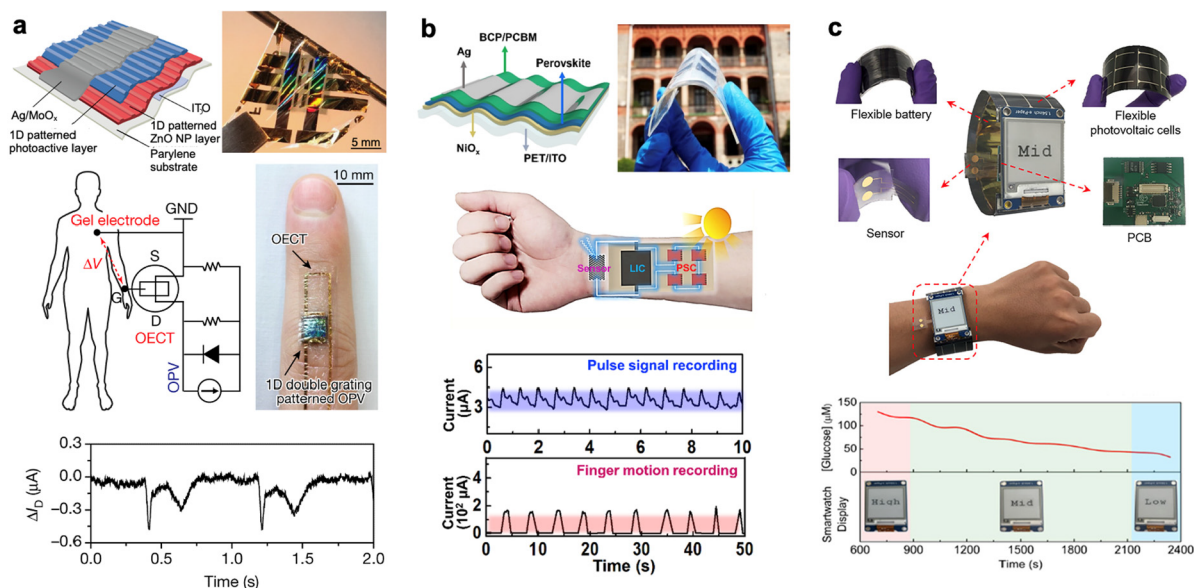


**Figure 23.** Photovoltaic cells for harvesting energy from the environment. **a**, An ultrathin organic photovoltaic cell integrated with an organic electrochemical transistor for wearable self-powered cardiac signal recording. Reproduced with permission from ref 458. Copyright 2018 Springer Nature. **b**, A flexible perovskite solar cell paired with a flexible lithium ion capacitor to self-power wearable strain sensors. Reproduced with permission from ref 462. Copyright 2019 Elsevier. **c**, A fully integrated smartwatch powered by a commercial flexible solar cell and a flexible battery for the continuous monitoring of sweat glucose. Reproduced with permission from ref 328. Copyright 2019 American Chemical Society.

of a giant magnetoelastic effect observed in a soft composite containing dispersed micromagnets in a porous silicone rubber matrix (Figure 22c).<sup>429</sup> Mechanical stress on this soft system would change the spacing and dipole alignment of the micromagnets, leading to local variations in the magnetic field. This giant magnetomechanical coupling (GMMC) layer was paired with a coil-patterned liquid-metal magnetic induction (MI) layer that converts the magnetic field variation caused by mechanical stress to electrical power via electromagnetic induction. In another account, a textile MEG with a power density of  $667 \mu\text{W cm}^{-2}$  under continuous hand tapping was fabricated by weaving soft magnetic fibers composed of nanomagnets in a silicone polymer with conductive yarns. An advantage of MEG-based energy harvesters is that they are waterproof, as magnetic fields experience minimal attenuation through water.

Triboelectric nanogenerators that harvest energy from static charges induced during the contact of two dissimilar objects via friction electrification were first introduced in 2012.<sup>449</sup> The TENG operated in a contact-separation mode wherein repeated contact and separation of the TENG electrodes, like the repeated mechanical pressures applied to the wearable PENGs and MEGs, would generate an AC voltage. Thus, wearable TENGs have also been developed to harvest energy from the heel strike action during walking and from joint bending during muscle contractions. However, TENGs can operate in other modes such as the lateral-sliding mode, free-standing mode, and the single-electrode mode.<sup>450,451</sup> The lateral-sliding mode and the free-standing mode enable the harvesting of triboelectric energy generated during a sliding motion between two objects, realizing the capture of energy from another dimension of motion. A wearable free-standing-mode flexible triboelectric nanogenerator (FTENG) was developed to capture triboelectric energy from repeated sliding of the arm against the torso, and fully powered a judiciously designed wearable wireless sensor system by human motion for the first time (Figure 22d).<sup>430</sup> Seamlessly integrated with the

wireless electronic circuit via commercial FPCB technology, the FTENG was able to generate  $41.6 \mu\text{W cm}^{-2}$  with a sliding frequency of 1.5 Hz, and charge a  $242 \mu\text{F}$  capacitor from 2.2 to 3.5 V 18 times during a 60 min running session. Each time the capacitor was charged to 3.5 V, it would power the electronic system to start up, acquire, and transmit one set of multiplexed sweat sensor data over BLE advertisements. The battery-free system was used to continuously monitor sweat pH and sodium levels during a running session.

As such, it was demonstrated that energy from body motion can provide sufficient power to a wireless wearable sweat sensor. While not discussed in this review, other types of energy harvesters such as PYNGs<sup>452</sup> and electromagnetic generators (EMG)<sup>453</sup> have been developed to harvest energy from body heat and motion. As elevated levels of motion are correlated with exercise and high power output, these energy harvesters are a great fit for exercise sweat-based fitness monitoring applications. On the other hand, generators based on body heat have the capacity to harvest energy in sedentary scenarios. However, a higher power density is desired for iontophoretic sweat stimulation, high frequency electrochemical measurement techniques, and low latency wireless communications.

**6.1.3. Harvesting Solar Energy from the Environment.** Harvesting energy from the biochemical or kinetic energy from our bodies often requires exercise or lacks power density. Harvesting ubiquitous energy such as light power from our environment can provide large amounts of power under various scenarios and activities including rest. Currently, crystalline silicon PV cell technologies are highly mature and are dominating the market due to their high conversion efficiencies and reliability. While silicon PV cells have reached 26.7% power conversion efficiency (PCE) under air mass 1.5 global (AM 1.5G) illumination,<sup>454</sup> they are not ideal candidates for powering wearable devices as they are rigid and have a low PCE under indoor illumination. On the other hand, solution processable organic or inorganic–organic

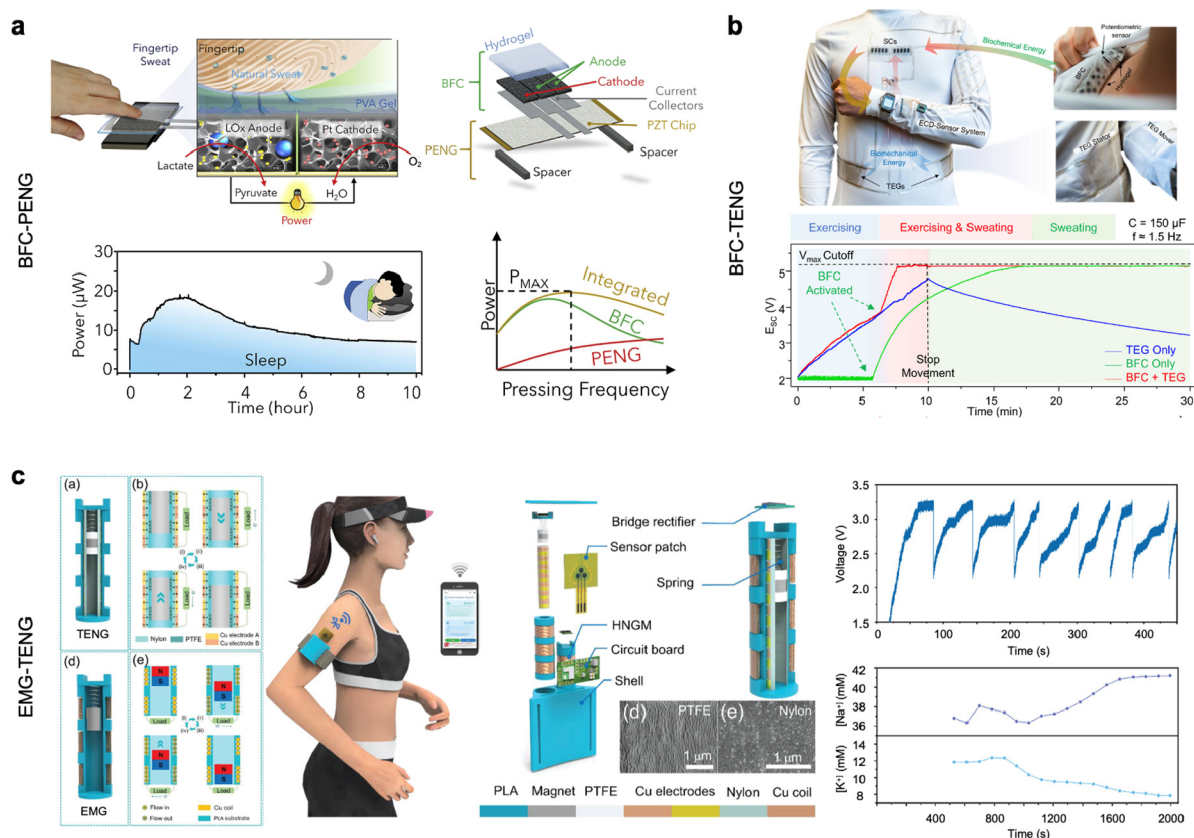


**Figure 24.** Hybrid energy harvesting from multiple energy sources. **a**, A hybrid energy harvester integrating a lactate biofuel cell and a piezoelectric nanogenerator for harvesting energy from natural fingertip sweat and finger tapping. Reproduced with permission from ref 466. Copyright 2021 Elsevier. **b**, A textile bioenergy microgrid integrating a biofuel cell and a triboelectric nanogenerator for harvesting energy from exercise induced sweat lactate and arm swinging motions. Reproduced with permission from ref 467 under CC BY 4.0. Copyright 2021 Yin et al. **c**, A spring-mass coupled hybrid generator integrating a triboelectric nanogenerator and electromagnetic nanogenerator for harvesting energy from exercise induced low-frequency vibrations. Reproduced with permission from ref 468. Copyright 2022 Wiley.

hybrid photoactive materials that can be processed at low temperatures have been used to fabricate flexible or stretchable solar cells on soft polymeric substrates.<sup>455,456</sup>

Compared to their inorganic counterparts, organic solar cells can be low-cost, lightweight, flexible, and biocompatible.<sup>457</sup> A wearable 3- $\mu\text{m}$ -thick ultraflexible nanograting-patterned organic photovoltaic (OPV) with a PCE of 10.49% under AM 1.5G illumination was developed and integrated with an organic electrochemical transistor-based sensor to achieve self-powered cardiac signal recording (Figure 23a).<sup>458</sup> The grating patterns on the OPV contributed to a surface plasmonic effect and antireflection effect that enhanced the PCE of the device across different illumination angles to enable an output power of over 10  $\text{mW cm}^{-2}$  on a sunny day, which is sufficient to power most wearable electronic functionalities. Furthermore, the device could deform to achieve highly conformal contact on the skin while maintaining a high power output. Despite various advantages, one downside of organic solar cells is their PCE.

Since their first emergence in 2009,<sup>459</sup> solar cells based on mixed organic–inorganic halide perovskites have been heavily researched due to their solution processability and unmatched photoelectric performance. Flexible perovskite solar cells have achieved efficiencies well over 20% under AM 1.5G illumination,<sup>460,461</sup> and there are reports of perovskite solar cells achieving efficiencies over 40% under low light LED (2700 K) illumination.<sup>461</sup> The capability of harvesting high

amounts of power in various lighting conditions is very attractive for powering wearable devices. Flexible perovskite solar cells with an efficiency of 14.01% have been integrated with a flexible lithium-ion capacitor to achieve a photo-rechargeable power source (Figure 23b).<sup>462</sup> As an application, this photorechargeable power source was used to self-power wearable strain sensors. While the high power output of flexible perovskite solar cells is attractive, perovskite materials are generally toxic, requiring special attention to the encapsulation of the device to prevent leaking. Nontoxic perovskite nanocrystals are also being explored as alternative photoactive materials.<sup>463</sup>

Another class of solar cells based on organic–inorganic hybrid materials are dye-sensitized solar cells. While lacking in terms of power conversion efficiency, dye-sensitized solar cells are characterized by their low cost and ease of fabrication, as well as their robustness, long-term stability, and relative nontoxicity.<sup>464,465</sup> In addition, these solar cells work well under low light intensity or indoor light. Due to their sustainability, pliability, and lightweight, dye-sensitized solar cells based on elastic conducting fibers are ideal candidates for textile-based photovoltaic devices.

Solar cells have also been employed for powering wearable sweat sensors. A fully integrated solar cell powered smartwatch was designed for the noninvasive and continuous monitoring of sweat glucose (Figure 23c).<sup>328</sup> For the power supply, a commercial flexible amorphous silicon solar cell and a custom



**Figure 25.** Wireless energy harvesting from the mobile phone. **a**, A bandage-like RFID sensor patch for the monitoring sweat  $\text{Na}^+$ . Reproduced with permission from ref 473. Copyright 2015 IEEE. **b**, A soft epidermal microfluidic device integrating an NFC-based wireless monitoring of sweat glucose and lactate. Reproduced with permission from ref 237. Copyright 2019 The American Association for the Advancement of Science. **c**, An NFC-based wireless sweat sensor system with a stretchable electrode array for the multiplexed monitoring of sweat  $\text{Na}^+$ ,  $\text{K}^+$ , pH, and glucose. Reproduced with permission from ref 474. Copyright 2019 Wiley.

developed flexible  $\text{Zn-MnO}_2$  battery were integrated as the watch strap. The commercial flexible solar cells have a PCE of 3.2% under AM 1.5G, and a PCE of 9.04% under low intensity room light ( $7.5 \text{ W m}^{-2}$ ). The electrochemical glucose sensor, PCB, and E-ink display were integrated into a dial platform to assess and classify the real time sweat glucose concentrations for displaying on the E-ink screen as high, medium, or low. The versatile system was assessed to monitor sweat glucose in various scenarios such as during iontophoretic sweat extraction, indoor biking, and outdoor running.

Solar cells that harvest energy from the environment can provide high power densities during various activities as long as there is sufficient light, both indoors and outdoors. For developing wearable solar cells, organic and perovskite materials have advantages over traditional inorganic materials as they can be solution processable, cost efficient, and highly flexible. Furthermore, organic solar cells have an advantage that they are biocompatible and safe, whereas perovskite solar cells display excellent power densities.

**6.1.4. Hybrid Energy Harvesting.** By combining different energy harvesting technologies, it is possible to extend the boundaries of potential operation scenarios and increase power conversion efficiencies of the energy harvesting module. Power can be complementarily harvested from multiple energy sources such as light and motion or sweat and motion to increase power output when multiple energy sources are available, and to sustain power output when one of the energy sources is absent. Additionally, power can also be synergistically extracted from a single energy source such as light or motion by integrating multiple energy harvesting mechanisms to increase the power conversion efficiency of the system.

In the context of sweat sensing, hybrid energy harvesting from sweat and motion is highly attractive. While the sedentary sweat rate in most body parts is too low for sweat extraction, the fingertip has a high passive perspiration rate that can be leveraged for touch-based natural sweat collection. A flexible and durable porous carbon-foam-based BFC and porous PVA gel was used to extract an average power of  $10.8 \mu\text{W}$  during 10 h of sleep from natural fingertip perspiration (Figure 24a).<sup>466</sup> A complementary PENG was vertically stacked with the BFC to additionally scavenge mechanical energy from finger pressing motions that can occur during daily activities such as typing and mouse clicking. At a pressing frequency and pressure of 6 beats per minute and 50 kPa, the BFC and PENG were individually able to charge a  $100 \mu\text{F}$  capacitor in 8 and 20 min, respectively. When combined, the hybrid system could charge

the capacitor in 4 min. In another account, a BFC module and a TENG module were combined as an e-textile bioenergy microgrid system that could harvest both biochemical and biomechanical energy during exercise to charge a flexible supercapacitor array and power a sweat sodium sensor with an electrochromic display (Figure 24b).<sup>467</sup> During a 10 min exercise session followed by 20 min of rest, the arm swing-based triboelectric generator alone could start charging a  $150 \mu\text{F}$  supercapacitor as soon as the exercise started, but stopped charging as soon as the exercise ended. On the other hand, the sweat-based BFC could only start charging the supercapacitor 6 min after exercise, but could continue to charge the supercapacitor after the exercise ended. The integrated system could rapidly fully charge the supercapacitor in 7 min and maintain the maximum voltage for over 30 min.

Solar cells and TENGs have also been combined to simultaneously scavenge energy from light and body motions.<sup>469–471</sup> Low-cost polymer fibers were used to assemble a dye-sensitized photovoltaic textile and a fabric TENG that were weaved into a  $320 \mu\text{m}$  thick single-layered interlaced hybrid power textile via an industrialized shuttle-flying process.<sup>469</sup> The highly deformable and breathable hybrid power textile with a size of  $4 \text{ cm} \times 5 \text{ cm}$  could stably deliver an output power of  $0.5 \text{ mW}$  from a human walking under sunlight ( $80 \text{ mW cm}^{-2}$ ). In another work, a double-layer structure self-powered textile was developed with a fiber-based dye-sensitized solar cell (5.64% PCE under AM 1.5G) top layer and a fiber-based super capacitor ( $1.9 \text{ mF cm}^{-1}$ ) bottom layer that are coupled as electrodes to construct a contact-separation mode TENG ( $0.91 \mu\text{A}$  during walking).<sup>470</sup>

Meanwhile, solar cells have also been integrated with TEGs to synergistically harvest the photoelectric and thermoelectric energy from light sources and the heat they generate. To develop a photovoltaic-thermoelectric hybrid generator with maximal power output, the cathode of the TEG was hybridized to the anode of the OPV module through vertical stacking.<sup>472</sup> The TEG could absorb and harvest energy from the long wavelength phonons that could not be exploited by the OPV, and the vertical stacking lead the TEG to reversely bias and inject electrons to the OPV. Through this hybridization, the open-circuit voltage losses of the OPV module were minimized, and the hybrid generator was able to harvest 46.3% more energy than the OPV module alone throughout the day at  $\Delta T = 10 \text{ K}$ . When worn on the forearm for 30 min, the hybrid generator could harvest up to  $34 \text{ mWh}$  during the day, and up to  $5.9 \text{ mWh}$  at night.

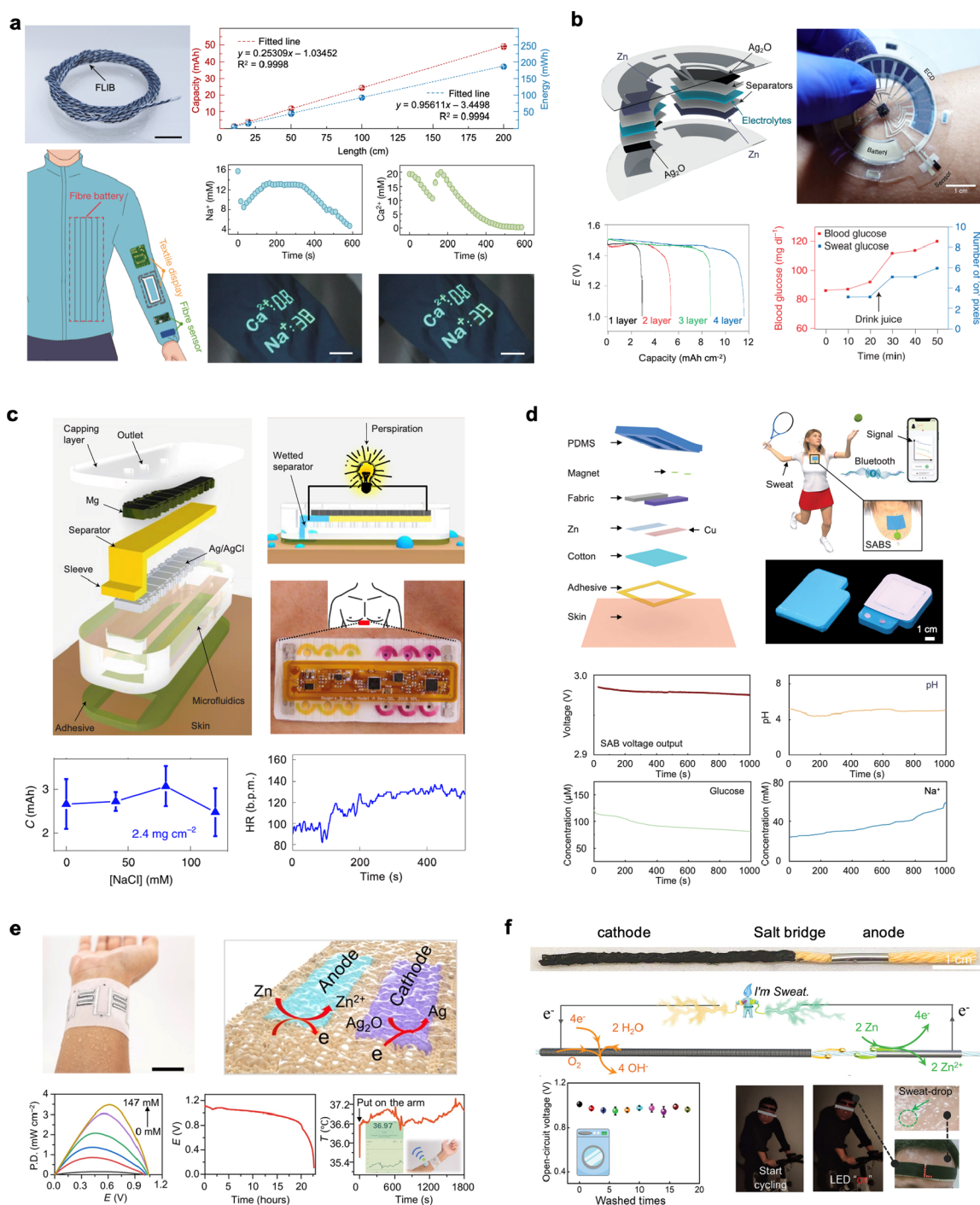


**Figure 26.** Energy storage: next generation batteries for powering wearable sweat sensors. **a**, A fiber-based e-textile lithium-ion battery for powering a wearable sweat sensor system that monitors and displays sweat  $\text{Na}^+$  and  $\text{Ca}^{2+}$  levels. Scale bar, 2 cm. Reproduced with permission from ref 478. Copyright 2021 Springer Nature. **b**, Screen-printed stretchable  $\text{AgO}$ -Zn battery powered epidermal sweat sensor patch for monitoring and displaying various sweat metabolite and electrolyte levels. Reproduced with permission from ref 480. Copyright 2022 Springer Nature. **c,d**, Epidermal sweat activated batteries for monitoring heart rate (**c**) and sweat biomarkers (pH, glucose, and  $\text{Na}^+$ ) (**d**). **c**, Reproduced with permission from ref 481. Copyright 2020 Springer Nature. **d**, Reproduced with permission from ref 482 under CC BY 4.0. Copyright 2022 Liu et al. **e,f**, Textile-based sweat activated batteries prepared on fabric (**e**) and on a cotton yarn (**f**). Scale bar, 3 cm. **e**, Reproduced with permission from ref 483. Copyright 2021 The American Association for the Advancement of Science. **f**, Reproduced with permission from ref 484 under CC BY 4.0. Copyright 2022 Xiao et al.

Next, a spring-mass coupled hybrid generator integrating a TENG and EMG was designed to harvest energy from low-frequency vibrations generated by human motion (Figure 24c).<sup>468</sup> Within a 3D-printed barrel structure embedded with electromagnetic winding coils and nylon film coated tribo-

electric interdigitated electrodes, a PTFE wrapped cylindrical magnet connected to a spring would slide up and down the barrel in response to mechanical vibrations to generate both electromagnetically and triboelectrically induced currents. Furthermore, the hybrid nanogenerator module was integrated

with a battery-free wireless sweat sensor module that could perform the selective monitoring and BLE advertisement of sweat  $\text{Na}^+$  and  $\text{K}^+$ . When running, the hybrid nanogenerator module could charge the storage capacitors ( $242 \mu\text{F}$ ) from 2.2 to 3.3 V within 33 to 60 s to perform a single cycle of sweat analyte measurements and data transmission. The integrated system was used to continuously monitor the sweat  $\text{Na}^+$  and  $\text{K}^+$  of a subject during 35 min of running.

**6.1.5. Wireless Energy Harvesting.** Another popular method for designing battery-free wireless wearable sweat sensors is to use radio frequency identification (RFID) technology commonly used for contactless payments. Through wireless inductive coupling between two conducting coils, an RFID tag (a wearable electronic sensor) can acquire power from an RFID reader (a mobile phone) for wireless data communication over the 13.56 MHz RF band. In 2015, an Adhesive RFID sensor patch for the potentiometric monitoring of sweat electrolytes was developed to operate on the standard ISO-15693 as a vicinity device (Figure 25a).<sup>473</sup> Since then, near-field communications (NFC), a subset of RFID technology, was popularized for higher levels of security and larger amounts of data exchange. A soft hybrid microfluidic system was developed for the visual colorimetric quantification of sweat chloride, pH, and sweat rate/loss, as well as the NFC-based wireless readout of the biofuel cell-based glucose and lactate sensors (Figure 25b).<sup>237</sup> Another NFC-based wearable sweat sensor system could perform the simultaneous monitoring of sweat glucose,  $\text{Na}^+$ ,  $\text{K}^+$ , and pH using a stretchable electrode array (Figure 25c).<sup>474</sup> While both BLE and NFC communication can enable wireless sensor data readout through a mobile app, NFC-based devices typically require close contact (<4 cm) for power and data exchange, which can be a limiting factor in certain applications. To extend the range of NFC communication, a long-range NFC reader can be used rather than a mobile phone.

To this end, various methods have been discussed for harvesting the energy necessary to power wearable electronics. To power wearable sweat sensors, biofuel cells have been used to harvest biochemical energy from sweat, nanogenerators have been used to harvest mechanical energy from body motions, photovoltaic cells have been used to harvest solar energy from ambient light, and NFC tags have been used to harvest electromagnetic energy from an RF field generated by a mobile phone. With sufficiently generated power, these energy harvesting modules can eliminate the need for bulky and potentially hazardous lithium-ion batteries, or at least reduce USB-based or wireless charging demands.

## 6.2. Wearable Energy Storage

Another way to eliminate rigid and bulky lithium-ion batteries from wearable devices is to replace them with thin and deformable wearable batteries or supercapacitors. To achieve deformable batteries, novel battery architectures incorporating island-bridge, origami, and textile structures, as well as novel battery materials incorporating intrinsically flexible and stretchable polymers have been developed. Furthermore, to address the safety concerns of lithium-ion batteries, alternate energy storage chemistries and biocompatible electrolytes such as sweat have been explored.

**6.2.1. Wearable Batteries.** Currently, most commercial wearable electronic devices are powered by rechargeable lithium-ion coin cell batteries as they boast the highest energy density. For transitioning from rigid wearables such as

smartwatches to soft and conformal wearables such as e-textiles or e-skins, flexible and stretchable lithium-ion batteries have been extensively developed using novel electrode architectures, including thin-film,<sup>475</sup> island-bridge,<sup>476</sup> origami,<sup>477</sup> and textile<sup>478</sup> structures.

Fiber lithium-ion batteries that can be woven into textiles are highly desirable for powering e-textile-based wearable sweat sensor systems. Through a novel, optimized, and scalable industrial process, meters of high-performance fiber lithium-ion batteries were mass-produced to have a high energy density of 85.69 W hour per kilogram (Figure 26a).<sup>478</sup> The capacity and energy of the fiber batteries increased linearly with fiber length, and the battery maintained over 80% of its capacity after 100,000 bending cycles. Furthermore, the batteries were woven into a jacket to power a fiber-based wearable sweat sensor system and display for the continuous and wireless monitoring of sweat  $\text{Na}^+$  and  $\text{Ca}^{2+}$  during exercise.

To address both the safety and flexibility concerns of lithium-ion batteries, alternate materials and battery chemistries have also been explored. Unlike lithium-ion batteries, which can be flammable, silver-zinc batteries operate based on aqueous chemistries that are not flammable. Fully layer-by-layer screen-printed via polymer-based composite inks, a flexible and rechargeable AgO-Zn battery with an areal capacity of up to  $54 \text{ mAh cm}^{-2}$  was developed to have customizable sizes and capacities.<sup>479</sup> In addition to the high capacity, the AgO-Zn battery had superior battery performance under pulsed high current discharge conditions when compared to a lithium battery. Furthermore, the batteries maintained their capacity and Coulombic efficiency after numerous bending cycles. A similar AgO-Zn battery was integrated into a screen-printed epidermal sweat sensor patch capable of displaying the concentration of various electrolytes or metabolites on an electrochromic display (Figure 26b).<sup>480</sup> The stretchable energy storage device reached an areal battery capacity of up to  $11.5 \text{ mAh cm}^{-2}$  with four layers of cathode loading and could power the microcontroller and electrochromic display to perform 10,000 sensing events over 5 days. Furthermore, the robust patch could be stretched at 20% strain for up to 1,500 cycles without deterioration in performance. Paired with a potentiometric glucose sensor, the sensor patch was used to monitor glucose levels in exercise sweat with the intake of sugary drinks.

However, batteries also require toxic electrolytes that are often acidic, alkaline, or ionic. Safe and biocompatible electrolytes such as sweat are suitable for activating batteries that are used for powering wearable sensor systems. Composed of a flexible Mg anode, a printed Ag/AgCl cathode, and a NaCl preloaded cellulose separator membrane, a flexible and biocompatible sweat-activated cell with an optimized area of  $0.46 \text{ cm}^2$  and capacity of  $\sim 3 \text{ mAh}$  was developed to power a multimodal wearable sensor system for up to 5 h (Figure 26c).<sup>481</sup> The sweat-activated cell has a specific capacity of  $\sim 67 \text{ Ah kg}^{-1}$  which is comparable to that of a commercial coin cell battery with a specific capacity of  $\sim 73 \text{ Ah kg}^{-1}$ . In addition, due to the preloading of the separator with NaCl, the battery capacity is independent of sweat electrolyte concentration. During on-body cycling studies, the sweat activated battery-powered continuous heart rate monitoring and data storage for NFC-based wireless data transmission.

High capacity sweat-activated batteries, incorporating a biocompatible reaction between Zn and  $\text{CuSO}_4$ , have also been developed for powering the real-time electrochemical

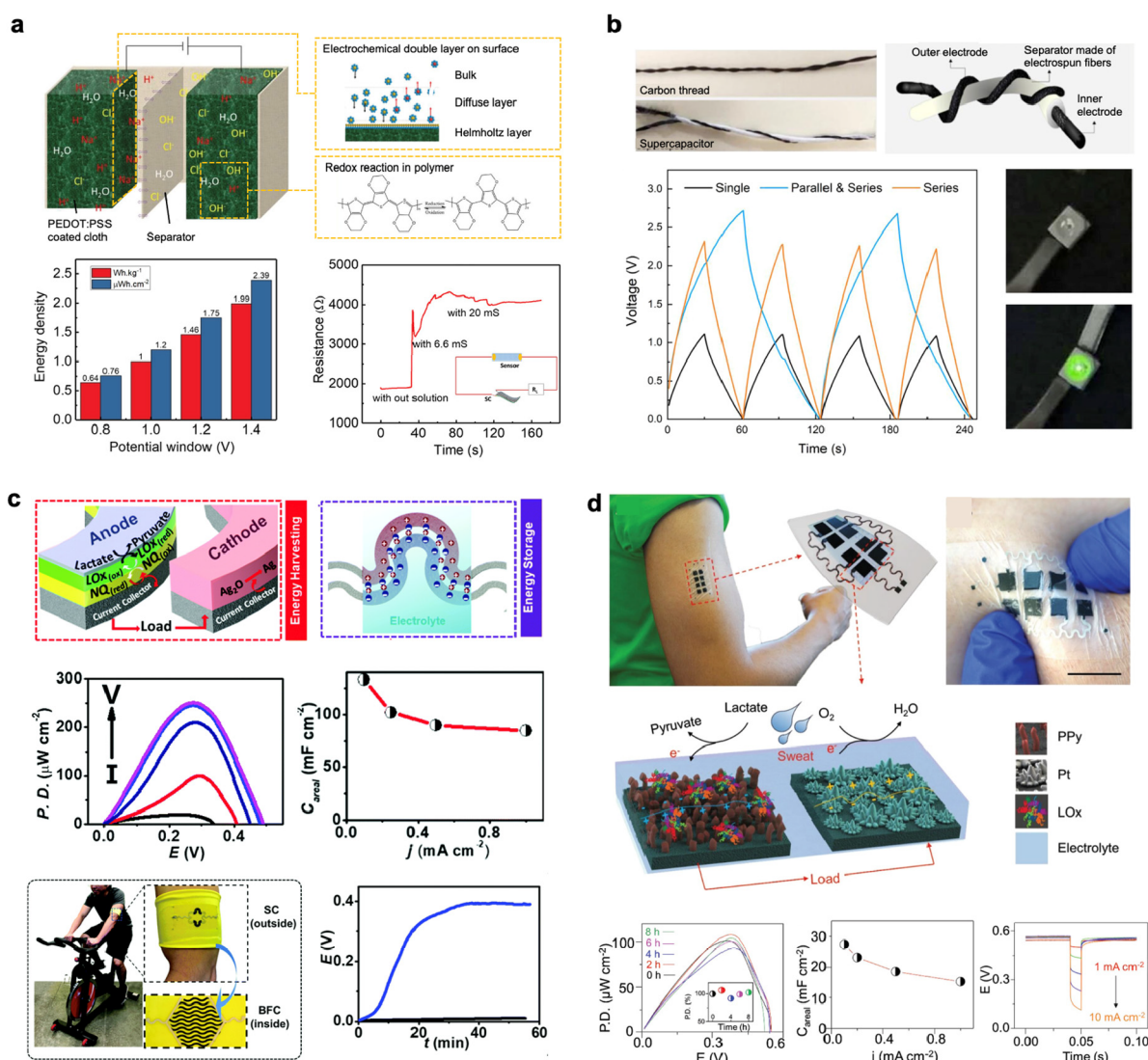


**Figure 27.** Energy storage: next generation sweat activated supercapacitors for powering wearable sweat sensors. **a**, A textile-based wearable supercapacitor based on a PEDOT:PSS-coated cloth using sweat as the electrolyte. Reproduced with permission from ref 487 under CC BY 4.0. Copyright 2020 Manjakkal et al. **b**, A twisted carbon threads-based supercapacitor using sweat as the electrolyte. Reproduced with permission from ref 489 under CC BY 4.0. Copyright 2020 Lima et al. **c**, Hybrid textile-based supercapacitor-biofuel system with a supercapacitor and biofuel cell on each side of a sweatband. Reproduced with permission from ref 490. Copyright 2018 Royal Society of Chemistry. **d**, An all-printed biosupercapacitor integrating a biofuel cell and a supercapacitor in a single footprint for harvesting and storing energy from sweat. Scale bar, 2 cm. Reproduced with permission from ref 491. Copyright 2021 Wiley.

monitoring of sweat biomarkers (pH, Na<sup>+</sup>, and glucose) and BLE data transmission (Figure 26d).<sup>482</sup> Encapsulated in a soft silicone shell, a Zn anode and a Cu cathode were sandwiched between nylon fabric bags containing electrolytes (KCl and CuSO<sub>4</sub>), and a hydrophilic cotton salt-bridge containing KCl to produce a high capacity of 42.5 mAh and a power density of 7.46 mW cm<sup>-2</sup>. The sweat-activated battery could operate for up to 6 h and was used to power a BLE-based wearable sweat sensor system to monitor sweat pH, Na<sup>+</sup>, and glucose during exercise.

Scalable textile-based sweat-activated batteries have also been developed.<sup>483,484</sup> Upon the discovery of printable and stretchable Ag flakes-poly(urethane-acrylate) (HPUA) electrodes that experience improved conductivity in the presence of sweat, a textile-based stretchable Zn-Ag<sub>2</sub>O battery with an Ag-HPUA current collector was developed (Figure 26e).<sup>483</sup> The textile, which was the substrate for printing the electrodes, also

served as the sweat absorbent and separator. In addition, the textile substrate could also be loaded with electrolyte inks, as the power density of the battery increased with electrolyte concentrations, reaching a density of 3.47 mW cm<sup>-2</sup> with a NaCl concentration of 147 mM. The battery, displaying a capacity of 4 mAh cm<sup>-2</sup> at a discharging current of 0.2 mA cm<sup>-2</sup>, was used to power a commercial wireless temperature sensor on a subject's arm. In a different work, a cotton yarn-based sweat-activated battery was developed by modifying segments of a yarn (salt bridge) with carbon-black (cathode) and Zn foil (anode) (Figure 26f).<sup>484</sup> The yarn-based sweat-activated battery, which can be woven into fabrics, exhibited a peak power density of 33.1 μW cm<sup>-2</sup> with 320 mM NaCl, and could light up a light-emitting diode (LED) when worn as a headband while biking.

Various alternatives have been developed to replace lithium coin cell batteries in wearable devices. Novel structures and

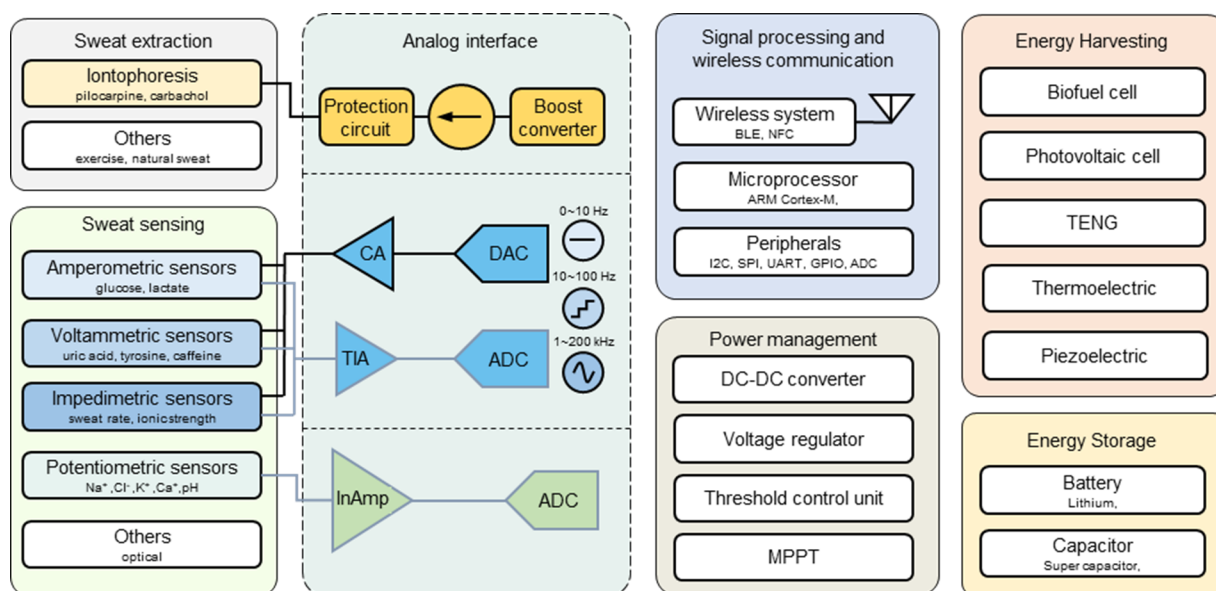


**Figure 28.** Electronic system block diagram of wearable sweat sensors. Control amplifier (CA), digital to analog converter (DAC), transimpedance amplifier (TIA), analog to digital converter (ADC), instrumentation amplifier (InAmp), serial peripheral interface (SPI), universal asynchronous receiver-transmitter (UART), general-purpose input/output (GPIO), direct current (DC).

novel organic materials have been explored to improve the flexibility of batteries, and alternate battery chemistries incorporating novel electrodes and electrolytes have been proposed to develop environmentally friendly and skin-safe batteries. In addition to their high biocompatibility, sweat-activated batteries are dry in the absence of sweat, reducing common battery issues such as electrolyte leakage, self-discharge, and poor shelf life.

**6.2.2. Wearable Supercapacitors.** Supercapacitors, or electrochemical capacitors, are another type of energy storage device characterized by their fast charging/discharging speeds and high current discharge abilities. Supercapacitors store charge through two main mechanisms: through physical capacitive storage in the electrochemical double layer formed near the electrode/electrolyte interface; and through pseudocapacitive chemical storage via charge transfer based on redox reactions occurring on the electrode surface.<sup>485</sup> Common strategies for increasing electrical double layer capacitance include maximizing the electrode surface area using carbon-based materials, whereas various transition metal-based materials and conducting polymers have been explored for increasing pseudocapacitance. Yarn-like, planar, and stacked structures have been used to develop conformable and wearable supercapacitors utilizing flexible substrates such as cotton, cellulose, and polymers.<sup>486</sup> This section will focus on discussing supercapacitors that utilize sweat as the electrolyte, or supercapacitors that are charged by sweat.<sup>487–491</sup>

A sweat-activated 2D-stacked textile supercapacitor was developed by coating a cellulose/polyester cloth with dimethyl sulfoxide-doped PEDOT:PSS as the active electrode (Figure 27a).<sup>487</sup> When activated with artificial sweat, the high conductivity and redox activity of the PEDOT:PSS electrode enabled both double layer capacitance and pseudocapacitance to contribute in achieving a high overall specific capacitance of  $8.94 \text{ F g}^{-1}$  ( $10 \text{ mF cm}^{-2}$ ) at  $1 \text{ mV s}^{-1}$ . The energy density and power density of the device scaled linearly with the potential window, which reached a maximum of  $1.31 \text{ V}$  with sweat equivalent electrolyte contents, where a specific capacitance of

$5.65 \text{ F g}^{-1}$ , as well as energy and power densities of  $1.36 \text{ W h kg}^{-1}$  and  $329.7 \text{ W kg}^{-1}$  were attained. As an application, the sweat-activated supercapacitor was used to self-power a textile-based saline sensor for sweat monitoring.

A sweat-activated yarn-based supercapacitor was developed by electrospinning cellulose acetate fibers around a polypyrrole (Ppy)-functionalized carbon thread, then twisting another Ppy-functionalized carbon thread symmetrically around it (Figure 27b).<sup>489</sup> When activated with a simulated sweat solution, the wire/yarn-based supercapacitor displayed a specific capacitance of  $2.3 \text{ F g}^{-1}$ , as well as energy and power densities of  $386.5 \text{ mWh kg}^{-1}$  and  $46.4 \text{ kW kg}^{-1}$ . By combining two supercapacitors in series with two supercapacitors in parallel, the sweat-activated supercapacitors could turn on a green LED with a minimum operating voltage of  $1.8 \text{ V}$ .

In comparison to sweat-activated batteries that can directly deliver stored energy when stimulated by sweat, sweat-activated supercapacitors need to be charged. To overcome this issue, wearable supercapacitors can also be conveniently integrated with sweat-activated biofuel cells for the simultaneous scavenging and storage of biochemical energy.<sup>490,491</sup> A textile-based hybrid supercapacitor–biofuel system was fabricated by screen-printing a  $\text{MnO}_2$ /carbon nanotube composites-based in-plane supercapacitor on the outside of the fabric sweat band, and an enzymatic lactate biofuel cell on the inside (Figure 27c).<sup>490</sup> The BFC, which achieved a power density of  $252 \mu\text{W cm}^{-2}$  with  $10 \text{ mM}$  lactate, directly charged the supercapacitor, which achieved maximum energy and power densities of  $17.5 \mu\text{W h cm}^{-2}$  and  $0.4 \text{ mW cm}^{-2}$ , respectively. When worn on a subject's arm during exercise, the hybrid system could charge the supercapacitor up to  $0.4 \text{ V}$ .

Through further integration, a biofuel cell and a supercapacitor were combined on the same footprint into a single stretchable epidermal biosupercapacitor (Figure 27d).<sup>491</sup> The biosupercapacitor, consisting of an LOx/NQ/PPy-based bioanode and a porous Pt-based cathode, was coated with a sweat-permeable PBS electrolyte hydrogel to interface with skin and serve as an electrolyte for the supercapacitor. The

screen-printed CNT-based composite ink and porous Pt are responsible for the large surface area and double layer capacitance, and the redox active PPy is responsible for the pseudocapacitive behavior of the biosupercapacitor. As an energy harvesting device, the biosupercapacitor could stably harvest around  $100 \mu\text{W cm}^{-2}$  in a solution containing 10 mM lactate. Meanwhile, as a supercapacitor, it achieved maximum areal capacitance and power densities of  $27.2 \text{ mF cm}^{-2}$  and  $0.22 \text{ mW cm}^{-2}$  ( $\approx 2.4 \text{ F g}^{-1}$  and  $\approx 20 \text{ mW g}^{-1}$ ). In the presence of 10 mM lactate, the biosupercapacitor could deliver and instantaneously recover from high power pulses with a current density of up to  $10 \text{ mA cm}^{-2}$ , reaching a maximum power density of  $1.7 \text{ mW cm}^{-2}$  with a pulsed discharge of  $7.5 \text{ mA cm}^{-2}$ . Utilizing island-bridge patterns and strain-enduring inks, the device was also highly resistant to repeated stretching cycles. During an on-body exercise trial with repeated pulsed discharges, the biosupercapacitor reached a maximum power output of  $343 \mu\text{W cm}^{-2}$  and could continue to deliver the pulsed discharges up to 4 h after the exercise stopped.

To summarize, various options have been explored for powering wearable sweat sensors. As with wearable systems in general, powering solutions for wearables need to have high deformability, a low footprint, and take into account safety and sustainability. Instead of conventionally used bulk inorganic materials, nanostructured and organic materials have been explored for developing a variety of biocompatible and flexible energy harvesting and energy storage devices. While sweat-activated batteries can achieve high energy densities and stably power wearable electronics for hours without any initial charging, they are difficult to recharge. On the other hand, sweat-activated supercapacitors can achieve high power densities and cyclic charging/discharging stabilities, but need to be charged with an external power supply such as an energy harvester before discharge. Next generation high power density energy harvesting devices coupled with high energy density rechargeable energy storage devices could endlessly power wearable electronic sweat sensors without the need for an external charger.

## 7. SYSTEM-LEVEL INTEGRATION

Iontophoresis electrodes, sensor arrays, and power sources are integrated into a wearable system through electronic circuitry that extracts and manages energy from a power source to supply a current through the iontophoresis electrodes for sweat stimulation, to acquire multiplexed electrical signals from sensors, and to process the sensor data for wireless transmission or display (Figure 28). When designing the electronic system for a wearable sweat sensor, it is critical to outline the requirements or constraints of the final design in terms of data precision, form factor, power consumption, and wireless communication range. With these guidelines in mind, it is possible to decide which type of electronic components or PCBs to utilize for circuit design.

### 7.1. Analog Interface

**7.1.1. Iontophoretic Sweat Stimulation.** The analog interface for wearable sweat sensors can be divided into two main categories: iontophoretic sweat stimulation control and electrochemical sweat analysis. For the controlled transdermal delivery of sweat inducing drugs (pilocarpine, carbachol), a high compliance voltage constant current source circuit is required. For reliable and safe sweat stimulation, a constant current density of around  $1.5 \text{ mA cm}^{-2}$  is often used, which

typically requires a compliance voltage between 10 and 40 V due to the high, dynamic, and variable impedance of the skin. As the remainder of the circuit generally operates below 5 V, a boost converter is required to generate the power supply for the current source. A variety of current source circuits have been used for wearable iontophoretic sweat stimulation: a voltage controlled current source using a differential amplifier and transistor was used for generating a variety of current waveforms,<sup>326</sup> and a commercial three terminal current source (LM334, Texas Instruments) was used to deliver a constant current.<sup>190</sup> Simple constant current sources based on active transistors or linear regulators could also be explored for generating constant currents independent of the load. While skin impedance is initially high, delivery of an iontophoretic current increases skin permeability and rapidly decreases skin impedance until it levels off to a value dependent upon applied current density.<sup>492</sup> With a limited compliance voltage, it often takes some time for the skin impedance to decrease and applied current to reach a desired level. With poor electrode contact, the current may never reach the desired value. Therefore, it is important to monitor the applied current using a current shunt monitor or a transimpedance amplifier (TIA). Finally, a protection circuit including a current limiter and switch should be employed for user safety and to isolate the iontophoresis circuit from the measurement circuit during sweat analysis.

**7.1.2. Sweat Analysis.** Various electrochemical measurement techniques have been utilized for quantifying biomarker levels in sweat. A potentiostatic circuit is required for amperometric and voltammetric measurements, where the current across the reference and working electrodes is measured in response to the application of a controlled potential across the reference and working electrodes of a three-electrode electrochemical system. Amperometric measurements are often paired with enzymatic electrodes for the detection of sweat metabolites such as glucose and lactate, whereas voltammetric measurements are often used for the direct detection of redox active biomarkers such as uric acid and tyrosine. Generally, two low input bias operational amplifiers (op-amps) are used to construct a potentiostat circuit to minimize undesired current flow into the reference electrode, including a control amplifier and a TIA. The control amplifier utilizes digital to analog converter (DAC) generated voltages to bias the reference electrode with respect to the working electrode, and the TIA converts the resultant current flowing through the counter and working electrodes into a potential that is acquired by an analog to digital converter (ADC). A constant potential is applied across the reference and working electrodes for amperometric measurements, whereas dynamic potential waveforms of various frequencies are applied for voltammetric measurements. Typically, the voltage sweep rate for voltammetric techniques is up to  $50 \text{ mV/s}$  for DPV, up to  $500 \text{ mV/s}$  for CV, up to  $5 \text{ V/s}$  for SWV, and up to  $500 \text{ V/s}$  for FSCV. Thus, while amperometric measurements can operate with low bandwidth operational amplifiers and long ADC measurement intervals to achieve a low power consumption, voltammetric measurements with higher frequency signals require higher bandwidth operational amplifiers and shorter ADC measurement intervals, which correlates to an increased power consumption.

Impedance measurements have been commonly used for sweat rate and sweat ionic strength sensors. Like potentiostatic circuits, impedance measurement circuits apply an alternating

current (AC) voltage signal across the sensor electrodes, and then measure the resulting current waveform to compute the magnitude and phase angle of the impedance. However, impedance measurements can require the handling of AC signals with frequencies as high as 200 kHz, and therefore require a circuit with significantly higher bandwidth and complexity, as well as quick and frequent ADC conversions. In addition, due to the difficulty of transmitting large amounts of resulting ADC data, impedance measurement circuits often incorporate a discrete Fourier transform (DFT) engine for the hardware-based processing of impedance data.

Open-circuit potentiometry (OCPT) is one of the most commonly used electrochemical techniques for wearable sweat sensors due to its simplicity and low power consumption. Typically used for the selective detection of sweat electrolytes, OCPT requires a high-impedance voltmeter for measuring the potential between the reference electrode and a working electrode (ISE). As the source impedance of potentiometric sensors can be high, they must be interfaced with a high input impedance voltage buffer to minimize current flow through the electrodes. Typically, a buffered reference voltage sets the potential of the reference electrode, and an instrumentation amplifier is used to buffer and amplify the potential difference between the reference and working electrodes, and that potential is then acquired by an ADC. For sweat electrolyte measurements, the sensor response is generally stable and therefore a low bandwidth instrumentation amplifier and a long ADC measurement interval can suffice the requirements for continuous monitoring, enabling low power and small footprint instrumentation. For multiplexed sensors requiring simultaneous potentiometric and amperometric measurements, the control amplifier from the potentiostat circuit can be shared for biasing the shared reference and counter electrodes.<sup>493</sup>

## 7.2. Signal Processing and Wireless Communications

Wearable devices typically contain a microcontroller and a BLE or NFC wireless system for signal processing. The microcontroller consists of a microprocessor that runs algorithms to control the rest of the electronic system through its peripherals (timers, ADC, etc.) and acquire and transmit accurate sweat sensor data while consuming the least power. For wireless communications, BLE and NFC are the most popular wireless communication protocols due to their low power and ease of integration into systems as mobile phones are often embedded with BLE and NFC capabilities. BLE devices operating at 2.4 GHz can transmit data up to ~100 m with a tiny antenna but requires a power supply to be on the device. On the other hand, NFC devices operating at 13.56 MHz can only transmit data up to ~10 cm with a larger antenna but do not require a power supply as the power is wirelessly transferred from the NFC reader. BLE system-on-chips (SoCs) that integrate a microcontroller and BLE radio such as nRF52832 (Nordic Semiconductor), CC2540 (Texas Instruments), PSoC 4 BLE (Infineon Technologies) have been popularly used for developing wearable sweat sensor devices. These devices are typically in deep sleep mode (<2  $\mu\text{A}$ ) and wake up intermittently to perform quick tasks or to transfer BLE data (5–20 mA) at connection intervals of up to 4 s, consuming an average current as low as 10  $\mu\text{A}$ . BLE SoCs are also sometimes integrated with antennas into system-on-modules (SOMs) or system-in-packages (SiPs) to save costs on antenna design and Federal Communications Commission (FCC) certification

fees. However, for mass production or customized circuit geometries, designing a custom antenna matching circuit with a BLE SoC may be more attractive. SoCs such as RF430FRL154H (Texas Instruments) integrating an NFC transponder with a microcontroller have also been used for the battery-free wireless transmission of wearable sweat sensor data.

## 7.3. Power Management

For battery-powered wearables, a power management circuit can be as simple as a single voltage regulator, or a direct current (DC)-DC converter followed by a voltage regulator depending on the battery voltage with respect to the operation voltage of the system. However, for prolonged device use and extended battery life, it is often beneficial to include charging and battery management circuits that make sure the battery safely charges and discharges within a desired temperature and current, and voltage range. Energy harvesting wearables often require additional circuitry to best utilize the scavenged electricity for either charging a battery or supercapacitor, or directly powering the electronics through capacitors. Energy harvesters such as biofuel cells or solar cells that generally output low DC voltages require DC-DC boost converters with dynamic maximum power point tracking to extract maximal energy while boosting the supply voltage above the system operation voltage for charging an energy storage device. Energy harvesters that output a DC voltage significantly higher than the system operation voltage, such as solar cells connected in series, can directly charge the energy storage device. On the other hand, energy harvesters such as TENGs and PENGs that output an AC voltage require a bridge rectifier for converting the AC voltage into a DC voltage that can charge the energy storage device either directly or through a boost converter depending on the magnitude of the voltage. Furthermore, energy harvesting wearables require a threshold control unit and protection circuit to regulate the charging and discharging of energy storage devices for safe and energy efficient powering of wearables. For example, the threshold control unit can allow an energy harvesting device to fully charge an energy storage device to an upper threshold voltage; then, the energy storage device can simultaneously be charged and discharged to power the electronics through a voltage regulator until the energy storage device reaches a lower threshold voltage; then, the energy storage device can stop discharging and get charged back to the upper threshold voltage. Power management integrated circuits (PMICs) that integrate these functionalities into a single chip greatly reduce system footprints and energy losses.<sup>494</sup>

## 7.4. Electronic Design Considerations

Depending on the application and types of sweat sensors needed, wearable devices can be integrated into various form factors and can be worn as accessories, textiles, or e-skins on various parts of the body. The overall form factor and scale of production of the device puts design constraints on the size, power, conformability, and cost of the electronic system. For example, when experimentally embedding a sweat sensor in the next generation of a fitness monitoring smartwatch, it may be desirable to have a circuit that is small, cheap, and adaptable, without concerns regarding the stretchability of the circuit. On the other hand, when developing an FDA-approved e-skin-based sweat sensor for disease diagnostic applications, it may be preferable to design a circuit that has better IP protection

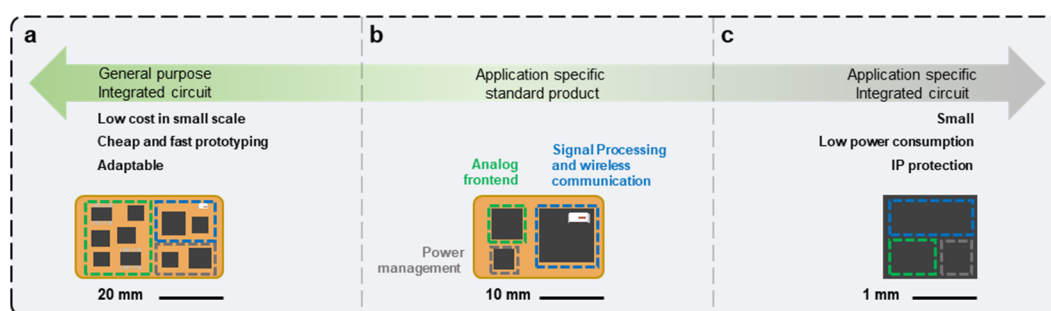


**Figure 29.** Strategies for choosing which types of integrated circuits to use for designing a wearable electronic device. a–c, Electronic components can be categorized based on degree of integration as general purpose integrated circuits (GPICs) (a), application specific standard products (ASSPs) (b), and application specific integrated circuits (ASICs) (c).

**Table 3. Application Specific Standard Products for Electrochemical Measurements**

Component	Manufacturer	Techniques	Current measurement range	Current measurement resolution	Size	Interface
AD5940 (ADuCM355)	Analog Devices Inc.	OCPT, AMP, CV, DPV, SWV, EIS	100 nA–5 mA (12 steps)	5.5 pA @ 100 nA	3.6 mm × 4.2 mm	SPI
LMP91000	Texas Instruments	AMP, CV	5–750 $\mu$ A (7 steps)	Depends on external ADC	4 mm × 4 mm	I2C and external ADC
SIC4341	Silicon Craft Technology	AMP, CV	2.5–20.0 $\mu$ A (2 steps)	10 nA @ 2.5 $\mu$ A	1.2 mm × 1.2 mm	NFC
MS02	Refresh AI Biosensor Co.	OCPT, AMP	100 $\mu$ A	Depends on external ADC	1.2 mm × 1.1 mm	I2C and external ADC

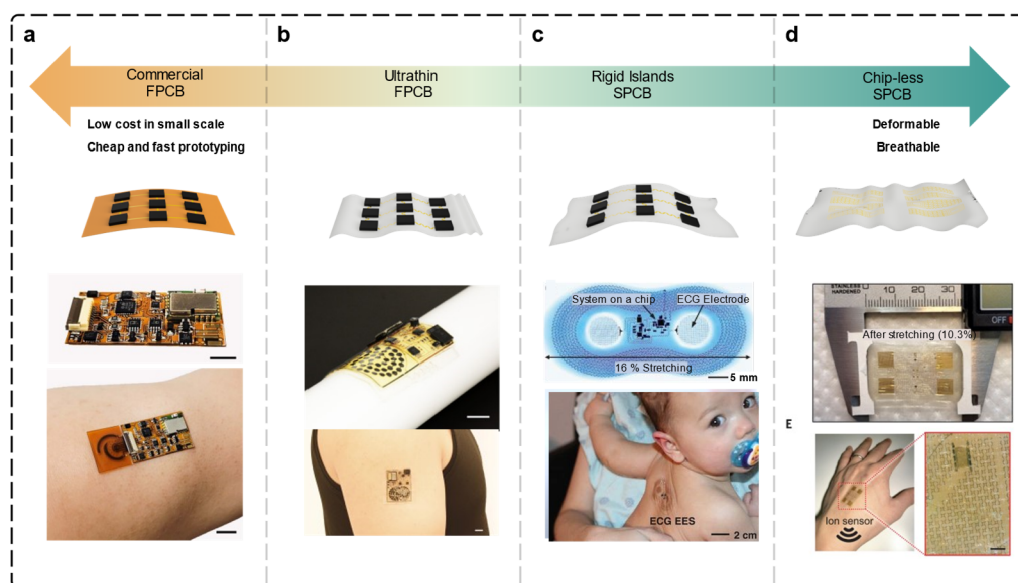


**Figure 30.** Approaches for designing a printed circuit board that can conform to skin. a–d, Printed circuit boards (PCBs) can be classified based on degree of deformability as commercial FPCBs (a), ultrathin FPCBs (b), rigid islands stretchable PCBs (SPCBs) (c), and chip-less SPCBs (d). Scale bars in a,b, 1 cm; scale bar in d, 500  $\mu$ m. a, Reproduced with permission from ref 87. Copyright 2022 Springer Nature. b, Reproduced with permission from ref 410. Copyright 2020 The American Association for the Advancement of Science. c, Reproduced with permission from ref 496 under CC BY 4.0. Copyright 2019 The American Association for the Advancement of Science. d, Reproduced with permission from ref 260. Copyright 2022 The American Association for the Advancement of Science.

and high stretchability with less concerns regarding the cost and adaptability of the circuit.

**7.4.1. Degree of Integration.** Choosing the right electronic components is a crucial step in designing the electronic system for a wearable sweat sensor (Figure 29). A sweat sensor circuit can be quickly developed and tested by routing multiple general-purpose integrated circuits (GPICs) as building blocks for achieving sweat sensor instrumentation, signal processing and wireless communication, as well as power management (Figure 29a). In addition to low costs, such an

approach is very adaptable as minor changes or additions can easily be made by swapping or adding a few GPICs. On the other hand, more resources can be devoted to developing application-specific integrated circuits (ASICs) that can integrate many or even all functionalities of a sweat sensor circuit (Figure 29c). Despite higher initial costs and difficulties in making modifications postfabrication, such an approach can yield smaller footprints, lower power consumption, and better IP protection. To bridge the gap, it is possible to utilize application specific standard products (ASSPs) that are

commercial-off-the-shelf (COTS) like GPICs, but often integrate more functionalities and are geared toward a more specific application (Figure 29b).

An electrochemical instrumentation circuit, for example, could be designed by using individual general-purpose op-amps, in-amps, voltage references, DACs, ADCs, and analog switches. Addition of an amperometric channel can be achieved by adding an extra TIA, and addition of a potentiometric channel can be achieved by adding an extra in-amp. However, several ASSPs for electrochemical instrumentation are commercially available for reducing size, power consumption, and even costs (Table 3). The AD5940 (Analog Devices Inc.) is a powerful analog frontend IC that can perform most standard electrochemical techniques (OCPT, amperometry (AMP), CV, DPV, SWV, EIS) independently as it contains an ADC and memory block for sequencing and data storage. It communicates with an external microcontroller (MCU) via serial peripheral interface (SPI) or there is a variation model ADuCM355 (Analog Devices Inc.) that integrates an MCU. LMP91000 (Texas Instruments) is another simpler option capable of potentiostatic techniques (AMP, CV), that relies on an external ADC and communicates with an external MCU via interintegrated circuit (I2C). SIC4341 (Silicon Craft Technology) is an NFC tag that directly communicates with an NFC reader to perform potentiostatic techniques (AMP, CV) with an on-chip ADC. Lastly, MS02 (Refresh AI Biosensor Co.) can perform OCPT and AMP through an external ADC and is controlled by an external MCU via I2C. For lower power and more specific applications, ASICs have also been designed for wearable sweat sensors.<sup>495</sup>

**7.4.2. Degree of Conformability.** After choosing the electronic components and designing the circuit schematic, the electronic components need to be routed via traces/interconnects and via on a substrate. Most reports of fully integrated wearable sweat sensor arrays contain an electronic system based on commercial FPCB technology (Figure 30a).<sup>87</sup> The FPCB-based system could bend around the wrist or forehead to be worn as a wristband or a headband. Commercial FPCB technologies based on PI substrates and copper traces enable low cost and rapid development. Typically, manufacturers can fabricate FPCBs to be thinner than 100  $\mu\text{m}$  and can stack up to 8 electrical layers. For improved flexibility and conformability, a biofuel-powered soft electronic skin for multiplexed sweat sensing was developed with an integrated 9  $\mu\text{m}$  thick FPCB, consisting of spin-coated PI and E-beam evaporated Cu traces (Figure 30b).<sup>410</sup> The battery-free ultrathin e-skin could conformally laminate onto the arm and maintain tight contact with the skin via medical tape.

However, some parts of the body can undergo large deformations, requiring e-skins to both conform and deform on the skin. Stretchable printed circuit boards (SPCBs) can be developed via rigid island structures, consisting of rigid electronic components and stretchable interconnects on elastomeric substrates. A battery-free and stretchable epidermal electronic system (EES) was developed to monitor vital-signs (ECG or photoplethysmography (PPG)) in infants (Figure 30c).<sup>496</sup> Serpentine-patterned copper foils were embedded in a PDMS substrate to serve as stretchable electrical interconnects as well as a stretchable magnetic loop antenna for NFC-based wireless power delivery and data transmission. The ECG EES could be stretched uniaxially up to 16% without plastic

deformation, and up to 20% without significant deterioration in antenna performance. A fully stretchable chip-less wireless e-skin was developed by patterning single-crystalline gallium nitride (GaN) piezoelectric films as surface acoustic wave (SAW) sensors and a near-field antenna on a perforated PDMS (20  $\mu\text{m}$ ) substrate (Figure 30d).<sup>260</sup> The GaN SAW sensor paired with an ISM could wirelessly monitor sweat  $\text{Na}^+$  levels as changes in  $\text{Na}^+$  ion concentrations would lead to changes in the resonant frequency of the SAW sensor, detected wirelessly by the antenna. The deformable GaN interconnects could withstand repeated bending and stretching (10.3% strain) cycles, and the total absence of rigid electronic components greatly improves the conformability and breathability of the e-skin device. In addition to patterning metallic thin films on stretchable substrates, stretchable interconnects can also be fabricated using intrinsically stretchable conductors such as liquid metals, or by blending conductive fillers with stretchable polymers.<sup>497</sup>

An intrinsically stretchable transistor array was fabricated by utilizing cross-linked styrene-ethylene-butylene-styrene (SEBS) as the dielectric, a “conjugated polymer/elastomer phase separation induced elasticity” (CONPHINE) film as the semiconductor, and carbon nanotubes as the electrodes.<sup>498</sup> The stretchable polymer transistor array achieved a device density of 347 transistors per square centimeter and could be configured as pseudo-CMOS circuits and logic gates. The transistor array was also applied on-skin to amplify arterial pulse signals. Further advances in stretchable transistors could eventually enable the development of stretchable integrated circuits and fully stretchable electronic systems capable of complex power management, sweat sensor instrumentation, signal processing, and wireless communication.

## 8. APPLICATIONS OF WEARABLE SWEAT SENSORS

The combination of materials innovations and various sensing modalities has enabled the rapid, sensitive, and selective detection of a broad range of targets in sweat. Recent advances in the development of superhydrophobic/superhydrophilic surface and epidermal microfluidics have also enabled the efficient sampling of minute amounts of sweat on the skin. The judicious combination of these state-of-the-art technologies with miniaturized circuits for signal preprocessing and wireless data transmission as well as data processing techniques for pattern recognition and prediction will revolutionize the current wearable sweat sensing landscape toward more practical application scenarios. To date, wearable sweat sensors have demonstrated immense potential in seven major areas, namely, fitness monitoring, cystic fibrosis diagnosis, dietary and nutrition monitoring, stress monitoring, therapeutic drug monitoring, substance abuse monitoring, and chronic disease monitoring and management.

### 8.1. Fitness Monitoring

Fitness and sports biometric tracking represents one of the first applications of wearable monitoring systems. The continuous, real-time physiological data acquired by wearable sensors noninvasively are crucial to the design of accurate treatment plans and personalized training programs to improve performance and alleviate injuries.<sup>499,500</sup> Various well-explored physiological biomarkers include heart rate (HR) and core temperature for physiological adaptation, exercise intensity, and physical exertion<sup>501,502</sup> and muscle oxygen saturation for performance optimization.<sup>503–505</sup> The emergence of wearable

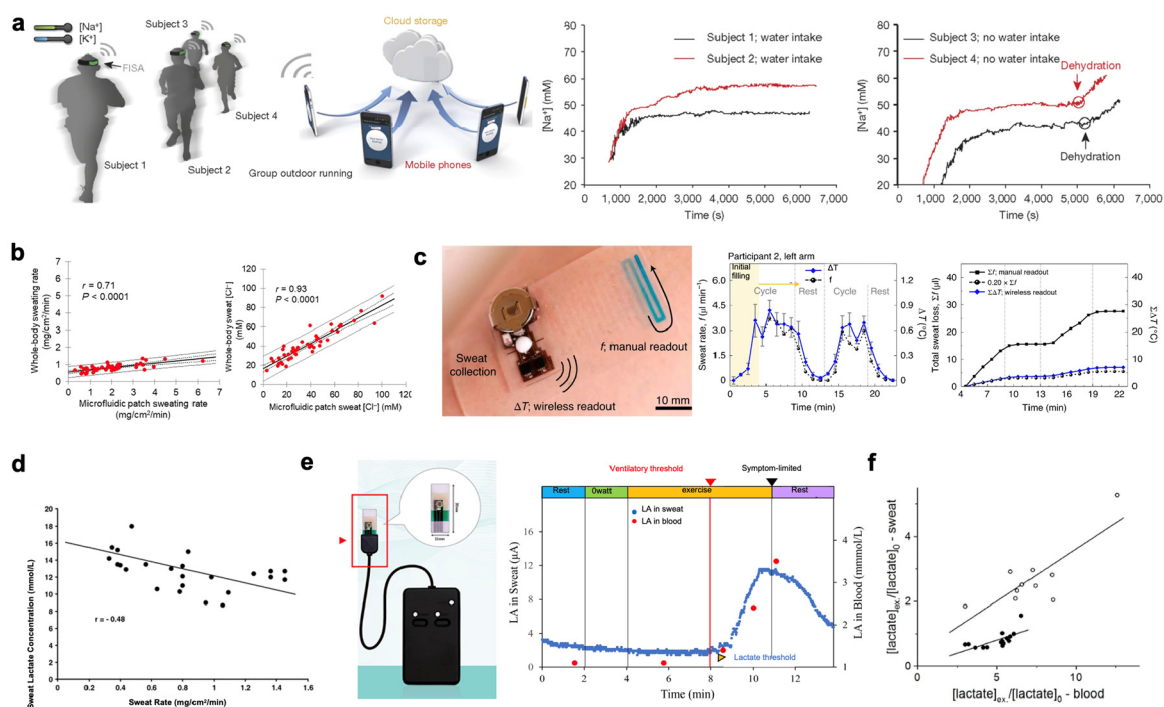


**Figure 31.** Wearable sensors for fitness and human performance monitoring. **a**, FISA enables multiplexed sweat analysis for dehydration identification during exercise. Reproduced with permission from ref 12. Copyright 2016 Springer Nature. **b**, Whole-body sweat rate versus regional sweat rate measured with microfluidic patches (left) and whole-body sweat chloride concentration versus regional sweat chloride measured with microfluidic patches. Reproduced with permission from ref 358. Copyright 2020 The American Association for the Advancement of Science. **c**, Thermistors-based flow sensor for wireless sweat rate monitoring validated with visual quantitation of sweat flow. Reproduced with permission from ref 255. Copyright 2021 Springer Nature. **d**, Sweat lactate concentration was found to be inversely related to sweat rate. Reproduced with permission from ref 512 under CC BY 4.0. Copyright 2010 Springer Nature. **e**, Wearable lactate sensor that tracked sweat lactate threshold in conjunction with ventilatory threshold. Reproduced with permission from ref 513 under CC BY 4.0. Copyright 2021 Seki et al. **f**, Correlations in variation rates of lactate concentrations between sweat from thigh (open circles), working muscle area or arm (closed circles), latent muscle area and blood. Reproduced with permission from ref 514. Copyright 2020 Wiley.

sweat biosensors that are capable of tracking various biochemical analytes beyond physical parameters provides an exciting alternative to human performance assessment.

Hydration status is a key application of on-field biochemical profile monitoring. While insufficient consumption of water causes dehydration, overconsumption may lead to hyponatremia.<sup>506</sup> Sweat sodium ( $\text{Na}^+$ ) and potassium ( $\text{K}^+$ ) are abundant electrolytes that are easily accessible for hydration status monitoring<sup>507,508</sup> and muscle activity prediction.<sup>509</sup> Sweat  $\text{Na}^+$  concentrations are closely related to the whole-body sweat rate and total  $\text{Na}^+$  loss from sweat. Using a proper model, regional sweat  $\text{Na}^+$  concentration (measured from absorbent patches on the forearm) can be used to calculate the whole-body sweat  $\text{Na}^+$  concentration, and subsequently the total whole body sweat  $\text{Na}^+$  loss can be estimated.<sup>510</sup> In 2016, a flexible and fully integrated sensor array (FISA) for monitoring sweat metabolites (glucose and lactate), electrolytes ( $\text{Na}^+$  and  $\text{K}^+$ ), and skin temperature was developed and evaluated with various physical activities such as cycling and running (Figure 31a).<sup>12</sup> Real-time, continuous sweat  $\text{Na}^+$  and  $\text{K}^+$  were monitored on a group of subjects during prolonged outdoor running. Sweat  $\text{Na}^+$  and  $\text{K}^+$  were stable for subjects with water intake after initial changes at the beginning of perspiration, whereas a substantial increase in  $\text{Na}^+$  and slight increase in sweat  $\text{K}^+$  were observed in subjects without water intake after 80 min, demonstrating the importance of sweat  $\text{Na}^+$  for dehydration monitoring.

Sweat chloride ( $\text{Cl}^-$ ) concentration is an alternative approach to measure an athlete's sodium imbalance and dehydration status.<sup>511</sup> A few studies reported soft, flexible epidermal platforms for the colorimetric detection of regional sweat chloride concentrations.<sup>235,239</sup> In one systematic study ( $n = 312$  athletes), the correlation between regional sweat rate and sweat  $\text{Cl}^-$  during competitive sports was assessed using a skin-interfaced wearable microfluidic device with a smartphone image processing platform.<sup>358</sup> Sweat rate measured with a microfluidic patch versus the whole-body sweat rate (calculated from the difference in pre- to postexercise body mass corrected for fluid intake and losses) showed a similar correlation regardless of body surface area normalization. The study also showed a strong relation between whole-body sweat  $\text{Cl}^-$  and  $\text{Na}^+$  ( $r^2 = 0.98$ ). Predicted whole-body sweat  $\text{Cl}^-$  concentrations based on regional  $\text{Cl}^-$  concentrations using a simple linear regression model showed a good correlation with measured whole-body sweat  $\text{Cl}^-$  concentrations ( $r^2 = 0.86$ ) (Figure 31b). Therefore, regional sweat  $\text{Cl}^-$  concentration could be used as an important metric for sweat  $\text{Na}^+$  loss and electrolyte replacement recommendation. To continuously quantify sweat loss, the same group also reported an approach based on the combination of a thermal actuator and precision thermistors-based flow sensor that transmits data wirelessly via Bluetooth (Figure 31c).<sup>255</sup> Wireless readings of sweat rate ( $\Delta T$ ) are comparable with manual readings of flow rate ( $f$ ) within a dye deposited serpentine microfluidic channel during cycling and at rest. The wireless flow rate increases during

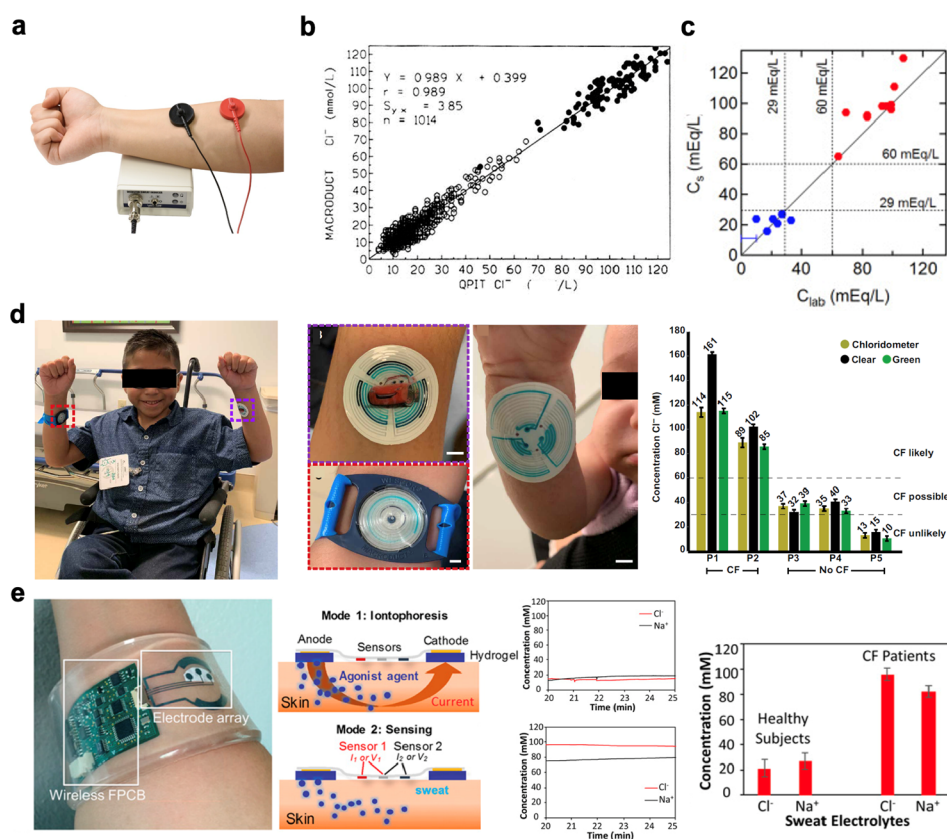


**Figure 32.** Wearable sensors for cystic fibrosis diagnostics. **a**, A commercial sweat test device for cystic fibrosis diagnosis. **b**, Correlation between chloride concentration obtained in sweat from CF (closed circles) and non-CF (open circles) subjects using Macroduct and from the QPIT method. Reproduced with permission from ref 528. Copyright 1994 Elsevier. **c**, Correlation between sweat chloride levels in CF (red circles) and non-CF (blue circles) subjects measured with a wearable sensor and with laboratory measurement. Reproduced with permission from ref 532. Copyright 2018 Elsevier. **d**, A soft epidermal microfluidic device for the *in situ* colorimetric quantitation of chloride in sweat. Scale bars, 5 mm. Reproduced with permission from ref 533. Copyright 2021 The American Association for the Advancement of Science. **e**, An integrated single battery-powered wearable device for localized sweat stimulation and sweat chloride analysis *in situ*. Reproduced with permission from ref 326. Copyright 2017 Proceedings of the National Academy of Sciences.

cycling and reaches a constant value, then decreases to a close-to-zero value at rest, demonstrating a good correlation between physical activity and sweat rate.

Serum metabolites like lactate and ammonia that are produced during anaerobic activity reveal important information on body exertion and exercise intensity.<sup>515</sup> Although many studies investigated the relationship between sweat lactate and exercise intensities, their results seem contradictory.<sup>516</sup> Some studies report proportional or inverse relations between lactate concentration and exercise intensity,<sup>512,517</sup> whereas some report that the relation is insignificant.<sup>518</sup> Such discrepancies could be a result of different sweat stimulation, collection, and analysis methods.<sup>516</sup> Results from conventional sweat collection methods tend to be confounded by evaporation and skin surface contamination issues.<sup>519</sup> Sweat rate is also found to influence lactate level as higher sweat rate results in a dilution of lactate in sweat. In one study, the relationships between the exercise intensity (exercise at 60, 70, and 80% of age-predicted maximum heart rate) and the sweat lactate concentration or the lactate excretion rate (LER, sweat lactate concentration multiplied by sweat rate) during a 90 min treadmill walking session were investigated.<sup>512</sup> It was found that the sweat lactate concentration decreased at higher exercise intensities, whereas the LER increased. The sweat lactate concentration was found to be inversely related to the

sweat rate ( $r = -0.48$ ) while the LER has a positive correlation with the sweat rate ( $r = 0.94$ ) (Figure 31d). The results imply that higher exercise intensities do elicit an increase in sweat lactate production, but the dilution effect caused by a higher sweat rate at higher exercise intensities confounds results from the uncorrected sweat lactate concentration readings.

Interestingly, all studies that normalize lactate concentration with sweat rate report a positive lactate-exercise intensity relationship.<sup>520</sup> The sweat lactate threshold ( $LT_1$ , first rise in lactate concentration during incremental exercise) and ventilatory threshold ( $VT_1$ )<sup>513</sup> (Figure 31e) was investigated with a wearable lactate sensor. The sweat  $LT_1$  correlated well with the  $LT_1$  in blood and  $VT_1$ , with a sharp continuous increase in sweat lactate concentration up until volitional exhaustion and decrease during recovery. The anatomical locations at which sweat is collected also influence the sweat lactate levels. It was found that sweat lactate concentration increases concurrently with blood lactate in body regions near working muscles but not near latent muscles (Figure 31f).<sup>514</sup>

In practice, the high levels of lactate in sweat during intense exercise may sometimes exceed the upper detection limit of common electrochemical enzymatic lactate sensors. Crespo and co-workers expand the detection range (1–50 mM) by restricting the lactate accessible to LOx with a plasticized polymeric layer containing ETH500.<sup>204</sup> At the same time, the

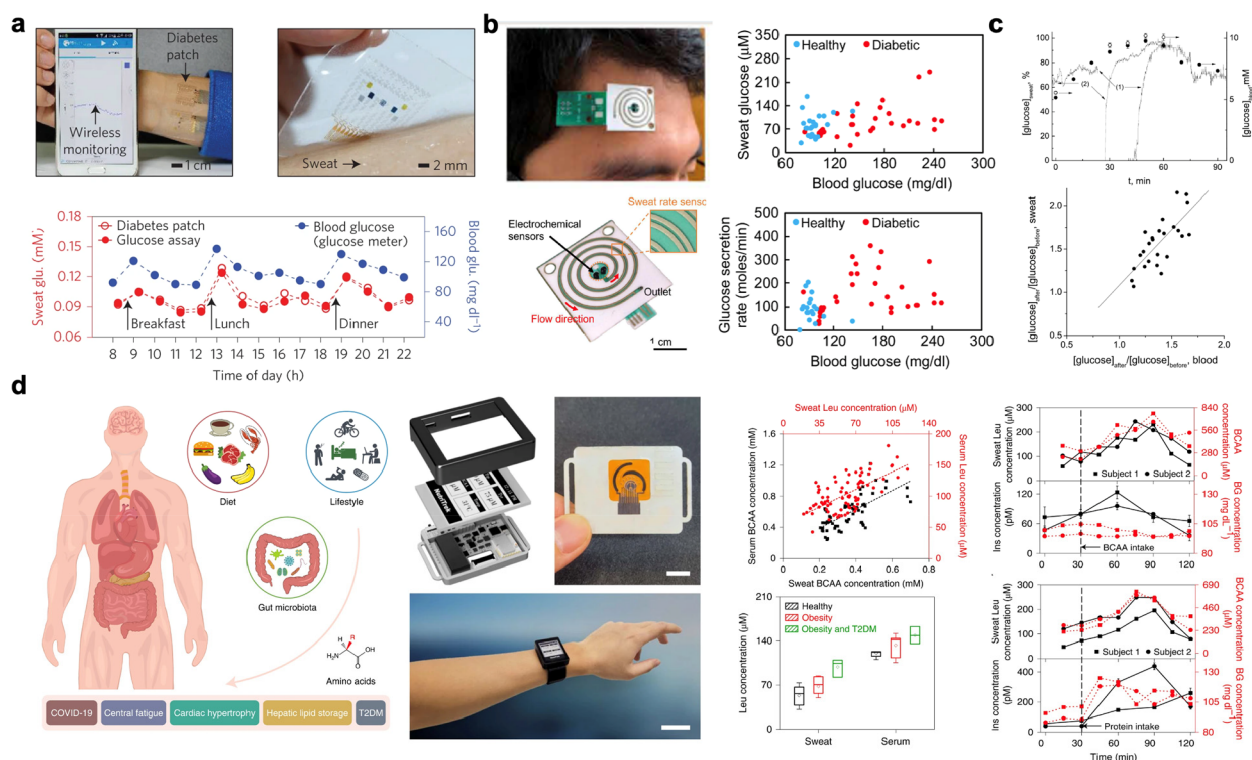


**Figure 33.** Wearable sensors for metabolic syndrome diagnostics. **a**, A wearable diabetes monitoring and feedback therapy patch consisting of a multimodal sensor patch for sweat glucose detection and a polymeric microneedles array for thermally activated drug delivery. Reproduced with permission from ref 198. Copyright 2016 Springer Nature. **b**, A roll-to-roll fabricated microfluidic patch with a regional sweat rate sensor and sweat glucose sensor demonstrate inconsistent correlation between sweat glucose or glucose secretion rate and blood glucose in healthy and diabetic subjects. Reproduced with permission from ref 541. Copyright 2019 The American Association for the Advancement of Science. **c**, The rates of glucose concentration increase in capillary blood and in iontophoretic sweat after glucose intake for 90 min demonstrate good correlation ( $r = 0.75$ ). Reproduced with permission from ref 542. Copyright 2019 American Chemical Society. **d**, A wearable MIP-based biosensor for the metabolic profiling of various amino acids and nutrients. Sweat Leucine/BCAAs demonstrate good correlation with blood with elevations observed in obese and diabetic subjects. Scale bars, 1 cm (top) and 5 cm (bottom). Reproduced with permission from ref 87. Copyright 2022 Springer Nature.

polymeric layer significantly reduces influences by pH and temperature, alleviating sources of error during on-body operation.

Stress monitoring is another major approach in managing an athlete's performance.<sup>521</sup> Optimizing training intensity and recovery duration allows athletes to maximize their performance. Overtraining may disturb normative physiological and immunological functions and also impair psychological processing.<sup>522,523</sup> The development and evaluation of wearable sweat sensors for stress monitoring will be discussed in detail in Section 8.4.

## 8.2. Cystic Fibrosis Diagnosis

In addition to sports physiology, sweat rate and sweat electrolyte levels are also routinely used for cystic fibrosis diagnosis. Cystic fibrosis (CF) is a fatal genetic disease caused by functional abnormalities in the CFTR membrane channel.<sup>524</sup> Disturbance in electrolyte transport in the reabsorptive duct of the sweat gland leads to a high salt loss in sweat.<sup>525</sup> Since the identification of  $\text{Cl}^-$  impermeability in the sweat duct of CF patients, quantitation of  $\text{Cl}^-$  in iontophoresis sweat has become the gold standard in the clinical diagnosis of CF, especially in newborn screening.<sup>526,527</sup> The Wesco Macroduct Sweat Test System is a popular commercial system in use at many CF testing centers (Figure 32a).<sup>528</sup> Compared with the original laborious quantitative pilocarpine iontophoresis test (QPIT), Macroduct eliminates

the need for weighing and reduces sweat evaporation. It also shows no clinically significant difference in the  $\text{Cl}^-$  concentration obtained compared with the QPIT method while demonstrating good discrimination of CF from non-CF groups based on sweat  $\text{Cl}^-$  concentrations (Figure 32b).<sup>528</sup> However, collecting sufficient volumes ( $>15 \mu\text{L}$  within 30 min) of sweat can be challenging in practice due to poor mechanical sealing of the collector and cumbersome protocols.<sup>529–531</sup> Advances in flexible electronics enable new wearable technologies that can circumvent the insufficient sweat volume problem by improving the form factor to provide conformal skin contact and allowing *in situ* sweat  $\text{Cl}^-$  analysis with minimal sweat volume.

A wearable sensor with an integrated salt bridge for real-time sweat  $\text{Cl}^-$  measurements was evaluated against laboratory testing.<sup>532</sup> The study observed stable sweat  $\text{Cl}^-$  readings (standard deviation  $<1 \text{ mEq/L}$  for 5 min) within 15 min after sweat induction with the Macroduct. The sweat volumes at detection time ( $13.1 \pm 11.4 \mu\text{L}$ ) were often lower than the minimum sweat volume required for laboratory testing, and the sensor demonstrated remarkable agreement ( $r = 0.97$ ) with laboratory measurements (Figure 32c). To resolve issues plaguing sweat collection in infants with fragile skin, the form factor and sweat collection efficiency was improved with a soft, epidermal microfluidic device capable of *in situ* colorimetric quantitation of chloride (Figure 32d).<sup>533</sup> The device

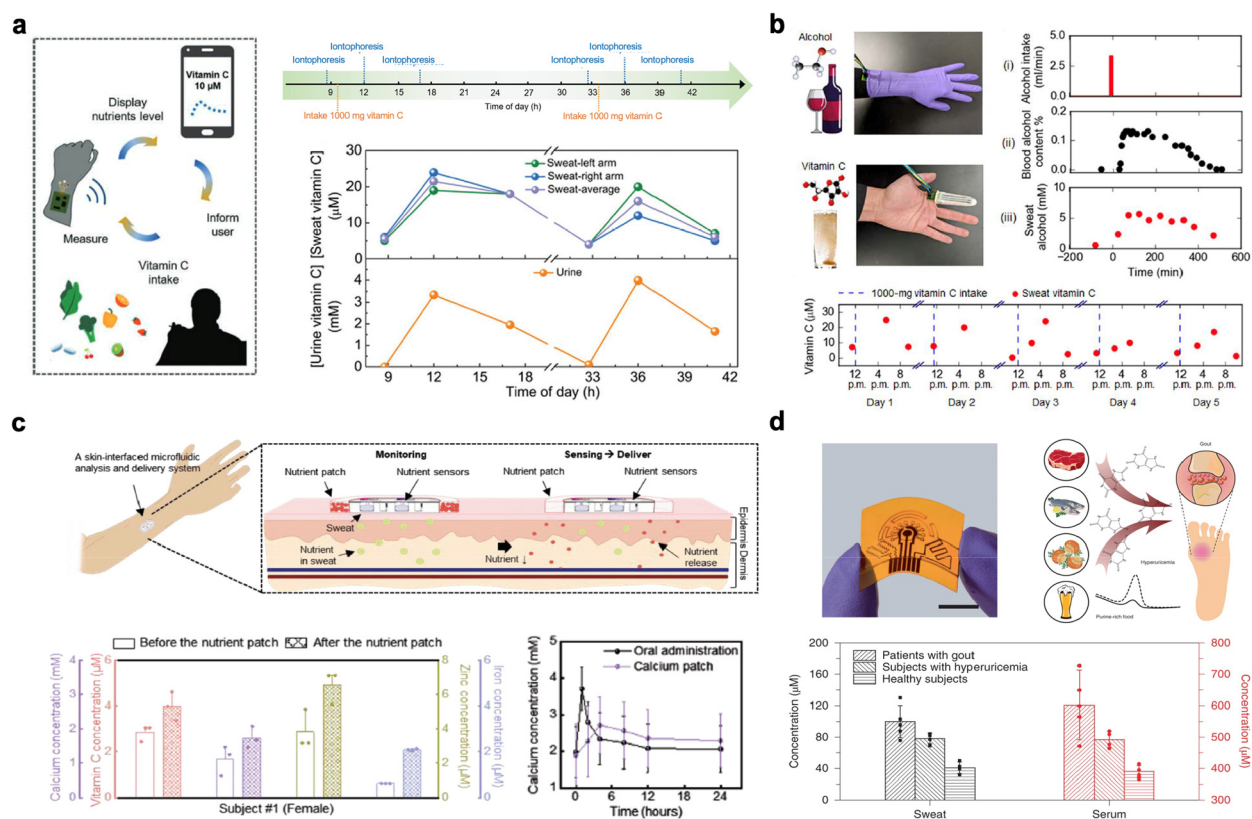


**Figure 34.** Wearable sensors for nutrition tracking. **a**, Vitamin C profiles in iontophoretic sweat and urine after vitamin C consumption for two consecutive days obtained with a wearable sensor. Reproduced with permission from ref 83. Copyright 2020 Wiley. **b**, Temporal profile of vitamin C and alcohol in natural thermoregulatory sweat after intake using a glove-based sensor for natural sweat accumulation and *in situ* analysis. Reproduced with permission from ref 321. Copyright 2020 The American Association for the Advancement of Science. **c**, A miniaturized for the colorimetric assessment of vitamin C, calcium, zinc, and iron, and transdermal nutrients delivery. Reproduced with permission from ref 547 under CC BY 4.0. Copyright 2021 Kim et al. **d**, A controlled purine-diet study of uric acid levels in subjects with gout, hyperuricemia, and healthy subjects using a wearable laser-engraved platform. Scale bar, 1 cm. Reproduced with permission from ref 75. Copyright 2019 Springer Nature.

significantly reduces sweat leakage and demonstrates comparable accuracy to existing technologies when validated with CF and non-CF subjects across age groups. Macroduct's cumbersome sweat stimulation and collection protocol can also be replaced with an integrated single battery-powered wearable device providing localized sweat stimulation and sweat  $\text{Cl}^-$  analysis *in situ*.<sup>326</sup> The device consists of an electrode array with sweat induction and sensing electrodes as well as a flexible printed circuit board enabling wireless data transmission (Figure 32e). The induction electrodes are coated with a thin layer of cholinergic agonist hydrogel for sweat stimulation. The microcontroller on the FPCB switches on/off respective circuits and electrical paths to switch between induction and sensing modes. The potentiometric  $\text{Na}^+$  and  $\text{Cl}^-$  stabilizes 20 min after iontophoresis for accurate electrolyte assessment. Average  $\text{Na}^+$  and  $\text{Cl}^-$  levels in healthy subjects measured by this platform were observed to be lower than those in the CF subject group, in agreement with literature values.

### 8.3. Dietary and Nutrition Monitoring

Nutrition intake and monitoring are essential for the management of several health conditions including metabolic syndrome, diabetes, and cardiovascular diseases.<sup>534–536</sup> Although the management of chronic disease involves multidimensional factors, nutritional monitoring and dietary intervention remains a crucial approach since diet is a readily

addressable risk factor in many chronic conditions.<sup>537</sup> The digitization of diaries and food frequency questionnaires into online surveys and apps has simplified the process for daily food intake monitoring. However, these methods suffer from biases in portion estimation and misreporting.<sup>538,539</sup> Wearable sweat sensors' capability to monitor nutritional information noninvasively and continuously offers the possibility for nutrient intake monitoring and guidance, and consequently chronic condition management.

The application of wearable sweat sensors for nutrient sensing has been demonstrated in several types of nutrients including metabolites, vitamins, minerals, and amino acids. Among all, sweat glucose is one of the most well explored nutrients owing to its significance in diabetes management. The awareness and implementation of blood glucose monitoring has led to significant progress in diabetes management. Current glucose monitoring is implemented by testing blood glucose levels from finger-pricked blood at fixed intervals using a portable glucose meter. The measurement of sweat glucose allows noninvasive detection and tracking of serum glucose continuously. The *in vitro* confirmation of the correlation between sweat glucose and blood glucose, and the need for a continuous, noninvasive glucose sampling approach has spurred recent growth in research on wearable sweat glucose sensors.<sup>540</sup> Earlier demonstrations of wearable devices for sweat glucose monitoring focused on the mapping of sweat glucose variation in correlation to serum glucose levels.<sup>12,349</sup> A

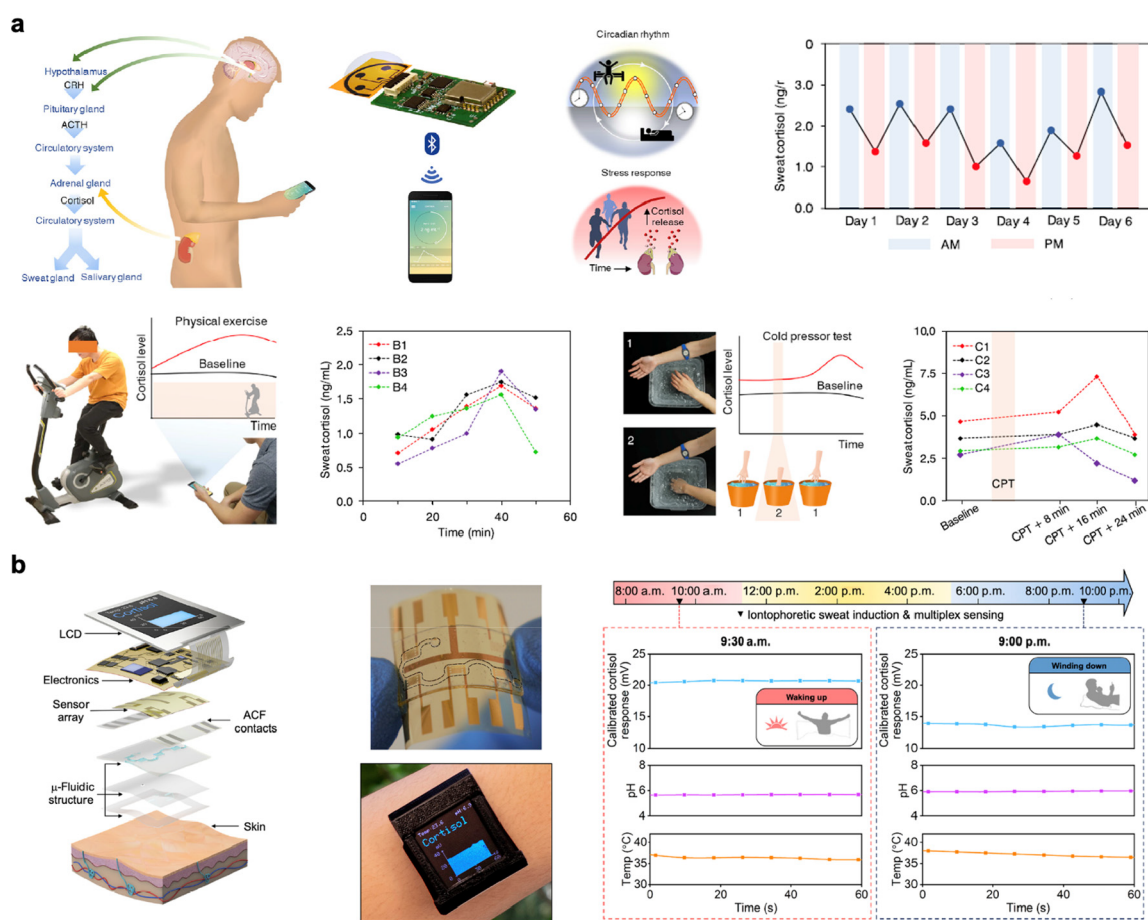


**Figure 35.** Wearable sensors for stress monitoring. **a**, A fully integrated, flexible, and wireless mHealth device, for stress response monitoring in sweat cortisol. Reproduced with permission from ref 93. Copyright 2020 Elsevier. **b**, A wearable aptamer-field-effect transistor-based smartwatch with signal correction algorithm for sweat cortisol detection. Reproduced with permission from ref 91. Copyright 2022 The American Association for the Advancement of Science.

wearable diabetes monitoring and feedback therapy patch consisting of a multimodal sensor patch for sweat glucose detection and a polymeric microneedle array for thermally activated drug delivery was developed.<sup>198</sup> The patch demonstrated that fluctuations of glucose levels in exercise-induced sweat monitored over a day matched well with blood glucose levels measured with both a commercial glucose assay kit and a glucose meter (Figure 33a). A roll-to-roll fabricated microfluidic patch with a regional sweat rate sensor and sweat glucose sensor was used to monitor sweat glucose and sweat rate continuously in iontophoretic sweat for 30 min. It was found that an individual's sweat glucose changes did not consistently reflect the actual blood glucose changes especially for fasting glucose levels.<sup>541</sup> Although the large variation in glucose levels could be potentially attributed to the dilution effect of different sweat rates,<sup>50</sup> the glucose secretion rate demonstrated a poorer correlation ( $r = 0.2$ ) (Figure 33b). Another study looked at the rates of glucose concentration increase in capillary blood and in iontophoretic sweat after glucose intake for 90 min and reported a good correlation between the variation rates ( $r = 0.75$ ) (Figure 33c).<sup>542</sup> Although the confounding sweat/blood glucose correlations reported in literature could be potentially attributed to skin contamination, sweat evaporation, variation in collection methods, and sweat dilution effects, it seems there is currently

no simple correlation or model to describe the sweat/blood glucose relation across healthy and diabetic subgroups.

In addition to glucose, amino acids (AAs) are closely related to dietary intakes and lifestyles. Elevated BCAAs, namely leucine, isoleucine, and valine, are closely related with obesity, insulin resistance, and important risk factors for type 2 diabetes mellitus (T2DM), cardiovascular diseases, and pancreatic cancer.<sup>543–545</sup> A wearable MIP-based biosensor was reported for the metabolic profiling of various AA and nutrients.<sup>87</sup> The good correlations between serum and sweat leucine ( $r = 0.66$ ) and BCAAs ( $r = 0.69$ ) across 3 subgroups (normal weight,  $n = 10$ ; obesity,  $n = 7$ ; and obesity with T2DM,  $n = 3$ ) obtained with the sensor indicate the potential of sweat BCAA for metabolic syndrome monitoring. Sweat Leucine/BCAAs increased in the 30–60 min after BCAA supplement or dietary intake and then decreased. Interestingly, healthy subjects showed higher increase in leucine after intake than subjects with obesity/T2DM, reflecting the difference in BCAA metabolism between these subgroups (Figure 33d).

The presence and wearable detection of various vitamins have been demonstrated by a few groups.<sup>546</sup> A wearable sensor explored the vitamin C profile in iontophoretic sweat and urine after vitamin C consumption. Correlations between sweat/urine vitamin C with blood levels were investigated for two consecutive days (Figure 34a).<sup>83</sup> In another study, an epidermal tattoo biosensor was used to monitor the temporal

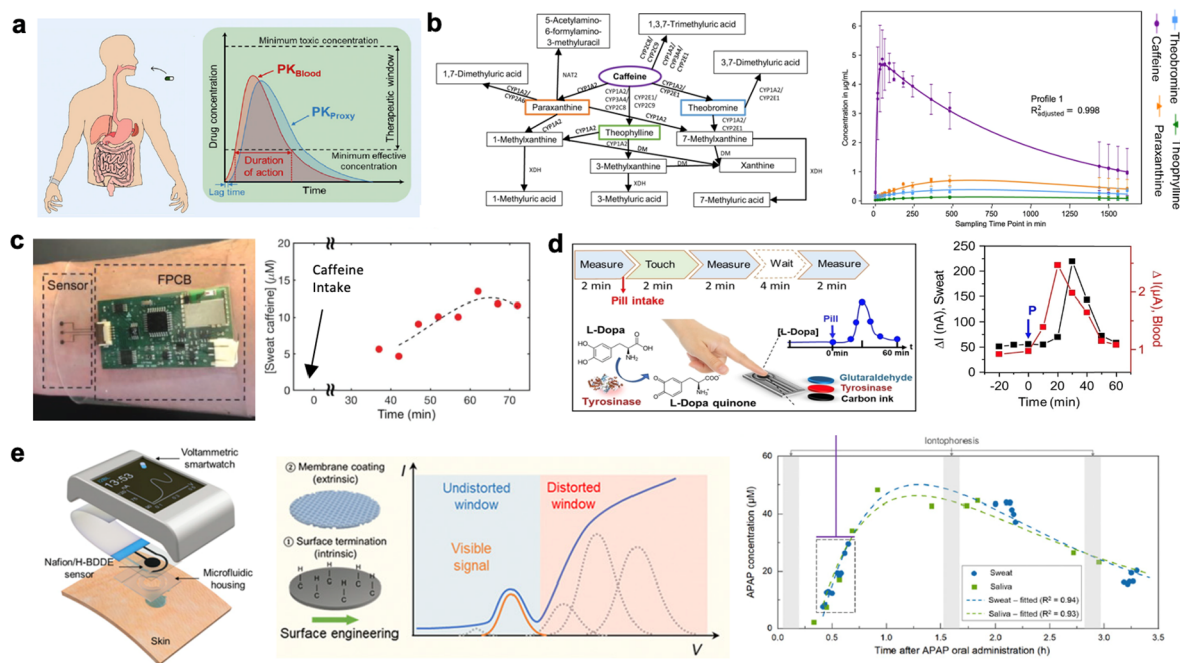


**Figure 36.** Wearable sensors for therapeutic drug monitoring. **a**, Therapeutic window based on pharmacokinetics and pharmacodynamics of drug concentrations in blood and alternative biofluids like sweat. Reproduced with permission from ref 567. Copyright 2020 Proceedings of the National Academy of Sciences. **b**, Catabolic products of caffeine found in fingertip sweat and metabolic networks facilitated discovery of dynamic metabolic patterns. Reproduced with permission from ref 568 under CC BY 4.0. Copyright 2021 Brunmair et al. **c**, A wearable sensor for the detection of an electroactive methylxanthine drug, caffeine. Reproduced with permission from ref 206. Copyright 2018 Wiley. **d**, Chronological profile of levodopa in natural sweat after intake using a wearable microfluidic fingertip patch. Reproduced with permission from ref 320. Copyright 2021 Wiley. **e**, Absorption and elimination kinetics of acetaminophen in sweat obtained with a wearable smart watch. Reproduced with permission from ref 567. Copyright 2020 Proceedings of the National Academy of Sciences.

increase and decrease of iontophoretic sweat vitamin C after intake of vitamin C pills and fruit juices. In both studies, sweat vitamin C levels increased with vitamin C dosage and correlated well with blood vitamin C levels. Therefore, sweat vitamin C may allow routine on-site assessment of nutritional health.<sup>191</sup> The temporal profile of vitamin C in natural thermoregulatory sweat after vitamin C intake was monitored over 10 h using a glove-based sensor for natural sweat accumulation and *in situ* analysis.<sup>321</sup> The peaking trend of sweat vitamin C over a 5-day intake study reflected the typical absorption and metabolism timeline of xenobiotics in the human body (Figure 34b). To expand the potential of wearable electronics beyond nutrient monitoring, a miniaturized system that integrated the colorimetric assessment of vitamin C, calcium, zinc, and iron, and a transdermal nutrient delivery patch was developed.<sup>547</sup> Human trials with the nutrient sensors demonstrated a temporal correlation between the sweat and blood concentrations. Comparisons of sweat nutrients after transdermal and oral nutrient delivery demonstrated the system's capabilities in nutritional balance monitoring and management (Figure 34c). In another study, the monitoring of sweat uric acid and tyrosine was investigated for metabolic and nutritional management with a laser-engraved wearable patch.<sup>75</sup> A controlled purine-diet study in subjects including participants with gout, hyperuricemia, or healthy uric acid levels demonstrated elevated sweat and serum uric acid levels in patients, suggesting the potential use of sweat uric acid as a biomarker for gout management (Figure 34d).

#### 8.4. Stress and Mental Health Monitoring

Stress is a 21st century epidemic affecting more than one-third of the global population, with a 25% increase in anxiety and

depression prevalence during the COVID-19 pandemic.<sup>548,549</sup>

At a personal level, persistent mental health issues increase the risk of cardiovascular disease and other diseases;<sup>550,551</sup> macroscopically speaking, mental health problems affect social stability and impose heavy medical and socioeconomic burdens on the society.<sup>552,553</sup> Real-time assessment and continuous monitoring of stress tackles the problem with a preventive approach by allowing early diagnosis and timely treatment initiation. Fitness trackers and smart watches with PPG or ECG features promise to transform healthcare toward consumer-centric models.<sup>554,555</sup> These consumer health devices monitor stress in real time by recording physiological parameters like heart rate and heart rate variability. However, they cannot quantify stress levels accurately due to the lack of specificity and sensitivity.<sup>556</sup> The development of wearable sensors that retrieve biochemical information in sweat noninvasively has enabled more accurate quantification of stress continuously in real-time.

Current wearable biosensors for stress quantitation primarily focus on the detection of cortisol in sweat. Cortisol is a glucocorticoid regulated by the hypothalamic-pituitary-adrenal (HPA) axis (Figure 35a).<sup>93,557</sup> Blood cortisol fluctuates in a diurnal manner with a peak concentration in the morning shortly after awakening and gradually decreases.<sup>558</sup> This circadian pattern is altered in patients with mental disorders such as major depressive disorder.<sup>559</sup> At the same time, cortisol is also secreted in response to both physical and psychological stress stimuli. A fully integrated, flexible, and wireless mHealth device, based on laser-engraved graphene and a competitive immunosensing strategy, was developed to investigate the correlation between sweat and serum cortisol and sweat

cortisol's stress response profile.<sup>93</sup> Iontophoretically induced sweat cortisol was found to correlate well with serum cortisol ( $r = 0.87$ ). An exploratory study that looked at sweat cortisol's circadian variation presented a reproducible pattern for up to 6 days (Figure 35a). The authors also investigated the dynamic response of sweat cortisol to stress stimuli. Sweat cortisol was observed to increase progressively and peak after 40 min of continuous biking, a form of physical stress. In the case of cold pressor test (CPT), an acute stressor, sweat cortisol increased after CPT and peaked between 8 to 16 min after CPT, following the trend of serum cortisol. Wearable sweat cortisol sensing devices have been evaluated by various groups by monitoring circadian patterns, performing constant workload biking, and CPT.<sup>284,311,312</sup>

A wearable aptamer-field-effect transistor-based smartwatch was developed to investigate sweat cortisol's response to both physical and psychological stress.<sup>91</sup> The FET substrate was embedded in a sweat sampling, routing, and analysis microfluidic module made from medical tapes. The performance of the FET sensors was validated by tracking salivary cortisol changes in a Trier Social Stress Test (TSST) and diurnal variations in both sweat and saliva samples (Figure 35b).

Although many devices have been developed for cortisol detection, the majority of the sensors were validated *in vitro*. For studies that ventured further into human studies, the number of subjects involved in stress response studies are typically limited. Furthermore, the potential lag of sweat cortisol to actual acute stressors has been barely explored. By far, the clinical relevance of sweat cortisol has only been inferred from serum trends. More direct evidence from longitudinal studies on patients with mental disorders is needed before sweat cortisol's practical implementation for preventative stress monitoring and management.

### 8.5. Therapeutic Drug Monitoring

Therapeutic drug monitoring (TDM) is a practice that measures the concentration of a drug or a related biomarker in biofluids to adjust dosing and maintain drugs in the bloodstream within a certain therapeutic window based on personalized treatment plans.<sup>560</sup> The emergence of clinical pharmacokinetics (PK) and pharmacodynamics (PD) has enabled the construction of therapeutic ranges for dosing determination to reduce drug toxicity while optimizing drug efficacy (Figure 36a). While the pharmacological effectiveness of certain drugs is predictable or can be easily determined by other more accessible approaches such as antihypertensive drugs and blood pressure, some drugs may have steep dose response curves (e.g., theophylline<sup>561</sup>), narrow therapeutic windows (e.g., lithium<sup>562</sup>), and/or unpredictable dose-blood concentration relationships (e.g., phenytoin<sup>563</sup>) such that close monitoring and dynamic dosing could improve pharmacological effectiveness. Traditional methods employed for measuring drug concentrations in blood include chromatographic approaches (HPLC,<sup>564</sup> LC-MS/MS<sup>565</sup>) and immunoassays.<sup>566</sup> Although there has been increasing efforts toward improving the throughput of these methods and cost reduction,<sup>192</sup> these approaches still require invasive blood sampling and testing at centralized laboratories. Recent development of wearable sweat biosensors that monitor drugs metabolized in sweat has created a wealth of opportunities for on-site continuous TDM at a low cost.

Although sweat is an unconventional source for drug metabolic monitoring as compared with blood or urine, it resolves the compliance issues surrounding traditional blood or urine sampling and enables facile time-course studies. A recent metabolic profiling of fingertip sweat demonstrated that sweat is a noninvasive, and reliable sample that can be easily collected by untrained personnel at short intervals for metabolic phenotyping.<sup>568</sup> The study identified various catabolic products of caffeine from fingertip sweat samples using LC-MS (Figure 36b). Moreover, dynamic metabolic network modeling was used to offset effects of sweat volume on the time-course study of caffeine catabolism. The model enabled the estimation of sweat rate and the visualization of the dynamic metabolic patterns of three major caffeine metabolic products, namely paraxanthine, theobromine, and theophylline of each subject.

Earlier examples of drug metabolic profiles in sweat identified with wearable biosensors are focused on electroactive drugs. In one study, a wearable platform with an electrochemical DPV sensing module was developed for the detection of an electroactive methylxanthine drug, caffeine (Figure 36c).<sup>206</sup> Variation of caffeine levels under different dosages and time points after intake was investigated. The work showed both the increase of sweat caffeine (peak at 60 min after intake) due to its absorption into the human circulatory system and the decline attributed to catabolism. The same group reported a wearable electrochemical enzymatic sweat band based on tyrosinase for levodopa (L-Dopa) detection toward Parkinson's disease management.<sup>192</sup> Adverse effects of long-term L-Dopa intake involve motor fluctuations, dyskinesia, and dystonia.<sup>569</sup> Monitoring the pharmacokinetic profiles of L-Dopa allows dosage optimization according to disease progression and reduction of side effects. Real-time metabolic profiles of L-Dopa in sweat samples from both iontophoretic induction and physical exercise were investigated after Fava bean intake. In another study, personalized pharmacokinetic tracking of drug concentrations after intake of L-Dopa oral pill was conducted using a touch-based detection of L-Dopa in fingertip sweat and capillary blood samples (Figure 36d).<sup>320</sup> L-Dopa concentrations in fingertip sweat were recorded in 10 min intervals and found to be closely related to blood profiles with  $\approx 10$  min of lag time, demonstrating the potential application of sweat TDM toward personalized pharmacotherapies. Another study observed a similar chronological profile of L-Dopa in natural sweat after 100 and 200 g broad bean intake using a wearable microfluidic fingertip patch with an enzymatic amperometric L-Dopa sensor (Figure 36d).<sup>253</sup> The levodopa concentration in sweat was also found to increase with increasing dosage.

Although voltammetry-based techniques enable the label-free detection of electroactive drugs in biofluids, the redox signatures of an electroactive target can be confounded by biofouling and distorted by endogenous interfering electroactive species in a complex biofluid. To mitigate biofouling and create an "undistorted potential window" within acetaminophen's dominant voltammetric response range, the surface of a boron-doped diamond working electrode (BDDE) was engineered to be hydrogen-terminated to decouple the influence from tryptophan and tyrosine, and concurrently coated with a negatively charged Nafion membrane to eliminate signals from negatively charged uric acid via charge repulsion.<sup>567</sup> The BDDE working electrode was integrated within a custom-developed smartwatch and a data processing

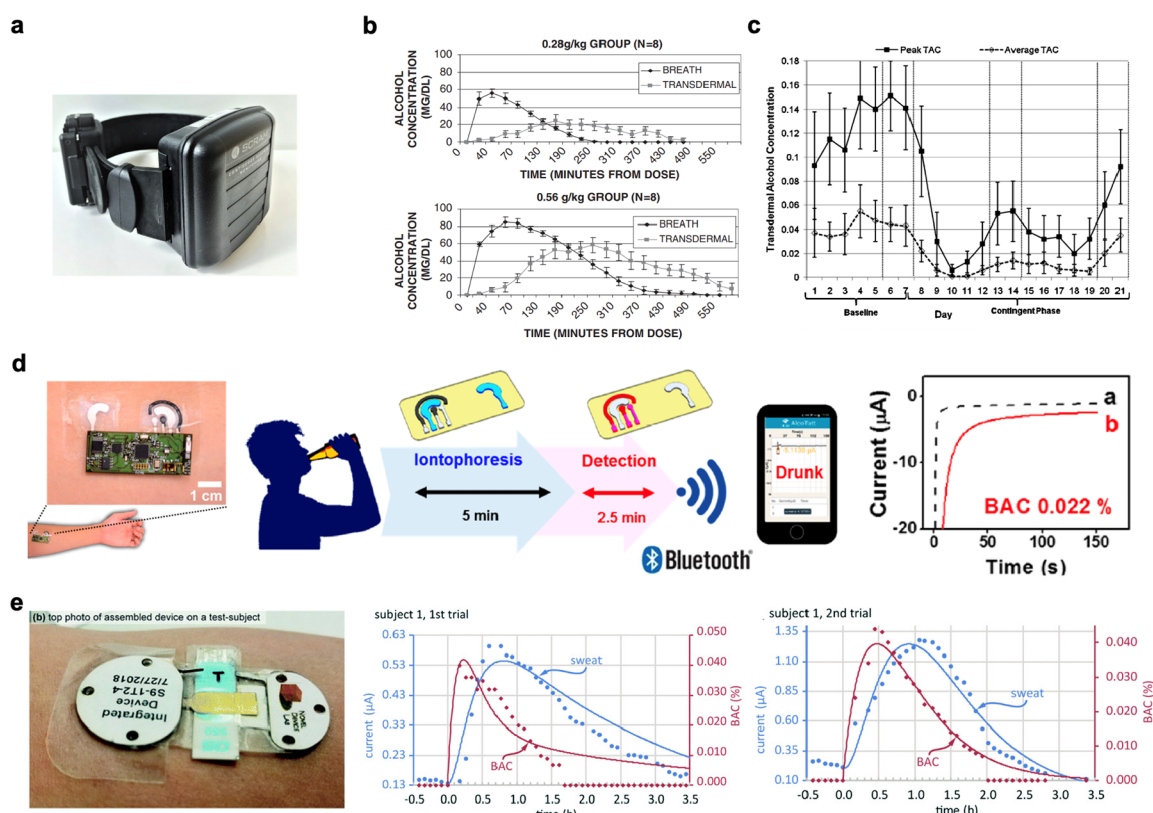


**Figure 37.** Wearable sensors for substance monitoring. **a**, Photo of a commercial continuous remote alcohol monitor. Reproduced with permission from ref 586. Copyright 2020 Elsevier. **b**, Pharmacokinetics of TAC and BrAC after intake. Reproduced with permission from ref 583. Copyright 2006 Wiley. **c**, Tracking of TAC for the contingency management of alcohol disorder. Reproduced with permission from ref 584. Copyright 2011 Elsevier. **d**, A flexible tattoo device with sweat induction electrodes for *in situ* epidermal sweat stimulation and alcohol sensing. Reproduced with permission from ref 190. Copyright 2016 American Chemical Society. **e**, A wearable sweat sensing device that combined an iontophoresis module with commercial screen-printed carbon electrodes for alcohol detection and comparison with blood alcohol metabolism. Reproduced with permission from ref 53. Copyright 2018 Royal Society of Chemistry.

framework for redox peak extraction that rendered drug readouts with minute-level temporal resolution (Figure 36e). Acetaminophen's pharmacokinetic profiles in both sweat and saliva captured by the smartwatch showed similar concentrations and absorption/elimination kinetics, motivating larger scale clinical studies toward sweat as a TDM matrix. Employing a similar engineering concept, the same group demonstrated the detection of three electroactive drugs, dipyrindamole, acetaminophen, and caffeine in artificial sweat on anodic-treated BDDE.<sup>570</sup>

### 8.6. Substance Abuse Monitoring

Although the discovery of sweat as a matrix for drug screening can be traced back to as early as 1911, its utility for forensic toxicology was not exploited until the 1990s due to difficulty in sweat collection and other analytical problems.<sup>571</sup> Since then, the commercialization of several sweat collection products like PharmChek has enabled the successful sweat testing of various substances of abuse including opiates, cocaine, lysergic acid diethylamide (LSD), and ethanol for criminal justice, employment, and outpatient clinical settings.<sup>572–575</sup> However, accurate drug screening from the collected sweat samples requires tedious extraction protocols and sensitive chromatographic methods with mass spectrometry or immunoassays.<sup>576–578</sup> These conventional analytical methods typically have long turnaround times and are expensive. The inter-personal variation in sweat rate and long duration required for

sufficient sweat collection precludes the wide adoption of sweat testing due to operational difficulties, irritation, and low subject acceptability.<sup>340,579</sup> The emergence of wearable flexible electronics with better form factors and POC sensing techniques that enable rapid target detection may address the technological bottleneck faced by conventional sweat testing and expand the application of sweat-based substance abuse detection to more scenarios like workplace drug testing and monitoring compliance which require on-site and/or continuous detection.

Sweat alcohol (ethanol) is one of the most well explored substances of abuse with a strong correlation to blood alcohol concentration (BAC).<sup>580</sup> Several commercial ankle-worn devices that monitor transdermal alcohol content by sampling natural sweat were developed for the identification of alcohol intoxication and monitoring court-ordered sobriety.<sup>581</sup> These devices are also used in clinical studies to track consumption and guide interventions for relapse prevention.<sup>582</sup> The Secure Continuous Remote Alcohol Monitor (SCRAM) is a widely adopted wearable device in justice systems and clinical trials (Figure 37a). It measures the sweat alcohol content using a platinum-based electrochemical fuel-cell through catalytic alcohol oxidation every 30 min. Data collected is uploaded via wired or wireless connection onto a secure web-based server for remote monitoring purposes. The SCRAM reports a correlation of 0.85 and 0.84 between transdermal alcohol concentration (TAC) and breath alcohol concentration

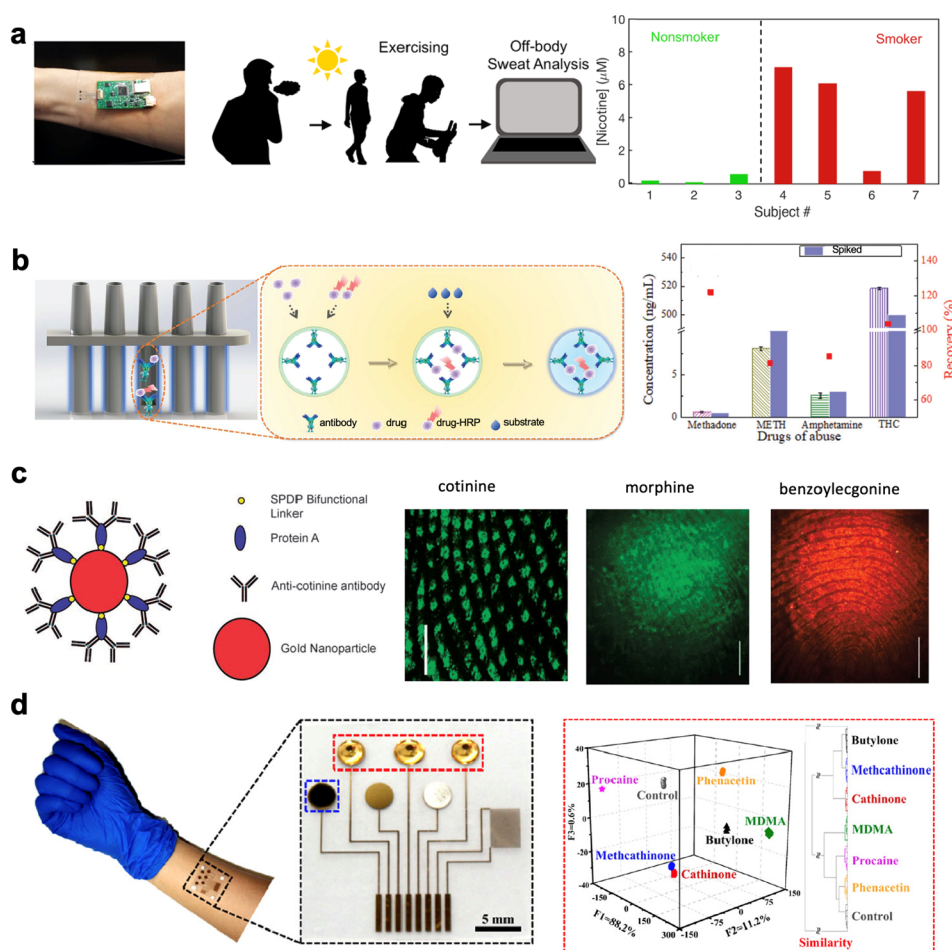


**Figure 38.** Wearable sensors for drug abuse detection. **a**, A wearable nicotine sensor for sweat nicotine levels monitoring during exercise. Reproduced with permission from ref 193. Copyright 2020 American Chemical Society. **b**, Detection of methadone, methamphetamine, amphetamine, and tetrahydrocannabinol spiked in artificial sweat with a rapid quantitative competitive immunoassay-based capillary array. Reproduced with permission from ref 291. Copyright 2020 Royal Society of Chemistry. **c**, Latent fingerprints containing narcotic drug metabolites fluorescently labeled with antibodies. Scale bars, 2 mm. Reproduced with permission from refs 590, 591. Copyright 2007 Wiley. Copyright 2010 American Chemical Society. **d**, A wearable electrochemical for the detection of psychoactive drugs in artificial sweat. Reproduced with permission from ref 302. Copyright 2022 American Chemical Society.

(BrAC) for both peak and area under the curve (AUC) measurements.<sup>583</sup> Comparison between pharmacokinetics of TAC and BrAC showed that TAC peaks were lower and occurred 2–3 h after BrAC (Figure 37b). In another study, the SCRAM was used to track TAC in a 21-day study on the contingency management of alcohol disorder in 2010 (Figure 37c).<sup>584</sup> The study demonstrated the feasibility of TAC monitoring for clinical purposes. Still, about 8% of self-reported alcohol use was not detected by SCRAM because the TAC was lower than 0.02 g/dL.

However, current wearable devices for TAC monitoring are rigid and bulky with low sensitivity. Their operation also depends heavily on the accumulation of natural sweat on the skin, which potentially contributes to the lag in TAC as compared with BAC. A study that combined iontophoresis and *in situ* amperometric alcohol detection in chemically induced sweat revealed that peak TAC occurred at a similar time as BAC.<sup>585</sup> A flexible tattoo device with sweat induction electrodes and an alcohol sensor for *in situ* epidermal sweat stimulation and sensing measured different levels of alcohol in sweat with no time lag (Figure 37d).<sup>190</sup> Another wearable sweat sensing device that combined an iontophoresis module

with commercial screen-printed carbon electrodes for alcohol detection stimulated and measured sweat ethanol continuously during a > 3 h study with baseline (no ethanol consumption) and ethanol consumption and metabolism (Figure 37e).<sup>53</sup> Sweat ethanol was observed as fast as 2.3 min after blood ethanol was raised and the overall pharmacokinetic curve lag time was found to be between 19.32 to 34.44 min.

Sweat alcohol content can also be indirectly monitored via the detection of ethanol metabolite, EtG, using nonfaradaic EIS.<sup>275</sup> A wearable system reported the continuous measurement of EtG for 9 h. These recent works on continuous sweat induction and analysis validated that sweat could provide prompt blood-correlated data for alcohol consumption monitoring.

Nicotine is another common substance of abuse. Tobacco consumption affects not only the smokers but also others exposed to secondhand smoke.<sup>587,588</sup> Monitoring sweat nicotine noninvasively allows proper evaluation of the exposure and scope of health risks among nonsmokers. A wearable enzymatic amperometric sweat nicotine sensor was developed to monitor sweat nicotine levels during exercise.<sup>193</sup> The sweat

band was capable of distinguishing smokers from nonsmokers (Figure 38a).

Although nonelectroactive substances of abuse are harder to detect with miniaturized systems and integrated with epidermal devices, several POC detection mechanisms have been proposed for the survey of illicit drugs in sweat. Four common drugs of abuse, methadone, methamphetamine, amphetamine, and tetrahydrocannabinol spiked in artificial sweat were detected with a rapid quantitative competitive immunoassay-based capillary arrays (Figure 38b).<sup>291</sup> The capillary array enabled rapid detection (~16 min) of four drugs at low concentrations with a low sweat volume (~4  $\mu$ L per analyte). In another study, methamphetamine in artificial sweat was detected using a wearable SERS sensor.<sup>589</sup> The feasibility of the SERS sensor was demonstrated by performing detection of sweat containing 2-fluoro-methamphetamine (2-FMA) on the human cadaver skin. Drug metabolites excreted in fingerprint sweat can also be labeled with fluorescent markers for direct imaging and on-site detection.<sup>590</sup> For example, antibody–nanoparticle conjugates were used to label latent fingerprints containing narcotic drug metabolites (morphine (metabolite of heroin), benzoylecgonine (metabolite of cocaine) or cotinine (metabolite of nicotine)), followed by fluorescent labeling with a fluorescently tagged secondary antibody (Figure 38c).<sup>591</sup> This method allows the direct visualization of fingerprints for biometric identification in conjunction with multiplexed narcotic drug screening. A wearable electrochemical aptasensor array constructed on flexible gold electrodes was developed for the detection of psychoactive drugs such as methylenedioxymethamphetamine and cathinone in artificial sweat.<sup>302</sup> The wearable aptasensor array identified 16 analytes with 100% accuracy after employing statistical methods for data analysis (Figure 38d). These portable and wearable formats proposed and tested *in vitro* may inspire future development and *in vivo* testing of autonomous, cost-effective wearable devices for illicit drug screening.

### 8.7. Chronic Diseases Management

Chronic diseases as the leading cause of death and disability account for more than two-thirds of all deaths in the United States.<sup>592</sup> The increasing prevalence of chronic diseases worldwide fueled by a rapidly growing aging population has created a huge demand for health care independence and affordability.<sup>593,594</sup> Wearable sweat sensors enable prolonged, (semi)continuous, and nonobtrusive monitoring of physiological information and could potentially play a huge role in chronic disease management and supporting clinical outcome predictions.

However, the application of wearable sweat sensors for chronic disease management has been rarely explored. Existing research on chronic disease management, if any, is predominantly centered around a few types of chronic conditions such as diabetes and metabolic syndromes, which have been discussed in previous sections. A major reason for the setback in chronic disease monitoring is the low abundance of disease-relevant biomarkers. Unlike the biomarkers for diabetes and metabolic syndrome (glucose and uric acid), the levels of inflammatory or cardiac biomarkers like cytokines and CRP are below the nanomolar range in blood and expected to be even lower in sweat. Information on the quantitative analysis of cytokines and proteins in sweat is also very limited as compared to their small molecule counterparts.<sup>98,99</sup> The lack

of a standardized and efficient sweat collection method also confounds results obtained from different studies. Recently, a soft, skin-interfaced microfluidic patch was used to rapidly capture and efficiently extract sweat from passive heating for cytokine analysis.<sup>56</sup> Results obtained from sweat collected from 10 subjects revealed that these cytokine concentrations are relatively independent of sweat rate. Therefore, measurements of sweat cytokine concentrations could potentially be directly correlated to plasma cytokine levels. This suggests that noninvasive monitoring of sweat cytokines may reveal information on inflammatory responses. A few recent examples of wearable nonfaradaic impedance sensors demonstrated the feasibility to detect several inflammatory markers, hormones, and neurotransmitters including IL-6, IL-8, IL-10, TNF- $\alpha$ , IFN- $\gamma$ , and CRP in natural sweat.<sup>278–283,595–599</sup> However, whether these markers do fluctuate with disease conditions will need to be tested across different disease subgroups with a larger sample size.

In summary, current advances in materials innovation, sensing modalities, sweat harvesting, and system powering and integration have enabled the continuous, noninvasive tracing of various sweat biomarkers for a broad range of applications. From sports physiology to human performance monitoring, and from dietary intake and nutrition monitoring to chronic disease management, the potential of wearable sweat sensors to revolutionize future consumer health and future clinical practices is more than apparent. Significant efforts have been devoted to the design and preliminary testing of prototypes for fitness tracking and nutrition monitoring. Compared with past literature reports in the prewearable technology era that seem contradictory, results from studies conducted with current wearable sensing technologies with better form factors, more efficient sweat sampling approaches, and *in situ* analysis capabilities have also started to converge, especially in the case of lactate and glucose. Still, the majority of the wearable sweat sensor reports included very limited human studies and on-body data since the studies were mostly oriented toward device evaluation. In addition to addressing technological challenges such as device functionalities, and manufacturing approaches, large-scale clinical case studies on not just the device validity alone but also the relevance, effectiveness, and timeliness of sweat biomarkers in reflecting physiological information will be the critical step toward the eventual practical adoption of wearable sweat sensors in various use case scenarios.

## 9. DATA PROCESSING FOR WEARABLE SWEAT SENSORS

Data processing is a critical aspect of wearable sweat sensors that enables the extraction of valuable health information from a wave of raw and unstructured sensor readouts. On the low level, data processing algorithms such as data smoothing, curve fitting, or peak detection enable the accurate calibration of biomarker concentrations from raw sensor data. On the higher level, these biomarker concentrations can be processed through learning algorithms to establish personalized baseline and cautionary biomarker levels, enabling personalized and preventative healthcare.

### 9.1. Multimodal Sensors

**9.1.1. Multiplexed Data Acquisition.** Given the success in the biosensor field, the natural next step is to integrate sensors onto wearable devices. By measuring multiple

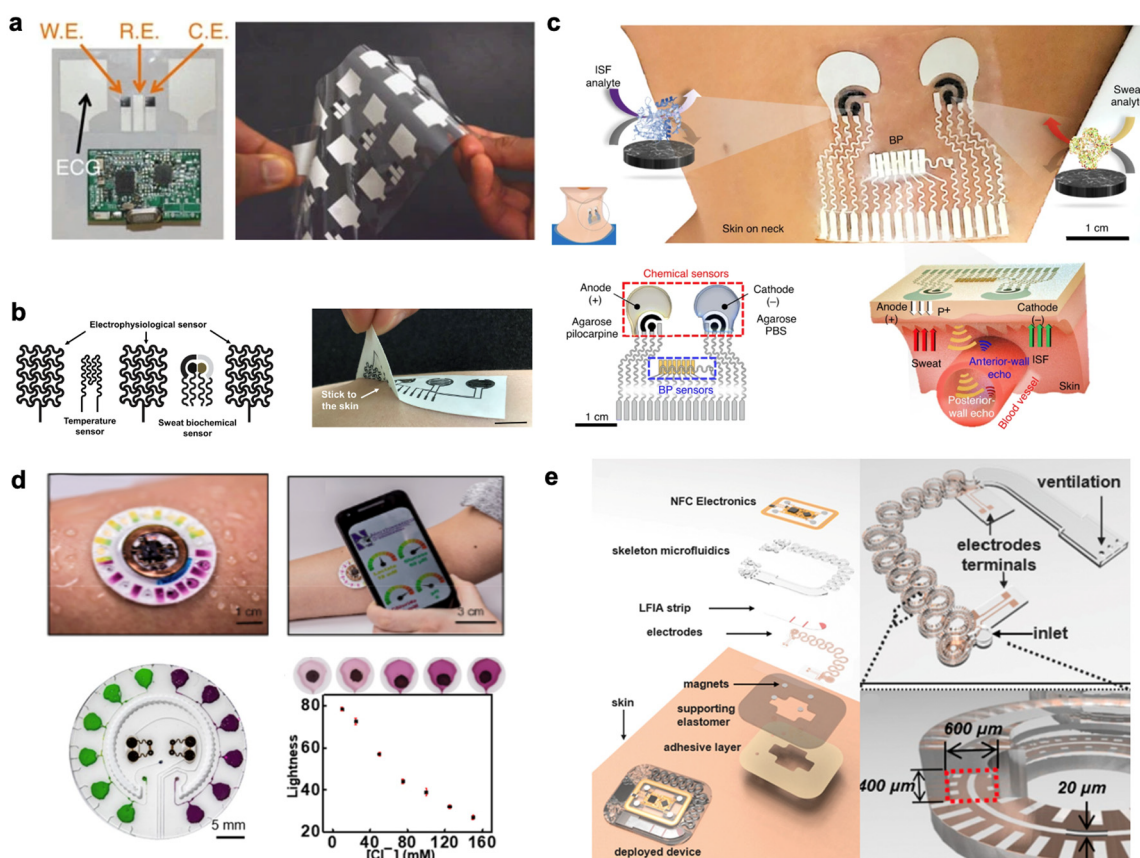


**Figure 39.** Multimodal data acquisition. **a**, Multimodal ECG and sweat lactate measuring device. Reproduced with permission from ref 138 under CC BY 4.0. Copyright 2016 Imani et al. **b**, Laser engraved biosensor with multiple sensing modalities and a high degree of flexibility. Scale bar, 1 cm. Reproduced with permission from ref 602. Copyright 2022 The American Association for the Advancement of Science. **c**, Wearable device with both sweat and ISF sensing capabilities. Reproduced with permission from ref 331 under CC BY 4.0. Copyright 2018 Wiley. **d**, Colorimetric wearable device with glucose and lactate sensors. Reproduced with permission from ref 237. Copyright 2019 The American Association for the Advancement of Science. **e**, Stress detecting wearable device integrated with lateral flow immunoassay. Reproduced with permission from ref 292 under CC BY 4.0. Copyright 2020 Proceedings of the National Academy of Sciences.

electrochemical or physical sensor readouts, one can potentially obtain an array of information ranging from skin temperature, heart rate, and blood pressure to more complex biochemical measurements used in the diagnosis of diseases like cancer or COVID.<sup>75,87,329,600,601</sup> To achieve this diagnostic power, wearable sweat sensors must be integrated with multiple sensing modalities. Simultaneous monitoring of ECG signals and sweat lactate concentrations have been reported, for example (Figure 39a).<sup>138</sup> ECG is well-known for its applications in cardiovascular health, while lactate can be used as an index of physical exhaustion. Coupling these two pieces of information into a single device gives health professionals both insight into tissue oxygenation from lactate and exertion from measured heart rates. Similarly, a laser-scribed sensor patch has been reported with the capability of measuring caffeine, uric acid, and glucose in sweat while accurately measuring heart rate and heart rate variation (Figure 39b).<sup>602</sup>

More recently, work has been done to push multimodal devices to not only detect sweat biomarkers (alcohol) but also interstitial fluid biomarkers (glucose) in hopes of painting a more complete picture of a user's health (Figure 39c).<sup>331</sup> In addition to multiplex biomarker detection, vital sign sensing of blood pressure and heart rate has been successfully integrated with biochemical sensors including lactate, alcohol, glucose, and caffeine.<sup>329</sup> The device thoughtfully utilizes ultrasonic

transducers for vital monitoring. Such transducers not only allow for that accurate measurement of these vitals, but were shown to exhibit minimal crosstalk with chemical sensors given an optimal operating distance away from these sensors. Further, the coupling of these sensors paints a picture of a user's health status by quantifying alcohol and caffeine consumption while also measuring exertion levels from vital sensors.

As the field has progressed, multiple sensing modalities have been implemented in devices as to achieve cheaper and easier device implementation. While the previously mentioned devices have a high degree of accuracy, they all rely on electrochemical analysis for which compartments like potentiostats, batteries, or Bluetooth radios are costly. Further, when such bulky components are inflexible, they can limit the potential to miniaturize the wearable device. A thin, flexible colorimetric device has been reported with the capability of measuring pH, sweat rate, chloride, lactate, and glucose (Figure 39d).<sup>237</sup> By utilizing a biofuel cell-based sensor in conjunction with NFC-based sensor readout and wireless communication, the need for a battery was removed, rendering the device battery-free. Multiple sensing modalities have also opened doors for the classification of more complex biophysical states. Stress states have been predicted with a sweat-based wearable device by measuring multiple stressed-related biomarkers (Figure 39e).<sup>292</sup> By integrating a lateral

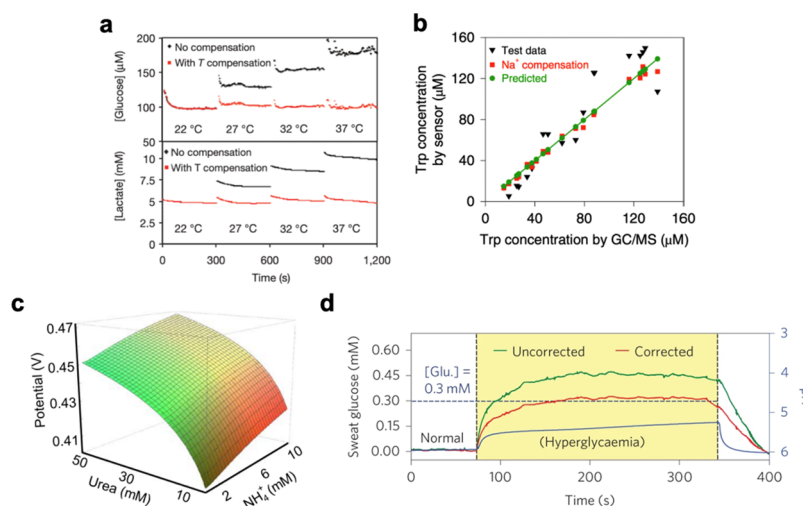


**Figure 40.** Sensor crosstalk and calibration. **a**, Influence of temperature on glucose and lactate sensors. Reproduced with permission from ref 12. Copyright 2016 Springer Nature. **b**, Influence of electrolyte (Na<sup>+</sup>) level on tryptophan biosensor response. Reproduced with permission from ref 87. Copyright 2022 Springer Nature. **c**, Influence of ammonium (NH<sub>4</sub><sup>+</sup>) on urea biosensors. Reproduced with permission from ref 410. Copyright 2020 The American Association for the Advancement of Science. **d**, Influence of pH on glucose biosensors. Reproduced with permission from ref 198. Copyright 2016 Springer Nature.

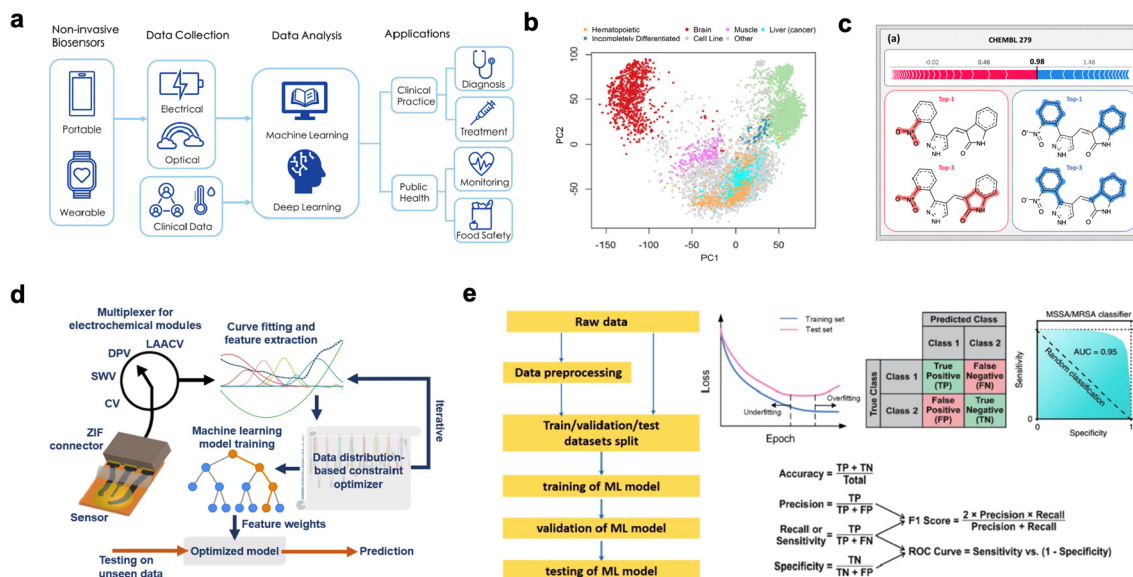


**Figure 41.** Data processing and machine learning. **a**, Broad overview of the machine learning experimental pipeline from biosensor fabrication to industry application. Reproduced with permission from ref 617. Copyright 2021 Wiley. **b**, Principal component analysis (PCA) analysis that can categorize different cell lines based on gene expression. Reproduced with permission from ref 618 under CC BY 4.0. Copyright 2016 Lenz et al. **c**, Shapley additive explanations (SHAP) analysis of two kinase inhibitors, displaying functional groups that help (red) or hurt (blue) its potency. Reproduced with permission from ref 615 under CC BY 4.0. Copyright 2020 Rodríguez-Pérez et al. **d**, Flowchart for extracting features from electrochemical measurements, training a model, and predicting analyte concentrations. Reproduced with permission from ref 619. Copyright 2022 Elsevier. **e**, Generic training process for a neural network. Reproduced with permission from ref 620. Copyright 2020 American Chemical Society.

flow immunoassay with fluorescence-based assays, simultaneous measurement of sweat cortisol and ascorbic acid levels is achieved. Cortisol, being well-known as the stress biomarker, can reveal an individual's stress levels while ascorbic acid (i.e., vitamin C) can correlate to immune response and potentially can be used in the treatment evaluation.

**9.1.2. Sensor Crosstalk and Calibration.** Another essential feature of multimodal sensors is their capability to self-calibrate other sensors on a wearable device, rendering the entire wearable system more accurate. Most of the aforementioned sensors, for example, rely on enzyme-based sensing, which can be influenced by operating temper-

atures.<sup>9,603–605</sup> On-skin temperature sensors could therefore serve a dual purpose to both measure skin temperature for diagnostic and calibrating sensor reading (Figure 40a).<sup>12</sup> This strategy was employed in a wearable sensor array for the continuous measurement of sweat glucose and lactate.<sup>606</sup> With the measured temperature and known temperature's influence on enzymatic sensor performance, glucose and lactate measurements can be calibrated. Similarly, a wearable system for the collection of exercise sweat to avoid hypoglycemic shock in diabetics has been reported.<sup>607</sup> Again, glucose measurements are normalized via temperature readouts showing the impact this method has on the wearable field.

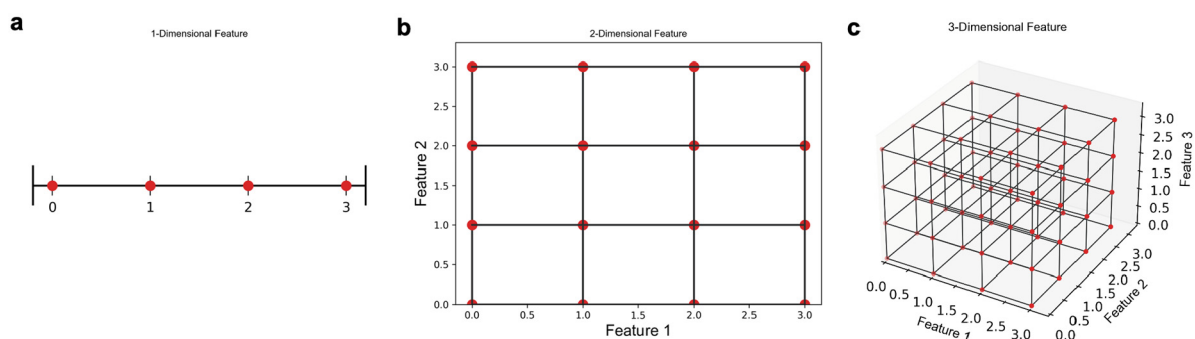


**Figure 42.** Exponential growth of feature space with input dimension. a–c, An evenly spaced sampling across a 1-dimensional feature space (4 data points) (a), a 2-dimensional feature space (16 data points) (b), and a 3-dimensional feature space (64 data points) (c).

Resistive temperature sensors should, however, take into consideration the effect of strain-responsive change in resistance as shown in laser-engraved graphene sensors.<sup>75</sup> Serpentine patterns could be adapted into temperature sensor designs to reduce the strain-induced change in resistance.

Chemical sensors in particular face many challenges with interferences from the complex matrix in biofluids, including various coexisting biomarkers which may skew the quantitation of the target biomarker. Reports have shown that the ionic strength of sweat (i.e.,  $\text{Na}^+$  concentrations) has the potential to influence a sensor's output signal (Figure 40b).<sup>87,608</sup> Moreover, as sweat rate could influence certain biomarker levels during exercises, sweat  $\text{Na}^+$  level (which showed a linear correlation with sweat rate) may be used to further calibrate sensors for continuous personalized monitoring. In addition, chemical measurements are susceptible to further signal drift depending on their chemical environment. For example, when  $\text{NH}_4^+$  level interferes with urea sensor reading, quantitation of urea would require simultaneous measurement of  $\text{NH}_4^+$  and real-time calibration (Figure 40c).<sup>410</sup> In addition to certain ions, pH could pose an influence on sweat chemical sensing. For example, glucose oxidase was shown to be affected by pH and requires pH calibration in real time (Figure 40d).<sup>198</sup>

Multimodal physiochemical sensing systems are highly promising for realizing precision medicine. The collected vital sign or physical parameter data could be used for calibrating the chemical sensor readings. Moreover, such data could supplement the molecular information and provide a comprehensive picture of an individual's health state, which is a crucial step in realizing precision medicine.

## 9.2. Machine Learning-Based Data Analysis

Wearable devices, in particular sweat sensors, have the potential to generate a spectrum of medical data, with each recorded biomarker painting an incomplete picture about the health of the patient. Artificial intelligence (AI), specifically machine learning (ML), offers a way to organize this information in an interpretable or useful manner. In the literature, ML has been applied to synthesize on-body biochemical profiles to predict the presence of diseases,<sup>609</sup> mental disorders,<sup>610</sup> emotional states,<sup>611</sup> drug intake, and nutritional levels<sup>612,613</sup> only using analytes in the sweat. By optimizing the expected ML accuracy, one can further determine which chemicals hold predictive information,<sup>614,615</sup> how to organize sensors on a patch,<sup>616</sup> as well as the optimal placement of sensors on the skin.<sup>616</sup> Each of these experiments can be broadly broken up into the following sections (Figure 41a): sensor design, on-body experiments, data processing,

feature extraction, ML model selection, and updating experimental parameters.<sup>617</sup> So far, this review has discussed the process of sensor design, on-body experiments, and data processing. The following section will go into feature extraction, ML model selection, and updating experimental parameters.

To achieve these goals, there are three general subcategories of ML algorithms one can utilize: supervised learning, unsupervised learning, and reinforcement learning. Unsupervised and reinforcement learning utilize unlabeled data (unmarked samples), requiring a large amount of data to make predictions. In a laboratory setting, this can be impractical for many emerging technologies still in the prototype stage that cannot generate a large quantity of high-quality data. Furthermore, these two methods are error-prone and can misinterpret ground truth for early experiments as the ML model is being refined. Because of these limitations, in this section, we will focus on supervised learning, the most common examples being convolutional neural networks (CNNs), support vector machines (SVMs), k-nearest neighbors (KNNs), logistical regression, and artificial neural networks.

**9.2.1. Curse of Dimensionality.** In machine learning, features refer to measurable properties or characteristics about an experiment. As there is no standard method to extract features, it is rather important to understand how features can broadly affect ML models. For supervised learning in wearable devices, each sweat analyte (such as uric acid) acts as an independent variable (feature) that potentially correlates with a quantifiable or observable event (e.g., gout). The more data one collects about a feature the more defined this association appears. From this point of view, a feature represents information added to a model. This leads many to believe that adding more information (features) to a model yields a better prediction. The following section will explore this idea further, highlighting the benefits and consequences of feature extraction.

The main deterrent for extracting features is that each piece of information carries an additional degree of freedom when solving for the underlying trend. In plain words, when building a model, each feature is not considered in isolation, but is rather compared against all existing inputs. As shown in Figure 42, as the dimensionality (number of features) increases, the feature space grows exponentially. Practically, with 4 data points evenly sampled across 1 feature, one would require 16 data points to achieve the same level of confidence in a 2-dimensional feature-space. For a fixed data set, this leads to a trade-off: adding more information to the model vs adding

more uncertainty about the connections between this information. Unfortunately, there is no universal standard limit to the number of features one should use for a given number of points. This is because in practice most data cannot be controlled and evenly sampled across a feature; rather, one might see duplicates or clusters inside a feature dimension.

In practice, this means that adding more features tends to initially increase the accuracy due to more information in the model; however, there exists a point when the accuracy will decrease with each new feature added. This occurs because in a small data set the model cannot extract meaningful trends from the feature-space. This phenomenon is referred to as the curse of dimensionality, also known as the peaking phenomenon or Hughes phenomenon. In plain terms, there exists a feature dimension where the average predictive power of any classifier degrades when increasing the feature space. Unfortunately, collecting data for novel sensors can often be arduous due to experimental error, time, as well as finding enough distinctive and representative subjects. Therefore, machine learning problems using wearable devices are often feature-limited by a small data set.

If data is not limited, collecting more points will add certainty to the model's final prediction, leading to the alternative question: how much data is too much. Luckily, there is no upper limit to the amount of data one could collect, as more data creates more certainty in the analysis. Nonetheless, in practice, one finds that the initial points drastically change the model's accuracy until it reaches a steady state. To determine if enough data has been collected, it is best to withhold some samples from the model as a validation set or test set and check whether their input has a significant effect on the model's final performance.

The best way to improve a model's accuracy, without adding more data, is to improve the feature extraction procedure, thereby reducing noise in the feature set. In machine learning, gathering clean, robust features from signals is preferred over utilizing extra, unnecessary information to make the same prediction.

**9.2.2. Feature Selection.** To remove features from a model, one must select the combination of features with the most nonoverlapping and relevant information to the prediction. There are a variety of well-known algorithms to accomplish this goal. The simplest method is to brute force try each feature combination, selecting the set that performs the best. Brute-force feature selection is widely used in the literature and has been applied to determine biomarkers in brain-machine interfaces,<sup>621</sup> to detect COVID-19 from acoustic waves,<sup>622</sup> and to detect breast cancer from images. This is because for a static model brute force feature selection is guaranteed to yield an optimal solution across multiple training sessions; however, it is computationally and time intensive, making it unreasonable for selecting information from a large feature pool, a large data set, or on a complex model due to the training time. Fortunately, there are alternative feature selection algorithms that can handle these cases, the most popular choices being principal component analysis (PCA), linear discriminant analysis (LDA), and Shapley additive explanations (SHAP).

In contrast to brute-force selection, LDA and PCA use a mathematical approach to eliminate features. PCA accomplishes this by transforming potentially correlated features into a basis set of orthogonal components using an eigenvalue decomposition. The final features are a linear combination of

the original set. Like the brute-force method, PCA analysis can be used in similar situations to predict breast cancer,<sup>623</sup> categorize gene expression from different cell lines (Figure 41b),<sup>618</sup> and analyze COVID-19.<sup>624</sup> Furthermore, PCA analysis has been used to find sweat metabolite combinations that are indicative of lung cancer.<sup>614,625</sup> Meanwhile, LDA reduces the feature dimension by looking for a subspace of features that maximizes the separation between two classifications. Like PCA, LDA has also been commonly used to detect breast cancer biomarkers.<sup>626,627</sup> Given that both methods have been applied to similar problems, one might wonder when one algorithm is preferred. PCA analysis is an unsupervised algorithm, making it optimal when working with unlabeled data or when looking for patterns in the features. In contrast, LDA works well when classifying data into groups. When both algorithms can be applied, LDA works better when the feature space is noisy, as PCA analysis will not overlook noise when creating a basis set in the feature space.

Recently, SHAP has become another popular feature selection tool. The SHAP analysis utilizes a game theory approach to explain an individual feature's contribution to the final prediction.<sup>628</sup> The SHAP value of feature A is calculated by taking the difference between the model's output with feature A and the average output after iterating through the feature-space of A.<sup>628</sup> SHAP values can be applied to discrete features for the detection of drugs in sweat<sup>629</sup> as well as in images to find important structural features for the activity prediction of chemicals<sup>615</sup> (Figure 41c). Despite providing greater insight into each feature, one drawback to the SHAP analysis is how computationally expensive the analysis is for many features due to training the model across the entire feature's dimension.

There are many other feature selection algorithms not discussed in this section such as local interpretable model-agnostic explanations (LIME),<sup>630</sup> single feature importance (SFI), and mean decrease accuracy (MDA). Some researchers have found that utilizing an aggregation of feature extraction techniques can improve the search for optimal feature combinations. Using an ensemble of feature selection methods will correct for any biases in one algorithm. The ensemble approach has been used in discovering important metabolites in a mouse's liver.<sup>631</sup> More research into ensemble feature selection methods will mitigate the problem of missing important features and aid in creating a more robust biomarker discovery tool; however, the biggest limitation of this technique is the computational time required for large feature pools.

**9.2.3. Model Selection.** There are a variety of machine learning models presented in the literature, each with broad, overlapping applications in the wearable space, which often make it hard to select the optimal algorithm to use. For quantifying chemicals in sweat, CNNs can measure lactate with an F1 score of 0.990,<sup>612</sup> decision trees can measure glucose with a root mean squared of 0.1 mg/dL,<sup>632</sup> KNNs can improve drifting errors in cortisol detection,<sup>633</sup> and KNNs can measure tyrosine and uric acid (Figure 41d).<sup>619</sup> On-body sensors have diagnosed depression from a random forest algorithm,<sup>610</sup> emotional states from support vector machines,<sup>611,634</sup> and stress from logistical regression.<sup>635</sup> From measuring chemicals in the sweat to psychological states, the use of different ML algorithms for similar problems highlights an important question: does the specific ML architecture matter when

most algorithms are interchangeable while still maintaining a high accuracy.

The simple answer is that ML models do not create the final trends in the input variables; rather, ML is a tool that connects information from the input-space to an observable output, if such a connection exists. As a tool, models can achieve the same results while taking different paths. In this regard, the choice of model often depends on situational parameters such as time/computational efficiency, interpretability, and reproducibility. In terms of efficiency, the rate limiting factor in the training time is model complexity. The benefit of complex neural architectures is that they have greater flexibility to adapt to any subtleties present in the feature space. This makes them extremely good at finding weak trends within the data, such as identifying ethnicity and age from sweat lipid profiles using a gradient boosting tree ensemble.<sup>636</sup> Unfortunately, complex models also require more data for training and risk overfitting noisy sensors. Furthermore, if the model is too complex, it becomes hard to create an interpretable mathematical expression relating the feature space to the final output. Using a complex 7-convolution layer CNN, a wearable device was able to monitor Parkinson's disease.<sup>637</sup> In this complex case, machine learning demonstrates the relevance of input features, but not why they are relevant. This makes it hard to reproduce and validate the outcome, due to small differences in the input space (i.e., electrodes, subjects, and sensing technique) as well as possible randomness inherent in the algorithm. A common example of poor interpretability, yet widely applicable, is deep learning networks, which have previously been used to surpass the limit of detection of six different metal ions in sweat.<sup>638</sup>

Model selection is a trade-off between simple architectures and high accuracy; however, it has underlying dependence on whether the model is meant to be interpretable, easily reproducible, and efficient.

**9.2.4. Machine Learning Inspired Designs.** After selecting a model, one can further extend the analysis to update experimental parameters. This is achieved by monitoring a model's accuracy change while varying different experimental attributes. Through this technique, one can find a combination of optimal antigen sensors to diagnose Lyme disease,<sup>616</sup> find the best placement of electrodes on the skin,<sup>616</sup> as well as optimize the material, structural, and excitation characteristics of gas sensors.<sup>639</sup> Upon finding an optimal configuration, one must recollect new data, extract features, and retrain the model (Figure 41e).<sup>620</sup> This process can be repeated multiple times, performing a gradient-descent search as one refines the final experimental parameters. When performed on a single subject, this method can aid in the development of a more personalized device for the patient.

**9.2.5. Machine Learning Discussions.** Machine learning can be applied to the development of physiochemical sensors, personalized healthcare, and biomarker discovery.<sup>51</sup> When developing machine learning models for wearable devices, there are a variety of factors to consider from input features to model architecture. Adding robust, nonoverlapping information is the best way to increase the accuracy of a model; however, selecting these features can often be challenging as different feature selection algorithms may favor specific combinations. Feature selection is further limited by the choice of model. When constructing a machine learning model, simple architectures with a small subset of features provide greater insight into the underlying mechanisms of how the

feature-space maps the health of the patient. Therefore, while it is attractive to work on complex designs with many features, limiting the scope of the analysis can afford a deeper understanding of how each feature pairing affects the final diagnosis and health of the patient.

The application of machine learning in wearable sweat biosensors is still a budding field. It is well-known in the machine learning community that features can greatly impact the final accuracy. Further investigations should look into biochemical features that can be extracted from wearable devices, especially considering the accuracy improvements that have already been seen in multimodal wearable devices when one considers the impacts of sweat rate, ionic strength, pH, and skin temperature. There is great potential for a device which measures these signals to improve the accuracy, as well as the sensitivity or selectivity, of coexisting chemical sensors. Another significant problem affecting the accuracy is noise in the form of motion artifact. Removing these artifacts to enable a system to measure the underlying signal could be of particularly high impact and help push wearable devices to the market.

### 9.3. Data Privacy

A customer's perception of their data security plays a vital role in their decision to adopt wearable technologies as determined by a risk-benefit analysis.<sup>640</sup> While the medical value of wearables is straightforward (as discussed in the sections above), the associated risk factors are a subject of speculation based on public opinion and news in the media. There is inherent danger in collecting and sharing health information with companies, between third parties, and with medical staff. For example, in 2021, major companies such as Fitbit (Google) and Apple were a part of a massive data breach where 61 million customers' name, age, gender, geographic location, and health information were all exposed in an online database without any password protection.<sup>641</sup> The problem is that many of these health trackers are not labeled as medical devices and therefore are not required to follow strict medical privacy standards, allowing companies to provide minimal security guarantees as well as sell health data for marketing and advertising purposes.<sup>641</sup> Exacerbating this issue, once data is collected, there is no statute of limitation for companies to erase health information, regardless of whether the customer has terminated their internal profile. As the public's perceived risk of data privacy grows above the reported benefit, customers will discontinue use of these wearable technologies.<sup>640</sup> Customer perception of their data privacy is therefore integral in their adoption of wearable devices.

**9.3.1. Medical Data Security.** There are two main entities that regulate the security of health information: the government and the device manufacturer. The United States Government secures the protection of medical data through the Health Insurance Portability and Accountability Act (HIPAA). In particular, HIPAA enumerates how to handle medical data through the Privacy Rule<sup>642</sup> and the Security Rule,<sup>643</sup> which applies to "business associates" dealing with "covered entities".<sup>644</sup> In broad terms, covered entities are health plans, healthcare clearinghouses, and healthcare providers that transmit medical information electronically,<sup>645</sup> while business associates use or disclose protected health information for a covered entity.<sup>646</sup> Under HIPAA protection, when sending medical information, companies must remove 18 key identifiers for security purposes, such as name, social

security, health numbers, and medical records.<sup>644</sup> However, companies can share private health data to third parties if the added entity agrees to protect the users' data according to HIPAA laws, where any data breaches are reported to the users.<sup>644</sup> Companies that violate these rules can be subjected to fines and criminal charges.

Despite these restrictions, not all wearables adhere to HIPAA guidelines as their products are not considered medical devices, but rather classified as wellness tools. Even for FDA-approved medical devices such as Fitbit (FDA approval in 2020) and Apple watch (FDA approval in 2021), not all wearables have to adhere to HIPAA guidelines as their products do not electronically transfer sensitive information. For example, a wearable device such as a fitness tracker that monitors a user's health and displays that information on a smart watch does not need to be HIPAA compliant as the entity does not share the data with a business associate or a covered entity, such as a physician.<sup>644</sup> This provides an illusion of data security to the customer, while exposing individuals to a variety of attacks. It should be noted that at the time of this review, the FDA is in the process of updating its guidelines for handling sensitive data and have already announced a new Office of Digital Transformation in 2021.

Without government regulation, companies themselves can still adhere to strict data security and privacy standards. During data storage, companies can secure against common hacks such as distributed denial of service (DDoS) attacks,<sup>647</sup> Structured Query Language (SQL) injections, or back door attacks. Two common methods to secure data include authentication, such as a pin number to validate the customer, and encryption, such as storing data on a blockchain. Blockchain works through decentralized data sharing, where an immutable data table is validated for authenticity by all users on the chain, preventing hackers from easily altering the records.<sup>648</sup> If a hacker does want to permanently change health information on the chain, they would have to hack into every user who stores a copy of that particular block. While this protects data storage, attacks on wearable devices can still occur during data transmission. Data transferred over WiFi, Bluetooth, or any near-field communication can be subjected to data leaks due to misconnections. Fortunately, there are a variety of different methods to protect data across the Internet of things, such as SecuWear: an open-source platform that identifies and mitigates potential software attacks against wearable devices.<sup>649</sup>

**9.3.2. Future of Data Privacy.** As the innovation in wearable technology scales, so does the collection and storage of private health information, creating a concern about the potential misuse of user medical data. The consequences of improperly handling sensitive information are that users can be targeted due to their security information and discriminated against based on their medical history. Due to this inherent risk, customers can often be skeptical about using wearable technology. The lack of trust in data protection, lack of control, and gaps in the legislature all contribute to this negative perception.<sup>640</sup> To increase the adoption of valuable medical devices, companies must properly consider the storage, transmission, and use-cases of sensitive medical information when developing their products.

## 10. PATH TO COMMERCIALIZATION

There is tremendous translational value in the technologies described in this review. Translational value is determined by

the ability to blend market and design factors in a way that meets a clinical need.<sup>650</sup> Wearable sweat sensors can address the need for noninvasive biomarker data collection. Applications of wearable sweat sensors include but are not limited to fitness and recovery, mental health, personalized healthcare, and telemedicine. High translational value establishes a path to commercialization. In this section, the medical device product life cycle is detailed along with industry and regulatory challenges. The emerging sweat sensing market is summarized, and future growth trends are discussed.

### 10.1. Product Life Cycle

The medical device product life cycle (Figure 43) begins with conception, design, and prototype development. During this

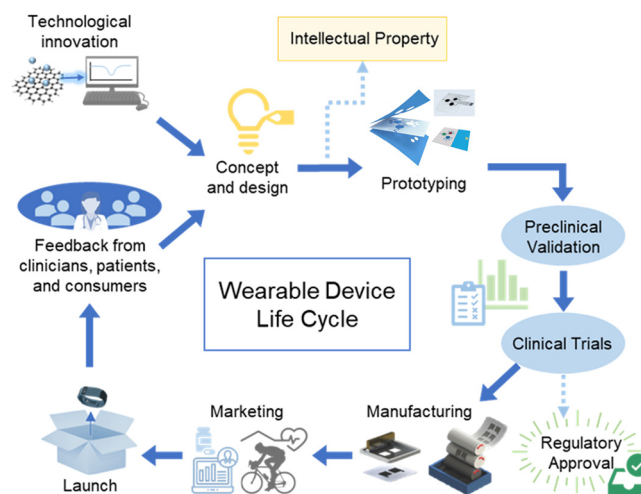


**Figure 43.** Wearable device product life cycle. Reproduced with permission from refs 430, 652. Copyright 2020 The American Association for the Advancement of Science. Copyright 2016 Wiley.

phase, it is important to file intellectual property and licensing.<sup>651</sup> Upon prototype development, design specifications are tested and verified. Considerations should be made for scaling feasibility via low-cost mass manufacturing techniques. Next, regulatory compliance strategy must be considered to bring the product to market in a timely manner. Preclinical investigation validates the product performance, identifies failure modes, and refines risk mitigation strategies. Product compliance with FDA regulations is evaluated based on robust clinical trials, the extent of which varies based on device classification. After FDA approval and product launch, postmarket risk is mitigated through adverse event reporting, surveillance, and patient focused registry. Product enhancements are also made based on market feedback from stakeholders and regulatory approval. Finally at the end of product life, it is important to communicate with stakeholders the timeline for the end of manufacturing, end of support, and end of availability.<sup>651</sup>

The medical device product life cycle may also be characterized by the device deployment duration, how long or often the device is in use by the patient.<sup>651</sup> Single-use, frequent use, and continuous use durations are determined by contextual design factors of the wearable device. How quickly and how often biomarker levels change may determine the required time resolution of measurements. While a single-point daily or weekly measurement may be sufficient to monitor or screen for certain abnormalities, one may need to integrate

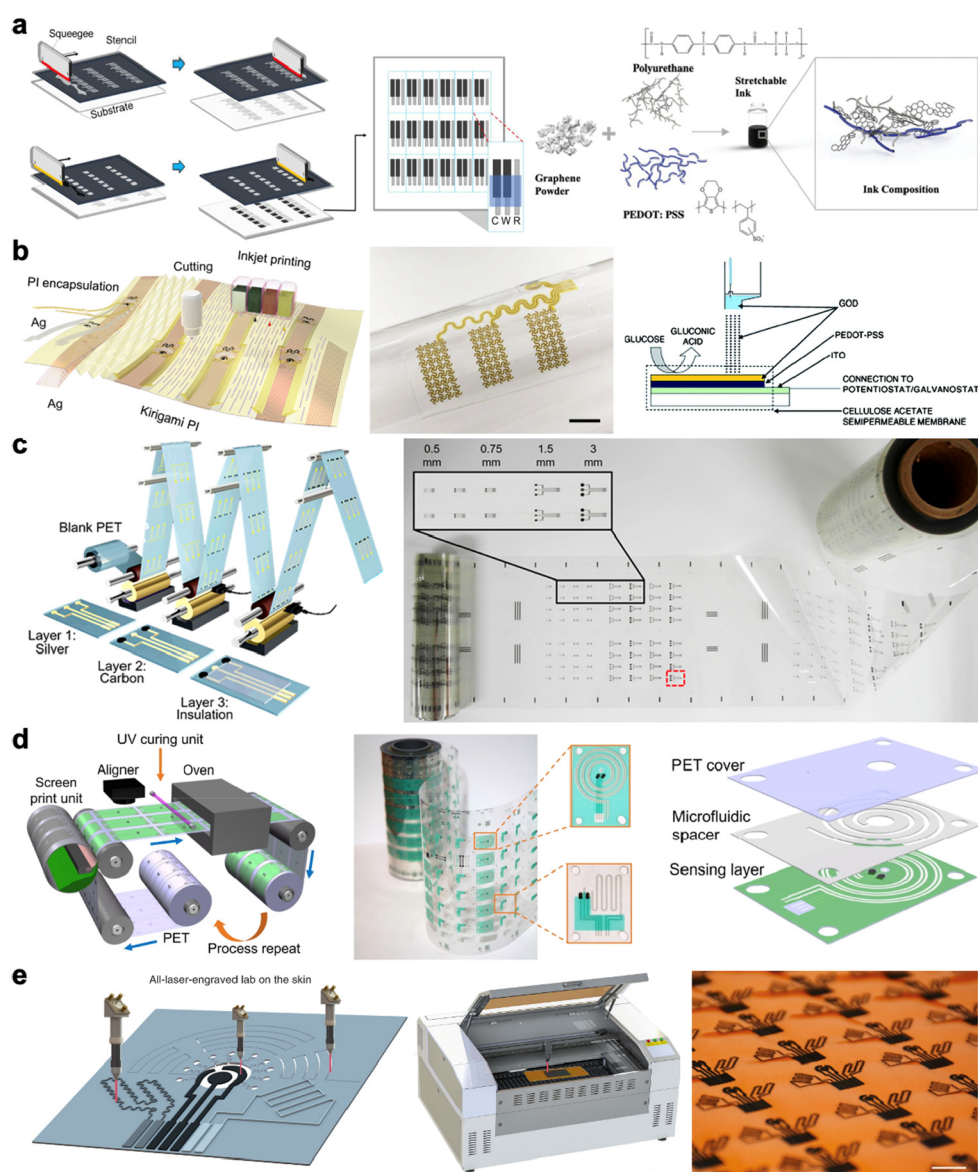


**Figure 44.** Mass manufacturing techniques for low-cost wearable electronics and microfluidic patches. **a**, Screen printed electrode fabrication and flexible graphene ink formulation. Reproduced with permission from refs 653, 655. Copyright 2022 American Chemical Society. Copyright 2019 Wiley. **b**, Inkjet printing of electrodes and bioink enzyme functionalization. Scale bar, 1 cm. Reproduced with permission from ref 137. Copyright 2022 The American Association for the Advancement of Science. **c**, Roll-to-roll electrode fabrication. Reproduced with permission from ref 135. Copyright 2018 American Chemical Society. **d**, Roll-to-roll lab-on-a-chip fabrication. Reproduced with permission from ref 541. Copyright 2019 The American Association for the Advancement of Science. **e**, Laser-engraved lab on the skin. Scale bar, 1 cm. Reproduced with permission from ref 75. Copyright 2019 Springer Nature.

continuous sampling to perform trend analysis and pattern recognition. For continuous use, the wearable deployment duration is determined by the limitations of the device itself (e.g., sweat generation, sensor degradation) or the monitoring context (e.g., period of exercise, treatment course). Device duration may inform the scale of deployment.

To make the devices accessible, the design should be scalable at low-cost using high-throughput manufacturing methods. Screen printing, inkjet printing, roll-to-roll (R2R) manufacturing, and laser engraving are all methods that achieve high efficiency patterning and good conductivity for the flexible electronics found in wearable sweat sensing platforms. Screen printing is one of the most established low-cost mass-manufacturing methods. Screen-printed electrodes are commercially available in a variety of conductive materials and

patterns with highly reliable offerings from companies such as DropSens by Metrohm. Screen printing uses a stencil to deposit functional inks onto a flexible substrate, while simultaneously removing excess ink (Figure 44a).<sup>653</sup> Screen printed film thickness is wide ranging (0.02–100  $\mu\text{m}$ ).<sup>654</sup> Many considerations go into formulating a conductive ink, including the nanomaterial properties, homogeneity, viscosity, and substrate compatibility. Laser-induced graphene on PI film may be harvested and made into an ink with ideal electrochemical and mechanical properties for flexible electronics.<sup>655</sup> Conductive (e.g., PEDOT:PSS) and elastomeric (e.g., polyester-polyurethane) binding agents can enhance the performance of conductive inks.<sup>655</sup> Surfactants and polymers prevent particle aggregation and are important additives to conductive inks, which require stable dispersion for low

Table 4. Wearable Sweat Sensor Market Landscape

Company/Product	Market Segment	Metrics	Transduction	FDA Clearance	
Epicore Biosystems	Gx Sweat Patch	Fitness (hydration)	Sweat rate, Cl <sup>-</sup>	Colorimetric	–
	Connected Hydration	Safety (hydration)	Sweat rate, electrolyte content, temperature, motion	Electrochemical	–
	My Skin Track pH	Skincare	pH	Colorimetric	–
	Discovery Patch	Diagnostics	None	n/a	Yes
Nix Biosensors	Fitness (hydration)	Sweat rate, electrolyte content	Electrochemical	–	
FlowBio		Sweat rate, electrolyte content	Electrochemical	–	
hDrop		Sweat rate, temperature	Electrochemical	–	
SM24	Fitness, diagnostics	Lactic acid, glucose, sweat rate	Electrochemical	–	
Onalabs	Fitness, diagnostics	Lactic acid, glucose	Electrochemical	–	
Graphwear	Diagnostics	Glucose	Electrochemical	–	
Xsensio		pH, Na <sup>+</sup> , K <sup>+</sup> , Ca <sup>2+</sup> , cortisol	Electrochemical	–	

resistivity.<sup>656</sup> High viscosity inks are required for screen printing, leading to challenges in creating fine pattern features and often resulting in resolutions on the order of tens of microns in commercial use.<sup>657</sup>

In inkjet printing, designs are digitally controlled and fabricated by droplet addition according to its design dot matrix (Figure 44b).<sup>137</sup> On-demand ink ejection generates droplets through piezoelectric, thermal, electrohydrodynamic, and other pulsatile methods.<sup>656</sup> Inkjet-printed films can vary in thickness based on additive droplet control and rheological properties of the ink. Ink viscosity and surface tension are important parameters for good printing quality and jetability. Bioinks have added challenges of biomolecular stability during printing and nonspecific adsorption to the ink tank resulting in protein loss (solved with BSA additive).<sup>656</sup> Inkjet printing is highly efficient with minimal materials wasted, reducing the cost per print. With high customizability and precise spatial control inkjet printing is ideal for printing complex patterns using multiple inks, as in the case of e-skins.<sup>137</sup> Biosensors can be fabricated by serial printing the electrodes and connections, encapsulation, functionalization, and entrapment.

R2R manufacturing is a technique that allows for sequential modifications, including pattern transfer, etching, gravure printing, heating, UV curing, and others.<sup>135,658</sup> R2R gravure printing uses an engraved cylinder that stamps a substrate feed and continually refreshes with ink as it rotates. The bending and rotations of the feed during R2R limit this process to flexible substrates.<sup>654</sup> In comparison to screen printing, R2R gravure printing mechanics can operate at faster speeds with high resolution and consistency, but ink deposition is relatively thin, around 10 μm, increasing the resistivity.<sup>654,657</sup> Using a bilayer working electrode scheme, thin R2R gravure printed carbon electrodes may be supported by a silver ink layer (Figure 44c).<sup>135</sup> This morphology enables high-throughput R2R manufacturing of flexible electronics while maintaining mechanical and electrochemical robustness. R2R manufacturing may be used for microfluidic fabrication and full device assembly (Figure 44d). R2R rotary electrode screen printing was combined with R2R laser cutting of microfluidics (bilayer microfluidic adhesive spacer and flexible PET cover) to assemble a wearable sweat sensor layer-by-layer.<sup>541</sup> A camera module was used to monitor the alignment of the printed layers during R2R rotary assembly. The R2R system produced 60 devices per minute on a 100 m web length.

Laser engraving is a bottom-up method for graphene electrode fabrication using a CO<sub>2</sub> laser cutter to directly carbonize polymeric substrates (e.g., PI) (Figure 44e).<sup>75,659</sup>

Laser-engraved graphene (LEG) is low-cost and high-throughput. LEG composition, porosity, impedance, and morphology may all be tuned using laser parameters.<sup>659</sup> Complex patterns can be easily made digitally with resolution limited only by the focus and power of the laser. Due to a lack of binding elastomers, the poor mechanical stability of LEG may result in disconnections and an open circuit, a problem exacerbated by repeated bending of flexible substrates.<sup>659</sup> The laser cutter may also be used to fabricate multilayered microfluidics rapidly by laser cutting channels, inlets, outlets, and sensing regions.<sup>75</sup> Lastly, individual devices may be cut from mass-printed sheets using camera-assisted laser cutting.<sup>541</sup>

FDA oversight is present at every step of the medical device product life cycle. However, noninvasive medical devices have fewer barriers to market entry. The foundation of FDA medical device regulations are based on the reasonable assurance of safety and efficacy (21 CFR 860.7(d,e)).<sup>651</sup> As noninvasive wearable devices, sweat sensing platforms exhibit the most risk when they include iontophoretic sweat induction and when they are used for a serious medical diagnosis. For reference, the Macroduct sweat iontophoresis system is registered as a Class II device. However, should the device be of demonstrated substantial equivalence to another legally U.S. marketed device, then the device is exempt of the 510(k) premarket notification and may be made immediately commercially available. The FDA approval process may also be bypassed under the condition that no medical claims are made for the device and the device is noninvasive with no biological interactions.

## 10.2. Emerging Market Landscape

To avoid the FDA regulatory process, many early stage sweat sensors are starting out in the consumer health and wellness space (Table 4). Sweat is induced during activity, so sweat stimulation is not needed in the wearable patch design. Rather than providing medical information, the data is regarded as a performance metric. Together these allow noninvasive wearable sweat sensors to be readily commercialized. The Gx sweat patch by Epicore Biosystems in partnership with PepsiCo and Gatorade is the first widespread commercially available wearable sweat patch. The flexible microfluidic adhesive patch captures sweat throughout exercise and collects sweat rate and electrolyte content data using a colorimetric output.<sup>660</sup> The corresponding app allows for real-time analysis using ML-enabled image processing.<sup>661</sup> The device has been validated for hydration monitoring across 312 athletes and in a variety of use conditions.<sup>358,661</sup>

Competitors to Epicore for hydration monitoring include Nix Biosensors, FlowBio, and hDrop.<sup>662,663</sup> In contrast to the Gx sweat patch, these devices utilize integrated electrical components. Nix calculates sweat rate, electrolyte loss rate, and sweat composition in the sweat collection channel and transmits this data wirelessly. The electronic pod is reusable and connects to a single use sweat patch.<sup>664</sup> hDrop is an armband that continuously monitors hydration through skin impedance sensing.<sup>665</sup> Lactic acid is an important indicator of exercise intensity and muscle fatigue during training. Onalabs is developing a sweat lactate sensor for athletes prior to venturing into the clinical space (they plan to incorporate additional biochemical sensors, including glucose detection).<sup>666</sup> SM24 is also working toward a wearable sweat-based sensor for real-time glucose, lactate, and hydration monitoring.<sup>667</sup>

Epicore as a company has focused heavily on the development of flexible microfluidic sweat collection systems, referred to as “epifluidics”. This establishes a template for mass customization, a marketing and manufacturing technique that allows for flexible, custom product features with low unit cost at mass production.<sup>668</sup> Custom biochemical sweat assays may be simple to deploy relative to changing the microfluidic structure. A colorimetric pH assay was used to assess skin health and personalized skincare needs in the My Skin Track pH platform designed with L’Oréal.<sup>669</sup> Customizable sweat assays are the basis for the Epicore Discovery Patch, which collects sweat, and extracts it into a cryovial for future analysis.<sup>660</sup> The Discovery Patch has been used to assess cytokines in sweat.<sup>56</sup> The Discovery Patch is registered as a 510(k) exempt Class I FDA device.

Expanding into clinical diagnostics requires regulatory approval. The Discovery Patch serves as a springboard to on-body diagnostic assays. Epicore has clinical studies in progress for applications including stroke rehabilitation, cystic fibrosis screening, prediabetes screening, and kidney disease screening.<sup>668</sup> In addition to Epicore, GraphWear is performing clinical studies in preparation for FDA review of their noninvasive continuous glucose monitor. If their trials further demonstrate similar performance to other continuous glucose monitors, they may be eligible for 510(k) clearance.<sup>670</sup> Swiss company Xsensio hopes to develop the first commercial Lab-on-Skin sensing platform for real-time biochemical sensing. Their approach utilizes miniaturized functionalized field-effect transistors for multiplexed biomarker detection, including Na<sup>+</sup>, K<sup>+</sup>, Ca<sup>2+</sup>, pH, and cortisol.<sup>220,671–673</sup>

Form and comfort are important criteria for product adoption. The Nix sweat patch uses kinesiology tape for flexible adhesion and comfort, which is a material commonly used by their targeted athletic demographic.<sup>664</sup> Epicore Biosystems has focused heavily on the development of a flexible microfluidic sweat collection system, which is the foundation of their devices. Form defines function for Epicore’s infant cystic fibrosis sweat sticker; the soft, flexible collection platform allows for low volume sweat collection and reduces leakage rates.<sup>674</sup> Current FDA-cleared standard sweat collection devices fail approximately 10–20% due to insufficient sweat collection, which the Epicore microfluidic patch resolves. Additionally, fun graphics on the sweat sticker were attractive to children and improved their perceived experience.<sup>675</sup>

Similar trends are seen in the wearable heart rate monitoring space. Early adoption in the fitness tracking space allowed for

continued market testing to improve sensing and diagnostic accuracy. Some smartwatches now have FDA-cleared applications like the AppleWatch and Apple’s corresponding ECG app for classifying signs of AFib and irregular rhythms.<sup>676</sup> With the rise in popularity of smartwatches and CGM patches, the U.S. market is primed to adopt wearable sweat sensing platforms.

Consumer adoption and physician adoption will likely vary, yet physician adoption is required to see transformative change and impact of sweat sensing technology in healthcare. Physician adoption first requires accurate data collection and FDA approval. Next, integrated data analytics and efficient summaries are required. High volume biometrics may be overwhelming and be ignored. It is important to communicate and work closely with physicians to understand what would be most informative for them. User interface and compatibility with current electronic medical systems are additional considerations that may impact clinical adoption. Lastly, developing a clinician-trusted brand dedicated to quality and medical-grade products is important.

Another market for wearable devices is research and clinical trials. Medidata Sensor Cloud (formerly MC10) and VivoSense provide services to collect, integrate, and analyze data from wearables in clinical trials. Medidata Sensor Cloud utilizes proprietary wearable patches (e.g., BioStamp nPoint) to collect medical-grade quality biometrics remotely.<sup>677</sup> Incorporating noninvasive wearable sweat sensors into clinical trials may provide important biochemical data. Wearable drug monitoring systems may determine pharmaceutical levels to maximize the efficacy of treatment while minimizing harmful side effects. Integrating vital sign sensors and contextual physiological biosensors may help better screen for important side effects.

Although few sweat sensors have been commercialized to date, many are in the pipeline. As of 2022, Epicore Biosystems has over 100 patents issued or pending.<sup>678</sup> The wearable device market was valued at \$19.45 billion in 2020 with expected growth to \$47.84 billion by 2026.<sup>679</sup> The rise of remote patient monitoring and telemedicine is a driver for market growth, along with the shift in healthcare from reactive to proactive intervention.<sup>680</sup> Medical grade wearables and predictive diagnostics will aid physicians and patients in better addressing health concerns. The FDA is actively responding with more fast-track approval paths for low-risk wearable devices that collect medical grade data while still maintaining high quality standards. The “Over-the-Counter Hearing Aid Act” of 2017 allows hearing aids to be sold direct to consumers without a prescription.<sup>680</sup> This paves the way for low-risk wearable devices to be made accessible upon deployment. The rollout of sweat sensors will diversify the wearable device market and the type of data available for continuous monitoring.

## 11. CHALLENGES AND FUTURE OUTLOOK

Research in the field of wearable sweat sensors has grown exponentially in the past decade (Figure 45). This rapid growth is primarily attributed to the vast opportunities in precision medicine and preventative healthcare offered by sweat sensing, as well as the technological advances in numerous fields of engineering that have realized the development of miniaturized wearable sweat sensing devices. With more and more wearable sweat sensing devices being developed every year, the major bottlenecks hindering the widespread commercial adoption of wearable sensors have become clearer.

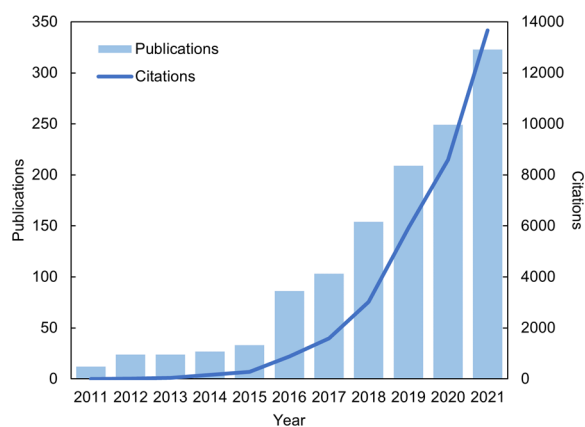


**Figure 45.** Number of annual publications and citations on “sweat sensing” from 2011 to 2021 according to Web of Science.

On the device side, it is critical to develop a compact and comfortable-to-wear wearable sweat sensing system that can extract sufficient volumes of sweat consistently throughout the day for accurate and continuous biomarker analysis via robust biosensors and low-power wireless electronic instrumentation. Initial studies on sweat biomarkers relied on sweat induction through exercise or heat, limiting the accessibility of sweat to very specific scenarios. Development of iontophoretic sweat stimulation as well as microfluidic and osmotic sweat collection technologies have enabled the collection of iontophoretic or even natural sweat in sedentary scenarios. However, current sweat extraction technologies still suffer from large inter-personal variations or insufficiencies in sweat volume or sweat duration. While enzymatic sensors and ion-selective electrodes have been extensively developed for the detection of common sweat electrolytes and metabolites that are relatively high in concentration, many trace-level biomarkers including hormones and lipids are challenging to assess continuously with traditional sensing mechanisms. It is important to develop novel sensor modalities for broadening the spectrum of detectable biomarkers, as well as to improve the sensitivity, selectivity, and stability of existing sensors for facilitating accurate and prolonged measurements. For compact and robust system-integration, low-power and precise electronic circuitry should be coupled with a compact power source. Furthermore, materials innovations are required at every end of the system, including the sensor, electronic circuit, battery, and energy harvester. An integrated sweat sensor system is as small and flexible as its largest and stiffest component, and therefore each element of the device can benefit from the integration of novel materials and structures that reduce footprint and stiffness. Nonetheless, a perfect wearable sweat sensor device on its own is not sufficient to validate its value for precision medicine.

Despite decades of research, many aspects of sweat gland physiology are still poorly understood. While advances in sensing modalities are widening the range of detectable biomarkers as well as improving the accuracy and detection limit of biomarker analysis, the exact partitioning mechanisms and blood correlations of sweat biomarkers require further study. 3D sweat gland models for simulating the partitioning pathways of various biomarkers and large-scale clinical validation studies driven by continuous wearable sweat sensing platforms can improve the contextualization of biomarkers with respect to health conditions. Furthermore, increased use

of wearable sweat sensors will generate overflowing data on sweat biomarkers that can be uploaded to the cloud and processed via big data and machine learning algorithms. Such algorithms have the potential to unveil inconspicuous correlations between sweat biomarkers and health conditions, even if the pathological pathways are not clear. Multiplexed biosensing using wearable sweat sensors coupled with machine learning-powered data analysis represent a new approach for modern biomarker discovery without the need of frequent hospital visits and toleration of invasive procedures.<sup>51</sup> However, with an influx of sensitive health data uploaded to the cloud, data privacy issues can arise. Additionally, considering that conventional von Neumann computing strategies are inefficient at processing large volumes of unstructured cloud data, neuromorphic edge computing technologies embedded in wearable devices have the potential to process data more securely and efficiently.

The aforementioned considerations present challenges but at the same time exciting opportunities in advancing skin-interfaced sweat sensors toward their practical applications in healthcare. The personalized data collected from wearable sweat sensors will serve as essential building blocks for personalized and precision medicine. At a personal level, the insights provided by wearable sweat sensors on an individual's health status encourage users to take an active role in health management. At the same time, the synergy between future consumer-facing wearable products with clinical-grade medical devices is expected to contribute to a connected network for researchers and clinicians and provide comprehensive insights into an individual patient. Ultimately, the seamless integration of wearable sweat sensors into a patient's daily life and care delivery process is envisioned to enhance precision medicine by allowing the timely initiation of personalized treatment to maximize health outcomes on an individual basis.

## AUTHOR INFORMATION

### Corresponding Author

**Wei Gao** – Andrew and Peggy Cherng Department of Medical Engineering, Division of Engineering and Applied Science, California Institute of Technology, Pasadena, California 91125, United States; [orcid.org/0000-0002-8503-4562](https://orcid.org/0000-0002-8503-4562); Email: [weigao@caltech.edu](mailto:weigao@caltech.edu)

### Authors

**Jihong Min** – Andrew and Peggy Cherng Department of Medical Engineering, Division of Engineering and Applied Science, California Institute of Technology, Pasadena, California 91125, United States; [orcid.org/0000-0002-5788-1473](https://orcid.org/0000-0002-5788-1473)

**Jiaobing Tu** – Andrew and Peggy Cherng Department of Medical Engineering, Division of Engineering and Applied Science, California Institute of Technology, Pasadena, California 91125, United States

**Changhao Xu** – Andrew and Peggy Cherng Department of Medical Engineering, Division of Engineering and Applied Science, California Institute of Technology, Pasadena, California 91125, United States; [orcid.org/0000-0002-6817-3341](https://orcid.org/0000-0002-6817-3341)

**Heather Lukas** – Andrew and Peggy Cherng Department of Medical Engineering, Division of Engineering and Applied Science, California Institute of Technology, Pasadena, California 91125, United States

**Soyoung Shin** – Andrew and Peggy Cherng Department of Medical Engineering, Division of Engineering and Applied Science, California Institute of Technology, Pasadena, California 91125, United States

**Yiran Yang** – Andrew and Peggy Cherng Department of Medical Engineering, Division of Engineering and Applied Science, California Institute of Technology, Pasadena, California 91125, United States; [orcid.org/0000-0001-8770-8746](https://orcid.org/0000-0001-8770-8746)

**Samuel A. Solomon** – Andrew and Peggy Cherng Department of Medical Engineering, Division of Engineering and Applied Science, California Institute of Technology, Pasadena, California 91125, United States

**Daniel Mukasa** – Andrew and Peggy Cherng Department of Medical Engineering, Division of Engineering and Applied Science, California Institute of Technology, Pasadena, California 91125, United States

Complete contact information is available at:

<https://pubs.acs.org/10.1021/acs.chemrev.2c00823>

### Author Contributions

<sup>‡</sup>J.M., J.T., C.X., and H.L. contributed equally to this work. CRediT: **Jihong Min** investigation, methodology, writing-original draft, writing-review & editing; **Jiaobing Tu** investigation, methodology, writing-original draft, writing-review & editing; **Changhao Xu** investigation, methodology, writing-original draft, writing-review & editing; **Heather Lukas** investigation, methodology, writing-original draft, writing-review & editing; **Soyoung Shin** investigation, methodology, writing-original draft, writing-review & editing; **Yiran Yang** investigation, methodology, writing-original draft, writing-review & editing; **Samuel A Solomon** investigation, methodology, writing-original draft, writing-review & editing; **Daniel Mukasa** investigation, methodology, writing-original draft, writing-review & editing; **Wei Gao** conceptualization, funding acquisition, investigation, project administration, supervision, writing-review & editing.

### Notes

The authors declare no competing financial interest.

### Biographies

Jihong Min is currently a Medical Engineering Ph.D. candidate at the California Institute of Technology. He received his B.S. in Electrical Engineering at the University of Illinois at Urbana–Champaign and M.S. in Medical Engineering at the California Institute of Technology. His current research interests include energy harvesting, wearable biosensors, and ingestible electronics.

Jiaobing Tu received her B.Eng. degree in Materials Science and Engineering from Imperial College London. She joined Prof. Wei Gao's research group in 2018 and is currently pursuing her Ph.D. degree in Medical Engineering at the California Institute of Technology. Her research interests include wearable electronics and biosensors.

Changhao Xu is currently a Ph.D. candidate in Professor Wei Gao group of Medical Engineering at the California Institute of Technology. He received his B.S. degree at Fudan University in 2018 and M.S. degree at California Institute of Technology in 2020. His current research interests include design and fabrication of wearable sensors, medical devices, and machine learning for health.

Heather Lukas is a current Ph.D. candidate in the Gao Research Group at the California Institute of Technology. She received her B.S.

in Biomedical Engineering with a minor in Business from Cornell University in 2019. Her current research interests focus on developing novel techniques for continuous biochemical sensing in sweat with applications in therapeutic and addictive drug monitoring.

Soyoung Shin is currently a Ph.D. candidate in the Department of Chemical Engineering at the California Institute of Technology. She received her B.S. degree in Chemical Engineering from the University of California, San Diego, in 2021. Her current research focuses wearable sweat-based biosensors.

Yiran Yang received her B.S. degree in Bioengineering from Rice University. She then joined Dr Wei Gao's research group and is currently pursuing her Ph.D. degree in Medical Engineering at Caltech. Her research interests include wearable electronics, biosensors, and nanomedicine. She is also a member of the Tau Beta Pi Engineering Honor Society.

Samuel A. Solomon is currently pursuing a doctorate in Medical Engineering at the California Institute of Technology. He received his Bachelor's degree in Chemistry-Biology and Physics at the Massachusetts Institute of Technology in 2020 with minors in Nuclear Engineering and Computer Science. His current research interests include intelligent wearable biosensors.

Daniel Mukasa is currently a Ph.D. candidate in Materials Science and Applied Physics at the California Institute of Technology. He received his Bachelor's degree in Physics from Oberlin College in 2019. His current research interests include wearable biosensors, computational materials design, and machine learning.

Wei Gao is currently an Assistant Professor of Medical Engineering at the California Institute of Technology. He received his Ph.D. degree in Chemical Engineering from the University of California, San Diego, in 2014. He then worked as a postdoctoral fellow in Electrical Engineering and Computer Sciences at the University of California, Berkeley, until 2017. His current research interests include flexible electronics, wearable biosensors, digital medicine, and micro/nanorobotics.

### ACKNOWLEDGMENTS

This project was supported by the National Institutes of Health grants R01HL155815 and R21DK13266, National Science Foundation grant 2145802, Office of Naval Research grants N00014-21-1-2483 and N00014-21-1-2845, American Cancer Society Research Scholar Grant RSG-21-181-01-CTPS, High Impact Pilot Research Award T31IP1666 from the Tobacco-Related Disease Research Program, Sloan Research Fellowship, and Heritage Medical Research Institute.

### REFERENCES

- (1) Yang, Y.; Gao, W. Wearable and Flexible Electronics for Continuous Molecular Monitoring. *Chem. Soc. Rev.* **2019**, *48*, 1465–1491.
- (2) Xu, C.; Yang, Y.; Gao, W. Skin-Interfaced Sensors in Digital Medicine: From Materials to Applications. *Matter* **2020**, *2*, 1414–1445.
- (3) Kim, J.; Campbell, A. S.; de Ávila, B. E.-F.; Wang, J. Wearable Biosensors for Healthcare Monitoring. *Nat. Biotechnol.* **2019**, *37*, 389–406.
- (4) Ates, H. C.; Nguyen, P. Q.; Gonzalez-Macia, L.; Morales-Narváez, E.; Güder, F.; Collins, J. J.; Dincer, C. End-to-End Design of Wearable Sensors. *Nat. Rev. Mater.* **2022**, *7*, 887–907.
- (5) Xu, S.; Kim, J.; Walter, J. R.; Ghaffari, R.; Rogers, J. A. Translational Gaps and Opportunities for Medical Wearables in Digital Health. *Sci. Transl. Med.* **2022**, *14*, No. eabn6036.

- (6) Wang, S.; Oh, J. Y.; Xu, J.; Tran, H.; Bao, Z. Skin-Inspired Electronics: An Emerging Paradigm. *Acc. Chem. Res.* **2018**, *51*, 1033–1045.
- (7) Ray, T. R.; Choi, J.; Bandodkar, A. J.; Krishnan, S.; Gutruf, P.; Tian, L.; Ghaffari, R.; Rogers, J. A. Bio-Integrated Wearable Systems: A Comprehensive Review. *Chem. Rev.* **2019**, *119*, 5461–5533.
- (8) Ometov, A.; Shubina, V.; Klus, L.; Skibińska, J.; Saafi, S.; Pascacio, P.; Flueratoru, L.; Gaibor, D. Q.; Chukhno, N.; Chukhno, O.; Ali, A.; Channa, A.; Svrtoka, E.; Qaim, W. B.; Casanova-Marqués, R.; Holcer, S.; Torres-Sospedra, J.; Casteleyn, S.; Ruggeri, G.; Araniti, G.; Burget, R.; Hosek, J.; Lohan, E. S. A Survey on Wearable Technology: History, State-of-the-Art and Current Challenges. *Comput. Netw.* **2021**, *193*, 108074.
- (9) Bariya, M.; Nyein, H. Y. Y.; Javey, A. Wearable Sweat Sensors. *Nat. Electron.* **2018**, *1*, 160–171.
- (10) Min, J.; Sempionatto, J. R.; Teymourian, H.; Wang, J.; Gao, W. Wearable Electrochemical Biosensors in North America. *Biosens. Bioelectron.* **2021**, *172*, 112750.
- (11) Yu, Y.; Nyein, H. Y. Y.; Gao, W.; Javey, A. Flexible Electrochemical Bioelectronics: The Rise of In Situ Bioanalysis. *Adv. Mater.* **2020**, *32*, 1902083.
- (12) Gao, W.; Emaminejad, S.; Nyein, H. Y. Y.; Challa, S.; Chen, K.; Peck, A.; Fahad, H. M.; Ota, H.; Shiraki, H.; Kiriya, D.; Lien, D.-H.; Brooks, G. A.; Davis, R. W.; Javey, A. Fully Integrated Wearable Sensor Arrays for Multiplexed *In Situ* Perspiration Analysis. *Nature* **2016**, *529*, 509–514.
- (13) Wilke, K.; Martin, A.; Terstegen, L.; Biel, S. S. A Short History of Sweat Gland Biology. *Int. J. Cosmet. Sci.* **2007**, *29*, 169–179.
- (14) Low, P. A. Evaluation of Sudomotor Function. *Clin. Neurophysiol.* **2004**, *115*, 1506–1513.
- (15) Klaka, P.; Grüdl, S.; Banowski, B.; Giesen, M.; Sättler, A.; Proksch, P.; Welss, T.; Förster, T. A Novel Organotypic 3D Sweat Gland Model with Physiological Functionality. *PLoS One* **2017**, *12*, No. e0182752.
- (16) Elpa, D. P.; Chiu, H.-Y.; Wu, S.-P.; Urban, P. L. Skin Metabolomics. *Trends Endocrinol. Metab.* **2021**, *32*, 66–75.
- (17) Shelley, W. B.; Hurley, H. J. The Physiology of the Human Axillary Apocrine Sweat Gland. *J. Invest. Dermatol.* **1953**, *20*, 285–297.
- (18) Sato, K.; Leidal, R.; Sato, F. Morphology and Development of an Apoeccrine Sweat Gland in Human Axillae. *Am. J. Physiol. Regul. Integr. Comp. Physiol.* **1987**, *252*, R166–R180.
- (19) Heikenfeld, J.; Jajack, A.; Feldman, B.; Granger, S. W.; Gaitonde, S.; Begtrup, G.; Katchman, B. A. Accessing Analytes in Biofluids for Peripheral Biochemical Monitoring. *Nat. Biotechnol.* **2019**, *37*, 407–419.
- (20) Tripathi, S. R.; Miyata, E.; Ishai, P. B.; Kawase, K. Morphology of Human Sweat Ducts Observed by Optical Coherence Tomography and Their Frequency of Resonance in the Terahertz Frequency Region. *Sci. Rep.* **2015**, *5*, 9071.
- (21) Lu, C. P.; Polak, L.; Rocha, A. S.; Pasolli, H. A.; Chen, S.-C.; Sharma, N.; Blanpain, C.; Fuchs, E. Identification of Stem Cell Populations in Sweat Glands and Ducts Reveals Roles in Homeostasis and Wound Repair. *Cell* **2012**, *150*, 136–150.
- (22) Diao, J.; Liu, J.; Wang, S.; Chang, M.; Wang, X.; Guo, B.; Yu, Q.; Yan, F.; Su, Y.; Wang, Y. Sweat Gland Organoids Contribute to Cutaneous Wound Healing and Sweat Gland Regeneration. *Cell Death Dis.* **2019**, *10*, 238.
- (23) Liu, N.; Huang, S.; Yao, B.; Xie, J.; Wu, X.; Fu, X. 3D Bioprinting Matrices with Controlled Pore Structure and Release Function Guide *In Vitro* Self-Organization of Sweat Gland. *Sci. Rep.* **2016**, *6*, 34410.
- (24) Cui, C.-Y.; Schlessinger, D. Eccrine Sweat Gland Development and Sweat Secretion. *Exp. Dermatol.* **2015**, *24*, 644–650.
- (25) Bovell, D. L. The Evolution of Eccrine Sweat Gland Research towards Developing a Model for Human Sweat Gland Function. *Exp. Dermatol.* **2018**, *27*, 544–550.
- (26) Sato, K.; Sato, F. Role of Calcium in Cholinergic and Adrenergic Mechanisms of Eccrine Sweat Secretion. *Am. J. Physiol.* **1981**, *241*, C113–C120.
- (27) Quinton, P. M. Cystic Fibrosis: Lessons from the Sweat Gland. *Physiology* **2007**, *22*, 212–225.
- (28) Mihályi, C.; Iordanov, I.; Töröcsik, B.; Csanády, L. Simple Binding of Protein Kinase A Prior to Phosphorylation Allows CFTR Anion Channels to Be Opened by Nucleotides. *Proc. Natl. Acad. Sci. U.S.A.* **2020**, *117*, 21740–21746.
- (29) Salinas, D. B.; Peng, Y.-H.; Horwich, B.; Wee, C. P.; Frisbee, E.; Maarek, J.-M. Image-Based  $\beta$ -Adrenergic Sweat Rate Assay Captures Minimal Cystic Fibrosis Transmembrane Conductance Regulator Function. *Pediatr. Res.* **2020**, *87*, 137–145.
- (30) Sonner, Z.; Wilder, E.; Gaillard, T.; Kasting, G.; Heikenfeld, J. Integrated Sudomotor Axon Reflex Sweat Stimulation for Continuous Sweat Analyte Analysis with Individuals at Rest. *Lab Chip* **2017**, *17*, 2550–2560.
- (31) Riedl, B.; Nischik, M.; Birklein, F.; Neundörfer, B.; Handwerker, H. O. Spatial Extension of Sudomotor Axon Reflex Sweating in Human Skin. *J. Auton. Nerv. Syst.* **1998**, *69*, 83–88.
- (32) Kihara, M.; Opfer-Gehrking, T. L.; Low, P. A. Comparison of Directly Stimulated with Axon-Reflex-Mediated Sudomotor Responses in Human Subjects and in Patients with Diabetes. *Muscle Nerve* **1993**, *16*, 655–660.
- (33) Low, P. A.; Opfer-Gehrking, T. L.; Kihara, M. *In Vivo* Studies on Receptor Pharmacology of the Human Eccrine Sweat Gland. *Clin. Auton. Res.* **1992**, *2*, 29–34.
- (34) Ohmi, M.; Tanigawa, M.; Wada, Y.; Haruna, M. Dynamic Analysis for Mental Sweating of a Group of Eccrine Sweat Glands on a Human Fingertip by Optical Coherence Tomography. *Skin Res. and Technol.* **2012**, *18*, 378–383.
- (35) Buono, M. J.; Ball, K. D.; Kolkhorst, F. W. Sodium Ion Concentration vs. Sweat Rate Relationship in Humans. *J. Appl. Physiol.* **2007**, *103*, 990–994.
- (36) Ohashi, T.; Gerrett, N.; Shinkawa, S.; Sato, T.; Miyake, R.; Kondo, N.; Mitsuzawa, S. Fluidic Patch Device to Sample Sweat for Accurate Measurement of Sweat Rate and Chemical Composition: A Proof-of-Concept Study. *Anal. Chem.* **2020**, *92*, 15534–15541.
- (37) Simmers, P.; Li, S. K.; Kasting, G.; Heikenfeld, J. Prolonged and Localized Sweat Stimulation by Iontophoretic Delivery of the Slowly-Metabolized Cholinergic Agent Carbachol. *J. of Dermatol. Sci.* **2018**, *89*, 40–51.
- (38) Shibasaki, M.; Crandall, C. G. Effect of Local Acetylcholinesterase Inhibition on Sweat Rate in Humans. *J. Appl. Physiol.* **2001**, *90*, 757–762.
- (39) Sato, K.; Dobson, R. L. Regional and Individual Variations in the Function of the Human Eccrine Sweat Gland. *J. Invest. Dermatology* **1970**, *54*, 443–449.
- (40) Patterson, M. J.; Galloway, S. D. R.; Nimmo, M. A. Variations in Regional Sweat Composition in Normal Human Males. *Experimental Physiology* **2000**, *85*, 869–875.
- (41) Cui, C.-Y.; Childress, V.; Piao, Y.; Michel, M.; Johnson, A. A.; Kunisada, M.; Ko, M. S. H.; Kaestner, K. H.; Marmorstein, A. D.; Schlessinger, D. Forkhead Transcription Factor FoxA1 Regulates Sweat Secretion through Bestrophin 2 Anion Channel and Na-K-Cl Cotransporter 1. *Proc. Natl. Acad. Sci. U.S.A.* **2012**, *109*, 1199–1203.
- (42) Bozoky, Z.; Ahmadi, S.; Milman, T.; Kim, T. H.; Du, K.; Di Paola, M.; Pasyk, S.; Pekhletski, R.; Keller, J. P.; Bear, C. E.; Forman-Kay, J. D. Synergy of CAMP and Calcium Signaling Pathways in CFTR Regulation. *Proc. Natl. Acad. Sci. U.S.A.* **2017**, *114*, No. E2086-E2095.
- (43) Berdiev, B. K.; Qadri, Y. J.; Benos, D. J. Assessment of the CFTR and ENaC Association. *Mol. Biosyst.* **2009**, *5*, 123–127.
- (44) Prompt, C. A.; Quinton, P. M. Functions of Calcium in Sweat Secretion. *Nature* **1978**, *272*, 171–172.
- (45) Thai, T. L.; Yu, L.; Galarza-Paez, L.; Wu, M. M.; Lam, H. Y. C.; Bao, H. F.; Duke, B. J.; Al-Khalili, O.; Ma, H.-P.; Liu, B.; Eaton, D. C. The Polarized Effect of Intracellular Calcium on the Renal Epithelial Sodium Channel Occurs as a Result of Subcellular Calcium Signaling

- Domains Maintained by Mitochondria. *J. Biol. Chem.* **2015**, *290*, 28805–28811.
- (46) Buono, M. J.; Claros, R.; DeBoer, T.; Wong, J. Na<sup>+</sup> Secretion Rate Increases Proportionally More than the Na<sup>+</sup> Reabsorption Rate with Increases in Sweat Rate. *J. Appl. Physiol.* **2008**, *105*, 1044–1048.
- (47) Sato, K.; Kang, W. H.; Saga, K.; Sato, K. T. Biology of Sweat Glands and Their Disorders. I. Normal Sweat Gland Function. *J. Am. Acad. Dermatol.* **1989**, *20*, 537–563.
- (48) Sato, K. Update on Pharmacology of the Eccrine Sweat Gland. *Trends Pharmacol. Sci.* **1984**, *5*, 391–393.
- (49) Weiner, J. S.; Van Heyningen, R. Lactic Acid and Sweat Gland Function. *Nature* **1949**, *164*, 351–352.
- (50) Jajack, A.; Brothers, M.; Kasting, G.; Heikenfeld, J. Enhancing Glucose Flux into Sweat by Increasing Paracellular Permeability of the Sweat Gland. *PLoS One* **2018**, *13*, No. e0200009.
- (51) Sempionatto, J. R.; Lasalde-Ramírez, J. A.; Mahato, K.; Wang, J.; Gao, W. Wearable Chemical Sensors for Biomarker Discovery in the Omics Era. *Nat. Rev. Chem.* **2022**, *6*, 899.
- (52) Sonner, Z.; Wilder, E.; Heikenfeld, J.; Kasting, G.; Beyette, F.; Swaile, D.; Sherman, F.; Joyce, J.; Hagen, J.; Kelley-Loughnane, N.; Naik, R. The Microfluidics of the Eccrine Sweat Gland, Including Biomarker Partitioning, Transport, and Biosensing Implications. *Biomicrofluidics* **2015**, *9*, 031301.
- (53) Hauke, A.; Simmers, P.; Ojha, Y. R.; Cameron, B. D.; Ballweg, R.; Zhang, T.; Twine, N.; Brothers, M.; Gomez, E.; Heikenfeld, J. Complete Validation of a Continuous and Blood-Correlated Sweat Biosensing Device with Integrated Sweat Stimulation. *Lab Chip* **2018**, *18*, 3750–3759.
- (54) Hooton, K.; Han, W.; Li, L. Comprehensive and Quantitative Profiling of the Human Sweat Submetabolome Using High-Performance Chemical Isotope Labeling LC-MS. *Anal. Chem.* **2016**, *88*, 7378–7386.
- (55) Kutysenko, V. P.; Molchanov, M.; Beskaravayny, P.; Uversky, V. N.; Timchenko, M. A. Analyzing and Mapping Sweat Metabolomics by High-Resolution NMR Spectroscopy. *PLoS One* **2011**, *6*, No. e28824.
- (56) Aranyosi, A. J.; Model, J. B.; Zhang, M. Z.; Lee, S. P.; Leech, A.; Li, W.; Seib, M. S.; Chen, S.; Reny, N.; Wallace, J.; Shin, M. H.; Bhandokar, A. J.; Choi, J.; Paller, A. S.; Rogers, J. A.; Xu, S.; Ghaffari, R. Rapid Capture and Extraction of Sweat for Regional Rate and Cytokine Composition Analysis Using a Wearable Soft Microfluidic System. *J. Invest. Dermatol.* **2021**, *141*, 433–437.
- (57) Hadorn, B.; Hanimann, F.; Anders, P.; Curtius, H.-C.; Halverson, R. Free Amino-Acids in Human Sweat from Different Parts of the Body. *Nature* **1967**, *215*, 416–417.
- (58) Sato, K.; Ohtsuyama, M.; Samman, G. Eccrine Sweat Gland Disorders. *J. Am. Acad. Dermatol.* **1991**, *24*, 1010–1014.
- (59) Dobson, R. L. The Human Eccrine Sweat Gland: Structural and Functional Interrelationships. *Arch. Environ. Health* **1965**, *11*, 423–429.
- (60) Sato, K. Sweat Induction from an Isolated Eccrine Sweat Gland. *Am. J. Physiol.* **1973**, *225*, 1147–1152.
- (61) Buono, M. J.; Stone, M.; Cannon, D. T. Leaching from the Stratum Corneum Does Not Explain the Previously Reported Elevated Potassium Ion Concentration in Sweat. *J. Basic Clin. Physiol. Pharmacol.* **2016**, *27*. DOI: 10.1515/jbcpp-2015-0097.
- (62) Schwartz, I. L.; Thaysen, J. H. EXCRETION OF SODIUM AND POTASSIUM IN HUMAN SWEAT I. *J. Clin. Invest.* **1956**, *35*, 114–120.
- (63) Adeva, M. M.; Souto, G.; Blanco, N.; Donapetry, C. Ammonium Metabolism in Humans. *Metabolism* **2012**, *61*, 1495–1511.
- (64) Sato, K. *Rev. Physiol., Biochem. Pharmacol.* Vol. 79; Reviews of Physiology, Biochemistry and Pharmacology; Springer-Verlag Springer e-books: Berlin, Heidelberg, 2005.
- (65) Moyer, J.; Wilson, D.; Finkelshtein, I.; Wong, B.; Potts, R. Correlation Between Sweat Glucose and Blood Glucose in Subjects with Diabetes. *Diabetes Technol. Ther.* **2012**, *14*, 398–402.
- (66) Murota, H.; Yamaga, K.; Ono, E.; Katayama, I. Sweat in the Pathogenesis of Atopic Dermatitis. *Allergol. Int.* **2018**, *67*, 455–459.
- (67) Komives, G. K.; Robinson, S.; Roberts, J. T. Urea Transfer across the Sweat Glands. *J. Appl. Physiol.* **1966**, *21*, 1681–1684.
- (68) Gordon, R. S.; Thompson, R. H.; Thrasher, D.; Benson, J. W. Genesis Of The Sweat: Plasma Urea Concentration Gradient. *J. Invest. Dermatol.* **1976**, *66*, 218–221.
- (69) Na, C. H.; Sharma, N.; Madugundu, A. K.; Chen, R.; Aksit, M. A.; Rosson, G. D.; Cutting, G. R.; Pandey, A. Integrated Transcriptomic and Proteomic Analysis of Human Eccrine Sweat Glands Identifies Missing and Novel Proteins. *Mol. Cell. Proteomics* **2019**, *18*, 1382–1395.
- (70) Keller, R. W.; Bailey, J. L.; Wang, Y.; Klein, J. D.; Sands, J. M. Urea Transporters and Sweat Response to Uremia. *Physiol. Rep.* **2016**, *4*, No. e12825.
- (71) Xie, L.; Jin, L.; Feng, J.; Lv, J. The Expression of AQP5 and UTs in the Sweat Glands of Uremic Patients. *Biomed. Res. Int.* **2017**, *2017*, 8629783.
- (72) Czarnowski, D.; Górski, J. Excretion of nitrogen compounds in sweat during a sauna. *Polym. Tyg. Lek.* **1991**, *46*, 186–187.
- (73) Huang, C.-T.; Chen, M.-L.; Huang, L.-L.; Mao, I.-F. Uric Acid and Urea in Human Sweat. *Chin. J. Physiol.* **2002**, *45*, 109–115.
- (74) Al-Tamer, Y. Y.; Hadi, E. A.; Al-Badrani, I. e. I. Sweat Urea, Uric Acid and Creatinine Concentrations in Uraemic Patients. *Urol. Res.* **1997**, *25*, 337–340.
- (75) Yang, Y.; Song, Y.; Bo, X.; Min, J.; Pak, O. S.; Zhu, L.; Wang, M.; Tu, J.; Kogan, A.; Zhang, H.; Hsiai, T. K.; Li, Z.; Gao, W. A Laser-Engraved Wearable Sensor for Sensitive Detection of Uric Acid and Tyrosine in Sweat. *Nat. Biotechnol.* **2020**, *38*, 217–224.
- (76) Ford, E. S.; Li, C.; Cook, S.; Choi, H. K. Serum Concentrations of Uric Acid and the Metabolic Syndrome Among US Children and Adolescents. *Circulation* **2007**, *115*, 2526–2532.
- (77) Baker, L. B.; Stofan, J. R.; Lukaski, H. C.; Horswill, C. A. Exercise-Induced Trace Mineral Element Concentration in Regional Versus Whole-Body Wash-Down Sweat. *Int. J. Sport Nutr. Exerc. Metab.* **2011**, *21*, 233–239.
- (78) Montain, S. J.; Chevront, S. N.; Lukaski, H. C. Sweat Mineral-Element Responses during 7 h of Exercise-Heat Stress. *Int. J. Sport Nutr. Exerc. Metab.* **2007**, *17*, 574–582.
- (79) Chinevere, T. D.; Kenefick, R. W.; Chevront, S. N.; Lukaski, H. C.; Sawka, M. N. Effect of Heat Acclimation on Sweat Minerals. *Med. Sci. Sports Exerc* **2008**, *40*, 886–891.
- (80) Ely, M. R.; Kenefick, R. W.; Chevront, S. N.; Chinevere, T. D.; Lacher, C. P.; Lukaski, H. C.; Montain, S. J. Surface Contamination Artificially Elevates Initial Sweat Mineral Concentrations. *J. Appl. Physiol.* **2011**, *110*, 1534–1540.
- (81) Gibiński, K.; Zmudziński, J.; Kumaszk, F.; Giec, L.; Waclawczyk, J. Calcium Transit to Thermal Sweat. *Acta. Biol. Med. Ger.* **1974**, *32*, 199–204.
- (82) Jahnen-Dechent, W.; Ketteler, M. Magnesium Basics. *Clin. Kidney J.* **2012**, *5*, i3–i14.
- (83) Zhao, J.; Nyein, H. Y. Y.; Hou, L.; Lin, Y.; Bariya, M.; Ahn, C. H.; Ji, W.; Fan, Z.; Javey, A. A Wearable Nutrition Tracker. *Adv. Mater.* **2021**, *33*, 2006444.
- (84) Shields, J. B.; Johnson, B. C.; Hamilton, T. S.; Mitchell, H. H. THE EXCRETION OF ASCORBIC ACID AND DEHYDROASCORBIC ACID IN SWEAT AND URINE UNDER DIFFERENT ENVIRONMENTAL CONDITIONS. *J. Biol. Chem.* **1945**, *161*, 351–356.
- (85) Hier, S. W.; Cornbleet, T.; Bergeim, O. The Amino Acids of Human Sweat. *J. Biol. Chem.* **1946**, *166*, 327–333.
- (86) Harvey, C. J.; LeBouf, R. F.; Stefaniak, A. B. Formulation and Stability of a Novel Artificial Human Sweat under Conditions of Storage and Use. *Toxicol. in Vitro* **2010**, *24*, 1790–1796.
- (87) Wang, M.; Yang, Y.; Min, J.; Song, Y.; Tu, J.; Mukasa, D.; Ye, C.; Xu, C.; Heflin, N.; McCune, J. S.; Hsiai, T. K.; Li, Z.; Gao, W. A Wearable Electrochemical Biosensor for the Monitoring of Metabolites and Nutrients. *Nat. Biomed. Eng.* **2022**, *6*, 1225–1235.

- (88) Mark, H.; Harding, C. R. Amino Acid Composition, Including Key Derivatives of Eccrine Sweat: Potential Biomarkers of Certain Atopic Skin Conditions. *Int. J. Cosmet. Sci.* **2013**, *35*, 163–168.
- (89) Dunstan, R. H.; Sparkes, D. L.; Dascombe, B. J.; Macdonald, M. M.; Evans, C. A.; Stevens, C. J.; Crompton, M. J.; Gottfries, J.; Franks, J.; Murphy, G.; Wood, R.; Roberts, T. K. Sweat Facilitated Amino Acid Losses in Male Athletes during Exercise at 32–34°C. *PLoS One* **2016**, *11*, No. e0167844.
- (90) Kirschbaum, C.; Hellhammer, D. H. Salivary Cortisol in Psychobiological Research: An Overview. *Neuropsychobiology* **2004**, *22*, 150–169.
- (91) Wang, B.; Zhao, C.; Wang, Z.; Yang, K.-A.; Cheng, X.; Liu, W.; Yu, W.; Lin, S.; Zhao, Y.; Cheung, K. M.; Lin, H.; Hojajji, H.; Weiss, P. S.; Stojanović, M. N.; Tomiyama, A. J.; Andrews, A. M.; Emaminejad, S. Wearable Aptamer-Field-Effect Transistor Sensing System for Noninvasive Cortisol Monitoring. *Sci. Adv.* **2022**, *8*, No. eabk0967.
- (92) Pearlmutter, P.; DeRose, G.; Samson, C.; Linehan, N.; Cen, Y.; Begdache, L.; Won, D.; Koh, A. Sweat and Saliva Cortisol Response to Stress and Nutrition Factors. *Sci. Rep.* **2020**, *10*, 19050.
- (93) Torrente-Rodríguez, R. M.; Tu, J.; Yang, Y.; Min, J.; Wang, M.; Song, Y.; Yu, Y.; Xu, C.; Ye, C.; IsHak, W. W.; Gao, W. Investigation of Cortisol Dynamics in Human Sweat Using a Graphene-Based Wireless MHealth System. *Matter* **2020**, *2*, 921–937.
- (94) Teruhisa, U.; Ryoji, H.; Taisuke, I.; Tatsuya, S.; Fumihiro, M.; Tatsuo, S. Use of Saliva for Monitoring Unbound Free Cortisol Levels in Serum. *Clin. Chim. Acta* **1981**, *110*, 245–253.
- (95) Reichmann, F.; Holzer, P. Neuropeptide Y: A Stressful Review. *Neuropeptides* **2016**, *55*, 99–109.
- (96) Cizza, G.; Marques, A. H.; Eskandari, F.; Christie, I. C.; Torvik, S.; Silverman, M. N.; Phillips, T. M.; Sternberg, E. M. Elevated Neuroimmune Biomarkers in Sweat Patches and Plasma of Premenopausal Women with Major Depressive Disorder in Remission: The POWER Study. *Biol. Psychiatry* **2008**, *64*, 907–911.
- (97) Csösz, E.; Emri, G.; Kalló, G.; Tsapralis, G.; Tözsér, J. Highly Abundant Defense Proteins in Human Sweat as Revealed by Targeted Proteomics and Label-Free Quantification Mass Spectrometry. *J. Eur. Acad. Dermatol. Venereol.* **2015**, *29*, 2024–2031.
- (98) Katchman, B. A.; Zhu, M.; Blain Christen, J.; Anderson, K. S. Eccrine Sweat as a Biofluid for Profiling Immune Biomarkers. *Prot. Clin. Appl.* **2018**, *12*, 1800010.
- (99) Yu, Y.; Prassas, I.; Muyltjens, C. M. J.; Diamandis, E. P. Proteomic and Peptidomic Analysis of Human Sweat with Emphasis on Proteolysis. *J. Proteomics* **2017**, *155*, 40–48.
- (100) Marques-Deak, A.; Cizza, G.; Eskandari, F.; Torvik, S.; Christie, I. C.; Sternberg, E. M.; Phillips, T. M. Measurement of Cytokines in Sweat Patches and Plasma in Healthy Women: Validation in a Controlled Study. *J. Immunol. Methods* **2006**, *315*, 99–109.
- (101) Jones, A. P.; Webb, L. M. C.; Anderson, A. O.; Leonardo, E. J.; Rot, A. Normal Human Sweat Contains Interleukin-8. *J. Leukoc. Biol.* **1995**, *57*, 434–437.
- (102) Black, J. *Biological Performance of Materials: Fundamentals of Biocompatibility*, 4th ed.; CRC Press: Taylor & Francis, 2005.
- (103) Black, J.; Hastings, G. *Handbook of Biomaterial Properties*, 1st ed.; Springer: New York, NY.
- (104) Lei, T.; Guan, M.; Liu, J.; Lin, H.-C.; Pfattner, R.; Shaw, L.; McGuire, A. F.; Huang, T.-C.; Shao, L.; Cheng, K.-T.; Tok, J. B.-H.; Bao, Z. Biocompatible and Totally Disintegrable Semiconducting Polymer for Ultrathin and Ultralightweight Transient Electronics. *Proc. Natl. Acad. Sci. U.S.A.* **2017**, *114*, 5107–5112.
- (105) Shi, X.; Zuo, Y.; Zhai, P.; Shen, J.; Yang, Y.; Gao, Z.; Liao, M.; Wu, J.; Wang, J.; Xu, X.; Tong, Q.; Zhang, B.; Wang, B.; Sun, X.; Zhang, L.; Pei, Q.; Jin, D.; Chen, P.; Peng, H. Large-Area Display Textiles Integrated with Functional Systems. *Nature* **2021**, *591*, 240–245.
- (106) Libanori, A.; Chen, G.; Zhao, X.; Zhou, Y.; Chen, J. Smart Textiles for Personalized Healthcare. *Nat. Electron.* **2022**, *5*, 142–156.
- (107) Wang, C.; Wang, C.; Huang, Z.; Xu, S. Materials and Structures toward Soft Electronics. *Adv. Mater.* **2018**, *30*, 1801368.
- (108) Guo, Y.; Zhong, M.; Fang, Z.; Wan, P.; Yu, G. A Wearable Transient Pressure Sensor Made with MXene Nanosheets for Sensitive Broad-Range Human-Machine Interfacing. *Nano Lett.* **2019**, *19*, 1143–1150.
- (109) Hwang, S.-W.; Tao, H.; Kim, D.-H.; Cheng, H.; Song, J.-K.; Rill, E.; Brenckle, M. A.; Panilaitis, B.; Won, S. M.; Kim, Y.-S.; Song, Y. M.; Yu, K. J.; Ameen, A.; Li, R.; Su, Y.; Yang, M.; Kaplan, D. L.; Zakin, M. R.; Slepian, M. J.; Huang, Y.; Omenetto, F. G.; Rogers, J. A. A Physically Transient Form of Silicon Electronics. *Science* **2012**, *337*, 1640–1644.
- (110) LI, Y. Perceptions of Temperature, Moisture and Comfort in Clothing during Environmental Transients. *Ergonomics* **2005**, *48*, 234–248.
- (111) Kim, D.-H.; Rogers, J. A. Stretchable Electronics: Materials Strategies and Devices. *Adv. Mater.* **2008**, *20*, 4887–4892.
- (112) Miyamoto, A.; Lee, S.; Cooray, N. F.; Lee, S.; Mori, M.; Matsuhisa, N.; Jin, H.; Yoda, L.; Yokota, T.; Itoh, A.; Sekino, M.; Kawasaki, H.; Ebihara, T.; Amagai, M.; Someya, T. Inflammation-Free, Gas-Permeable, Lightweight, Stretchable on-Skin Electronics with Nanomeses. *Nat. Nanotechnol.* **2017**, *12*, 907–913.
- (113) Ma, Z.; Huang, Q.; Xu, Q.; Zhuang, Q.; Zhao, X.; Yang, Y.; Qiu, H.; Yang, Z.; Wang, C.; Chai, Y.; Zheng, Z. Permeable Superelastic Liquid-Metal Fibre Mat Enables Biocompatible and Monolithic Stretchable Electronics. *Nat. Mater.* **2021**, *20*, 859–868.
- (114) Wang, Y.; Lee, S.; Wang, H.; Jiang, Z.; Jimbo, Y.; Wang, C.; Wang, B.; Kim, J. J.; Koizumi, M.; Yokota, T.; Someya, T. Robust, Self-Adhesive, Reinforced Polymeric Nanofilms Enabling Gas-Permeable Dry Electrodes for Long-Term Application. *Proc. Natl. Acad. Sci. U.S.A.* **2021**, *118*, No. e2111904118.
- (115) Datta, R. S.; Syed, N.; Zavabeti, A.; Jannat, A.; Mohiuddin, M.; Rokunuzzaman, M.; Zhang, B. Y.; Rahman, M. A.; Atkin, P.; Messalea, K. A.; Ghasemian, M. B.; Gaspera, E. D.; Bhattacharyya, S.; Fuhrer, M. S.; Russo, S. P.; McConville, C. F.; Esrafilzadeh, D.; Kalantar-Zadeh, K.; Daeneke, T. Flexible Two-Dimensional Indium Tin Oxide Fabricated Using a Liquid Metal Printing Technique. *Nat. Electron.* **2020**, *3*, 51–58.
- (116) Byun, S.-H.; Sim, J. Y.; Zhou, Z.; Lee, J.; Qazi, R.; Walicki, M. C.; Parker, K. E.; Haney, M. P.; Choi, S. H.; Shon, A.; Gereau, G. B.; Bilbily, J.; Li, S.; Liu, Y.; Yeo, W.-H.; McCall, J. G.; Xiao, J.; Jeong, J.-W. Mechanically Transformative Electronics, Sensors, and Implantable Devices. *Sci. Adv.* **2019**, *5*, No. eaay0418.
- (117) Dickey, M. D. Stretchable and Soft Electronics Using Liquid Metals. *Adv. Mater.* **2017**, *29*, 1606425.
- (118) Liu, S.; Shah, D. S.; Kramer-Bottiglio, R. Highly Stretchable Multilayer Electronic Circuits Using Biphasic Gallium-Indium. *Nat. Mater.* **2021**, *20*, 851–858.
- (119) Liu, Y.; Liu, J.; Chen, S.; Lei, T.; Kim, Y.; Niu, S.; Wang, H.; Wang, X.; Foudeh, A. M.; Tok, J. B.-H.; Bao, Z. Soft and Elastic Hydrogel-Based Microelectronics for Localized Low-Voltage Neuro-modulation. *Nat. Biomed. Eng.* **2019**, *3*, 58–68.
- (120) Cao, Y.; Morrissey, T. G.; Acome, E.; Allec, S. I.; Wong, B. M.; Keplinger, C.; Wang, C. A Transparent, Self-Healing, Highly Stretchable Ionic Conductor. *Adv. Mater.* **2017**, *29*, 1605099.
- (121) Matsuhisa, N.; Inoue, D.; Zalar, P.; Jin, H.; Matsuba, Y.; Itoh, A.; Yokota, T.; Hashizume, D.; Someya, T. Printable Elastic Conductors by *in Situ* Formation of Silver Nanoparticles from Silver Flakes. *Nat. Mater.* **2017**, *16*, 834–840.
- (122) Jung, D.; Lim, C.; Shim, H. J.; Kim, Y.; Park, C.; Jung, J.; Han, S. I.; Sunwoo, S.-H.; Cho, K. W.; Cha, G. D.; Kim, D. C.; Koo, J. H.; Kim, J. H.; Hyeon, T.; Kim, D.-H. Highly Conductive and Elastic Nanomembrane for Skin Electronics. *Science* **2021**, *373*, 1022–1026.
- (123) Kim, D.-H.; Lu, N.; Ma, R.; Kim, Y.-S.; Kim, R.-H.; Wang, S.; Wu, J.; Won, S. M.; Tao, H.; Islam, A.; Yu, K. J.; Kim, T.; Chowdhury, R.; Ying, M.; Xu, L.; Li, M.; Chung, H.-J.; Keum, H.; McCormick, M.; Liu, P.; Zhang, Y.-W.; Omenetto, F. G.; Huang, Y.; Coleman, T.; Rogers, J. A. Epidermal Electronics. *Science* **2011**, *333*, 838–843.

- (124) Bandodkar, A. J.; Jia, W.; Yardimci, C.; Wang, X.; Ramirez, J.; Wang, J. Tattoo-Based Noninvasive Glucose Monitoring: A Proof-of-Concept Study. *Anal. Chem.* **2015**, *87*, 394–398.
- (125) Lee, S.; Reuveny, A.; Reeder, J.; Lee, S.; Jin, H.; Liu, Q.; Yokota, T.; Sekitani, T.; Ioyama, T.; Abe, Y.; Suo, Z.; Someya, T. A Transparent Bending-Insensitive Pressure Sensor. *Nat. Nanotechnol.* **2016**, *11*, 472–478.
- (126) Lipomi, D. J.; Vosgueritchian, M.; Tee, B. C.-K.; Hellstrom, S. L.; Lee, J. A.; Fox, C. H.; Bao, Z. Skin-like Pressure and Strain Sensors Based on Transparent Elastic Films of Carbon Nanotubes. *Nat. Nanotechnol.* **2011**, *6*, 788–792.
- (127) Cui, N.; Song, Y.; Tan, C.-H.; Zhang, K.; Yang, X.; Dong, S.; Xie, B.; Huang, F. Stretchable Transparent Electrodes for Conformable Wearable Organic Photovoltaic Devices. *npj Flex. Electron.* **2021**, *5*, 31.
- (128) Jiang, N.; Chang, X.; Hu, D.; Chen, L.; Wang, Y.; Chen, J.; Zhu, Y. Flexible, Transparent, and Antibacterial Ionogels toward Highly Sensitive Strain and Temperature Sensors. *Chem. Eng. J.* **2021**, *424*, 130418.
- (129) Kim, D.-H.; Viventi, J.; Amsden, J. J.; Xiao, J.; Vigeland, L.; Kim, Y.-S.; Blanco, J. A.; Panilaitis, B.; Frechette, E. S.; Contreras, D.; Kaplan, D. L.; Omenetto, F. G.; Huang, Y.; Hwang, K.-C.; Zakin, M. R.; Litt, B.; Rogers, J. A. Dissolvable Films of Silk Fibroin for Ultrathin Conformal Bio-Integrated Electronics. *Nat. Mater.* **2010**, *9*, 511–517.
- (130) Schwartz, G.; Tee, B. C.-K.; Mei, J.; Appleton, A. L.; Kim, D. H.; Wang, H.; Bao, Z. Flexible Polymer Transistors with High Pressure Sensitivity for Application in Electronic Skin and Health Monitoring. *Nat. Commun.* **2013**, *4*, 1859.
- (131) Wang, C.; Li, X.; Hu, H.; Zhang, L.; Huang, Z.; Lin, M.; Zhang, Z.; Yin, Z.; Huang, B.; Gong, H.; Bhaskaran, S.; Gu, Y.; Makihata, M.; Guo, Y.; Lei, Y.; Chen, Y.; Wang, C.; Li, Y.; Zhang, T.; Chen, Z.; Pisano, A. P.; Zhang, L.; Zhou, Q.; Xu, S. Monitoring of the Central Blood Pressure Waveform via a Conformal Ultrasonic Device. *Nat. Biomed. Eng.* **2018**, *2*, 687–695.
- (132) Wang, C.; Chen, X.; Wang, L.; Makihata, M.; Liu, H.-C.; Zhou, T.; Zhao, X. Bioadhesive Ultrasound for Long-Term Continuous Imaging of Diverse Organs. *Science* **2022**, *377*, 517–523.
- (133) Wang, S.; Xu, J.; Wang, W.; Wang, G.-J. N.; Rastak, R.; Molina-Lopez, F.; Chung, J. W.; Niu, S.; Feig, V. R.; Lopez, J.; Lei, T.; Kwon, S.-K.; Kim, Y.; Foudeh, A. M.; Ehrlich, A.; Gasperini, A.; Yun, Y.; Murmann, B.; Tok, J. B.-H.; Bao, Z. Skin Electronics from Scalable Fabrication of an Intrinsically Stretchable Transistor Array. *Nature* **2018**, *555*, 83–88.
- (134) Sim, K.; Chen, S.; Li, Z.; Rao, Z.; Liu, J.; Lu, Y.; Jang, S.; Ershad, F.; Chen, J.; Xiao, J.; Yu, C. Three-Dimensional Curvy Electronics Created Using Conformal Additive Stamp Printing. *Nat. Electron.* **2019**, *2*, 471–479.
- (135) Bariya, M.; Shahpar, Z.; Park, H.; Sun, J.; Jung, Y.; Gao, W.; Nyein, H. Y. Y.; Liaw, T. S.; Tai, L.-C.; Ngo, Q. P.; Chao, M.; Zhao, Y.; Hettick, M.; Cho, G.; Javey, A. Roll-to-Roll Gravure Printed Electrochemical Sensors for Wearable and Medical Devices. *ACS Nano* **2018**, *12*, 6978–6987.
- (136) Valentine, A. D.; Busbee, T. A.; Boley, J. W.; Raney, J. R.; Chortos, A.; Kotikian, A.; Berrigan, J. D.; Durstock, M. F.; Lewis, J. A. Hybrid 3D Printing of Soft Electronics. *Adv. Mater.* **2017**, *29*, 1703817.
- (137) Yu, Y.; Li, J.; Solomon, S. A.; Min, J.; Tu, J.; Guo, W.; Xu, C.; Song, Y.; Gao, W. All-Printed Soft Human-Machine Interface for Robotic Physicochemical Sensing. *Sci. Robot.* **2022**, *7*, No. eabn0495.
- (138) Imani, S.; Bandodkar, A. J.; Mohan, A. M. V.; Kumar, R.; Yu, S.; Wang, J.; Mercier, P. P. A Wearable Chemical-Electrophysiological Hybrid Biosensing System for Real-Time Health and Fitness Monitoring. *Nat. Commun.* **2016**, *7*, 11650.
- (139) Bakker, E.; Bühlmann, P.; Pretsch, E. Carrier-Based Ion-Selective Electrodes and Bulk Optodes. 1. General Characteristics. *Chem. Rev.* **1997**, *97*, 3083–3132.
- (140) Bakker, E.; Pretsch, E. Potentiometric Sensors for Trace-Level Analysis. *Trends Anal. Chem.* **2005**, *24*, 199–207.
- (141) Li, X.-G.; Feng, H.; Huang, M.-R.; Gu, G.-L.; Moloney, M. G. Ultrasensitive Pb(II) Potentiometric Sensor Based on Copolyaniline Nanoparticles in a Plasticizer-Free Membrane with a Long Lifetime. *Anal. Chem.* **2012**, *84*, 134–140.
- (142) Javanbakht, M.; Fard, S. E.; Mohammadi, A.; Abdouss, M.; Ganjali, M. R.; Norouzi, P.; Safaraliev, L. Molecularly Imprinted Polymer Based Potentiometric Sensor for the Determination of Hydroxyzine in Tablets and Biological Fluids. *Anal. Chim. Acta* **2008**, *612*, 65–74.
- (143) Alizadeh, T.; Akhoundian, M. A Novel Potentiometric Sensor for Promethazine Based on a Molecularly Imprinted Polymer (MIP): The Role of MIP Structure on the Sensor Performance. *Electrochim. Acta* **2010**, *55*, 3477–3485.
- (144) Liang, R.; Zhang, R.; Qin, W. Potentiometric Sensor Based on Molecularly Imprinted Polymer for Determination of Melamine in Milk. *Sens. Actuators B Chem.* **2009**, *141*, 544–550.
- (145) Schazmann, B.; Morris, D.; Slater, C.; Beirne, S.; Fay, C.; Reuveny, R.; Moyna, N.; Diamond, D. A Wearable Electrochemical Sensor for the Real-Time Measurement of Sweat Sodium Concentration. *Anal. Methods* **2010**, *2*, 342–348.
- (146) Bandodkar, A. J.; Hung, V. W. S.; Jia, W.; Valdes-Ramirez, G.; Windmiller, J. R.; Martinez, A. G.; Ramirez, J.; Chan, G.; Kerman, K.; Wang, J. Tattoo-Based Potentiometric Ion-Selective Sensors for Epidermal pH Monitoring. *Analyst* **2013**, *138*, 123–128.
- (147) Nyein, H. Y. Y.; Gao, W.; Shahpar, Z.; Emaminejad, S.; Challa, S.; Chen, K.; Fahad, H. M.; Tai, L.-C.; Ota, H.; Davis, R. W.; Javey, A. A Wearable Electrochemical Platform for Noninvasive Simultaneous Monitoring of Ca<sup>2+</sup> and pH. *ACS Nano* **2016**, *10*, 7216–7224.
- (148) Anastasova, S.; Crewther, B.; Bemnowicz, P.; Curto, V.; Ip, H. M.; Rosa, B.; Yang, G.-Z. A Wearable Multisensing Patch for Continuous Sweat Monitoring. *Bios. Bioelectron.* **2017**, *93*, 139–145.
- (149) Gupta, V. K.; Kumar, S.; Singh, R.; Singh, L. P.; Shoor, S. K.; Sethi, B. Cadmium (II) Ion Sensing through p-Tert-Butyl Calix[6]-Arene Based Potentiometric Sensor. *J. Mol. Liq.* **2014**, *195*, 65–68.
- (150) Hu, J.; Stein, A.; Bühlmann, P. Rational Design of All-Solid-State Ion-Selective Electrodes and Reference Electrodes. *Trends Anal. Chem.* **2016**, *76*, 102–114.
- (151) Guinovart, T.; Crespo, G. A.; Rius, F. X.; Andrade, F. J. A Reference Electrode Based on Polyvinyl Butyral (PVB) Polymer for Decentralized Chemical Measurements. *Anal. Chim. Acta* **2014**, *821*, 72–80.
- (152) Bandodkar, A. J.; Molinnus, D.; Mirza, O.; Guinovart, T.; Windmiller, J. R.; Valdés-Ramírez, G.; Andrade, F. J.; Schöning, M. J.; Wang, J. Epidermal Tattoo Potentiometric Sodium Sensors with Wireless Signal Transduction for Continuous Non-Invasive Sweat Monitoring. *Biosens. Bioelectron.* **2014**, *54*, 603–609.
- (153) Guinovart, T.; Bandodkar, A. J.; Windmiller, J. R.; Andrade, F. J.; Wang, J. A Potentiometric Tattoo Sensor for Monitoring Ammonium in Sweat. *Analyst* **2013**, *138*, 7031–7038.
- (154) Wang, S.; Wu, Y.; Gu, Y.; Li, T.; Luo, H.; Li, L.-H.; Bai, Y.; Li, L.; Liu, L.; Cao, Y.; Ding, H.; Zhang, T. Wearable Sweatband Sensor Platform Based on Gold Nanodendrite Array as Efficient Solid Contact of Ion-Selective Electrode. *Anal. Chem.* **2017**, *89*, 10224–10231.
- (155) Parrilla, M.; Cuartero, M.; Crespo, G. A. Wearable Potentiometric Ion Sensors. *Trends Anal. Chem.* **2019**, *110*, 303–320.
- (156) Jaworska, E.; Mazur, M.; Maksymiuk, K.; Michalska, A. Fate of Poly(3-Octylthiophene) Transducer in Solid Contact Ion-Selective Electrodes. *Anal. Chem.* **2018**, *90*, 2625–2630.
- (157) Manjakkal, L.; Dervin, S.; Dahiya, R. Flexible Potentiometric pH Sensors for Wearable Systems. *RSC Adv.* **2020**, *10*, 8594–8617.
- (158) Bobacka, J. Conducting Polymer-Based Solid-State Ion-Selective Electrodes. *Electroanalysis* **2006**, *18*, 7–18.
- (159) Fibbioli, M.; Bandyopadhyay, K.; Liu, S.-G.; Echegoyen, L.; Enger, O.; Diederich, F.; Bühlmann, P.; Pretsch, E. Redox-Active Self-Assembled Monolayers as Novel Solid Contacts for Ion-Selective Electrodes. *Chem. Commun.* **2000**, *0*, 339–340.
- (160) Fibbioli, M.; Bandyopadhyay, K.; Liu, S.-G.; Echegoyen, L.; Enger, O.; Diederich, F.; Gingery, D.; Bühlmann, P.; Persson, H.;

- Suter, U. W.; Pretsch, E. Redox-Active Self-Assembled Monolayers for Solid-Contact Polymeric Membrane Ion-Selective Electrodes. *Chem. Mater.* **2002**, *14*, 1721–1729.
- (161) Grygolowicz-Pawlak, E.; Wyglądacz, K.; Sęk, S.; Bilewicz, R.; Brzózka, Z.; Malinowska, E. Studies on Ferrocene Organothiols Monolayer as an Intermediate Phase of Potentiometric Sensors with Gold Inner Contact. *Sens. Actuators B Chem.* **2005**, *111–112*, 310–316.
- (162) Grygolowicz-Pawlak, E.; Plachecka, K.; Brzózka, Z.; Malinowska, E. Further Studies on the Role of Redox-Active Monolayer as Intermediate Phase of Solid-State Sensors. *Sens. Actuators B Chem.* **2007**, *123*, 480–487.
- (163) Machado, A. A. S. C. Conductive Epoxy-Based Ion-Selective Electrodes. A Review. *Analyst* **1994**, *119*, 2263–2274.
- (164) Samsonova, E. N.; Lutov, V. M.; Mikhelson, K. N. Solid-Contact Ionophore-Based Electrode for Determination of pH in Acidic Media. *J. Solid State Electrochem.* **2009**, *13*, 69–75.
- (165) Gabrielli, C.; Hémeury, P.; Liatsi, P.; Masure, M.; Perrot, H. An Electrogravimetric Study of an All-Solid-State Potassium Selective Electrode with Prussian Blue as the Electroactive Solid Internal Contact. *J. Electrochem. Soc.* **2005**, *152*, H219.
- (166) Zou, X. U.; Cheong, J. H.; Taitt, B. J.; Bühlmann, P. Solid Contact Ion-Selective Electrodes with a Well-Controlled Co(II)/Co(III) Redox Buffer Layer. *Anal. Chem.* **2013**, *85*, 9350–9355.
- (167) Ishige, Y.; Klink, S.; Schuhmann, W. Intercalation Compounds as Inner Reference Electrodes for Reproducible and Robust Solid-Contact Ion-Selective Electrodes. *Angew. Chem., Int. Ed. Engl.* **2016**, *55*, 4831–4835.
- (168) Fouskaki, M.; Chaniotakis, N. Fullerene-Based Electrochemical Buffer Layer for Ion-Selective Electrodes. *Analyst* **2008**, *133*, 1072–1075.
- (169) Li, J.; Yin, T.; Qin, W. An All-Solid-State Polymeric Membrane Pb<sup>2+</sup>-Selective Electrode with Bimodal Pore C<sub>60</sub> as Solid Contact. *Anal. Chim. Acta* **2015**, *876*, 49–54.
- (170) Crespo, G. A.; Macho, S.; Rius, F. X. Ion-Selective Electrodes Using Carbon Nanotubes as Ion-to-Electron Transducers. *Anal. Chem.* **2008**, *80*, 1316–1322.
- (171) Crespo, G. A.; Gugs, D.; Macho, S.; Rius, F. X. Solid-Contact PH-Selective Electrode Using Multi-Walled Carbon Nanotubes. *Bioanal. Chem.* **2009**, *395*, 2371–2376.
- (172) Parra, E. J.; Crespo, G. A.; Riu, J.; Ruiz, A.; Rius, F. X. Ion-Selective Electrodes Using Multi-Walled Carbon Nanotubes as Ion-to-Electron Transducers for the Detection of Perchlorate. *Analyst* **2009**, *134*, 1905–1910.
- (173) Ping, J.; Wang, Y.; Wu, J.; Ying, Y. Development of an All-Solid-State Potassium Ion-Selective Electrode Using Graphene as the Solid-Contact Transducer. *Electrochem. Commun.* **2011**, *13*, 1529–1532.
- (174) Ping, J.; Wang, Y.; Ying, Y.; Wu, J. Application of Electrochemically Reduced Graphene Oxide on Screen-Printed Ion-Selective Electrode. *Anal. Chem.* **2012**, *84*, 3473–3479.
- (175) Ping, J.; Wang, Y.; Fan, K.; Tang, W.; Wu, J.; Ying, Y. High-Performance Flexible Potentiometric Sensing Devices Using Free-Standing Graphene Paper. *J. Mater. Chem. B* **2013**, *1*, 4781–4791.
- (176) Paczosa-Bator, B.; Cabaj, L.; Piech, R.; Skupień, K. Platinum Nanoparticles Intermediate Layer in Solid-State Selective Electrodes. *Analyst* **2012**, *137*, 5272–5277.
- (177) Paczosa-Bator, B.; Cabaj, L.; Piech, R.; Skupień, K. Potentiometric Sensors with Carbon Black Supporting Platinum Nanoparticles. *Anal. Chem.* **2013**, *85*, 10255–10261.
- (178) Zeng, X.; Qin, W. A Solid-Contact Ca<sup>2+</sup>-Selective Electrode Based on an Inorganic Redox Buffer of Ag@AgCl/1-Tetradecyl-3-Methylimidazolium Chloride as Ion-to-Electron Transducer. *Talanta* **2020**, *209*, 120570.
- (179) Mendecki, L.; Mirica, K. A. Conductive Metal-Organic Frameworks as Ion-to-Electron Transducers in Potentiometric Sensors. *ACS Appl. Mater. Interfaces* **2018**, *10*, 19248–19257.
- (180) Bühlmann, P.; Umezawa, Y.; Rondinini, S.; Vertova, A.; Pigiucci, A.; Bertesago, L. Lifetime of Ion-Selective Electrodes Based on Charged Ionophores. *Anal. Chem.* **2000**, *72*, 1843–1852.
- (181) Kisiel, A.; Kaluza, D.; Paterczyk, B.; Maksymiuk, K.; Michalska, A. Quantifying Plasticizer Leakage from Ion-Selective Membranes - a Nanosponge Approach. *Analyst* **2020**, *145*, 2966–2974.
- (182) De Marco, R.; Veder, J.-P.; Clarke, G.; Nelson, A.; Prince, K.; Pretsch, E.; Bakker, E. Evidence of a Water Layer in Solid-Contact Polymeric Ion Sensors. *Phys. Chem. Chem. Phys.* **2008**, *10*, 73–76.
- (183) Veder, J.-P.; De Marco, R.; Clarke, G.; Chester, R.; Nelson, A.; Prince, K.; Pretsch, E.; Bakker, E. Elimination of Undesirable Water Layers in Solid-Contact Polymeric Ion-Selective Electrodes. *Anal. Chem.* **2008**, *80*, 6731–6740.
- (184) Shao, Y.; Ying, Y.; Ping, J. Recent Advances in Solid-Contact Ion-Selective Electrodes: Functional Materials, Transduction Mechanisms, and Development Trends. *Chem. Soc. Rev.* **2020**, *49*, 4405–4465.
- (185) Vorotyntsev, M. A.; Heinze, J. Charging Process in Electron Conducting Polymers: Dimerization Model. *Electrochim. Acta* **2001**, *46*, 3309–3324.
- (186) Yeung, K. K.; Huang, T.; Hua, Y.; Zhang, K.; Yuen, M. M. F.; Gao, Z. Recent Advances in Electrochemical Sensors for Wearable Sweat Monitoring: A Review. *IEEE Sens. J.* **2021**, *21*, 14522–14539.
- (187) Cheng, X.; Wang, B.; Zhao, Y.; Hojaiji, H.; Lin, S.; Shih, R.; Lin, H.; Tamayosa, S.; Ham, B.; Stout, P.; Salahi, K.; Wang, Z.; Zhao, C.; Tan, J.; Emaminejad, S. A Mediator-Free Electroenzymatic Sensing Methodology to Mitigate Ionic and Electroactive Interferents' Effects for Reliable Wearable Metabolite and Nutrient Monitoring. *Adv. Funct. Mater.* **2020**, *30*, 1908507.
- (188) Lin, Y.; Bariya, M.; Nyein, H. Y. Y.; Kivimäki, L.; Uusitalo, S.; Jansson, E.; Ji, W.; Yuan, Z.; Happonen, T.; Liedert, C.; Hiltunen, J.; Fan, Z.; Javey, A. Porous Enzymatic Membrane for Nanotextured Glucose Sweat Sensors with High Stability toward Reliable Non-invasive Health Monitoring. *Adv. Funct. Mater.* **2019**, *29*, 1902521.
- (189) Jia, W.; Bandodkar, A. J.; Valdés-Ramírez, G.; Windmiller, J. R.; Yang, Z.; Ramírez, J.; Chan, G.; Wang, J. Electrochemical Tattoo Biosensors for Real-Time Noninvasive Lactate Monitoring in Human Perspiration. *Anal. Chem.* **2013**, *85*, 6553–6560.
- (190) Kim, J.; Jeerapan, I.; Imani, S.; Cho, T. N.; Bandodkar, A.; Cinti, S.; Mercier, P. P.; Wang, J. Noninvasive Alcohol Monitoring Using a Wearable Tattoo-Based Ionophoretic-Biosensing System. *ACS Sens.* **2016**, *1*, 1011–1019.
- (191) Sempionatto, J. R.; Khorshed, A. A.; Ahmed, A.; De Loyola e Silva, A. N.; Barfidokht, A.; Yin, L.; Goud, K. Y.; Mohamed, M. A.; Bailey, E.; May, J.; Aebischer, C.; Chatelle, C.; Wang, J. Epidermal Enzymatic Biosensors for Sweat Vitamin C: Toward Personalized Nutrition. *ACS Sens.* **2020**, *5*, 1804–1813.
- (192) Tai, L.-C.; Liaw, T. S.; Lin, Y.; Nyein, H. Y. Y.; Bariya, M.; Ji, W.; Hettick, M.; Zhao, C.; Zhao, J.; Hou, L.; Yuan, Z.; Fan, Z.; Javey, A. Wearable Sweat Band for Noninvasive Levodopa Monitoring. *Nano Lett.* **2019**, *19*, 6346–6351.
- (193) Tai, L.-C.; Ahn, C. H.; Nyein, H. Y. Y.; Ji, W.; Bariya, M.; Lin, Y.; Li, L.; Javey, A. Nicotine Monitoring with a Wearable Sweat Band. *ACS Sens.* **2020**, *5*, 1831–1837.
- (194) Karyakin, A. A.; Karyakina, E. E.; Gorton, L. On the Mechanism of H<sub>2</sub>O<sub>2</sub> Reduction at Prussian Blue Modified Electrodes. *Electrochem. Commun.* **1999**, *1*, 78–82.
- (195) Besteman, K.; Lee, J.-O.; Wiertz, F. G. M.; Heering, H. A.; Dekker, C. Enzyme-Coated Carbon Nanotubes as Single-Molecule Biosensors. *Nano Lett.* **2003**, *3*, 727–730.
- (196) Xia, H.; Tang, H.; Zhou, B.; Li, Y.; Zhang, X.; Shi, Z.; Deng, L.; Song, R.; Li, L.; Zhang, Z.; Zhou, J. Mediator-Free Electron-Transfer on Patternable Hierarchical Meso/Macro Porous Bienzyme Interface for Highly-Sensitive Sweat Glucose and Surface Electromyography Monitoring. *Sens. Actuators B Chem.* **2020**, *312*, 127962.
- (197) Paul, A.; Vyas, G.; Paul, P.; Srivastava, D. N. Gold-Nanoparticle-Encapsulated ZIF-8 for a Mediator-Free Enzymatic

- Glucose Sensor by Amperometry. *ACS Appl. Nano Mater.* **2018**, *1*, 3600–3607.
- (198) Lee, H.; Choi, T. K.; Lee, Y. B.; Cho, H. R.; Ghaffari, R.; Wang, L.; Choi, H. J.; Chung, T. D.; Lu, N.; Hyeon, T.; Choi, S. H.; Kim, D.-H. A Graphene-Based Electrochemical Device with Thermoresponsive Microneedles for Diabetes Monitoring and Therapy. *Nat. Nanotechnol.* **2016**, *11*, 566–572.
- (199) Zhao, Y.; Zhai, Q.; Dong, D.; An, T.; Gong, S.; Shi, Q.; Cheng, W. Highly Stretchable and Strain-Insensitive Fiber-Based Wearable Electrochemical Biosensor to Monitor Glucose in the Sweat. *Anal. Chem.* **2019**, *91*, 6569–6576.
- (200) He, W.; Wang, C.; Wang, H.; Jian, M.; Lu, W.; Liang, X.; Zhang, X.; Yang, F.; Zhang, Y. Integrated Textile Sensor Patch for Real-Time and Multiplex Sweat Analysis. *Sci. Adv.* **2019**, *5*, No. eaax0649.
- (201) Lei, Y.; Zhao, W.; Zhang, Y.; Jiang, Q.; He, J.-H.; Baumner, A. J.; Wolfbeis, O. S.; Wang, Z. L.; Salama, K. N.; Alshareef, H. N. A MXene-Based Wearable Biosensor System for High-Performance In Vitro Perspiration Analysis. *Small* **2019**, *15*, 1901190.
- (202) Karyakin, A. A. Prussian Blue and Its Analogues: Electrochemistry and Analytical Applications. *Electroanalysis* **2001**, *13*, 813–819.
- (203) del Río, J. S.; Henry, O. Y. F.; Jolly, P.; Ingber, D. E. An Antifouling Coating That Enables Affinity-Based Electrochemical Biosensing in Complex Biological Fluids. *Nat. Nanotechnol.* **2019**, *14*, 1143–1149.
- (204) Xuan, X.; Pérez-Ràfols, C.; Chen, C.; Cuartero, M.; Crespo, G. A. Lactate Biosensing for Reliable On-Body Sweat Analysis. *ACS Sens.* **2021**, *6*, 2763–2771.
- (205) Lin, S.; Cheng, X.; Zhu, J.; Wang, B.; Jelinek, D.; Zhao, Y.; Wu, T.-Y.; Horrillo, A.; Tan, J.; Yeung, J.; Yan, W.; Forman, S.; Coller, H. A.; Milla, C.; Emaminejad, S. Wearable Microneedle-Based Electrochemical Aptamer Biosensing for Precision Dosing of Drugs with Narrow Therapeutic Windows. *Sci. Adv.* **2022**, *8*, No. eabq4539.
- (206) Tai, L.-C.; Gao, W.; Chao, M.; Bariya, M.; Ngo, Q. P.; Shahpar, Z.; Nyein, H. Y. Y.; Park, H.; Sun, J.; Jung, Y.; Wu, E.; Fahad, H. M.; Lien, D.-H.; Ota, H.; Cho, G.; Javey, A. Methylxanthine Drug Monitoring with Wearable Sweat Sensors. *Adv. Mater.* **2018**, *30*, 1707442.
- (207) Schwerdt, H. N.; Zhang, E.; Kim, M. J.; Yoshida, T.; Stanwicks, L.; Amemori, S.; Dagdeviren, H. E.; Langer, R.; Cima, M. J.; Graybiel, A. M. Cellular-Scale Probes Enable Stable Chronic Subsecond Monitoring of Dopamine Neurochemicals in a Rodent Model. *Commun. Biol.* **2018**, *1*, 144.
- (208) Bard, A. J.; Faulkner, L. R. *Electrochemical Methods: Fundamentals and Applications*, 2nd ed.; Wiley, 2002; Vol. 38, pp 1364–1365.
- (209) Laborda, E.; González, J.; Molina, A. Recent Advances on the Theory of Pulse Techniques: A Mini Review. *Electrochem. Commun.* **2014**, *43*, 25–30.
- (210) Sanghavi, B. J.; Varhue, W.; Chávez, J. L.; Chou, C.-F.; Swami, N. S. Electrokinetic Preconcentration and Detection of Neuropeptides at Patterned Graphene-Modified Electrodes in a Nanochannel. *Anal. Chem.* **2014**, *86*, 4120–4125.
- (211) Gao, W.; Nyein, H. Y. Y.; Shahpar, Z.; Fahad, H. M.; Chen, K.; Emaminejad, S.; Gao, Y.; Tai, L.-C.; Ota, H.; Wu, E.; Bullock, J.; Zeng, Y.; Lien, D.-H.; Javey, A. Wearable Microsensor Array for Multiplexed Heavy Metal Monitoring of Body Fluids. *ACS Sens.* **2016**, *1*, 866–874.
- (212) Feig, D. I.; Kang, D.-H.; Johnson, R. J. Uric Acid and Cardiovascular Risk. *N. Engl. J. Med.* **2008**, *359*, 1811–1821.
- (213) Russo, P. A.; Mitchell, G. A.; Tanguay, R. M. Tyrosinemia: A Review. *Pediatr. Dev. Pathol.* **2001**, *4*, 212–221.
- (214) Tchounwou, P. B.; Yedjou, C. G.; Patlolla, A. K.; Sutton, D. J. Heavy Metal Toxicity and the Environment. *Molecular, Clinical and Environmental Toxicology: Volume 3: Environmental Toxicology* **2012**, *101*, 133–164.
- (215) Hubbard, A. T.; Stickney, J. L.; Soriaga, M. P.; Chia, V. K. F.; Rosasco, S. D.; Schardt, B. C.; Solomun, T.; Song, D.; White, J. H.; Wieckowski, A. Electrochemical Processes at Well-Defined Surfaces. *J. Electroanal. Chem. Interfacial Electrochem.* **1984**, *168*, 43–66.
- (216) Sánchez-Cortés, S.; Francioso, O.; Garcia-Ramos, J. V.; Ciavatta, C.; Gessa, C. Catechol Polymerization in the Presence of Silver Surface. *Colloids Surf. A Physicochem. Eng. Asp.* **2001**, *176*, 177–184.
- (217) Cooper, S. E.; Venton, B. J. Fast-Scan Cyclic Voltammetry for the Detection of Tyramine and Octopamine. *Anal. Bioanal. Chem.* **2009**, *394*, 329–336.
- (218) Li, M.-Z.; Han, S.-T.; Zhou, Y. Recent Advances in Flexible Field-Effect Transistors toward Wearable Sensors. *Adv. Intell. Syst.* **2020**, *2*, 2000113.
- (219) Nakata, S.; Shiomi, M.; Fujita, Y.; Arie, T.; Akita, S.; Takei, K. A Wearable pH Sensor with High Sensitivity Based on a Flexible Charge-Coupled Device. *Nat. Electron.* **2018**, *1*, 596.
- (220) Garcia-Cordero, E.; Bellando, F.; Zhang, J.; Wildhaber, F.; Longo, J.; Guérin, H.; Ionescu, A. M. Three-Dimensional Integrated Ultra-Low-Volume Passive Microfluidics with Ion-Sensitive Field-Effect Transistors for Multiparameter Wearable Sweat Analyzers. *ACS Nano* **2018**, *12*, 12646–12656.
- (221) Liu, Q.; Liu, Y.; Wu, F.; Cao, X.; Li, Z.; Alharbi, M.; Abbas, A. N.; Amer, M. R.; Zhou, C. Highly Sensitive and Wearable In2O3 Nanoribbon Transistor Biosensors with Integrated On-Chip Gate for Glucose Monitoring in Body Fluids. *ACS Nano* **2018**, *12*, 1170–1178.
- (222) Ohayon, D.; Nikiforidis, G.; Savva, A.; Giugni, A.; Wustoni, S.; Palanisamy, T.; Chen, X.; Maria, I. P.; Di Fabrizio, E.; Costa, P. M. F. J.; McCulloch, I.; Inal, S. Biofuel Powered Glucose Detection in Bodily Fluids with an N-Type Conjugated Polymer. *Nat. Mater.* **2020**, *19*, 456–463.
- (223) Liao, C.; Mak, C.; Zhang, M.; Chan, H. L. W.; Yan, F. Flexible Organic Electrochemical Transistors for Highly Selective Enzyme Biosensors and Used for Saliva Testing. *Adv. Mater.* **2015**, *27*, 676–681.
- (224) Minami, T.; Sato, T.; Minamiki, T.; Fukuda, K.; Kumaki, D.; Tokito, S. A Novel OFET-Based Biosensor for the Selective and Sensitive Detection of Lactate Levels. *Biosens. Bioelectron.* **2015**, *74*, 45–48.
- (225) Pappa, A. M.; Ohayon, D.; Giovannitti, A.; Maria, I. P.; Savva, A.; Uguz, I.; Rivnay, J.; McCulloch, I.; Owens, R. M.; Inal, S. Direct Metabolite Detection with an N-Type Accumulation Mode Organic Electrochemical Transistor. *Sci. Adv.* **2018**, *4*, No. eaat0911.
- (226) Torsi, L.; Magliulo, M.; Manoli, K.; Palazzo, G. Organic Field-Effect Transistor Sensors: A Tutorial Review. *Chem. Soc. Rev.* **2013**, *42*, 8612–8628.
- (227) Shim, H.; Ershad, F.; Patel, S.; Zhang, Y.; Wang, B.; Chen, Z.; Marks, T. J.; Facchetti, A.; Yu, C. An Elastic and Reconfigurable Synaptic Transistor Based on a Stretchable Bilayer Semiconductor. *Nat. Electron.* **2022**, *5*, 660–671.
- (228) Sim, K.; Ershad, F.; Zhang, Y.; Yang, P.; Shim, H.; Rao, Z.; Lu, Y.; Thukral, A.; Elgalad, A.; Xi, Y.; Tian, B.; Taylor, D. A.; Yu, C. An Epicardial Bioelectronic Patch Made from Soft Rubbery Materials and Capable of Spatiotemporal Mapping of Electrophysiological Activity. *Nat. Electron.* **2020**, *3*, 775–784.
- (229) Park, S.; Liao, Z.; Ibarlucea, B.; Qi, H.; Lin, H.-H.; Becker, D.; Melidonie, J.; Zhang, T.; Sahabudeen, H.; Baraban, L.; Baek, C.-K.; Zheng, Z.; Zschech, E.; Fery, A.; Heine, T.; Kaiser, U.; Cuniberti, G.; Dong, R.; Feng, X. Two-Dimensional Boronate Ester Covalent Organic Framework Thin Films with Large Single Crystalline Domains for a Neuromorphic Memory Device. *Angew. Chem., Int. Ed.* **2020**, *59*, 8218–8224.
- (230) Yokota, T.; Nakamura, T.; Kato, H.; Mochizuki, M.; Tada, M.; Uchida, M.; Lee, S.; Koizumi, M.; Yukita, W.; Takimoto, A.; Someya, T. A Conformable Imager for Biometric Authentication and Vital Sign Measurement. *Nat. Electron.* **2020**, *3*, 113–121.
- (231) Khodagholy, D.; Curto, V. F.; Fraser, K. J.; Gurfinkel, M.; Byrne, R.; Diamond, D.; Malliaras, G. G.; Benito-Lopez, F.; Owens, R. M. Organic Electrochemical Transistor Incorporating an Ionogel as a Solid State Electrolyte for Lactate Sensing. *J. Mater. Chem.* **2012**, *22*, 4440–4443.

- (232) Ghittorelli, M.; Lingstedt, L.; Romele, P.; Crăciun, N. I.; Kovács-Vajna, Z. M.; Blom, P. W. M.; Torricelli, F. High-Sensitivity Ion Detection at Low Voltages with Current-Driven Organic Electrochemical Transistors. *Nat. Commun.* **2018**, *9*, 1441.
- (233) Noriega, R.; Rivnay, J.; Vandewal, K.; Koch, F. P. V.; Stingselin, N.; Smith, P.; Toney, M. F.; Salleo, A. A General Relationship between Disorder, Aggregation and Charge Transport in Conjugated Polymers. *Nat. Mater.* **2013**, *12*, 1038–1044.
- (234) Trovato, V.; Sfameni, S.; Rando, G.; Rosace, G.; Libertino, S.; Ferri, A.; Plutino, M. R. A Review of Stimuli-Responsive Smart Materials for Wearable Technology in Healthcare: Retrospective, Perspective, and Prospective. *Molecules* **2022**, *27*, 5709.
- (235) Reeder, J. T.; Choi, J.; Xue, Y.; Gutruf, P.; Hanson, J.; Liu, M.; Ray, T.; Bandothkar, A. J.; Avila, R.; Xia, W.; Krishnan, S.; Xu, S.; Barnes, K.; Pahnke, M.; Ghaffari, R.; Huang, Y.; Rogers, J. A. Waterproof, Electronics-Enabled, Epidermal Microfluidic Devices for Sweat Collection, Biomarker Analysis, and Thermography in Aquatic Settings. *Sci. Adv.* **2019**, *5*, No. eaau6356.
- (236) He, X.; Xu, T.; Gu, Z.; Gao, W.; Xu, L.-P.; Pan, T.; Zhang, X. Flexible and Superwetable Bands as a Platform toward Sweat Sampling and Sensing. *Anal. Chem.* **2019**, *91*, 4296–4300.
- (237) Bandothkar, A. J.; Gutruf, P.; Choi, J.; Lee, K.; Sekine, Y.; Reeder, J. T.; Jeang, W. J.; Aranyosi, A. J.; Lee, S. P.; Model, J. B.; Ghaffari, R.; Su, C.-J.; Leshock, J. P.; Ray, T.; Verrillo, A.; Thomas, K.; Krishnamurthi, V.; Han, S.; Kim, J.; Krishnan, S.; Hang, T.; Rogers, J. A. Battery-Free, Skin-Interfaced Microfluidic/Electronic Systems for Simultaneous Electrochemical, Colorimetric, and Volumetric Analysis of Sweat. *Sci. Adv.* **2019**, *5*, No. eaav3294.
- (238) Wang, L.; Xu, T.; He, X.; Zhang, X. Flexible, Self-Healable, Adhesive and Wearable Hydrogel Patch for Colorimetric Sweat Detection. *J. Mater. Chem. C* **2021**, *9*, 14938–14945.
- (239) Koh, A.; Kang, D.; Xue, Y.; Lee, S.; Pielak, R. M.; Kim, J.; Hwang, T.; Min, S.; Banks, A.; Bastien, P.; Manco, M. C.; Wang, L.; Ammann, K. R.; Jang, K.-I.; Won, P.; Han, S.; Ghaffari, R.; Paik, U.; Slepian, M. J.; Balooch, G.; Huang, Y.; Rogers, J. A. A Soft, Wearable Microfluidic Device for the Capture, Storage, and Colorimetric Sensing of Sweat. *Sci. Transl. Med.* **2016**, *8*, 366ra165–366ra165.
- (240) Xiao, J.; Liu, Y.; Su, L.; Zhao, D.; Zhao, L.; Zhang, X. Microfluidic Chip-Based Wearable Colorimetric Sensor for Simple and Facile Detection of Sweat Glucose. *Anal. Chem.* **2019**, *91*, 14803–14807.
- (241) Jeon, H.-J.; Kim, H. S.; Chung, E.; Lee, D. Y. Nanozyme-Based Colorimetric Biosensor with a Systemic Quantification Algorithm for Noninvasive Glucose Monitoring. *Theranostics* **2022**, *12*, 6308–6338.
- (242) Chen, J.; Ma, Q.; Li, M.; Chao, D.; Huang, L.; Wu, W.; Fang, Y.; Dong, S. Glucose-Oxidase like Catalytic Mechanism of Noble Metal Nanozymes. *Nat. Commun.* **2021**, *12*, 3375.
- (243) Sengupta, P.; Pramanik, K.; Datta, P.; Sarkar, P. Chemically Modified Carbon Nitride-Chitin-Acetic Acid Hybrid as a Metal-Free Bifunctional Nanozyme Cascade of Glucose Oxidase-Peroxidase for “Click off” Colorimetric Detection of Peroxide and Glucose. *Biosens. Bioelectron.* **2020**, *154*, 112072.
- (244) Zheng, J.; Zhu, M.; Kong, J.; Li, Z.; Jiang, J.; Xi, Y.; Li, F. Microfluidic Paper-Based Analytical Device by Using Pt Nanoparticles as Highly Active Peroxidase Mimic for Simultaneous Detection of Glucose and Uric Acid with Use of a Smartphone. *Talanta* **2022**, *237*, 122954.
- (245) Sekine, Y.; Kim, S. B.; Zhang, Y.; Bandothkar, A. J.; Xu, S.; Choi, J.; Irie, M.; Ray, T. R.; Kohli, P.; Kozai, N.; Sugita, T.; Wu, Y.; Lee, K.; Lee, K.-T.; Ghaffari, R.; Rogers, J. A. A Fluorometric Skin-Interfaced Microfluidic Device and Smartphone Imaging Module for in Situ Quantitative Analysis of Sweat Chemistry. *Lab Chip* **2018**, *18*, 2178–2186.
- (246) Mogera, U.; Guo, H.; Namkoong, M.; Rahman, M. S.; Nguyen, T.; Tian, L. Wearable Plasmonic Paper-Based Microfluidics for Continuous Sweat Analysis. *Sci. Adv.* **2022**, *8*, No. eabn1736.
- (247) Wang, Y.; Zhao, C.; Wang, J.; Luo, X.; Xie, L.; Zhan, S.; Kim, J.; Wang, X.; Liu, X.; Ying, Y. Wearable Plasmonic-Metasurface Sensor for Noninvasive and Universal Molecular Fingerprint Detection on Biointerfaces. *Sci. Adv.* **2021**, *7*, No. eabe4553.
- (248) Zhou, Z.; Shu, T.; Sun, Y.; Si, H.; Peng, P.; Su, L.; Zhang, X. Luminescent Wearable Biosensors Based on Gold Nanocluster Networks for “Turn-on” Detection of Uric Acid, Glucose and Alcohol in Sweat. *Biosens. Bioelectron.* **2021**, *192*, 113530.
- (249) He, X.; Fan, C.; Luo, Y.; Xu, T.; Zhang, X. Flexible Microfluidic Nanoplasmonic Sensors for Refreshable and Portable Recognition of Sweat Biochemical Fingerprint. *npj Flex. Electron.* **2022**, *6*, 60.
- (250) Choi, J.; Xue, Y.; Xia, W.; Ray, T. R.; Reeder, J. T.; Bandothkar, A. J.; Kang, D.; Xu, S.; Huang, Y.; Rogers, J. A. Soft, Skin-Mounted Microfluidic Systems for Measuring Secretory Fluidic Pressures Generated at the Surface of the Skin by Eccrine Sweat Glands. *Lab Chip* **2017**, *17*, 2572–2580.
- (251) Choi, J.; Kang, D.; Han, S.; Kim, S. B.; Rogers, J. A. Thin, Soft, Skin-Mounted Microfluidic Networks with Capillary Bursting Valves for Chrono-Sampling of Sweat. *Adv. Healthc. Mater.* **2017**, *6*, 1601355.
- (252) Nyein, H. Y. Y.; Tai, L.-C.; Ngo, Q. P.; Chao, M.; Zhang, G. B.; Gao, W.; Bariya, M.; Bullock, J.; Kim, H.; Fahad, H. M.; Javey, A. A Wearable Microfluidic Sensing Patch for Dynamic Sweat Secretion Analysis. *ACS Sens.* **2018**, *3*, 944–952.
- (253) Nyein, H. Y. Y.; Bariya, M.; Tran, B.; Ahn, C. H.; Brown, B. J.; Ji, W.; Davis, N.; Javey, A. A Wearable Patch for Continuous Analysis of Thermoregulatory Sweat at Rest. *Nat. Commun.* **2021**, *12*, 1823.
- (254) Lin, H.; Yu, W.; Dios Suarez, J. E. D.; Athavan, H.; Wang, Y.; Yeung, C.; Lin, S.; Sankararaman, S.; Milla, C.; Emaminejad, S. Autonomous Wearable Sweat Rate Monitoring Based on Digitized Microbubble Detection. *Lab Chip* **2022**, *22*, 4267–4275.
- (255) Kwon, K.; Kim, J. U.; Deng, Y.; Krishnan, S. R.; Choi, J.; Jang, H.; Lee, K.; Su, C.-J.; Yoo, I.; Wu, Y.; Lipschultz, L.; Kim, J.-H.; Chung, T. S.; Wu, D.; Park, Y.; Kim, T.; Ghaffari, R.; Lee, S.; Huang, Y.; Rogers, J. A. An On-Skin Platform for Wireless Monitoring of Flow Rate, Cumulative Loss and Temperature of Sweat in Real Time. *Nat. Electron.* **2021**, *4*, 302–312.
- (256) Choi, D.-H.; Gonzales, M.; Kitchen, G. B.; Phan, D.-T.; Searson, P. C. A Capacitive Sweat Rate Sensor for Continuous and Real-Time Monitoring of Sweat Loss. *ACS Sens.* **2020**, *5*, 3821–3826.
- (257) Reeder, J. T.; Xue, Y.; Franklin, D.; Deng, Y.; Choi, J.; Prado, O.; Kim, R.; Liu, C.; Hanson, J.; Ciraldo, J.; Bandothkar, A. J.; Krishnan, S.; Johnson, A.; Patnaude, E.; Avila, R.; Huang, Y.; Rogers, J. A. Resettable Skin Interfaced Microfluidic Sweat Collection Devices with Chemesthetic Hydration Feedback. *Nat. Commun.* **2019**, *10*, 5513.
- (258) Scarpa, E.; Mastronardi, V. M.; Guido, F.; Algieri, L.; Qaltieri, A.; Fiammengo, R.; Rizzi, F.; De Vittorio, M. Wearable Piezoelectric Mass Sensor Based on pH Sensitive Hydrogels for Sweat pH Monitoring. *Sci. Rep.* **2020**, *10*, 10854.
- (259) Han, W.; He, H.; Zhang, L.; Dong, C.; Zeng, H.; Dai, Y.; Xing, L.; Zhang, Y.; Xue, X. A Self-Powered Wearable Noninvasive Electronic-Skin for Perspiration Analysis Based on Piezo-Biosensing Unit Matrix of Enzyme/ZnO Nanoarrays. *ACS Appl. Mater. Interfaces* **2017**, *9*, 29526–29537.
- (260) Kim, Y.; Suh, J. M.; Shin, J.; Liu, Y.; Yeon, H.; Qiao, K.; Kum, H. S.; Kim, C.; Lee, H. E.; Choi, C.; Kim, H.; Lee, D.; Lee, J.; Kang, J.-H.; Park, B.-I.; Kang, S.; Kim, J.; Kim, S.; Perozek, J. A.; Wang, K.; Park, Y.; Kishen, K.; Kong, L.; Palacios, T.; Park, J.; Park, M.-C.; Kim, H.; Lee, Y. S.; Lee, K.; Bae, S.-H.; Kong, W.; Han, J.; Kim, J. Chip-Less Wireless Electronic Skins by Remote Epitaxial Freestanding Compound Semiconductors. *Science* **2022**, *377*, 859–864.
- (261) Tu, J.; Torrente-Rodríguez, R. M.; Wang, M.; Gao, W. The Era of Digital Health: A Review of Portable and Wearable Affinity Biosensors. *Adv. Funct. Mater.* **2020**, *30*, 1906713.
- (262) Morales, M. A.; Halpern, J. M. Guide to Selecting a Biorecognition Element for Biosensors. *Bioconjugate Chem.* **2018**, *29*, 3231–3239.
- (263) Campuzano, S.; Yáñez-Sedeño, P.; Pingarrón, J. M. Electrochemical Bioaffinity Sensors for Salivary Biomarkers Detection. *Trends Anal. Chem.* **2017**, *86*, 14–24.

- (264) Chen, Y.-T.; Lee, Y.-C.; Lai, Y.-H.; Lim, J.-C.; Huang, N.-T.; Lin, C.-T.; Huang, J.-J. Review of Integrated Optical Biosensors for Point-of-Care Applications. *Biosensors* **2020**, *10*, 209.
- (265) Narita, F.; Wang, Z.; Kurita, H.; Li, Z.; Shi, Y.; Jia, Y.; Soutis, C. A Review of Piezoelectric and Magnetostrictive Biosensor Materials for Detection of COVID-19 and Other Viruses. *Adv. Mater.* **2021**, *33*, 2005448.
- (266) Lasia, A. Electrochemical Impedance Spectroscopy and Its Applications. In *Modern Aspects of Electrochemistry*; Conway, B. E., Bockris, J. O., White, R. E., Eds.; Modern Aspects of Electrochemistry; Springer US: Boston, MA, 2002; pp 143–248.
- (267) Chen, C.; Wang, J. Optical Biosensors: An Exhaustive and Comprehensive Review. *Analyst* **2020**, *145*, 1605–1628.
- (268) Sajid, M.; Kawde, A.-N.; Daud, M. Designs, Formats and Applications of Lateral Flow Assay: A Literature Review. *J. Saudi Chem. Soc.* **2015**, *19*, 689–705.
- (269) Shrivastav, A. M.; Cvelbar, U.; Abdulhalim, I. A Comprehensive Review on Plasmonic-based Biosensors used in Viral Diagnostics. *Commun. Biol.* **2021**, *4*, 70.
- (270) Liu, J.; Geng, Z.; Fan, Z.; Liu, J.; Chen, H. Point-of-Care Testing Based on Smartphone: The Current State-of-the-Art (2017–2018). *Biosens. Bioelectron.* **2019**, *132*, 17–37.
- (271) Rogers, K. R. Principles of Affinity-Based Biosensors. *Mol. Biotechnol.* **2000**, *14*, 109–129.
- (272) Satija, J.; Punjabi, N.; Mishra, D.; Mukherji, S. Plasmonic-ELISA: Expanding Horizons. *RSC Adv.* **2016**, *6*, 85440–85456.
- (273) Sia, S. K.; Kricka, L. J. Microfluidics and Point-of-Care Testing. *Lab Chip* **2008**, *8*, 1982–1983.
- (274) Vestergaard, M.; Keran, K.; Tamiya, E. An Overview of Label-Free Electrochemical Protein Sensors. *Sensors* **2007**, *7*, 3442–3458.
- (275) Panneer Selvam, A.; Muthukumar, S.; Kamakoti, V.; Prasad, S. A Wearable Biochemical Sensor for Monitoring Alcohol Consumption Lifestyle through Ethyl Glucuronide (EtG) Detection in Human Sweat. *Sci. Rep.* **2016**, *6*, 23111.
- (276) Munje, R. D.; Muthukumar, S.; Jagannath, B.; Prasad, S. A New Paradigm in Sweat Based Wearable Diagnostics Biosensors Using Room Temperature Ionic Liquids (RTILs). *Sci. Rep.* **2017**, *7*, 1950.
- (277) Jagannath, B.; Lin, K.-C.; Pali, M.; Sankhala, D.; Muthukumar, S.; Prasad, S. A Sweat-Based Wearable Enabling Technology for Real-Time Monitoring of IL-1 $\beta$  and CRP as Potential Markers for Inflammatory Bowel Disease. *Inflamm. Bowel Dis.* **2020**, *26*, 1533–1542.
- (278) Jagannath, B.; Lin, K.-C.; Pali, M.; Sankhala, D.; Muthukumar, S.; Prasad, S. Temporal Profiling of Cytokines in Passively Expressed Sweat for Detection of Infection Using Wearable Device. *Bioeng. Transl. Med.* **2021**, *6*, No. e10220.
- (279) Upasham, S.; Prasad, S. SLOCK (Sensor for Circadian Clock): Passive Sweat-Based Chronobiology Tracker. *Lab Chip* **2020**, *20*, 1947–1960.
- (280) Kothari, A.; Jagannath, B.; Muthukumar, S.; Prasad, S. An Observational Study for Detection and Quantification of Interferon- $\gamma$  in Sweat toward Inflammation Monitoring. *Biosens. Bioelectron.: X* **2022**, *10*, 100122.
- (281) Churcher, N. K. M.; Upasham, S.; Rice, P.; Bhadsavle, S.; Prasad, S. Development of a Flexible, Sweat-Based Neuropeptide Y Detection Platform. *RSC Adv.* **2020**, *10*, 23173–23186.
- (282) Upasham, S.; Rice, P.; Pali, M.; Prasad, S. FLOCK -Flare Clock: Passive Sweat-Based Eczematous Flare Detection System. *Biosens. Bioelectron.: X* **2022**, *10*, 100120.
- (283) Kinnamon, D.; Ghanta, R.; Lin, K.-C.; Muthukumar, S.; Prasad, S. Portable Biosensor for Monitoring Cortisol in Low-Volume Perspired Human Sweat. *Sci. Rep.* **2017**, *7*, 13312.
- (284) Lee, H.-B.; Meeseepong, M.; Trung, T. Q.; Kim, B.-Y.; Lee, N.-E. A Wearable Lab-on-a-Patch Platform with Stretchable Nanostructured Biosensor for Non-Invasive Immunodetection of Biomarker in Sweat. *Biosens. Bioelectron.* **2020**, *156*, 112133.
- (285) Nah, J. S.; Barman, S. C.; Zahed, M. A.; Sharifuzzaman, Md.; Yoon, H.; Park, C.; Yoon, S.; Zhang, S.; Park, J. Y. A Wearable Microfluidics-Integrated Impedimetric Immunosensor Based on Ti3C2Tx MXene Incorporated Laser-Burned Graphene for Non-invasive Sweat Cortisol Detection. *Sens. Actuators B Chem.* **2021**, *329*, 129206.
- (286) Laochai, T.; Yukird, J.; Promphet, N.; Qin, J.; Chailapakul, O.; Rodthongkum, N. Non-Invasive Electrochemical Immunosensor for Sweat Cortisol Based on L-Cys/AuNPs/ MXene Modified Thread Electrode. *Biosens. Bioelectron.* **2022**, *203*, 114039.
- (287) Sekar, M.; Pandiaraj, M.; Bhansali, S.; Ponpandian, N.; Viswanathan, C. Carbon Fiber Based Electrochemical Sensor for Sweat Cortisol Measurement. *Sci. Rep.* **2019**, *9*, 403.
- (288) Madhu, S.; Anthuuvan, A. J.; Ramasamy, S.; Manickam, P.; Bhansali, S.; Nagamony, P.; Chinnuswamy, V. ZnO Nanorod Integrated Flexible Carbon Fibers for Sweat Cortisol Detection. *ACS Appl. Electron. Mater.* **2020**, *2*, 499–509.
- (289) Cheng, C.; Li, X.; Xu, G.; Lu, Y.; Low, S. S.; Liu, G.; Zhu, L.; Li, C.; Liu, Q. Battery-Free, Wireless, and Flexible Electrochemical Patch for in Situ Analysis of Sweat Cortisol via near Field Communication. *Biosens. Bioelectron.* **2021**, *172*, 112782.
- (290) Aizawa, M.; Thomas, J. D. R.; Higgins, I. J.; Albery, W. J.; Akhtar, M.; Lowe, C. R.; Higgins, I. J. Immunosensors. *Philos. Trans. R. Soc.* **1987**, *316*, 121–134.
- (291) Xue, W.; Tan, X.; Oo, M. K. K.; Kulkarni, G.; Ilgen, M. A.; Fan, X. Rapid and Sensitive Detection of Drugs of Abuse in Sweat by Multiplexed Capillary Based Immuno-Biosensors. *Analyst* **2020**, *145*, 1346–1354.
- (292) Kim, S.; Lee, B.; Reeder, J. T.; Seo, S. H.; Lee, S.-U.; Hourlier-Fargette, A.; Shin, J.; Sekine, Y.; Jeong, H.; Oh, Y. S.; Aranyosi, A. J.; Lee, S. P.; Model, J. B.; Lee, G.; Seo, M.-H.; Kwak, S. S.; Jo, S.; Park, G.; Han, S.; Park, I.; Jung, H.-I.; Ghaffari, R.; Koo, J.; Braun, P. V.; Rogers, J. A. Soft, Skin-Interfaced Microfluidic Systems with Integrated Immunoassays, Fluorometric Sensors, and Impedance Measurement Capabilities. *Proc. Natl. Acad. Sci. U. S. A.* **2020**, *117*, 27906–27915.
- (293) De Meyer, T.; Muyllderms, S.; Depicker, A. Nanobody-Based Products as Research and Diagnostic Tools. *Trends Biotechnol.* **2014**, *32*, 263–270.
- (294) Gray, A.; Bradbury, A. R. M.; Knappik, A.; Plückthun, A.; Borrebaeck, C. A. K.; Dübel, S. Animal-Free Alternatives and the Antibody Iceberg. *Nat. Biotechnol.* **2020**, *38*, 1234–1239.
- (295) Tu, J.; Gao, W. Ethical Considerations of Wearable Technologies in Human Research. *Adv. Healthc. Mater.* **2021**, *10*, 2100127.
- (296) Zheng, J.; Yang, R.; Shi, M.; Wu, C.; Fang, X.; Li, Y.; Li, J.; Tan, W. Rationally Designed Molecular Beacons for Bioanalytical and Biomedical Applications. *Chem. Soc. Rev.* **2015**, *44*, 3036–3055.
- (297) Rusconi, C. P.; Scardino, E.; Layzer, J.; Pitoc, G. A.; Ortel, T. L.; Monroe, D.; Sullenger, B. A. RNA Aptamers as Reversible Antagonists of Coagulation Factor IXa. *Nature* **2002**, *419*, 90–94.
- (298) Song, S.; Wang, L.; Li, J.; Fan, C.; Zhao, J. Aptamer-Based Biosensors. *Trends Anal. Chem.* **2008**, *27*, 108–117.
- (299) Pali, M.; Jagannath, B.; Lin, K.-C.; Upasham, S.; Sankhalab, D.; Upashama, S.; Muthukumar, S.; Prasad, S. CATCH (Cortisol Apta WATCH): ‘Bio-Mimic Alarm’ to Track Anxiety, Stress, Immunity in Human Sweat. *Electrochim. Acta* **2021**, *390*, 138834.
- (300) Churcher, N. K. M.; Greyling, C.; Upasham, S.; Lin, K.-C.; Rice, P.; Pali, M.; Spiro, J.; Prasad, S. AptaStrenor (Aptamer-Based Sensor for Stress Monitoring): The Interrelationship between NPY and Cortisol towards Chronic Disease Monitoring. *Biosens. Bioelectron.: X* **2022**, *10*, 100145.
- (301) Liu, T.-L.; Dong, Y.; Chen, S.; Zhou, J.; Ma, Z.; Li, J. Battery-Free, Tuning Circuit-Inspired Wireless Sensor Systems for Detection of Multiple Biomarkers in Bodily Fluids. *Sci. Adv.* **2022**, *8*, No. eabo7049.
- (302) Zhang, X.; Tang, Y.; Wu, H.; Wang, Y.; Niu, L.; Li, F. Integrated Aptasensor Array for Sweat Drug Analysis. *Anal. Chem.* **2022**, *94*, 7936–7943.

- (303) An, J. E.; Kim, K. H.; Park, S. J.; Seo, S. E.; Kim, J.; Ha, S.; Bae, J.; Kwon, O. S. Wearable Cortisol Aptasensor for Simple and Rapid Real-Time Monitoring. *ACS Sens.* **2022**, *7*, 99–108.
- (304) Dalirirad, S.; Steckl, A. J. Aptamer-Based Lateral Flow Assay for Point of Care Cortisol Detection in Sweat. *Sens. Actuat. B: Chem.* **2019**, *283*, 79–86.
- (305) Liu, L. S.; Wang, F.; Ge, Y.; Lo, P. K. Recent Developments in Aptasensors for Diagnostic Applications. *ACS Appl. Mater. Interfaces* **2021**, *13*, 9329–9358.
- (306) Minagawa, H.; Onodera, K.; Fujita, H.; Sakamoto, T.; Akitomi, J.; Kaneko, N.; Shiratori, I.; Kuwahara, M.; Horii, K.; Waga, I. Selection, Characterization and Application of Artificial DNA Aptamer Containing Appended Bases with Sub-Nanomolar Affinity for a Salivary Biomarker. *Sci. Rep.* **2017**, *7*, 42716.
- (307) Wang, F.; Liu, L. S.; Lau, C. H.; Han Chang, T. J.; Tam, D. Y.; Leung, H. M.; Tin, C.; Lo, P. K. Synthetic  $\alpha$ -l-Threose Nucleic Acids Targeting Bcl-2 Show Gene Silencing and in Vivo Antitumor Activity for Cancer Therapy. *ACS Appl. Mater. Interfaces* **2019**, *11*, 38510–38518.
- (308) Selvolini, G.; Marrazza, G. MIP-Based Sensors: Promising New Tools for Cancer Biomarker Determination. *Sensors* **2017**, *17*, 718.
- (309) Liu, Y.-L.; Liu, R.; Qin, Y.; Qiu, Q.-F.; Chen, Z.; Cheng, S.-B.; Huang, W.-H. Flexible Electrochemical Urea Sensor Based on Surface Molecularly Imprinted Nanotubes for Detection of Human Sweat. *Anal. Chem.* **2018**, *90*, 13081–13087.
- (310) Chen, M.-M.; Cheng, S.-B.; Ji, K.; Gao, J.; Liu, Y.-L.; Wen, W.; Zhang, X.; Wang, S.; Huang, W.-H. Construction of a Flexible Electrochemiluminescence Platform for Sweat Detection. *Chem. Sci.* **2019**, *10*, 6295–6303.
- (311) Tang, W.; Yin, L.; Sempionatto, J. R.; Moon, J.-M.; Teymourian, H.; Wang, J. Touch-Based Stressless Cortisol Sensing. *Adv. Mater.* **2021**, *33*, 2008465.
- (312) Parlak, O.; Keene, S. T.; Marais, A.; Curto, V. F.; Salleo, A. Molecularly Selective Nanoporous Membrane-Based Wearable Organic Electrochemical Device for Noninvasive Cortisol Sensing. *Sci. Adv.* **2018**, *4*, No. eaar2904.
- (313) Kanokpaka, P.; Chang, L.-Y.; Wang, B.-C.; Huang, T.-H.; Shih, M.-J.; Hung, W.-S.; Lai, J.-Y.; Ho, K.-C.; Yeh, M.-H. Self-Powered Molecular Imprinted Polymers-Based Triboelectric Sensor for Noninvasive Monitoring Lactate Levels in Human Sweat. *Nano Energy* **2022**, *100*, 107464.
- (314) Verheyen, E.; Schillemans, J. P.; van Wijk, M.; Demeniex, M.-A.; Hennink, W. E.; van Nostrum, C. F. Challenges for the Effective Molecular Imprinting of Proteins. *Biomaterials* **2011**, *32*, 3008–3020.
- (315) Leppälüoto, J. Human Thermoregulation in Sauna. *Ann. Clin. Res.* **1988**, *20*, 240–243.
- (316) Zech, M.; Benesch, M.; Hepp, J.; Polifka, S.; Glaser, B. Sauna, Sweat and Science II - Do We Sweat What We Drink? *Isot. Environ. Health Stud.* **2019**, *55*, 394–403.
- (317) Chen, Y.-L.; Kuan, W.-H.; Liu, C.-L. Comparative Study of the Composition of Sweat from Eccrine and Apocrine Sweat Glands during Exercise and in Heat. *Int. J. Environ. Res. Public Health* **2020**, *17*, 3377.
- (318) Lin, S.; Wang, B.; Zhao, Y.; Shih, R.; Cheng, X.; Yu, W.; Hojajji, H.; Lin, H.; Hoffman, C.; Ly, D.; Tan, J.; Chen, Y.; Di Carlo, D.; Milla, C.; Emaminejad, S. Natural Perspiration Sampling and in Situ Electrochemical Analysis with Hydrogel Micropatches for User-Identifiable and Wireless Chemo/Biosensing. *ACS Sens.* **2020**, *5*, 93–102.
- (319) Souza, S. L.; Graça, G.; Oliva, A. Characterization of Sweat Induced with Pilocarpine, Physical Exercise, and Collected Passively by Metabolomic Analysis. *Skin Res. Technol.* **2018**, *24*, 187–195.
- (320) Moon, J.-M.; Teymourian, H.; De la Paz, E.; Sempionatto, J. R.; Mahato, K.; Sonsa-ard, T.; Huang, N.; Longardner, K.; Litvan, I.; Wang, J. Non-Invasive Sweat-Based Tracking of L-Dopa Pharmacokinetic Profiles Following an Oral Tablet Administration. *Angew. Chem., Int. Ed.* **2021**, *60*, 19074.
- (321) Bariya, M.; Li, L.; Ghattamaneni, R.; Ahn, C. H.; Nyein, H. Y. Y.; Tai, L.-C.; Javey, A. Glove-Based Sensors for Multimodal Monitoring of Natural Sweat. *Sci. Adv.* **2020**, *6*, No. eabb8308.
- (322) Lin, P.-H.; Sheu, S.-C.; Chen, C.-W.; Huang, S.-C.; Li, B.-R. Wearable Hydrogel Patch with Noninvasive, Electrochemical Glucose Sensor for Natural Sweat Detection. *Talanta* **2022**, *241*, 123187.
- (323) Sempionatto, J. R.; Moon, J.-M.; Wang, J. Touch-Based Fingertip Blood-Free Reliable Glucose Monitoring: Personalized Data Processing for Predicting Blood Glucose Concentrations. *ACS Sens.* **2021**, *6*, 1875–1883.
- (324) Low, P. A.; Caskey, P. E.; Tuck, R. R.; Fealey, R. D.; Dyck, P. J. Quantitative Sudomotor Axon Reflex Test in Normal and Neuropathic Subjects. *Ann. Neurol.* **1983**, *14*, 573–580.
- (325) Aromdee, C.; Fawcett, J. P.; Ferguson, M. M.; Ledger, R. Serum Pilocarpine Esterase Activity and Response to Oral Pilocarpine. *Biochem. Mol. Med.* **1996**, *59*, 57–61.
- (326) Emaminejad, S.; Gao, W.; Wu, E.; Davies, Z. A.; Yin Yin Nyein, H.; Challa, S.; Ryan, S. P.; Fahad, H. M.; Chen, K.; Shahpar, Z.; Talebi, S.; Milla, C.; Javey, A.; Davis, R. W. Autonomous Sweat Extraction and Analysis Applied to Cystic Fibrosis and Glucose Monitoring Using a Fully Integrated Wearable Platform. *Proc. Natl. Acad. Sci. U.S.A.* **2017**, *114*, 4625–4630.
- (327) Li, S.; Hart, K.; Norton, N.; Ryan, C. A.; Gugliani, L.; Prausnitz, M. R. Administration of Pilocarpine by Microneedle Patch as a Novel Method for Cystic Fibrosis Sweat Testing. *Bioeng. Transl. Med.* **2021**, *6*. DOI: 10.1002/btm2.10222.
- (328) Zhao, J.; Lin, Y.; Wu, J.; Nyein, H. Y. Y.; Bariya, M.; Tai, L.-C.; Chao, M.; Ji, W.; Zhang, G.; Fan, Z.; Javey, A. A Fully Integrated and Self-Powered Smartwatch for Continuous Sweat Glucose Monitoring. *ACS Sens.* **2019**, *4*, 1925–1933.
- (329) Sempionatto, J. R.; Lin, M.; Yin, L.; De la paz, E.; Pei, K.; Sonsa-ard, T.; de Loyola Silva, A. N.; Khorshed, A. A.; Zhang, F.; Tostado, N.; Xu, S.; Wang, J. An Epidemic Patch for the Simultaneous Monitoring of Haemodynamic and Metabolic Biomarkers. *Nat. Biomed. Eng.* **2021**, *5*, 737–748.
- (330) Paul, B.; Demuru, S.; Lafaye, C.; Saubade, M.; Briand, D. Printed Iontophoretic-Integrated Wearable Microfluidic Sweat-Sensing Patch for On-Demand Point-Of-Care Sweat Analysis. *Adv. Mater. Technol.* **2021**, *6*, 2000910.
- (331) Kim, J.; Sempionatto, J. R.; Imani, S.; Hartel, M. C.; Barfidokht, A.; Tang, G.; Campbell, A. S.; Mercier, P. P.; Wang, J. Simultaneous Monitoring of Sweat and Interstitial Fluid Using a Single Wearable Biosensor Platform. *Adv. Sci.* **2018**, *5*, 1800880.
- (332) Brothers, M. C.; DeBrosse, M.; Grigsby, C. C.; Naik, R. R.; Hussain, S. M.; Heikenfeld, J.; Kim, S. S. Achievements and Challenges for Real-Time Sensing of Analytes in Sweat within Wearable Platforms. *Acc. Chem. Res.* **2019**, *52*, 297–306.
- (333) Simmers, P.; Yuan, Y.; Sonner, Z.; Heikenfeld, J. Membrane Isolation of Repeated-Use Sweat Stimulants for Mitigating Both Direct Dermal Contact and Sweat Dilution. *Biomicrofluidics* **2018**, *12*, 034101.
- (334) Gomez, C. C. S.; Marson, F. A. L.; Servidoni, M. F.; Ribeiro, A. F.; Ribeiro, M. A. G. O.; Gama, V. A. L.; Costa, E. T.; Ribeiro, J. D.; Vieira Junior, F. U. Evaluation of Continuous Constant Current and Continuous Pulsed Current in Sweat Induction for Cystic Fibrosis Diagnosis. *BMC Pulm. Med.* **2018**, *18*, 153.
- (335) Herrmann, F.; Mandol, L. Studies of pH of Sweat Produced by Different Forms of Stimulation. *J. Invest. Dermatol.* **1955**, *24*, 225–246.
- (336) Verde, T.; Shephard, R. J.; Corey, P.; Moore, R. Sweat Composition in Exercise and in Heat. *J. Appl. Physiol.* **1982**, *53*, 1540–1545.
- (337) Agrawal, K.; Waller, J. D.; Pedersen, T. L.; Newman, J. W. Effects of Stimulation Technique, Anatomical Region, and Time on Human Sweat Lipid Mediator Profiles. *Prostaglandins Other Lipid Mediat.* **2018**, *134*, 84–92.
- (338) Harshman, S. W.; Pitsch, R. L.; Schaeublin, N. M.; Smith, Z. K.; Strayer, K. E.; Phelps, M. S.; Qualley, A. V.; Cowan, D. W.; Rose, S. D.; O'Connor, M. L.; Eckerle, J. J.; Das, T.; Barbey, A. K.; Strang,

- A. J.; Martin, J. A. Metabolomic Stability of Exercise-Induced Sweat. *J. Chromatogr. B* **2019**, *1126–1127*, 121763.
- (339) Hussain, J. N.; Mantri, N.; Cohen, M. M. Working Up a Good Sweat - The Challenges of Standardising Sweat Collection for Metabolomics Analysis. *Clin. Biochem. Rev.* **2017**, *38*, 13–34.
- (340) De Giovanni, N.; Fucci, N. The Current Status of Sweat Testing For Drugs of Abuse: A Review. *Curr. Med. Chem.* **2013**, *20*, 545–561.
- (341) Liu, C.; Xu, T.; Wang, D.; Zhang, X. The Role of Sampling in Wearable Sweat Sensors. *Talanta* **2020**, *212*, 120801.
- (342) Francis, J.; Stamper, I.; Heikenfeld, J.; Gomez, E. F. Digital Nanoliter to Milliliter Flow Rate Sensor with in Vivo Demonstration for Continuous Sweat Rate Measurement. *Lab Chip* **2019**, *19*, 178–185.
- (343) Zhao, F. J.; Bonmarin, M.; Chen, Z. C.; Larson, M.; Fay, D.; Runnoe, D.; Heikenfeld, J. Ultra-Simple Wearable Local Sweat Volume Monitoring Patch Based on Swellable Hydrogels. *Lab Chip* **2020**, *20*, 168–174.
- (344) Katseli, V.; Economou, A.; Kokkinos, C. Smartphone-Addressable 3D-Printed Electrochemical Ring for Nonenzymatic Self-Monitoring of Glucose in Human Sweat. *Anal. Chem.* **2021**, *93*, 3331–3336.
- (345) Liu, H.; Qing, H.; Li, Z.; Han, Y. L.; Lin, M.; Yang, H.; Li, A.; Lu, T. J.; Li, F.; Xu, F. Paper: A Promising Material for Human-Friendly Functional Wearable Electronics. *Mater. Sci. Eng. R: Reports* **2017**, *112*, 1–22.
- (346) Huang, X.; Liu, Y.; Chen, K.; Shin, W.-J.; Lu, C.-J.; Kong, G.-W.; Patnaik, D.; Lee, S.-H.; Cortes, J. F.; Rogers, J. A. Stretchable, Wireless Sensors and Functional Substrates for Epidermal Characterization of Sweat. *Small* **2014**, *10*, 3083–3090.
- (347) Shu, Y.; Su, T.; Lu, Q.; Shang, Z.; Xu, Q.; Hu, X. Highly Stretchable Wearable Electrochemical Sensor Based on Ni-Co MOF Nanosheet-Decorated Ag/RGO/PU Fiber for Continuous Sweat Glucose Detection. *Anal. Chem.* **2021**, *93*, 16222–16230.
- (348) Baker, L. B.; De Chavez, P. J. D.; Ungaro, C. T.; Sopeña, B. C.; Nuccio, R. P.; Reimel, A. J.; Barnes, K. A. Exercise Intensity Effects on Total Sweat Electrolyte Losses and Regional vs. Whole-Body Sweat  $[Na^+]$ ,  $[Cl^-]$ , and  $[K^+]$ . *Eur. J. Appl. Physiol.* **2019**, *119*, 361–375.
- (349) Lee, H.; Song, C.; Hong, Y. S.; Kim, M.; Cho, H. R.; Kang, T.; Shin, K.; Choi, S. H.; Hyeon, T.; Kim, D.-H. Wearable/Disposable Sweat-Based Glucose Monitoring Device with Multistage Transdermal Drug Delivery Module. *Sci. Adv.* **2017**, *3*, No. e1601314.
- (350) Ichimura, Y.; Kuritsubo, T.; Nagamine, K.; Nomura, A.; Shitanda, I.; Tokito, S. A Fully Screen-Printed Potentiometric Chloride Ion Sensor Employing a Hydrogel-Based Touchpad for Simple and Non-Invasive Daily Electrolyte Analysis. *Anal. Bioanal. Chem.* **2021**, *413*, 1883–1891.
- (351) Nagamine, K.; Mano, T.; Nomura, A.; Ichimura, Y.; Izawa, R.; Furusawa, H.; Matsui, H.; Kumaki, D.; Tokito, S. Noninvasive Sweat-Lactate Biosensor Employing a Hydrogel-Based Touch Pad. *Sci. Rep.* **2019**, *9*, 10102.
- (352) Twine, N. B.; Norton, R. M.; Brothers, M. C.; Hauke, A.; Gomez, E. F.; Heikenfeld, J. Open Nanofluidic Films with Rapid Transport and No Analyte Exchange for Ultra-Low Sample Volumes. *Lab Chip* **2018**, *18*, 2816–2825.
- (353) Heikenfeld, J. Non-Invasive Analyte Access and Sensing through Eccrine Sweat: Challenges and Outlook circa 2016. *Electroanalysis* **2016**, *28*, 1242–1249.
- (354) Rebouillat, S.; Pla, F. State of the Art Manufacturing and Engineering of Nanocellulose: A Review of Available Data and Industrial Applications. *J. Biomater. Nanobiotechnol.* **2013**, *4*, 165–188.
- (355) Sen, S.; Martin, J. D.; Argyropoulos, D. S. Review of Cellulose Non-Derivatizing Solvent Interactions with Emphasis on Activity in Inorganic Molten Salt Hydrates. *ACS Sustainable Chem. Eng.* **2013**, *1*, 858–870.
- (356) Alizadeh, A.; Burns, A.; Lenigk, R.; Gettings, R.; Ashe, J.; Porter, A.; McCaul, M.; Barrett, R.; Diamond, D.; White, P.; Skeath, P.; Tomczak, M. A Wearable Patch for Continuous Monitoring of Sweat Electrolytes during Exertion. *Lab Chip* **2018**, *18*, 2632–2641.
- (357) Lin, H.; Zhao, Y.; Lin, S.; Wang, B.; Yeung, C.; Cheng, X.; Wang, Z.; Cai, T.; Yu, W.; King, K.; Tan, J.; Salahi, K.; Hojaiji, H.; Emaminejad, S. A Rapid and Low-Cost Fabrication and Integration Scheme to Render 3D Microfluidic Architectures for Wearable Biofluid Sampling, Manipulation, and Sensing. *Lab Chip* **2019**, *19*, 2844–2853.
- (358) Baker, L. B.; Model, J. B.; Barnes, K. A.; Anderson, M. L.; Lee, S. P.; Lee, K. A.; Brown, S. D.; Reimel, A. J.; Roberts, T. J.; Nuccio, R. P.; Bonsignore, J. L.; Ungaro, C. T.; Carter, J. M.; Li, W.; Seib, M. S.; Reeder, J. T.; Aranyosi, A. J.; Rogers, J. A.; Ghaffari, R. Skin-Interfaced Microfluidic System with Personalized Sweating Rate and Sweat Chloride Analytics for Sports Science Applications. *Sci. Adv.* **2020**, *6*, No. eabe3929.
- (359) Wang, J. D.; Douville, N. J.; Takayama, S.; ElSayed, M. Quantitative Analysis of Molecular Absorption into PDMS Microfluidic Channels. *Ann. Biomed. Eng.* **2012**, *40*, 1862–1873.
- (360) Toepke, M. W.; Beebe, D. J. PDMS Absorption of Small Molecules and Consequences in Microfluidic Applications. *Lab Chip* **2006**, *6*, 1484–1486.
- (361) Kim, S. B.; Koo, J.; Yoon, J.; Hourlier-Fargette, A.; Lee, B.; Chen, S.; Jo, S.; Choi, J.; Oh, Y. S.; Lee, G.; Won, S. M.; Aranyosi, A. J.; Lee, S. P.; Model, J. B.; Braun, P. V.; Ghaffari, R.; Park, C.; Rogers, J. A. Soft, Skin-Interfaced Microfluidic Systems with Integrated Enzymatic Assays for Measuring the Concentration of Ammonia and Ethanol in Sweat. *Lab Chip* **2020**, *20*, 84–92.
- (362) Zhang, Y.; Guo, H.; Kim, S. B.; Wu, Y.; Ostojich, D.; Park, S. H.; Wang, X.; Weng, Z.; Li, R.; Bhandodkar, A. J.; Sekine, Y.; Choi, J.; Xu, S.; Quaggin, S.; Ghaffari, R.; Rogers, J. A. Passive Sweat Collection and Colorimetric Analysis of Biomarkers Relevant to Kidney Disorders Using a Soft Microfluidic System. *Lab Chip* **2019**, *19*, 1545–1555.
- (363) Choi, J.; Bhandodkar, A. J.; Reeder, J. T.; Ray, T. R.; Turnquist, A.; Kim, S. B.; Nyberg, N.; Hourlier-Fargette, A.; Model, J. B.; Aranyosi, A. J.; Xu, S.; Ghaffari, R.; Rogers, J. A. Soft, Skin-Integrated Multifunctional Microfluidic Systems for Accurate Colorimetric Analysis of Sweat Biomarkers and Temperature. *ACS Sens.* **2019**, *4*, 379–388.
- (364) Kim, S. B.; Zhang, Y.; Won, S. M.; Bhandodkar, A. J.; Sekine, Y.; Xue, Y.; Koo, J.; Harshman, S. W.; Martin, J. A.; Park, J. M.; Ray, T. R.; Crawford, K. E.; Lee, K.-T.; Choi, J.; Pitsch, R. L.; Grigsby, C. C.; Strang, A. J.; Chen, Y.-Y.; Xu, S.; Kim, J.; Koh, A.; Ha, J. S.; Huang, Y.; Kim, S. W.; Rogers, J. A. Super-Absorbent Polymer Valves and Colorimetric Chemistries for Time-Sequenced Discrete Sampling and Chloride Analysis of Sweat via Skin-Mounted Soft Microfluidics. *Small* **2018**, *14*, No. e1703334.
- (365) Lin, H.; Tan, J.; Zhu, J.; Lin, S.; Zhao, Y.; Yu, W.; Hojaiji, H.; Wang, B.; Yang, S.; Cheng, X.; Wang, Z.; Tang, E.; Yeung, C.; Emaminejad, S. A Programmable Epidermal Microfluidic Valving System for Wearable Biofluid Management and Contextual Biomarker Analysis. *Nat. Commun.* **2020**, *11*, 4405.
- (366) Naik, A. R.; Warren, B.; Burns, A.; Lenigk, R.; Morse, J.; Alizadeh, A.; Watkins, J. J. Electrowetting Valves for Sweat-Based Microfluidics. *Microfluid. Nanofluid.* **2021**, *25*, 2.
- (367) Zhang, Y.; Chen, Y.; Huang, J.; Liu, Y.; Peng, J.; Chen, S.; Song, K.; Ouyang, X.; Cheng, H.; Wang, X. Skin-Interfaced Microfluidic Devices with One-Opening Chambers and Hydrophobic Valves for Sweat Collection and Analysis. *Lab Chip* **2020**, *20*, 2635–2645.
- (368) Porwal, P. R.; Thompson, S. M.; Walters, D. K.; Jamal, T. Heat Transfer and Fluid Flow Characteristics in Multistaged Tesla Valves. *Numer. Heat Transfer; A: Appl.* **2018**, *73*, 347–365.
- (369) Shi, H.; Cao, Y.; Zeng, Y.; Zhou, Y.; Wen, W.; Zhang, C.; Zhao, Y.; Chen, Z. Wearable Tesla Valve-Based Sweat Collection Device for Sweat Colorimetric Analysis. *Talanta* **2022**, *240*, 123208.
- (370) Taylor, L. D.; Cerankowski, L. D. Preparation of Films Exhibiting a Balanced Temperature Dependence to Permeation by

Aqueous Solutions—a Study of Lower Consolute Behavior. *J. Polym. Sci.: Polym. Chem. Ed.* **1975**, *13*, 2551–2570.

(371) Yi, Z.; Feng, H.; Zhou, X.; Shui, L. Design of an Open Electrowetting on Dielectric Device Based on Printed Circuit Board by Using a Parafilm M. *Front. Phys.* **2020**, *8*. DOI: 10.3389/fphy.2020.00193.

(372) Quilliet, C.; Berge, B. Electrowetting: A Recent Outbreak. *Curr. Opin. Colloid Interface Sci.* **2001**, *6*, 34–39.

(373) Koo, C. K. W.; He, F.; Nugen, S. R. An Inkjet-Printed Electrowetting Valve for Paper-Fluidic Sensors. *Analyst* **2013**, *138*, 4998–5004.

(374) Saha, T.; Fang, J.; Mukherjee, S.; Dickey, M. D.; Velev, O. D. Wearable Osmotic-Capillary Patch for Prolonged Sweat Harvesting and Sensing. *ACS Appl. Mater. Interfaces* **2021**, *13*, 8071–8081.

(375) Saha, T.; Songkakul, T.; Knisely, C. T.; Yokus, M. A.; Daniele, M. A.; Dickey, M. D.; Bozkurt, A.; Velev, O. D. Wireless Wearable Electrochemical Sensing Platform with Zero-Power Osmotic Sweat Extraction for Continuous Lactate Monitoring. *ACS Sens.* **2022**, *7*, 2037–2048.

(376) Saha, T.; Fang, J.; Mukherjee, S.; Knisely, C. T.; Dickey, M. D.; Velev, O. D. Osmotically Enabled Wearable Patch for Sweat Harvesting and Lactate Quantification. *Micromachines* **2021**, *12*, 1513.

(377) Camplisson, C. K.; Schilling, K. M.; Pedrotti, W. L.; Stone, H. A.; Martinez, A. W. Two-Ply Channels for Faster Wicking in Paper-Based Microfluidic Devices. *Lab Chip* **2015**, *15*, 4461–4466.

(378) Songok, J.; Toivakka, M. Enhancing Capillary-Driven Flow for Paper-Based Microfluidic Channels. *ACS Appl. Mater. Interfaces* **2016**, *8*, 30523–30530.

(379) Shay, T.; Saha, T.; Dickey, M. D.; Velev, O. D. Principles of Long-Term Fluids Handling in Paper-Based Wearables with Capillary-Evaporative Transport. *Biomicrofluidics* **2020**, *14*, 034112.

(380) Yetisen, A. K.; Akram, M. S.; Lowe, C. R. Paper-Based Microfluidic Point-of-Care Diagnostic Devices. *Lab Chip* **2013**, *13*, 2210–2251.

(381) Abbasiasl, T.; Mirlou, F.; Istif, E.; Koydemir, H. C.; Beker, L. A Wearable Paper-Integrated Microfluidic Device for Sequential Analysis of Sweat Based on Capillary Action. *Sens. Diagn.* **2022**, *1*, 775–786.

(382) Washburn, E. W. The Dynamics of Capillary Flow. *Phys. Rev.* **1921**, *17*, 273–283.

(383) Baker, J.; Hong, L.; Blanch, H.; Prausnitz, J. M. Effect of Initial Total Monomer Concentration on the Swelling Behavior of Cationic Acrylamide-Based Hydrogels. *Macromolecules* **1994**, *27*, 1446–1454.

(384) Razmjou, A.; Liu, Q.; Simon, G. P.; Wang, H. Bifunctional Polymer Hydrogel Layers as Forward Osmosis Draw Agents for Continuous Production of Fresh Water Using Solar Energy. *Environ. Sci. Technol.* **2013**, *47*, 13160–13166.

(385) Fu, F.; Wang, J.; Tan, Y.; Yu, J. Super-Hydrophilic Zwitterionic Polymer Surface Modification Facilitates Liquid Transportation of Microfluidic Sweat Sensors. *Macromol. Rapid Commun.* **2022**, *43*, 2100776.

(386) Son, J.; Bae, G. Y.; Lee, S.; Lee, G.; Kim, S. W.; Kim, D.; Chung, S.; Cho, K. Cactus-Spine-Inspired Sweat-Collecting Patch for Fast and Continuous Monitoring of Sweat. *Adv. Mater.* **2021**, *33*, 2102740.

(387) Dai, B.; Li, K.; Shi, L.; Wan, X.; Liu, X.; Zhang, F.; Jiang, L.; Wang, S. Bioinspired Janus Textile with Conical Micropores for Human Body Moisture and Thermal Management. *Adv. Mater.* **2019**, *31*, 1904113.

(388) Nordström, M.; Marie, R.; Calleja, M.; Boisen, A. Rendering SU-8 Hydrophilic to Facilitate Use in Micro Channel Fabrication. *J. Micromech. Microeng.* **2004**, *14*, 1614.

(389) Hemmilä, S.; Cauich-Rodriguez, J. V.; Kreutzer, J.; Kallio, P. Rapid, Simple, and Cost-Effective Treatments to Achieve Long-Term Hydrophilic PDMS Surfaces. *Appl. Surf. Sci.* **2012**, *258*, 9864–9875.

(390) Yao, M.; Fang, J. Hydrophilic PEO-PDMS for Microfluidic Applications. *J. Micromech. Microeng.* **2012**, *22*, 025012.

(391) Männel, M. J.; Weigel, N.; Hauck, N.; Heida, T.; Thiele, J. Combining Hydrophilic and Hydrophobic Materials in 3D Printing

for Fabricating Microfluidic Devices with Spatial Wettability. *Adv. Mater. Technol.* **2021**, *6*, 2100094.

(392) Oyama, T. G.; Oyama, K.; Taguchi, M. A Simple Method for Production of Hydrophilic, Rigid, and Sterilized Multi-Layer 3D Integrated Polydimethylsiloxane Microfluidic Chips. *Lab Chip* **2020**, *20*, 2354–2363.

(393) Sun, T.; Feng, L.; Gao, X.; Jiang, L. Bioinspired Surfaces with Special Wettability. *Acc. Chem. Res.* **2005**, *38*, 644–652.

(394) Mishra, H.; Schrader, A. M.; Lee, D. W.; Gallo, A. Jr.; Chen, S.-Y.; Kaufman, Y.; Das, S.; Israelachvili, J. N. Time-Dependent Wetting Behavior of PDMS Surfaces with Bioinspired, Hierarchical Structures. *ACS Appl. Mater. Interfaces* **2016**, *8*, 8168–8174.

(395) Gu, Y.; Zhou, S.; Yang, J. Aza-Michael Addition Chemistry for Tuning the Phase Separation of PDMS/PEG Blend Coatings and Their Anti-Fouling Potentials. *Macromol. Chem. Phys.* **2020**, *221*, 1900477.

(396) Trantidou, T.; Elani, Y.; Parsons, E.; Ces, O. Hydrophilic Surface Modification of PDMS for Droplet Microfluidics Using a Simple, Quick, and Robust Method via PVA Deposition. *Microsyst. Nanoeng.* **2017**, *3*, 16091.

(397) Choi, C.-H.; Lee, H.; Weitz, D. A. Rapid Patterning of PDMS Microfluidic Device Wettability Using Syringe-Vacuum-Induced Segmented Flow in Nonplanar Geometry. *ACS Appl. Mater. Interfaces* **2018**, *10*, 3170–3174.

(398) Higaki, Y.; Inutsuka, Y.; Sakamaki, T.; Terayama, Y.; Takenaka, A.; Higaki, K.; Yamada, N. L.; Moriwaki, T.; Ikemoto, Y.; Takahara, A. Effect of Charged Group Spacer Length on Hydration State in Zwitterionic Poly(Sulfobetaine) Brushes. *Langmuir* **2017**, *33*, 8404–8412.

(399) He, X.; Xu, T.; Gao, W.; Xu, L.-P.; Pan, T.; Zhang, X. Flexible Superwetable Tapes for On-Site Detection of Heavy Metals. *Anal. Chem.* **2018**, *90*, 14105–14110.

(400) Zhao, Z.; Li, Q.; Chen, L.; Zhao, Y.; Gong, J.; Li, Z.; Zhang, J. A Thread/Fabric-Based Band as a Flexible and Wearable Microfluidic Device for Sweat Sensing and Monitoring. *Lab Chip* **2021**, *21*, 916–932.

(401) He, X.; Yang, S.; Pei, Q.; Song, Y.; Liu, C.; Xu, T.; Zhang, X. Integrated Smart Janus Textile Bands for Self-Pumping Sweat Sampling and Analysis. *ACS Sens.* **2020**, *5*, 1548–1554.

(402) He, X.; Fan, C.; Xu, T.; Zhang, X. Biospired Janus Silk E-Textiles with Wet-Thermal Comfort for Highly Efficient Biofluid Monitoring. *Nano Lett.* **2021**, *21*, 8880–8887.

(403) Peng, Z.; Liu, R.; Xu, Z.; Chi, H.; Wang, Z.; Zhao, Y. Directional Sweat Transport Window Based on Hydrophobic/Hydrophilic Janus Fabric Enables Continuous Transfer and Monitoring of Sweat. *Appl. Mater. Today* **2022**, *29*, 101623.

(404) Bandodkar, A. J.; Jia, W.; Yardımcı, C.; Wang, X.; Ramirez, J.; Wang, J. Tattoo-Based Noninvasive Glucose Monitoring: A Proof-of-Concept Study. *Anal. Chem.* **2015**, *87*, 394–398.

(405) Hojaiji, H.; Zhao, Y.; Gong, M. C.; Mallajosyula, M.; Tan, J.; Lin, H.; Hojaiji, A. M.; Lin, S.; Milla, C.; Madni, A. M.; Emaminejad, S. An Autonomous Wearable System for Diurnal Sweat Biomarker Data Acquisition. *Lab Chip* **2020**, *20*, 4582–4591.

(406) Kang, D. H. P.; Chen, M.; Ogunseitan, O. A. Potential Environmental and Human Health Impacts of Rechargeable Lithium Batteries in Electronic Waste. *Environ. Sci. Technol.* **2013**, *47*, 5495–5503.

(407) Manjakkal, L.; Yin, L.; Nathan, A.; Wang, J.; Dahiya, R. Energy Autonomous Sweat-Based Wearable Systems. *Adv. Mater.* **2021**, *33*, 2100899.

(408) Rong, G.; Zheng, Y.; Sawan, M. Energy Solutions for Wearable Sensors: A Review. *Sensors* **2021**, *21*, 3806.

(409) Song, Y.; Mukasa, D.; Zhang, H.; Gao, W. Self-Powered Wearable Biosensors. *Acc. Mater. Res.* **2021**, *2*, 184–197.

(410) Yu, Y.; Nassar, J.; Xu, C.; Min, J.; Yang, Y.; Dai, A.; Doshi, R.; Huang, A.; Song, Y.; Gehlhar, R.; Ames, A. D.; Gao, W. Biofuel-Powered Soft Electronic Skin with Multiplexed and Wireless Sensing for Human-Machine Interfaces. *Sci. Robot.* **2020**, *5*, No. eaaz7946.

- (411) Kwon, C. H.; Ko, Y.; Shin, D.; Kwon, M.; Park, J.; Bae, W. K.; Lee, S. W.; Cho, J. High-Power Hybrid Biofuel Cells Using Layer-by-Layer Assembled Glucose Oxidase-Coated Metallic Cotton Fibers. *Nat. Commun.* **2018**, *9*, 4479.
- (412) Wang, C.; Shim, E.; Chang, H.-K.; Lee, N.; Kim, H. R.; Park, J. Sustainable and High-Power Wearable Glucose Biofuel Cell Using Long-Term and High-Speed Flow in Sportswear Fabrics. *Biosens. Bioelectron.* **2020**, *169*, 112652.
- (413) Sun, M.; Gu, Y.; Pei, X.; Wang, J.; Liu, J.; Ma, C.; Bai, J.; Zhou, M. A Flexible and Wearable Epidermal Ethanol Biofuel Cell for On-Body and Real-Time Bioenergy Harvesting from Human Sweat. *Nano Energy* **2021**, *86*, 106061.
- (414) Miyake, T.; Haneda, K.; Yoshino, S.; Nishizawa, M. Flexible, Layered Biofuel Cells. *Biosens. Bioelectron.* **2013**, *40*, 45–49.
- (415) Jia, W.; Valdés-Ramírez, G.; Bandodkar, A. J.; Windmiller, J. R.; Wang, J. Epidermal Biofuel Cells: Energy Harvesting from Human Perspiration. *Angew. Chem., Int. Ed.* **2013**, *52*, 7233–7236.
- (416) Jia, W.; Wang, X.; Imani, S.; Bandodkar, A. J.; Ramirez, J.; Mercier, P. P.; Wang, J. Wearable Textile Biofuel Cells for Powering Electronics. *J. Mater. Chem. A* **2014**, *2*, 18184–18189.
- (417) Jeerapan, I.; Sempionatto, J. R.; Pavinatto, A.; You, J.-M.; Wang, J. Stretchable Biofuel Cells as Wearable Textile-Based Self-Powered Sensors. *J. Mater. Chem. A* **2016**, *4*, 18342–18353.
- (418) Wang, J.; Sun, M.; Pei, X.; Zheng, L.; Ma, C.; Liu, J.; Cao, M.; Bai, J.; Zhou, M. Flexible Biofuel Cell-In-A-Tube (iezTube): An Entirely Self-Contained Biofuel Cell for Wearable Green Bio-energy Harvesting. *Adv. Funct. Mater.* **2022**, *32*, 2209697.
- (419) Bandodkar, A. J.; You, J.-M.; Kim, N.-H.; Gu, Y.; Kumar, R.; Mohan, A. M. V.; Kurniawan, J.; Imani, S.; Nakagawa, T.; Parish, B.; Parthasarathy, M.; Mercier, P. P.; Xu, S.; Wang, J. Soft, Stretchable, High Power Density Electronic Skin-Based Biofuel Cells for Scavenging Energy from Human Sweat. *Energy Environ. Sci.* **2017**, *10*, 1581–1589.
- (420) Chen, X.; Yin, L.; Lv, J.; Gross, A. J.; Le, M.; Gutierrez, N. G.; Li, Y.; Jeerapan, I.; Giroud, F.; Berezovska, A.; O'Reilly, R. K.; Xu, S.; Cosnier, S.; Wang, J. Stretchable and Flexible Buckypaper-Based Lactate Biofuel Cell for Wearable Electronics. *Adv. Funct. Mater.* **2019**, *29*, 1905785.
- (421) Mohammadifar, M.; Tahernia, M.; Yang, J. H.; Koh, A.; Choi, S. Biopower-on-Skin: Electricity Generation from Sweat-Eating Bacteria for Self-Powered E-Skins. *Nano Energy* **2020**, *75*, 104994.
- (422) Chen, Z.; Yao, Y.; Lv, T.; Yang, Y.; Liu, Y.; Chen, T. Flexible and Stretchable Enzymatic Biofuel Cell with High Performance Enabled by Textile Electrodes and Polymer Hydrogel Electrolyte. *Nano Lett.* **2022**, *22*, 196–202.
- (423) Ryu, J.; Choi, S. Bioelectricity Production from Sweat-Activated Germination of Bacterial Endospores. *Biosens. Bioelectron.* **2021**, *186*, 113293.
- (424) Su, Y.; Lu, L.; Zhou, M. Wearable Microbial Fuel Cells for Sustainable Self-Powered Electronic Skins. *ACS Appl. Mater. Interfaces* **2022**, *14*, 8664–8668.
- (425) Ryu, J.; Landers, M.; Choi, S. A Sweat-Activated, Wearable Microbial Fuel Cell for Long-Term, on-Demand Power Generation. *Biosens. Bioelectron.* **2022**, *205*, 114128.
- (426) Liu, X.; Ueki, T.; Gao, H.; Woodard, T. L.; Nevin, K. P.; Fu, T.; Fu, S.; Sun, L.; Lovley, D. R.; Yao, J. Microbial Biofilms for Electricity Generation from Water Evaporation and Power to Wearables. *Nat. Commun.* **2022**, *13*, 4369.
- (427) Wang, Y.; Zhu, W.; Deng, Y.; Fu, B.; Zhu, P.; Yu, Y.; Li, J.; Guo, J. Self-Powered Wearable Pressure Sensing System for Continuous Healthcare Monitoring Enabled by Flexible Thin-Film Thermoelectric Generator. *Nano Energy* **2020**, *73*, 104773.
- (428) Jeong, C. K.; Baek, C.; Kingon, A. I.; Park, K.; Kim, S. Lead-Free Perovskite Nanowire-Employed Piezopolymer for Highly Efficient Flexible Nanocomposite Energy Harvester. *Small* **2018**, *14*, 1704022.
- (429) Zhou, Y.; Zhao, X.; Xu, J.; Fang, Y.; Chen, G.; Song, Y.; Li, S.; Chen, J. Giant Magnetoelastic Effect in Soft Systems for Bioelectronics. *Nat. Mater.* **2021**, *20*, 1670–1676.
- (430) Song, Y.; Min, J.; Yu, Y.; Wang, H.; Yang, Y.; Zhang, H.; Gao, W. Wireless Battery-Free Wearable Sweat Sensor Powered by Human Motion. *Sci. Adv.* **2020**, *6*, No. eaay9842.
- (431) Feng, R.; Tang, F.; Zhang, N.; Wang, X. Flexible, High-Power Density, Wearable Thermoelectric Nanogenerator and Self-Powered Temperature Sensor. *ACS Appl. Mater. Interfaces* **2019**, *11*, 38616–38624.
- (432) Ren, W.; Sun, Y.; Zhao, D.; Aili, A.; Zhang, S.; Shi, C.; Zhang, J.; Geng, H.; Zhang, J.; Zhang, L.; Xiao, J.; Yang, R. High-Performance Wearable Thermoelectric Generator with Self-Healing, Recycling, and Lego-like Reconfiguring Capabilities. *Sci. Adv.* **2021**, *7*, No. eabe0586.
- (433) Nozariasmarz, A.; Collins, H.; Dsouza, K.; Polash, M. H.; Hosseini, M.; Hyland, M.; Liu, J.; Malhotra, A.; Ortiz, F. M.; Mohaddes, F.; Ramesh, V. P.; Sargolzaeiaval, Y.; Snouwaert, N.; Öztürk, M. C.; Vashae, D. Review of Wearable Thermoelectric Energy Harvesting: From Body Temperature to Electronic Systems. *Appl. Energy* **2020**, *258*, 114069.
- (434) Kim, C. S.; Yang, H. M.; Lee, J.; Lee, G. S.; Choi, H.; Kim, Y. J.; Lim, S. H.; Cho, S. H.; Cho, B. J. Self-Powered Wearable Electrocardiography Using a Wearable Thermoelectric Power Generator. *ACS Energy Lett.* **2018**, *3*, 501–507.
- (435) Karthikeyan, V.; Surjadi, J. U.; Wong, J. C. K.; Kannan, V.; Lam, K.-H.; Chen, X.; Lu, Y.; Roy, V. A. L. Wearable and Flexible Thin Film Thermoelectric Module for Multi-Scale Energy Harvesting. *J. Power Sources* **2020**, *455*, 227983.
- (436) Wang, Y.; Shi, Y.; Mei, D.; Chen, Z. Wearable Thermoelectric Generator to Harvest Body Heat for Powering a Miniaturized Accelerometer. *Appl. Energy* **2018**, *215*, 690–698.
- (437) Lee, B.; Cho, H.; Park, K. T.; Kim, J.-S.; Park, M.; Kim, H.; Hong, Y.; Chung, S. Author Correction: High-Performance Compliant Thermoelectric Generators with Magnetically Self-Assembled Soft Heat Conductors for Self-Powered Wearable Electronics. *Nat. Commun.* **2021**, *12*, 1289.
- (438) Choi, J.; Jung, Y.; Yang, S. J.; Oh, J. Y.; Oh, J.; Jo, K.; Son, J. G.; Moon, S. E.; Park, C. R.; Kim, H. Flexible and Robust Thermoelectric Generators Based on All-Carbon Nanotube Yarn without Metal Electrodes. *ACS Nano* **2017**, *11*, 7608–7614.
- (439) Sun, T.; Zhou, B.; Zheng, Q.; Wang, L.; Jiang, W.; Snyder, G. J. Stretchable Fabric Generates Electric Power from Woven Thermoelectric Fibers. *Nat. Commun.* **2020**, *11*, 572.
- (440) Wan, K.; Taroni, P. J.; Liu, Z.; Liu, Y.; Tu, Y.; Santagiuliana, G.; Hsia, I.; Zhang, H.; Fenwick, O.; Krause, S.; Baxendale, M.; Schroeder, B. C.; Bilotti, E. Flexible and Stretchable Self-Powered Multi-Sensors Based on the N-Type Thermoelectric Response of Polyurethane/Na<sub>x</sub>(Ni-ett)<sub>n</sub> Composites. *Adv. Electron. Mater.* **2019**, *5*, 1900582.
- (441) Shenck, N. S.; Paradiso, J. A. Energy Scavenging with Shoe-Mounted Piezoelectrics. *IEEE Micro* **2001**, *21*, 30–42.
- (442) Wang, Z. L.; Song, J. Piezoelectric Nanogenerators Based on Zinc Oxide Nanowire Arrays. *Sensan* **2006**, *312*, 242–246.
- (443) Deng, W.; Zhou, Y.; Libanori, A.; Chen, G.; Yang, W.; Chen, J. Piezoelectric Nanogenerators for Personalized Healthcare. *Chem. Soc. Rev.* **2022**, *51*, 3380–3435.
- (444) Zhang, C.; Fan, W.; Wang, S.; Wang, Q.; Zhang, Y.; Dong, K. Recent Progress of Wearable Piezoelectric Nanogenerators. *ACS Appl. Electron. Mater.* **2021**, *3*, 2449–2467.
- (445) Zhang, Z.; Chen, Y.; Guo, J. ZnO Nanorods Patterned-Textile Using a Novel Hydrothermal Method for Sandwich Structured-Piezoelectric Nanogenerator for Human Energy Harvesting. *Physica E: Low Dimens. Syst. Nanostruct.* **2019**, *105*, 212–218.
- (446) Nour, E. S.; Sandberg, M. O.; Willander, M.; Nur, O. Handwriting Enabled Harvested Piezoelectric Power Using ZnO Nanowires/Polymers Composite on Paper Substrate. *Nano Energy* **2014**, *9*, 221–228.
- (447) Chung, S. Y.; Kim, S.; Lee, J.; Kim, K.; Kim, S.; Kang, C.; Yoon, S.; Kim, Y. S. All-Solution-Processed Flexible Thin Film Piezoelectric Nanogenerator. *Adv. Mater.* **2012**, *24*, 6022–6027.
- (448) Zhang, M.; Gao, T.; Wang, J.; Liao, J.; Qiu, Y.; Yang, Q.; Xue, H.; Shi, Z.; Zhao, Y.; Xiong, Z.; Chen, L. A Hybrid Fibers Based

Wearable Fabric Piezoelectric Nanogenerator for Energy Harvesting Application. *Nano Energy* **2015**, *13*, 298–305.

(449) Fan, F.-R.; Tian, Z.-Q.; Lin Wang, Z. Flexible Triboelectric Generator. *Nano Energy* **2012**, *1*, 328–334.

(450) Wang, H.; Han, M.; Song, Y.; Zhang, H. Design, Manufacturing and Applications of Wearable Triboelectric Nanogenerators. *Nano Energy* **2021**, *81*, 105627.

(451) Kim, W.-G.; Kim, D.-W.; Tcho, I.-W.; Kim, J.-K.; Kim, M.-S.; Choi, Y.-K. Triboelectric Nanogenerator: Structure, Mechanism, and Applications. *ACS Nano* **2021**, *15*, 258–287.

(452) Xue, H.; Yang, Q.; Wang, D.; Luo, W.; Wang, W.; Lin, M.; Liang, D.; Luo, Q. A Wearable Pyroelectric Nanogenerator and Self-Powered Breathing Sensor. *Nano Energy* **2017**, *38*, 147–154.

(453) Maharjan, P.; Bhatta, T.; Salauddin Rasel, M.; Salauddin, Md.; Toyabur Rahman, M.; Park, J. Y. High-Performance Cycloid Inspired Wearable Electromagnetic Energy Harvester for Scavenging Human Motion Energy. *Appl. Energy* **2019**, *256*, 113987.

(454) Yoshikawa, K.; Kawasaki, H.; Yoshida, W.; Irie, T.; Konishi, K.; Nakano, K.; Uto, T.; Adachi, D.; Kanematsu, M.; Uzu, H.; Yamamoto, K. Silicon Heterojunction Solar Cell with Interdigitated Back Contacts for a Photoconversion Efficiency over 26%. *Nat. Energy* **2017**, *2*, 17032.

(455) Dauzon, E.; Sallenave, X.; Plesse, C.; Goubard, F.; Amassian, A.; Anthopoulos, T. D. Pushing the Limits of Flexibility and Stretchability of Solar Cells: A Review. *Adv. Mater.* **2021**, *33*, 2101469.

(456) Hashemi, S. A.; Ramakrishna, S.; Aberle, A. G. Recent Progress in Flexible-Wearable Solar Cells for Self-Powered Electronic Devices. *Energy Environ. Sci.* **2020**, *13*, 685–743.

(457) Fukuda, K.; Yu, K.; Someya, T. The Future of Flexible Organic Solar Cells. *Adv. Energy Mater.* **2020**, *10*, 2000765.

(458) Park, S.; Heo, S. W.; Lee, W.; Inoue, D.; Jiang, Z.; Yu, K.; Jinno, H.; Hashizume, D.; Sekino, M.; Yokota, T.; Fukuda, K.; Tajima, K.; Someya, T. Self-Powered Ultra-Flexible Electronics via Nano-Grating-Patterned Organic Photovoltaics. *Nature* **2018**, *561*, 516–521.

(459) Kojima, A.; Teshima, K.; Shirai, Y.; Miyasaka, T. Organometal Halide Perovskites as Visible-Light Sensitizers for Photovoltaic Cells. *J. Am. Chem. Soc.* **2009**, *131*, 6050–6051.

(460) Yang, L.; Feng, J.; Liu, Z.; Duan, Y.; Zhan, S.; Yang, S.; He, K.; Li, Y.; Zhou, Y.; Yuan, N.; Ding, J.; Liu, S. Record-Efficiency Flexible Perovskite Solar Cells Enabled by Multifunctional Organic Ions Interface Passivation. *Adv. Mater.* **2022**, *34*, 2201681.

(461) He, X.; Chen, J.; Ren, X.; Zhang, L.; Liu, Y.; Feng, J.; Fang, J.; Zhao, K.; Liu, S. 40.1% Record Low-Light Solar-Cell Efficiency by Holistic Trap-Passivation Using Micrometer-Thick Perovskite Film. *Adv. Mater.* **2021**, *33*, 2100770.

(462) Li, C.; Cong, S.; Tian, Z.; Song, Y.; Yu, L.; Lu, C.; Shao, Y.; Li, J.; Zou, G.; Rummeli, M. H.; Dou, S.; Sun, J.; Liu, Z. Flexible Perovskite Solar Cell-Driven Photo-Rechargeable Lithium-Ion Capacitor for Self-Powered Wearable Strain Sensors. *Nano Energy* **2019**, *60*, 247–256.

(463) Aina, S.; Villacampa, B.; Bernechea, M. Earth-Abundant Non-Toxic Perovskite Nanocrystals for Solution Processed Solar Cells. *Mater. Adv.* **2021**, *2*, 4140–4151.

(464) Bandara, T. M. W. J.; Hansadi, J. M. C.; Bella, F. A Review of Textile Dye-Sensitized Solar Cells for Wearable Electronics. *Ionics* **2022**, *28*, 2563–2583.

(465) Yang, Z.; Deng, J.; Sun, X.; Li, H.; Peng, H. Stretchable, Wearable Dye-Sensitized Solar Cells. *Adv. Mater.* **2014**, *26*, 2643–2647.

(466) Yin, L.; Moon, J.-M.; Sempionatto, J. R.; Lin, M.; Cao, M.; Trifonov, A.; Zhang, F.; Lou, Z.; Jeong, J.-M.; Lee, S.-J.; Xu, S.; Wang, J. A Passive Perspiration Biofuel Cell: High Energy Return on Investment. *Joule* **2021**, *5*, 1888–1904.

(467) Yin, L.; Kim, K. N.; Lv, J.; Tehrani, F.; Lin, M.; Lin, Z.; Moon, J.-M.; Ma, J.; Yu, J.; Xu, S.; Wang, J. A Self-Sustainable Wearable Multi-Modular E-Textile Bioenergy Microgrid System. *Nat. Commun.* **2021**, *12*, 1542.

(468) Gai, Y.; Wang, E.; Liu, M.; Xie, L.; Bai, Y.; Yang, Y.; Xue, J.; Qu, X.; Xi, Y.; Li, L.; Luo, D.; Li, Z. A Self-Powered Wearable Sensor for Continuous Wireless Sweat Monitoring. *Small Methods* **2022**, *6*, 2200653.

(469) Chen, J.; Huang, Y.; Zhang, N.; Zou, H.; Liu, R.; Tao, C.; Fan, X.; Wang, Z. L. Micro-Cable Structured Textile for Simultaneously Harvesting Solar and Mechanical Energy. *Nat. Energy* **2016**, *1*, 16138.

(470) Wen, Z.; Yeh, M.-H.; Guo, H.; Wang, J.; Zi, Y.; Xu, W.; Deng, J.; Zhu, L.; Wang, X.; Hu, C.; Zhu, L.; Sun, X.; Wang, Z. L. Self-Powered Textile for Wearable Electronics by Hybridizing Fiber-Shaped Nanogenerators, Solar Cells, and Supercapacitors. *Sci. Adv.* **2016**, *2*, No. e1600097.

(471) Ren, Z.; Zheng, Q.; Wang, H.; Guo, H.; Miao, L.; Wan, J.; Xu, C.; Cheng, S.; Zhang, H. Wearable and Self-Cleaning Hybrid Energy Harvesting System Based on Micro/Nanostructured Haze Film. *Nano Energy* **2020**, *67*, 104243.

(472) Kim, Y. J.; Park, S. E.; Cho, B. J. A Wearable Organic Photovoltaic-Thermoelectric (OPV-TE) Hybrid Generator to Minimize the Open-Circuit Voltage Losses of OPV Module. *Nano Energy* **2022**, *93*, 106775.

(473) Rose, D. P.; Ratterman, M. E.; Griffin, D. K.; Hou, L.; Kelley-Loughnane, N.; Naik, R. R.; Hagen, J. A.; Papautsky, I.; Heikenfeld, J. C. Adhesive RFID Sensor Patch for Monitoring of Sweat Electrolytes. *IEEE Trans. Biomed. Eng.* **2015**, *62*, 1457–1465.

(474) Xu, G.; Cheng, C.; Liu, Z.; Yuan, W.; Wu, X.; Lu, Y.; Low, S. S.; Liu, J.; Zhu, L.; Ji, D.; Li, S.; Chen, Z.; Wang, L.; Yang, Q.; Cui, Z.; Liu, Q. Battery-Free and Wireless Epidermal Electrochemical System with All-Printed Stretchable Electrode Array for Multiplexed In Situ Sweat Analysis. *Adv. Mater. Technol.* **2019**, *4*, 1800658.

(475) Koo, M.; Park, K.-I.; Lee, S. H.; Suh, M.; Jeon, D. Y.; Choi, J. W.; Kang, K.; Lee, K. J. Bendable Inorganic Thin-Film Battery for Fully Flexible Electronic Systems. *Nano Lett.* **2012**, *12*, 4810–4816.

(476) Xu, S.; Zhang, Y.; Cho, J.; Lee, J.; Huang, X.; Jia, L.; Fan, J. A.; Su, Y.; Su, J.; Zhang, H.; Cheng, H.; Lu, B.; Yu, C.; Chuang, C.; Kim, T.; Song, T.; Shigeta, K.; Kang, S.; Dagdeviren, C.; Petrov, I.; Braun, P. V.; Huang, Y.; Paik, U.; Rogers, J. A. Stretchable Batteries with Self-Similar Serpentine Interconnects and Integrated Wireless Recharging Systems. *Nat. Commun.* **2013**, *4*, 1543.

(477) Song, Z.; Ma, T.; Tang, R.; Cheng, Q.; Wang, X.; Krishnaraju, D.; Panat, R.; Chan, C. K.; Yu, H.; Jiang, H. Origami Lithium-Ion Batteries. *Nat. Commun.* **2014**, *5*, 3140.

(478) He, J.; Lu, C.; Jiang, H.; Han, F.; Shi, X.; Wu, J.; Wang, L.; Chen, T.; Wang, J.; Zhang, Y.; Yang, H.; Zhang, G.; Sun, X.; Wang, B.; Chen, P.; Wang, Y.; Xia, Y.; Peng, H. Scalable Production of High-Performing Woven Lithium-Ion Fibre Batteries. *Nature* **2021**, *597*, 57–63.

(479) Yin, L.; Scharf, J.; Ma, J.; Doux, J.-M.; Redquest, C.; Le, V. L.; Yin, Y.; Ortega, J.; Wei, X.; Wang, J.; Meng, Y. S. High Performance Printed AgO-Zn Rechargeable Battery for Flexible Electronics. *Joule* **2021**, *5*, 228–248.

(480) Yin, L.; Cao, M.; Kim, K. N.; Lin, M.; Moon, J.-M.; Sempionatto, J. R.; Yu, J.; Liu, R.; Wicker, C.; Trifonov, A.; Zhang, F.; Hu, H.; Moreto, J. R.; Go, J.; Xu, S.; Wang, J. A Stretchable Epidermal Sweat Sensing Platform with an Integrated Printed Battery and Electrochromic Display. *Nat. Electron.* **2022**, *5*, 694–705.

(481) Bandodkar, A. J.; Lee, S. P.; Huang, I.; Li, W.; Wang, S.; Su, C.-J.; Jeang, W. J.; Hang, T.; Mehta, S.; Nyberg, N.; Gutruf, P.; Choi, J.; Koo, J.; Reeder, J. T.; Tseng, R.; Ghaffari, R.; Rogers, J. A. Sweat-Activated Biocompatible Batteries for Epidermal Electronic and Microfluidic Systems. *Nat. Electron.* **2020**, *3*, 554–562.

(482) Liu, Y.; Huang, X.; Zhou, J.; Yiu, C. K.; Song, Z.; Huang, W.; Nejad, S. K.; Li, H.; Wong, T. H.; Yao, K.; Zhao, L.; Yoo, W.; Park, W.; Li, J.; Huang, Y.; Lam, H. R.; Song, E.; Guo, X.; Wang, Y.; Dai, Z.; Chang, L.; Li, W. J.; Xie, Z.; Yu, X. Stretchable Sweat-Activated Battery in Skin-Integrated Electronics for Continuous Wireless Sweat Monitoring. *Adv. Sci.* **2022**, *9*, 2104635.

(483) Lv, J.; Thangavel, G.; Li, Y.; Xiong, J.; Gao, D.; Ciou, J.; Tan, M. W. M.; Aziz, I.; Chen, S.; Chen, J.; Zhou, X.; Poh, W. C.; Lee, P. S.

Printable Elastomeric Electrodes with Sweat-Enhanced Conductivity for Wearables. *Sci. Adv.* **2021**, *7*, No. eabg8433.

(484) Xiao, G.; Ju, J.; Lu, H.; Shi, X.; Wang, X.; Wang, W.; Xia, Q.; Zhou, G.; Sun, W.; Li, C. M.; Qiao, Y.; Lu, Z. A Weavable and Scalable Cotton-Yarn-Based Battery Activated by Human Sweat for Textile Electronics. *Adv. Sci.* **2022**, *9*, 2103822.

(485) Xue, Q.; Sun, J.; Huang, Y.; Zhu, M.; Pei, Z.; Li, H.; Wang, Y.; Li, N.; Zhang, H.; Zhi, C. Recent Progress on Flexible and Wearable Supercapacitors. *Small* **2017**, *13*, 1701827.

(486) Atta, M. M.; Fahim, R. A. Flexible and Wearable Supercapacitors: A Short Review. *J. Energy Storage* **2021**, *44*, 103475.

(487) Manjakkal, L.; Pullanchiyodan, A.; Yogeswaran, N.; Hosseini, E. S.; Dahiya, R. A Wearable Supercapacitor Based on Conductive PEDOT:PSS-Coated Cloth and a Sweat Electrolyte. *Adv. Mater.* **2020**, *32*, 1907254.

(488) Selvam, S.; Park, Y.; Yim, J. Design and Testing of Autonomous Chargeable and Wearable Sweat/Ionic Liquid-Based Supercapacitors. *Adv. Sci.* **2022**, *9*, 2201890.

(489) Lima, N.; Baptista, A. C.; Faustino, B. M. M.; Taborda, S.; Marques, A.; Ferreira, I. Carbon Threads Sweat-Based Supercapacitors for Electronic Textiles. *Sci. Rep.* **2020**, *10*, 7703.

(490) Lv, J.; Jeerapan, I.; Tehrani, F.; Yin, L.; Silva-Lopez, C. A.; Jang, J.-H.; Joshua, D.; Shah, R.; Liang, Y.; Xie, L.; Soto, F.; Chen, C.; Karshalev, E.; Kong, C.; Yang, Z.; Wang, J. Sweat-Based Wearable Energy Harvesting-Storage Hybrid Textile Devices. *Energy Environ. Sci.* **2018**, *11*, 3431–3442.

(491) Lv, J.; Yin, L.; Chen, X.; Jeerapan, I.; Silva, C. A.; Li, Y.; Le, M.; Lin, Z.; Wang, L.; Trifonov, A.; Xu, S.; Cosnier, S.; Wang, J. Wearable Biosupercapacitor: Harvesting and Storing Energy from Sweat. *Adv. Funct. Mater.* **2021**, *31*, 2102915.

(492) Oh, S. Y.; Guy, R. H. Effects of Iontophoresis on the Electrical Properties of Human Skin in Vivo. *Int. J. Pharm.* **1995**, *124*, 137–142.

(493) Ma, D.; Ghoreishizadeh, S. S.; Georgiou, P. Concurrent Potentiometric and Amperometric Sensing With Shared Reference Electrodes. *IEEE Sensors J.* **2021**, *21*, 5720–5727.

(494) Talkhooncheh, A. H.; Yu, Y.; Agarwal, A.; Kuo, W. W.-T.; Chen, K.-C.; Wang, M.; Hoskuldottir, G.; Gao, W.; Emami, A. A Biofuel-Cell-Based Energy Harvester With 86% Peak Efficiency and 0.25-V Minimum Input Voltage Using Source-Adaptive MPPT. *IEEE J. Solid-State Circuits* **2021**, *56*, 715–728.

(495) Voulgari, E.; Krummenacher, F.; Kayal, M. ANTIGONE: A Programmable Energy-Efficient Current Digitizer for an ISFET Wearable Sweat Sensing System. *Sensors* **2021**, *21*, 2074.

(496) Chung, H. U.; Kim, B. H.; Lee, J. Y.; Lee, J.; Xie, Z.; Ibler, E. M.; Lee, K.; Banks, A.; Jeong, J. Y.; Kim, J.; Ogle, C.; Grande, D.; Yu, Y.; Jang, H.; Assem, P.; Ryu, D.; Kwak, J. W.; Namkoong, M.; Park, J. B.; Lee, Y.; Kim, D. H.; Ryu, A.; Jeong, J.; You, K.; Ji, B.; Liu, Z.; Huo, Q.; Feng, X.; Deng, Y.; Xu, Y.; Jang, K.-I.; Kim, J.; Zhang, Y.; Ghaffari, R.; Rand, C. M.; Schau, M.; Hamvas, A.; Weese-Mayer, D. E.; Huang, Y.; Lee, S. M.; Lee, C. H.; Shanbhag, N. R.; Paller, A. S.; Xu, S.; Rogers, J. A. Binodal, Wireless Epidermal Electronic Systems with in-Sensor Analytics for Neonatal Intensive Care. *Science* **2019**, *363*, No. eaau0780.

(497) Matsuhisa, N.; Chen, X.; Bao, Z.; Someya, T. Materials and Structural Designs of Stretchable Conductors. *Chem. Soc. Rev.* **2019**, *48*, 2946–2966.

(498) Wang, S.; Xu, J.; Wang, W.; Wang, G.-J. N.; Rastak, R.; Molina-Lopez, F.; Chung, J. W.; Niu, S.; Feig, V. R.; Lopez, J.; Lei, T.; Kwon, S.-K.; Kim, Y.; Foudeh, A. M.; Ehrlich, A.; Gasperini, A.; Yun, Y.; Murmann, B.; Tok, J. B.-H.; Bao, Z. Skin Electronics from Scalable Fabrication of an Intrinsically Stretchable Transistor Array. *Nature* **2018**, *555*, 83–88.

(499) Li, R. T.; Kling, S. R.; Salata, M. J.; Cupp, S. A.; Sheehan, J.; Voos, J. E. Wearable Performance Devices in Sports Medicine. *Sports Health* **2016**, *8*, 74–78.

(500) Seshadri, D. R.; Li, R. T.; Voos, J. E.; Rowbottom, J. R.; Alfes, C. M.; Zorman, C. A.; Drummond, C. K. Wearable Sensors for Monitoring the Internal and External Workload of the Athlete. *npj Digit. Med.* **2019**, *2*, 71.

(501) Gabbett, T. J. The Training—Injury Prevention Paradox: Should Athletes Be Training Smarter and Harder? *Br. J. Sports Med.* **2016**, *50*, 273–280.

(502) Strath, S. J.; Swartz, A. M.; Bassett, D. R.; O'Brien, W. L.; King, G. A.; Ainsworth, B. E. Evaluation of Heart Rate as a Method for Assessing Moderate Intensity Physical Activity. *Med. Sci. Sports Exerc.* **2000**, *32*, S465–70.

(503) Esteve-Lanao, J.; Foster, C.; Seiler, S.; Lucia, A. Impact of training intensity distribution on performance in endurance athletes. *J. Strength Cond. Res.* **2007**, *21* (3), 943–949.

(504) Seiler, K. S.; Kjerland, G. Ø. Quantifying Training Intensity Distribution in Elite Endurance Athletes: Is There Evidence for an “Optimal” Distribution? *Scand. J. Med. Sci. Sports* **2006**, *16*, 49–56.

(505) Armstrong, L. E.; Casa, D. J.; Millard-Stafford, M.; Moran, D. S.; Pyne, S. W.; Roberts, W. O. Exertional Heat Illness during Training and Competition. *Med. Sci. Sports Exerc.* **2007**, *39*, S56–S72.

(506) Hew-Butler, T.; Rosner, M. H.; Fowkes-Godek, S.; Dugas, J. P.; Hoffman, M. D.; Lewis, D. P.; Maughan, R. J.; Miller, K. C.; Montain, S. J.; Rehrer, N. J.; Roberts, W. O.; Rogers, I. R.; Siegel, A. J.; Stuempfle, K. J.; Winger, J. M.; Verbalis, J. G. Statement of the Third International Exercise-Associated Hyponatremia Consensus Development Conference, Carlsbad, California, 2015. *Clin. J. Sport Med.* **2015**, *25*, 303–320.

(507) Baker, L. B. Sweating Rate and Sweat Sodium Concentration in Athletes: A Review of Methodology and Intra/Interindividual Variability. *Sports Med.* **2017**, *47*, 111–128.

(508) Baker, L. B.; Barnes, K. A.; Anderson, M. L.; Passe, D. H.; Stofan, J. R. Normative Data for Regional Sweat Sodium Concentration and Whole-Body Sweating Rate in Athletes. *J. Sports Sci.* **2016**, *34*, 358–368.

(509) Medbø, J. I.; Sejersted, O. M. Plasma Potassium Changes with High Intensity Exercise. *J. Physiol.* **1990**, *421*, 105–122.

(510) Baker, L. B.; Stofan, J. R.; Hamilton, A. A.; Horswill, C. A. Comparison of Regional Patch Collection vs. Whole Body Washdown for Measuring Sweat Sodium and Potassium Loss during Exercise. *J. Appl. Physiol.* **2009**, *107*, 887–895.

(511) Seshadri, D. R.; Li, R. T.; Voos, J. E.; Rowbottom, J. R.; Alfes, C. M.; Zorman, C. A.; Drummond, C. K. Wearable Sensors for Monitoring the Physiological and Biochemical Profile of the Athlete. *NPJ. Digit. Med.* **2019**, *2*, 72.

(512) Buono, M. J.; Lee, N. V. L.; Miller, P. W. The Relationship between Exercise Intensity and the Sweat Lactate Excretion Rate. *J. Physiol. Sci.* **2010**, *60*, 103–107.

(513) Seki, Y.; Nakashima, D.; Shiraiishi, Y.; Ryuzaki, T.; Ikura, H.; Miura, K.; Suzuki, M.; Watanabe, T.; Nagura, T.; Matsumoto, M.; Nakamura, M.; Sato, K.; Fukuda, K.; Katsumata, Y. A Novel Device for Detecting Anaerobic Threshold Using Sweat Lactate during Exercise. *Sci. Rep.* **2021**, *11*, 4929.

(514) Karpova, E. V.; Laptev, A. I.; Andreev, E. A.; Karyakina, E. E.; Karyakin, A. A. Relationship Between Sweat and Blood Lactate Levels During Exhaustive Physical Exercise. *ChemElectroChem.* **2020**, *7*, 191–194.

(515) Mitsubayashi, K.; Suzuki, M.; Tamiya, E.; Karube, I. Analysis of Metabolites in Sweat as a Measure of Physical Condition. *Anal. Chim. Acta* **1994**, *289*, 27–34.

(516) Derbyshire, P. J.; Barr, H.; Davis, F.; Higson, S. P. J. Lactate in Human Sweat: A Critical Review of Research to the Present Day. *J. Physiol. Sci.* **2012**, *62*, 429–440.

(517) Araki, T.; Matsushita, K.; Umeno, K.; Tsujino, A.; Toda, Y. Effect of Physical Training on Exercise-Induced Sweating in Women. *J. Appl. Physiol.* **1981**, *51*, 1526–1532.

(518) Fellmann, N.; Grizard, G.; Coudert, J. Human Frontal Sweat Rate and Lactate Concentration during Heat Exposure and Exercise. *J. Appl. Physiol.* **1983**, *54*, 355–360.

(519) Mena-Bravo, A.; Luque de Castro, M. D. Sweat: A Sample with Limited Present Applications and Promising Future in Metabolomics. *J. Pharm. Biomed. Anal.* **2014**, *90*, 139–147.

- (520) Van Hoovels, K.; Xuan, X.; Cuartero, M.; Gijssels, M.; Swarén, M.; Crespo, G. A. Can Wearable Sweat Lactate Sensors Contribute to Sports Physiology? *ACS Sens.* **2021**, *6*, 3496–3508.
- (521) Crocker, P.; Graham, T. Coping by Competitive Athletes with Performance Stress: Gender Differences and Relationships with Affect. *Sport Psychologist* **1995**, *9*, 325–338.
- (522) Kuipers, H. Training and Overtraining: An Introduction. *Med. Sci. Sports Exerc.* **1998**, *30*, 1137–1139.
- (523) Angeli, A.; Minetto, M.; Dovio, A.; Paccotti, P. The Overtraining Syndrome in Athletes: A Stress-Related Disorder. *J. Endocrinol. Invest.* **2004**, *27*, 603–612.
- (524) Cutting, G. R. MODIFIER GENETICS: Cystic Fibrosis. *Annu. Rev. Genom. Hum. Genet.* **2005**, *6*, 237–260.
- (525) Quinton, P. M. Chloride Impermeability in Cystic Fibrosis. *Nature* **1983**, *301*, 421–422.
- (526) Farrell, P. M.; Rosenstein, B. J.; White, T. B.; Accurso, F. J.; Castellani, C.; Cutting, G. R.; Durie, P. R.; LeGrys, V. A.; Massie, J.; Parad, R. B.; Rock, M. J.; Campbell, P. W. Guidelines for Diagnosis of Cystic Fibrosis in Newborns through Older Adults: Cystic Fibrosis Foundation Consensus Report. *J. Pediatr.* **2008**, *153*, S4–S14.
- (527) Ooi, C. Y.; Castellani, C.; Keenan, K.; Avolio, J.; Volpi, S.; Boland, M.; Kovesi, T.; Bjornson, C.; Chilvers, M. A.; Morgan, L.; van Wylick, R.; Kent, S.; Price, A.; Solomon, M.; Tam, K.; Taylor, L.; Malitt, K.-A.; Ratjen, F.; Durie, P. R.; Gonska, T. Inconclusive Diagnosis of Cystic Fibrosis After Newborn Screening. *Pediatrics* **2015**, *135*, e1377–e1385.
- (528) Hammond, K. B.; Turcios, N. L.; Gibson, L. E. Clinical Evaluation of the Macroduct Sweat Collection System and Conductivity Analyzer in the Diagnosis of Cystic Fibrosis. *J. Pediatr.* **1994**, *124*, 255–260.
- (529) Cirilli, N.; Southern, K. W.; Buzzetti, R.; Barben, J.; Nährlich, L.; Munck, A.; Wilschanski, M.; De Boeck, K.; Derichs, N. Real Life Practice of Sweat Testing in Europe. *J. Cyst. Fibros.* **2018**, *17*, 325–332.
- (530) LeGrys, V. A.; McColley, S. A.; Li, Z.; Farrell, P. M. The Need for Quality Improvement in Sweat Testing Infants after Newborn Screening for Cystic Fibrosis. *J. Pediatr.* **2010**, *157*, 1035–1037.
- (531) Farrell, P. M.; Sommerburg, O. Toward Quality Improvement in Cystic Fibrosis Newborn Screening: Progress and Continuing Challenges. *J. Cyst. Fibros.* **2016**, *15*, 267–269.
- (532) Choi, D.-H.; Thaxton, A.; Jeong, I. c.; Kim, K.; Sosnay, P. R.; Cutting, G. R.; Searson, P. C. Sweat Test for Cystic Fibrosis: Wearable Sweat Sensor vs. Standard Laboratory Test. *J. Cyst. Fibros.* **2018**, *17*, e35–e38.
- (533) Ray, T. R.; Ivanovic, M.; Curtis, P. M.; Franklin, D.; Guventurk, K.; Jeang, W. J.; Chafetz, J.; Gaertner, H.; Young, G.; Rebollo, S.; Model, J. B.; Lee, S. P.; Ciraldo, J.; Reeder, J. T.; Hourlier-Fargette, A.; Bandodkar, A. J.; Choi, J.; Aranyosi, A. J.; Ghaffari, R.; McColley, S. A.; Haymond, S.; Rogers, J. A. Soft, Skin-Interfaced Sweat Stickers for Cystic Fibrosis Diagnosis and Management. *Sci. Transl. Med.* **2021**, *13*, No. eabd8109.
- (534) Riccardi, G.; Rivellese, A. A. Dietary Treatment of the Metabolic Syndrome — the Optimal Diet. *Br. J. Nutr.* **2000**, *83*, S143–S148.
- (535) Hu, F. B. Globalization of Diabetes: The Role of Diet, Lifestyle, and Genes. *Diabetes Care* **2011**, *34*, 1249–1257.
- (536) Kromhout, D. Diet and Cardiovascular Diseases. *J. Nutr. Health Aging* **2001**, *5*, 144–149.
- (537) *Diet, Nutrition, and the Prevention of Chronic Diseases: Report of a WHO-FAO Expert Consultation; [Joint WHO-FAO Expert Consultation on Diet, Nutrition, and the Prevention of Chronic Diseases, 2002, Geneva, Switzerland]*; Weltgesundheitsorganisation, FAO, Eds.; WHO technical report series; World Health Organization: Geneva, 2003.
- (538) Stubbs, R. J.; O'Reilly, L. M.; Whybrow, S.; Fuller, Z.; Johnstone, A. M.; Livingstone, M. B. E.; Ritz, P.; Horgan, G. W. Measuring the Difference between Actual and Reported Food Intakes in the Context of Energy Balance under Laboratory Conditions. *Br. J. Nutr.* **2014**, *111*, 2032–2043.
- (539) Rennie, K. L.; Coward, A.; Jebb, S. A. Estimating Under-Reporting of Energy Intake in Dietary Surveys Using an Individualised Method. *Br. J. Nutr.* **2007**, *97*, 1169–1176.
- (540) Moyer, J.; Wilson, D.; Finkelshtein, I.; Wong, B.; Potts, R. Correlation Between Sweat Glucose and Blood Glucose in Subjects with Diabetes. *Diabetes Technol. Ther.* **2012**, *14*, 398–402.
- (541) Nyein, H. Y. Y.; Bariya, M.; Kivimäki, L.; Uusitalo, S.; Liaw, T. S.; Jansson, E.; Ahn, C. H.; Hangasky, J. A.; Zhao, J.; Lin, Y.; Happonen, T.; Chao, M.; Liedert, C.; Zhao, Y.; Tai, L.-C.; Hiltunen, J.; Javey, A. Regional and Correlative Sweat Analysis Using High-Throughput Microfluidic Sensing Patches toward Decoding Sweat. *Sci. Adv.* **2019**, *5*, No. eaaw9906.
- (542) Karpova, E. V.; Shcherbacheva, E. V.; Galushin, A. A.; Vokhmyanina, D. V.; Karyakina, E. E.; Karyakin, A. A. Noninvasive Diabetes Monitoring through Continuous Analysis of Sweat Using Flow-Through Glucose Biosensor. *Anal. Chem.* **2019**, *91*, 3778–3783.
- (543) Lynch, C. J.; Adams, S. H. Branched-Chain Amino Acids in Metabolic Signalling and Insulin Resistance. *Nat. Rev. Endocrinol.* **2014**, *10*, 723–736.
- (544) Wang, T. J.; Larson, M. G.; Vasan, R. S.; Cheng, S.; Rhee, E. P.; McCabe, E.; Lewis, G. D.; Fox, C. S.; Jacques, P. F.; Fernandez, C.; O'Donnell, C. J.; Carr, S. A.; Mootha, V. K.; Florez, J. C.; Souza, A.; Melander, O.; Clish, C. B.; Gerszten, R. E. Metabolite Profiles and the Risk of Developing Diabetes. *Nat. Med.* **2011**, *17*, 448–453.
- (545) Mayers, J. R.; Wu, C.; Clish, C. B.; Kraft, P.; Torrence, M. E.; Fiske, B. P.; Yuan, C.; Bao, Y.; Townsend, M. K.; Tworoger, S. S.; Davidson, S. M.; Papagiannakopoulos, T.; Yang, A.; Dayton, T. L.; Ogino, S.; Stampfer, M. J.; Giovannucci, E. L.; Qian, Z. R.; Rubinson, D. A.; Ma, J.; Sesso, H. D.; Gaziano, J. M.; Cochrane, B. B.; Liu, S.; Wactawski-Wende, J.; Manson, J. E.; Pollak, M. N.; Kimmelman, A. C.; Souza, A.; Pierce, K.; Wang, T. J.; Gerszten, R. E.; Fuchs, C. S.; Vander Heiden, M. G.; Wolpin, B. M. Elevation of Circulating Branched-Chain Amino Acids Is an Early Event in Human Pancreatic Adenocarcinoma Development. *Nat. Med.* **2014**, *20*, 1193–1198.
- (546) Sempionatto, J. R.; Montiel, V. R.-V.; Vargas, E.; Teymourian, H.; Wang, J. Wearable and Mobile Sensors for Personalized Nutrition. *ACS Sens.* **2021**, *6*, 1745–1760.
- (547) Kim, J.; Wu, Y.; Luan, H.; Yang, D. S.; Cho, D.; Kwak, S. S.; Liu, S.; Ryu, H.; Ghaffari, R.; Rogers, J. A. A Skin-Interfaced, Miniaturized Microfluidic Analysis and Delivery System for Colorimetric Measurements of Nutrients in Sweat and Supply of Vitamins Through the Skin. *Adv. Sci.* **2022**, *9*, 2103331.
- (548) Wainberg, M. L.; Scorza, P.; Shultz, J. M.; Helpman, L.; Mootz, J. J.; Johnson, K. A.; Neria, Y.; Bradford, J.-M. E.; Oquendo, M. A.; Arbuckle, M. R. Challenges and Opportunities in Global Mental Health: A Research-to-Practice Perspective. *Curr. Psychiatry. Rep.* **2017**, *19*, 28.
- (549) COVID-19 pandemic triggers 25% increase in prevalence of anxiety and depression worldwide. <https://www.who.int/news/item/02-03-2022-covid-19-pandemic-triggers-25-increase-in-prevalence-of-anxiety-and-depression-worldwide> (accessed 2022-10-18).
- (550) Goldstein, D. S. *Stress, Catecholamines, and Cardiovascular Disease*; Oxford University Press: New York, NY, 1995; pp xxii, 539.
- (551) Steptoe, A.; Kivimäki, M. Stress and Cardiovascular Disease. *Nat. Rev. Cardiol.* **2012**, *9*, 360–370.
- (552) Report: Mental Illness Will Cost the World \$16 Trillion (USD) by 2030. *Ment. Health Wkly.* **2018**, *28*, 7–8.
- (553) Kesner, L.; Horáček, J. Global Adversities, the Media, and Mental Health. *Front. Psychiatry* **2022**, *12*. DOI: 10.3389/fpsyt.2021.809239
- (554) Gay, V.; Leijdekkers, P. Bringing Health and Fitness Data Together for Connected Health Care: Mobile Apps as Enablers of Interoperability. *J. Med. Internet Res.* **2015**, *17*, No. e260.
- (555) Hsiao, K.-L.; Chen, C.-C. What Drives Smartwatch Purchase Intention? Perspectives from Hardware, Software, Design, and Value. *Telemat. Inform.* **2018**, *35*, 103–113.
- (556) Coulon, S. M.; Monroe, C. M.; West, D. S. A Systematic, Multi-Domain Review of Mobile Smartphone Apps for Evidence-Based Stress Management. *Am. J. Prev. Med.* **2016**, *51*, 95–105.

- (557) Nicolson, N. A. Measurement of Cortisol. In *Handbook of physiological research methods in health psychology*; Sage Publications, Inc: Thousand Oaks, CA, 2008; pp 37–74.
- (558) Sherman, B.; Wysham, W.; Pfohl, B. Age-Related Changes in the Circadian Rhythm of Plasma Cortisol in Man. *J. Clin. Endocrinol. Metab.* **1985**, *61*, 439–443.
- (559) Keller, J.; Flores, B.; Gomez, R. G.; Solvason, H. B.; Kenna, H.; Williams, G. H.; Schatzberg, A. F. Cortisol Circadian Rhythm Alterations in Psychotic Major Depression. *Biol. Psychiatry* **2006**, *60*, 275–281.
- (560) Kang, J.-S.; Lee, M.-H. Overview of Therapeutic Drug Monitoring. *Korean J. Int. Med.* **2009**, *24*, 1–10.
- (561) Ogilvie, R. I. Clinical Pharmacokinetics of Theophylline. *Clin. Pharmacokinet.* **1978**, *3*, 267–293.
- (562) Amdisen, A. Serum Level Monitoring and Clinical Pharmacokinetics of Lithium. *Clin. Pharmacokinet.* **1977**, *2*, 73–92.
- (563) Richens, A. Clinical Pharmacokinetics of Phenytoin. *Clin. Pharmacokinet.* **1979**, *4*, 153–169.
- (564) Shihabi, Z. K. Review of Drug Analysis with Direct Serum Injection on the HPLC Column. *J. Liq. Chromatogr.* **1988**, *11*, 1579–1593.
- (565) Adaway, J. E.; Keevil, B. G. Therapeutic Drug Monitoring and LC-MS/MS. *J. Chromatogr. B* **2012**, *883–884*, 33–49.
- (566) Carlier, M.; Stove, V.; Wallis, S. C.; De Waele, J. J.; Verstraete, A. G.; Lipman, J.; Roberts, J. A. Assays for Therapeutic Drug Monitoring of  $\beta$ -Lactam Antibiotics: A Structured Review. *Int. J. Antimicrob. Agents* **2015**, *46*, 367–375.
- (567) Lin, S.; Yu, W.; Wang, B.; Zhao, Y.; En, K.; Zhu, J.; Cheng, X.; Zhou, C.; Lin, H.; Wang, Z.; Hojaiji, H.; Yeung, C.; Milla, C.; Davis, R. W.; Emaminejad, S. Noninvasive Wearable Electroactive Pharmaceutical Monitoring for Personalized Therapeutics. *Proc. Natl. Acad. Sci. U.S.A.* **2020**, *117*, 19017–19025.
- (568) Brunmair, J.; Gotsmy, M.; Niederstaetter, L.; Neuditschko, B.; Bileck, A.; Slany, A.; Feuerstein, M. L.; Langbauer, C.; Janker, L.; Zanghellini, J.; Meier-Menches, S. M.; Gerner, C. Finger Sweat Analysis Enables Short Interval Metabolic Biomonitoring in Humans. *Nat. Commun.* **2021**, *12*, 5993.
- (569) Marsden, C. D. Problems with Long-Term Levodopa Therapy for Parkinson's Disease. *Clin. Neuropharmacol.* **1994**, *17*, S32–S44.
- (570) Lin, S.; Wang, B.; Yu, W.; Castillo, K.; Hoffman, C.; Cheng, X.; Zhao, Y.; Gao, Y.; Wang, Z.; Lin, H.; Hojaiji, H.; Tan, J.; Emaminejad, S. Design Framework and Sensing System for Noninvasive Wearable Electroactive Drug Monitoring. *ACS Sens.* **2020**, *5*, 265–273.
- (571) Kintz, P. Drug Testing in Addicts: A Comparison Between Urine, Sweat, and Hair. *Ther. Drug Monit.* **1996**, *18*, 450–455.
- (572) Brunet, B. R.; Barnes, A. J.; Choo, R. E.; Mura, P.; Jones, H. E.; Huestis, M. A. Monitoring Pregnant Women's Illicit Opiate and Cocaine Use With Sweat Testing. *Ther. Drug Monit.* **2010**, *32*, 40–49.
- (573) Joseph, R. E., Jr; Oyler, J. M.; Wstadik, A. T.; Oluo, C.; Cone, E. J. Drug Testing with Alternative Matrices I. Pharmacological Effects and Disposition of Cocaine and Codeine in Plasma, Sebum, and Stratum Corneum. *J. Anal. Toxicol.* **1998**, *22*, 6–17.
- (574) Kintz, P. Excretion of MBDB and BDB in Urine, Saliva, and Sweat Following Single Oral Administration. *J. Anal. Toxicol.* **1997**, *21*, 570–575.
- (575) Kintz, P.; Villain, M.; Cirimele, V.; Goullé, J. P.; Ludes, B. [Crime under the influence of psychoactive drugs: the problem of the duration of detection]. *Acta. Clin. Belg.* **2002**, *57* (Suppl 1), 24–30.
- (576) Fogerson, R.; Schoendorfer, D.; Fay, J.; Spiehler, V. Qualitative Detection of Opiates in Sweat by EIA and GC-MS. *J. Anal. Toxicol.* **1997**, *21*, 451–458.
- (577) Jadoon, S.; Karim, S.; Akram, M. R.; Kalsoom Khan, A.; Zia, M. A.; Siddiqi, A. R.; Murtaza, G. Recent Developments in Sweat Analysis and Its Applications. *Int. J. Anal. Chem.* **2015**, *2015*, No. e164974.
- (578) Kintz, P.; Tracqui, A.; Mangin, P.; Edel, Y. Sweat Testing in Opioid Users with a Sweat Patch. *J. Anal. Toxicol.* **1996**, *20*, 393–397.
- (579) Kintz, P.; Brenneisen, R.; Bundeli, P.; Mangin, P. Sweat Testing for Heroin and Metabolites in a Heroin Maintenance Program. *Clin. Chem.* **1997**, *43*, 736–739.
- (580) Buono, M. J. Sweat Ethanol Concentrations Are Highly Correlated with Co-Existing Blood Values in Humans. *Exp. Physiol.* **1999**, *84*, 401–404.
- (581) Tison, J.; Nichols, J. L.; Casanova, T.; Chaudhary, N. K. *Comparative Study and Evaluation of SCRAM Use, Recidivism Rates, and Characteristics*; DTNH22-09-D-00133, Task 1; Preusser Research Group, Inc., 2015.
- (582) van Egmond, K.; Wright, C. J. C.; Livingston, M.; Kuntsche, E. Wearable Transdermal Alcohol Monitors: A Systematic Review of Detection Validity, and Relationship Between Transdermal and Breath Alcohol Concentration and Influencing Factors. *Alcohol. Clin. Exp. Res.* **2020**, *44*, 1918–1932.
- (583) Sakai, J. T.; Mikulich-Gilbertson, S. K.; Long, R. J.; Crowley, T. J. Validity of Transdermal Alcohol Monitoring: Fixed and Self-Regulated Dosing. *Alcohol. Clin. Exp. Res.* **2006**, *30*, 26–33.
- (584) Barnett, N. P.; Tidey, J.; Murphy, J. G.; Swift, R.; Colby, S. M. Contingency Management for Alcohol Use Reduction: A Pilot Study Using a Transdermal Alcohol Sensor. *Drug Alcohol Depend.* **2011**, *118*, 391–399.
- (585) Gamella, M.; Campuzano, S.; Manso, J.; Rivera, G. G. de; López-Colino, F.; Reviejo, A. J.; Pingarrón, J. M. A Novel Non-Invasive Electrochemical Biosensing Device for in Situ Determination of the Alcohol Content in Blood by Monitoring Ethanol in Sweat. *Anal. Chim. Acta* **2014**, *806*, 1–7.
- (586) Villalba, K.; Cook, C.; Dévieux, J. G.; Ibanez, G. E.; Oghogho, E.; Neira, C.; Cook, R. L. Facilitators and Barriers to a Contingency Management Alcohol Intervention Involving a Transdermal Alcohol Sensor. *Heliyon* **2020**, *6*, No. e03612.
- (587) Bloch, M.; Althabe, F.; Onyamboko, M.; Kaseba-Sata, C.; Castilla, E. E.; Freire, S.; Garces, A. L.; Parida, S.; Goudar, S. S.; Kadir, M. M.; Goco, N.; Thornberry, J.; Daniels, M.; Bartz, J.; Hartwell, T.; Moss, N.; Goldenberg, R. Tobacco Use and Secondhand Smoke Exposure During Pregnancy: An Investigative Survey of Women in 9 Developing Nations. *Am. J. Public Health* **2008**, *98*, 1833–1840.
- (588) Hackshaw, A.; Morris, J. K.; Boniface, S.; Tang, J.-L.; Milenković, D. Low Cigarette Consumption and Risk of Coronary Heart Disease and Stroke: Meta-Analysis of 141 Cohort Studies in 55 Study Reports. *Br. Med. J.* **2018**, *360*, j5855.
- (589) Koh, E. H.; Lee, W.-C.; Choi, Y.-J.; Moon, J.-I.; Jang, J.; Park, S.-G.; Choo, J.; Kim, D.-H.; Jung, H. S. A Wearable Surface-Enhanced Raman Scattering Sensor for Label-Free Molecular Detection. *ACS Appl. Mater. Interfaces* **2021**, *13*, 3024–3032.
- (590) Leggett, R.; Lee-Smith, E. E.; Jickells, S. M.; Russell, D. A. Intelligent" Fingerprinting: Simultaneous Identification of Drug Metabolites and Individuals by Using Antibody-Functionalized Nanoparticles. *Angew. Chem., Int. Ed.* **2007**, *46*, 4100–4103.
- (591) Hazarika, P.; Jickells, S. M.; Wolff, K.; Russell, D. A. Multiplexed Detection of Metabolites of Narcotic Drugs from a Single Latent Fingerprint. *Anal. Chem.* **2010**, *82*, 9150–9154.
- (592) Raghupathi, W.; Raghupathi, V. An Empirical Study of Chronic Diseases in the United States: A Visual Analytics Approach to Public Health. *Int. J. Environ. Res. Public Health* **2018**, *15*, 431.
- (593) Buja, A.; Damiani, G.; Gini, R.; Visca, M.; Federico, B.; Donato, D.; Francesconi, P.; Marini, A.; Donatini, A.; Brugaletta, S.; Baldo, V.; Bellentani, M. D. Systematic Age-Related Differences in Chronic Disease Management in a Population-Based Cohort Study: A New Paradigm of Primary Care Is Required. *PLoS One* **2014**, *9*, No. e91340.
- (594) Maresova, P.; Javanmardi, E.; Barakovic, S.; Barakovic Husic, J.; Tomson, S.; Krejcar, O.; Kuca, K. Consequences of Chronic Diseases and Other Limitations Associated with Old Age - a Scoping Review. *BMC Public Health* **2019**, *19*, 1431.
- (595) Upasham, S.; Prasad, S. Tuning SLOCK toward Chronic Disease Diagnostics and Management: Label-free Sweat Interleukin-31 Detection. *ACS Omega* **2021**, *6*, 20422–20432.

- (596) Upasham, S.; Osborne, O.; Prasad, S. Demonstration of Sweat-Based Circadian Diagnostic Capability of SLOCK Using Electrochemical Detection Modalities. *RSC Adv.* **2021**, *11*, 7750–7765.
- (597) Upasham, S.; Thai, K.; Muthyala, R.; Prasad, S. Flexible, Low Volume Detection of Chronobiology Biomarkers from Human Sweat. *Analyst* **2020**, *145*, 784–796.
- (598) Upasham, S.; Rice, P.; Shahub, S.; Dhamu, V. N.; Prasad, S. Passive Sweat-Based Pruritic Cytokine Detection and Monitoring System. *ECS Sens. Plus* **2022**, *1*, 031602.
- (599) Upasham, S.; Bhide, A.; Lin, K.-C.; Prasad, S. Point-of-Use Sweat Biosensor to Track the Endocrine-Inflammation Relationship for Chronic Disease Monitoring. *Future Sci. OA* **2021**, *7*, FSO628.
- (600) Torrente-Rodríguez, R. M.; Lukas, H.; Tu, J.; Min, J.; Yang, Y.; Xu, C.; Rossiter, H. B.; Gao, W. SARS-CoV-2 RapidPlex: A Graphene-Based Multiplexed Telemedicine Platform for Rapid and Low-Cost COVID-19 Diagnosis and Monitoring. *Matter* **2020**, *3*, 1981–1998.
- (601) Lukas, H.; Xu, C.; Yu, Y.; Gao, W. Emerging Telemedicine Tools for Remote COVID-19 Diagnosis, Monitoring, and Management. *ACS Nano* **2020**, *14*, 16180–16193.
- (602) Zhao, G.; Ling, Y.; Su, Y.; Chen, Z.; Mathai, C. J.; Emeje, O.; Brown, A.; Alla, D. R.; Huang, J.; Kim, C.; Chen, Q.; He, X.; Stalla, D.; Xu, Y.; Chen, Z.; Chen, P.-Y.; Gangopadhyay, S.; Xie, J.; Yan, Z. Laser-Scribed Conductive, Photoactive Transition Metal Oxide on Soft Elastomers for Janus on-Skin Electronics and Soft Actuators. *Sci. Adv.* **2022**, *8*, No. eabp9734.
- (603) Prieto, M. A.; Vazquez, J. A.; Murado, M. A. A New and General Model to Describe, Characterize, Quantify and Classify the Interactive Effects of Temperature and pH on the Activity of Enzymes. *Analyst* **2015**, *140*, 3587–3602.
- (604) Wiorek, A.; Parrilla, M.; Cuartero, M.; Crespo, G. A. Epidermal Patch with Glucose Biosensor: pH and Temperature Correction toward More Accurate Sweat Analysis during Sport Practice. *Anal. Chem.* **2020**, *92*, 10153–10161.
- (605) Jobst, G.; Moser, L.; Varahram, M.; Svasek, P.; Aschauer, E.; Trajanoski, Z.; Wach, P.; Kotanko, P.; Skrabal, F.; Urban, G. Thin-Film Microbiosensors for Glucose-Lactate Monitoring. *Anal. Chem.* **1996**, *68*, 3173–3179.
- (606) Yokus, M. A.; Songkakul, T.; Pozdin, V. A.; Bozkurt, A.; Daniele, M. A. Wearable Multiplexed Biosensor System toward Continuous Monitoring of Metabolites. *Biosens. Bioelectron.* **2020**, *153*, 112038.
- (607) Hong, Y. J.; Lee, H.; Kim, J.; Lee, M.; Choi, H. J.; Hyeon, T.; Kim, D. H. Multifunctional Wearable System that Integrates Sweat-Based Sensing and Vital-Sign Monitoring to Estimate Pre-/Post-Exercise Glucose Levels. *Adv. Funct. Mater.* **2018**, *28*, 1805754.
- (608) Pei, X.; Sun, M.; Wang, J.; Bai, J.; Bo, X.; Zhou, M. A Bifunctional Fully Integrated Wearable Tracker for Epidermal Sweat and Wound Exudate Multiple Biomarkers Monitoring. *Small* **2022**, *18*, 2205061.
- (609) Zhou, Z.; Alvarez, D.; Milla, C.; Zare, R. N. Proof of Concept for Identifying Cystic Fibrosis from Perspiration Samples. *Proc. Natl. Acad. Sci. U.S.A.* **2019**, *116*, 24408–24412.
- (610) Kumar, S.; Chong, I. Correlation Analysis to Identify the Effective Data in Machine Learning: Prediction of Depressive Disorder and Emotion States. *Int. J. Environ. Res. Public Health* **2018**, *15*, 2907.
- (611) Sharma, K.; Castellini, C.; van den Broek, E. L.; Albu-Schaeffer, A.; Schwenker, F. A Dataset of Continuous Affect Annotations and Physiological Signals for Emotion Analysis. *Sci. Data* **2019**, *6*, 196.
- (612) Yüzer, E.; Doğan, V.; Kılıç, V.; Şen, M. Smartphone Embedded Deep Learning Approach for Highly Accurate and Automated Colorimetric Lactate Analysis in Sweat. *Sens. Actuators B Chem.* **2022**, *371*, 132489.
- (613) Monge, J.; Postolache, O.; Plopa, O.; Trandabat, A.; Schreiner, O.; Schreiner, T. Glucose Detection in Sweat Using Biosensors. *IEEE E-Health Bioengineering Conference*, 2019, DOI: 10.1109/EHB47216.2019.8970023.
- (614) Delgado-Povedano, M. del M.; Calderón-Santiago, M.; Priego-Capote, F.; Jurado-Gámez, B.; Luque de Castro, M. D. Recent Advances in Human Sweat Metabolomics for Lung Cancer Screening. *Metabolomics* **2016**, *12*, 166.
- (615) Rodríguez-Pérez, R.; Bajorath, J. Interpretation of Machine Learning Models Using Shapley Values: Application to Compound Potency and Multi-Target Activity Predictions. *J. Comput. Aided Mol. Des.* **2020**, *34*, 1013–1026.
- (616) Ballard, Z.; Brown, C.; Madni, A. M.; Ozcan, A. Machine Learning and Computation-Enabled Intelligent Sensor Design. *Nat. Mach. Intell.* **2021**, *3*, S56–S65.
- (617) Zhang, K.; Wang, J.; Liu, T.; Luo, Y.; Loh, X. J.; Chen, X. Machine Learning-Reinforced Noninvasive Biosensors for Healthcare. *Adv. Healthcare Mater.* **2021**, *10*, 2100734.
- (618) Lenz, M.; Müller, F.-J.; Zenke, M.; Schuppert, A. Principal Components Analysis and the Reported Low Intrinsic Dimensionality of Gene Expression Microarray Data. *Sci. Rep.* **2016**, *6*, 25696.
- (619) Kammarchedu, V.; Butler, D.; Ebrahimi, A. A Machine Learning-Based Multimodal Electrochemical Analytical Device Based on EMoSx-LIG for Multiplexed Detection of Tyrosine and Uric Acid in Sweat and Saliva. *Anal. Chim. Acta* **2022**, *1232*, 340447.
- (620) Cui, F.; Yue, Y.; Zhang, Y.; Zhang, Z.; Zhou, H. S. Advancing Biosensors with Machine Learning. *ACS Sens.* **2020**, *5*, 3346–3364.
- (621) Mend, M.; Kullmann, W. H. Human Computer Interface with Online Brute Force Feature Selection. *Biomed. Technol. (Berl)* **2012**, *57*, 659–662.
- (622) Stasak, B.; Huang, Z.; Razavi, S.; Joachim, D.; Epps, J. Automatic Detection of COVID-19 Based on Short-Duration Acoustic Smartphone Speech Analysis. *J. Healthc. Inform. Res.* **2021**, *5*, 201–217.
- (623) Hasan, H.; Tahir, N. M. Feature Selection of Breast Cancer Based on Principal Component Analysis. *IEEE Int. Conf. Signal Image Processing Appl.* **2010**, 242–245.
- (624) Fujisawa, K.; Shimo, M.; Taguchi, Y.-H.; Ikematsu, S.; Miyata, R. PCA-Based Unsupervised Feature Extraction for Gene Expression Analysis of COVID-19 Patients. *Sci. Rep.* **2021**, *11*, 17351.
- (625) Calderón-Santiago, M.; Priego-Capote, F.; Turck, N.; Robin, X.; Jurado-Gámez, B.; Sanchez, J. C.; Luque de Castro, M. D. Human Sweat Metabolomics for Lung Cancer Screening. *Anal. Bioanal. Chem.* **2015**, *407*, 5381–5392.
- (626) Chan, H.-P.; Wei, D.; Helvie, M. A.; Sahiner, B.; Adler, D. D.; Goodsitt, M. M.; Petrick, N. Computer-Aided Classification of Mammographic Masses and Normal Tissue: Linear Discriminant Analysis in Texture Feature Space. *Phys. Med. Biol.* **1995**, *40*, 857–876.
- (627) Suhail, Z.; Denton, E. R. E.; Zwigelaar, R. Classification of Micro-Calcification in Mammograms Using Scalable Linear Fisher Discriminant Analysis. *Med. Biol. Eng. Comput.* **2018**, *56*, 1475–1485.
- (628) Lundberg, S. M.; Lee, S.-I. A Unified Approach to Interpreting Model Predictions. *Proceedings of the 31st International Conference on Neural Information Processing Systems 2017*; pp 4768–4777.
- (629) Bittremieux, W.; Advani, R. S.; Jarmusch, A. K.; Aguirre, S.; Lu, A.; Dorrestein, P. C.; Tsunoda, S. M. Physicochemical Properties Determining Drug Detection in Skin. *Clinical Translational Sci.* **2022**, *15*, 761–770.
- (630) Ribeiro, M. T.; Singh, S.; Guestrin, C. Why Should I Trust You?: Explaining the Predictions of Any Classifier. *arXiv:1602.04938* **2016**. DOI: 10.48550/arXiv.1602.04938.
- (631) Shahrjooihighighi, A.; Frigui, H.; Zhang, X.; Wei, X.; Shi, B.; Trabelsi, A. An Ensemble Feature Selection Method for Biomarker Discovery. *IEEE Int. Conf. Signal Process. Comput. Control* **2017**, 416–421.
- (632) Sankhala, D.; Sardesai, A. U.; Pali, M.; Lin, K.-C.; Jagannath, B.; Muthukumar, S.; Prasad, S. A Machine Learning-Based on-Demand Sweat Glucose Reporting Platform. *Sci. Rep.* **2022**, *12*, 2442.

- (633) Shahub, S.; Upasham, S.; Ganguly, A.; Prasad, S. Machine Learning Guided Electrochemical Sensor for Passive Sweat Cortisol Detection. *Sens. Bio-Sens. Res.* **2022**, *38*, 100527.
- (634) Ayata, D.; Yaslan, Y.; Kamasak, M. Emotion recognition via galvanic skin response: Comparison of machine learning algorithms and feature extraction methods. *IU-J. Electr. Electron. Eng.* **2017**, *17*, 3129–3136.
- (635) Pandey, P. S. Machine Learning and IoT for Prediction and Detection of Stress. *International Conference on Computational Science and Its Applications*, 2017. DOI: [10.1109/ICCSA.2017.8000018](https://doi.org/10.1109/ICCSA.2017.8000018).
- (636) Zhou, Z.; Zare, R. N. Personal Information from Latent Fingerprints Using Desorption Electrospray Ionization Mass Spectrometry and Machine Learning. *Anal. Chem.* **2017**, *89*, 1369–1372.
- (637) Um, T. T.; Pfister, F. M. J.; Pichler, D.; Endo, S.; Lang, M.; Hirche, S.; Fietzek, U.; Kulić, D. Data Augmentation of Wearable Sensor Data for Parkinson's Disease Monitoring Using Convolutional Neural Networks. *Proceedings of the 19th ACM International Conference on Multimodal Interaction*; Association for Computing Machinery: New York, NY, 2017; pp 216–220.
- (638) Cho, S.-Y.; Lee, Y.; Lee, S.; Kang, H.; Kim, J.; Choi, J.; Ryu, J.; Joo, H.; Jung, H.-T.; Kim, J. Finding Hidden Signals in Chemical Sensors Using Deep Learning. *Anal. Chem.* **2020**, *92*, 6529–6537.
- (639) Potyralo, R. A.; Brewer, J.; Cheng, B.; Carpenter, M. A.; Houlihan, N.; Kolmakov, A. Bio-Inspired Gas Sensing: Boosting Performance with Sensor Optimization Guided by “Machine Learning. *Faraday Discuss.* **2020**, *223*, 161–182.
- (640) Li, H.; Wu, J.; Gao, Y.; Shi, Y. Examining Individuals' Adoption of Healthcare Wearable Devices: An Empirical Study from Privacy Calculus Perspective. *Int. J. Med. Inform.* **2016**, *88*, 8–17.
- (641) Report: Fitness Tracker Data Breach Exposed 61 Million Records and User Data Online. Website Planet. <https://www.websiteplanet.com/blog/gethealth-leak-report/> (accessed 2022-09-20).
- (642) Rights (OCR), O. for C. HIPAA Privacy Rule. HHS.gov. <https://www.hhs.gov/hipaa/for-professionals/privacy/index.html> (accessed 2022-09-20).
- (643) Rights (OCR), O. for C. Security Rule. HHS.gov. <https://www.hhs.gov/hipaa/for-professionals/security/index.html> (accessed 2022-09-20).
- (644) Newman, T.; Kreick, J. Impact of HIPAA (and Other Federal Law) on Wearable Technology. *SMU Sci. Tech. L. Rev.* **2015**, *18* (4), 429.
- (645) Rights (OCR), O. for C. Covered Entities and Business Associates. HHS.gov. <https://www.hhs.gov/hipaa/for-professionals/covered-entities/index.html> (accessed 2022-09-20).
- (646) Rights (OCR), O. for C. Business Associates. HHS.gov. <https://www.hhs.gov/hipaa/for-professionals/privacy/guidance/business-associates/index.html> (accessed 2022-09-20).
- (647) Arış, A.; Oktuğ, S. F.; Yalçın, S. B. Ö. Internet-of-Things security: Denial of service attacks. *23rd Signal Processing and Communications Applications Conference (SIU)*, Malatya, Turkey, 2015; pp 903–906.
- (648) Xie, Y.; Lu, L.; Gao, F.; He, S.; Zhao, H.; Fang, Y.; Yang, J.; An, Y.; Ye, Z.; Dong, Z. Integration of Artificial Intelligence, Blockchain, and Wearable Technology for Chronic Disease Management: A New Paradigm in Smart Healthcare. *Curr. Med. Sci.* **2021**, *41*, 1123–1133.
- (649) Hale, M. L.; Lotfy, K.; Gamble, R. F.; Walter, C.; Lin, J. Developing a Platform to Evaluate and Assess the Security of Wearable Devices. *Digit. Commun. Netw.* **2019**, *5*, 147–159.
- (650) Seshadri, D. R.; Magliato, S.; Voos, J. E.; Drummond, C. Clinical Translation of Biomedical Sensors for Sports Medicine. *J. Med. Biol. Eng.* **2019**, *43*, 66–81.
- (651) Fiedler, B. A.; David, Y. Chapter 1 - Reframing Product Life Cycle for Medical Devices. In *Managing Medical Devices Within a Regulatory Framework*; Fiedler, B. A., Ed.; Elsevier, 2017; pp 3–16.
- (652) Kim, J.; Kumar, R.; Bandodkar, A. J.; Wang, J. Advanced Materials for Printed Wearable Electrochemical Devices: A Review. *Adv. Electron. Mater.* **2017**, *3*, 1600260.
- (653) Barros Azeredo, N. F.; Ferreira Santos, M. S.; Sempionatto, J. R.; Wang, J.; Angnes, L. Screen-Printed Technologies Combined with Flow Analysis Techniques: Moving from Benchtop to Everywhere. *Anal. Chem.* **2022**, *94*, 250–268.
- (654) Blayo, A.; Pineaux, B. Printing Processes and Their Potential for RFID Printing. In *Proceedings of the 2005 joint conference on Smart objects and ambient intelligence: innovative context-aware services: usages and technologies*; sOc-EUSAI '05; Association for Computing Machinery: New York, NY, 2005; pp 27–30.
- (655) Tehrani, F.; Beltrán-Gastélum, M.; Sheth, K.; Karajic, A.; Yin, L.; Kumar, R.; Soto, F.; Kim, J.; Wang, J.; Barton, S.; Mueller, M.; Wang, J. Laser-Induced Graphene Composites for Printed, Stretchable, and Wearable Electronics. *Adv. Mater. Technol.* **2019**, *4*, 1900162.
- (656) Li, J.; Rossignol, F.; Macdonald, J. Inkjet Printing for Biosensor Fabrication: Combining Chemistry and Technology for Advanced Manufacturing. *Lab Chip* **2015**, *15*, 2538–2558.
- (657) Grau, G.; Cen, J.; Kang, H.; Kitsomboonloha, R.; Scheideler, W. J.; Subramanian, V. Gravure-Printed Electronics: Recent Progress in Tooling Development, Understanding of Printing Physics, and Realization of Printed Devices. *Flex. Print. Electron.* **2016**, *1*, 023002.
- (658) Bae, S.; Kim, H.; Lee, Y.; Xu, X.; Park, J.-S.; Zheng, Y.; Balakrishnan, J.; Lei, T.; Ri Kim, H.; Song, Y. I.; Kim, Y.-J.; Kim, K. S.; Özyilmaz, B.; Ahn, J.-H.; Hong, B. H.; Iijima, S. Roll-to-Roll Production of 30-Inch Graphene Films for Transparent Electrodes. *Nat. Nanotechnol.* **2010**, *5*, 574–578.
- (659) Wang, M.; Yang, Y.; Gao, W. Laser-Engraved Graphene for Flexible and Wearable Electronics. *Trends Chem.* **2021**, *3*, 969–981.
- (660) Epicore Biosystems. Epicore Biosystems. <https://www.epicorebiosystems.com/> (accessed 2022-08-08).
- (661) Baker, L. B.; Seib, M. S.; Barnes, K. A.; Brown, S. D.; King, M. A.; De Chavez, P. J. D.; Qu, S.; Archer, J.; Wolfe, A. S.; Stofan, J. R.; Carter, J. M.; Wright, D. E.; Wallace, J.; Yang, D. S.; Liu, S.; Anderson, J.; Fort, T.; Li, W.; Wright, J. A.; Lee, S. P.; Model, J. B.; Rogers, J. A.; Aranyosi, A. J.; Ghaffari, R. Skin-Interfaced Microfluidic System with Machine Learning-Enabled Image Processing of Sweat Biomarkers in Remote Settings. *Adv. Mater. Technol.* **2022**, *7* (11), 2200249.
- (662) Gidado, I. M.; Qassem, M.; Triantis, I. F.; Kyriacou, P. A. Review of Advances in the Measurement of Skin Hydration Based on Sensing of Optical and Electrical Tissue Properties. *Sensors* **2022**, *22*, 7151.
- (663) FLOWBIO. <https://www.flowbio.com/> (accessed 2022-11-01).
- (664) Product. Nix Biosensors. <https://nixbiosensors.com/pages/product> (accessed 2022-08-08).
- (665) hDrop Hydration Wearable Monitor - Dehydration Sensor. <https://hdroptech.com/> (accessed 2022-08-08).
- (666) Inicio. Onalabs. <https://www.onalabs.com/en/> (accessed 2022-11-01).
- (667) *Sweati is a wearable patch that tracks glucose by analyzing your sweat.* SM24. <https://www.sm24.ai/blogs/news/sweati-is-a-wearable-patch-that-tracks-glucose-by-analyzing-your-sweat> (accessed 2022-11-01).
- (668) *Patch Analyzes Sweat to Monitor, Diagnose Health Issues.* Healthcare Packaging. <https://www.healthcarepackaging.com/machinery-materials/adherence-delivery/article/13295801/patch-analyzes-sweat-to-monitor-diagnose-health-issues> (accessed 2022-08-08).
- (669) *My Skin Track pH by La Roche-Posay won the CES 2019 Innovation Award.* <https://www.loreal.com/en/news/science-and-technology/research-innovation/my-skin-track-ph-by-la-roche-posay-won-the-ces-2019-innovation-award/> (accessed 2022-08-08).
- (670) G. T., Inc. GraphWear. <https://www.graphwear.co> (accessed 2022-10-31).
- (671) *Lab-on-Skin™ Technology - Xsensio | Lab-on-Skin™ Sensing Platform.* <https://xsensio.com/lab-on-skin-technology/> (accessed 2022-11-01).
- (672) Zhang, J.; Rupakula, M.; Bellando, F.; Garcia Cordero, E.; Longo, J.; Wildhaber, F.; Herment, G.; Guérin, H.; Ionescu, A. M.

Sweat Biomarker Sensor Incorporating Picowatt, Three-Dimensional Extended Metal Gate Ion Sensitive Field Effect Transistors. *ACS Sens.* **2019**, *4*, 2039–2047.

(673) Sheibani, S.; Capua, L.; Kamaei, S.; Akbari, S. S. A.; Zhang, J.; Guerin, H.; Ionescu, A. M. Extended Gate Field-Effect-Transistor for Sensing Cortisol Stress Hormone. *Commun. Mater.* **2021**, *2*, 10.

(674) Ray, T. R.; Ivanovic, M.; Curtis, P. M.; Franklin, D.; Guventurk, K.; Jeang, W. J.; Chafetz, J.; Gaertner, H.; Young, G.; Rebollo, S.; Model, J. B.; Lee, S. P.; Ciraldo, J.; Reeder, J. T.; Hourlier-Fargette, A.; Bandodkar, A. J.; Choi, J.; Aranyosi, A. J.; Ghaffari, R.; McColley, S. A.; Haymond, S.; Rogers, J. A. Soft, Skin-Interfaced Sweat Stickers for Cystic Fibrosis Diagnosis and Management. *Sci. Transl. Med.* **2021**, *13*, No. eabd8109.

(675) *Cystic Fibrosis Updates in Care: Part II — The “Sweat Sticker” and Clinician Q&A*. Pulmonology Advisor. <https://www.pulmonologyadvisor.com/home/topics/obstructive-lung-disease/cystic-fibrosis-updates-in-care-part-ii-the-sweat-sticker-and-clinician-qa/> (accessed 2022-08-08).

(676) *Apple Watch monitoring features for AFib, Parkinson’s cleared by FDA*. MedTech Dive. <https://www.medtechdive.com/news/apple-watch-afib-parkinsons-fda-clearance/625424/> (accessed 2022-11-08).

(677) *Medidata Sensor Cloud | Wearables in Clinical Trials*. Medidata Solutions. <https://www.medidata.com/en/clinical-trial-products/patient-centric-clinical-trials/wearable-sensors/> (accessed 2022-11-08).

(678) Anderson, C. *Epicore Adds Sweat Sensor Tech with Eccrine Systems Buyout*. Inside Precision Medicine. <https://www.insideprecisionmedicine.com/topics/translational-research/biomarkers-topic/epicore-adds-sweat-sensor-tech-with-eccrine-systems-buyout/> (accessed 2022-08-08).

(679) *Wearable Devices Market Size, Share | 2022 - 27 | Industry Growth*. <https://www.mordorintelligence.com/industry-reports/global-wearable-medical-device-market-industry> (accessed 2022-10-30).

(680) CB Insights. *From Wearables To Telemedicine To Direct-To-Consumer Prescriptions, Here’s How Healthcare Is Becoming Consumer-Centric*. CB Insights. <https://app.cbinsights.com/research/consumer-healthcare-relationship-expert-intelligence/> (accessed 2022-11-06).

(681) Baker, L. B.; Barnes, K. A.; Anderson, M. L.; Passe, D. H.; Stofan, J. R. Normative Data for Regional Sweat Sodium Concentration and Whole-Body Sweating Rate in Athletes. *J. Sports Sci.* **2016**, *34*, 358–368.

(682) Bulmer, M. G.; Forwell, G. D. The Concentration of Sodium in Thermal Sweat. *J. Physiol.* **1956**, *132*, 115–122.

(683) Baker, L. B.; Ungaro, C. T.; Sopeña, B. C.; Nuccio, R. P.; Reimel, A. J.; Carter, J. M.; Stofan, J. R.; Barnes, K. A. Body Map of Regional vs. Whole Body Sweating Rate and Sweat Electrolyte Concentrations in Men and Women during Moderate Exercise-Heat Stress. *J. Appl. Physiol.* **2018**, *124*, 1304–1318.

(684) Faria, A. G.; Marson, F. A. L.; Gomez, C. C. S.; Servidoni, M. de F.; Ribeiro, A. F.; Ribeiro, J. D. Thirty Years of Sweat Chloride Testing at One Referral Center. *Front. Pediatr.* **2017**, *5*, 222.

(685) Sato, K.; Kang, W. H.; Saga, K.; Sato, K. T. Biology of Sweat Glands and Their Disorders. I. Normal Sweat Gland Function. *J. Am. Acad. Dermatol.* **1989**, *20*, 537–563.

(686) Czarnowski, D.; Górski, J.; Józwiuk, J.; Boroń-Kaczmarek, A. Plasma Ammonia Is the Principal Source of Ammonia in Sweat. *Europ. J. Appl. Physiol.* **1992**, *65*, 135–137.

(687) Goodwin, M. L.; Harris, J. E.; Hernández, A.; Gladden, L. B. Blood Lactate Measurements and Analysis during Exercise: A Guide for Clinicians. *J. Diabetes Sci. Technol.* **2007**, *1*, 558–569.

(688) Green, J. M.; Bishop, P. A.; Muir, I. H.; McLester Jr, J. R.; Heath, H. E. Effects of High and Low Blood Lactate Concentrations on Sweat Lactate Response. *Int. J. Sports Med.* **2000**, *21*, 556–560.

(689) Fellmann, N.; Grizard, G.; Coudert, J. Human Frontal Sweat Rate and Lactate Concentration during Heat Exposure and Exercise. *J. Appl. Physiol.* **1983**, *54*, 355–360.

(690) Derbyshire, P. J.; Barr, H.; Davis, F.; Higson, S. P. J. Lactate in Human Sweat: A Critical Review of Research to the Present Day. *J. Physiol. Sci.* **2012**, *62*, 429–440.

(691) Sakharov, D. A.; Shkurnikov, M. U.; Vagin, M. Yu.; Yashina, E. I.; Karyakin, A. A.; Tonevitsky, A. G. Relationship between Lactate Concentrations in Active Muscle Sweat and Whole Blood. *Bull. Exp. Biol. Med.* **2010**, *150*, 83–85.

(692) Green, J. M.; Pritchett, R. C.; Crews, T. R.; McLester, J. R.; Tucker, D. C. Sweat Lactate Response between Males with High and Low Aerobic Fitness. *Eur. J. Appl. Physiol.* **2004**, *91*, 1–6.

(693) Alvear-Ordenes, I.; García-López, D.; De Paz, J. A.; González-Gallego, J. Sweat Lactate, Ammonia, and Urea in Rugby Players. *Int. J. Sports Med.* **2005**, *26*, 632–637.

(694) Buono, M. J.; Lee, N. V. L.; Miller, P. W. The Relationship between Exercise Intensity and the Sweat Lactate Excretion Rate. *J. Physiol. Sci.* **2010**, *60*, 103–107.

(695) Boysen, T. C.; Yanagawa, S.; Sato, F.; Sato, K. A Modified Anaerobic Method of Sweat Collection. *J. Appl. Physiol.* **1984**, *56*, 1302–1307.

(696) Sakaguchi, K.; Hirota, Y.; Hashimoto, N.; Ogawa, W.; Hamaguchi, T.; Matsuo, T.; Miyagawa, J.-I.; Namba, M.; Sato, T.; Okada, S.; Tomita, K.; Matsuhashi, M.; Kaneto, H.; Kosugi, K.; Maegawa, H.; Nakajima, H.; Kashiwagi, A. Evaluation of a Minimally Invasive System for Measuring Glucose Area under the Curve during Oral Glucose Tolerance Tests: Usefulness of Sweat Monitoring for Precise Measurement. *J. Diabetes Sci. Technol.* **2013**, *7*, 678–688.

(697) Martin, A.; Saathoff, M.; Kuhn, F.; Max, H.; Terstegen, L.; Natsch, A. A Functional ABCC11 Allele Is Essential in the Biochemical Formation of Human Axillary Odor. *J. Invest. Dermatol.* **2010**, *130*, 529–540.

(698) Buono, M. J. Sweat Ethanol Concentrations Are Highly Correlated with Co-Existing Blood Values in Humans. *Exp. Physiol.* **1999**, *84*, 401–404.

(699) Tsunoda, M.; Hirayama, M.; Tsuda, T.; Ohno, K. Noninvasive Monitoring of Plasma L-Dopa Concentrations Using Sweat Samples in Parkinson’s Disease. *Clin. Chim. Acta* **2015**, *442*, 52–55.

(700) He, J.; Lu, C.; Jiang, H.; Han, F.; Shi, X.; Wu, J.; Wang, L.; Chen, T.; Wang, J.; Zhang, Y.; Yang, H.; Zhang, G.; Sun, X.; Wang, B.; Chen, P.; Wang, Y.; Xia, Y.; Peng, H. Scalable Production of High-Performing Woven Lithium-Ion Fibre Batteries. *Nature* **2021**, *597*, 57–63.

(701) Nguyen, P. Q.; Soenksen, L. R.; Donghia, N. M.; Angenent-Mari, N. M.; de Puig, H.; Huang, A.; Lee, R.; Slomovic, S.; Galbersanini, T.; Lansberry, G.; Sallum, H. M.; Zhao, E. M.; Niemi, J. B.; Collins, J. J. Wearable Materials with Embedded Synthetic Biology Sensors for Biomolecule Detection. *Nat. Biotechnol.* **2021**, *39*, 1366–1374.

(702) Matzeu, G.; Mogas-Soldevila, L.; Li, W.; Naidu, A.; Turner, T. H.; Gu, R.; Blumeris, P. R.; Song, P.; Pascal, D. G.; Guidetti, G.; Li, M.; Omenetto, F. G. Large-Scale Patterning of Reactive Surfaces for Wearable and Environmentally Deployable Sensors. *Adv. Mater.* **2020**, *32*, 2001258.

(703) Ladd, C.; So, J.-H.; Muth, J.; Dickey, M. D. 3D Printing of Free Standing Liquid Metal Microstructures. *Adv. Mater.* **2013**, *25*, 5081–5085.

(704) Molina-Lopez, F.; Gao, T. Z.; Kraft, U.; Zhu, C.; Öhlund, T.; Pfattner, R.; Feig, V. R.; Kim, Y.; Wang, S.; Yun, Y.; Bao, Z. Inkjet-Printed Stretchable and Low Voltage Synaptic Transistor Array. *Nat. Commun.* **2019**, *10*, 2676.

(705) Lipani, L.; Dupont, B. G. R.; Doungmene, F.; Marken, F.; Tyrrell, R. M.; Guy, R. H.; Ilie, A. Non-Invasive, Transdermal, Path-Selective and Specific Glucose Monitoring via a Graphene-Based Platform. *Nat. Nanotechnol.* **2018**, *13*, 504–511.

(706) Choi, S.; Han, S. I.; Jung, D.; Hwang, H. J.; Lim, C.; Bae, S.; Park, O. K.; Tschabrunn, C. M.; Lee, M.; Bae, S. Y.; Yu, J. W.; Ryu, J. H.; Lee, S.-W.; Park, K.; Kang, P. M.; Lee, W. B.; Nezafat, R.; Hyeon, T.; Kim, D.-H. Highly Conductive, Stretchable and Biocompatible Ag-Au Core-Sheath Nanowire Composite for Wearable and Implantable Bioelectronics. *Nat. Nanotechnol.* **2018**, *13*, 1048–1056.

(707) Cao, Q.; Kim, H.; Pimparkar, N.; Kulkarni, J. P.; Wang, C.; Shim, M.; Roy, K.; Alam, M. A.; Rogers, J. A. Medium-Scale Carbon Nanotube Thin-Film Integrated Circuits on Flexible Plastic Substrates. *Nature* **2008**, *454*, 495–500.

(708) Kaltenbrunner, M.; Sekitani, T.; Reeder, J.; Yokota, T.; Kuribara, K.; Tokuhara, T.; Drack, M.; Schwödiauer, R.; Graz, I.; Bauer-Gogonea, S.; Bauer, S.; Someya, T. An Ultra-Lightweight Design for Imperceptible Plastic Electronics. *Nature* **2013**, *499*, 458–463.

(709) Oh, J. Y.; Rondeau-Gagné, S.; Chiu, Y.-C.; Chortos, A.; Lissel, F.; Wang, G.-J. N.; Schroeder, B. C.; Kurosawa, T.; Lopez, J.; Katsumata, T.; Xu, J.; Zhu, C.; Gu, X.; Bae, W.-G.; Kim, Y.; Jin, L.; Chung, J. W.; Tok, J. B.-H.; Bao, Z. Intrinsically Stretchable and Healable Semiconducting Polymer for Organic Transistors. *Nature* **2016**, *539*, 411–415.

(710) Xu, S.; Zhang, Y.; Jia, L.; Mathewson, K. E.; Jang, K.-I.; Kim, J.; Fu, H.; Huang, X.; Chava, P.; Wang, R.; Bhole, S.; Wang, L.; Na, Y. J.; Guan, Y.; Flavin, M.; Han, Z.; Huang, Y.; Rogers, J. A. Soft Microfluidic Assemblies of Sensors, Circuits, and Radios for the Skin. *Science* **2014**, *344*, 70–74.

(711) Yuk, H.; Varela, C. E.; Nabzdyk, C. S.; Mao, X.; Padera, R. F.; Roche, E. T.; Zhao, X. Dry Double-Sided Tape for Adhesion of Wet Tissues and Devices. *Nature* **2019**, *575*, 169–174.

(712) Yuk, H.; Wu, J.; Zhao, X. Hydrogel Interfaces for Merging Humans and Machines. *Nat. Rev. Mater.* **2022**, *7*, 935–952.

(713) Sun, J.-Y.; Zhao, X.; Illeperuma, W. R. K.; Chaudhuri, O.; Oh, K. H.; Mooney, D. J.; Vlassak, J. J.; Suo, Z. Highly Stretchable and Tough Hydrogels. *Nature* **2012**, *489*, 133–136.

(714) Deng, J.; Yuk, H.; Wu, J.; Varela, C. E.; Chen, X.; Roche, E. T.; Guo, C. F.; Zhao, X. Electrical Bioadhesive Interface for Bioelectronics. *Nat. Mater.* **2021**, *20*, 229–236.

(715) Tang, T.-C.; Tham, E.; Liu, X.; Yehl, K.; Rovner, A. J.; Yuk, H.; de la Fuente-Nunez, C.; Isaacs, F. J.; Zhao, X.; Lu, T. K. Hydrogel-Based Biocontainment of Bacteria for Continuous Sensing and Computation. *Nat. Chem. Biol.* **2021**, *17*, 724–731.

(716) Yuk, H.; Wu, J.; Sarrafian, T. L.; Mao, X.; Varela, C. E.; Roche, E. T.; Griffiths, L. G.; Nabzdyk, C. S.; Zhao, X. Rapid and Coagulation-Independent Haemostatic Sealing by a Paste Inspired by Barnacle Glue. *Nat. Biomed. Eng.* **2021**, *5*, 1131–1142.

## Recommended by ACS

### How Saliva Interferes with Colorimetric Gold Nanoparticle Aptasensors: Understanding and Mitigating Surface Interactions

Anindita Sen, Justin M. Hodgkiss, *et al.*

APRIL 02, 2023  
ACS SENSORS

READ 

### Fully Biodegradable and Long-Term Operational Primary Zinc Batteries as Power Sources for Electronic Medicine

Xueying Huang, Lan Yin, *et al.*

MARCH 10, 2023  
ACS NANO

READ 

### Challenges of Emerging Wearable Sensors for Remote Monitoring toward Telemedicine Healthcare

Surachate Kalasin and Werasak Surareunghai

JANUARY 11, 2023  
ANALYTICAL CHEMISTRY

READ 

### Determinants of Superselectivity—Practical Concepts for Application in Biology and Medicine

Galina V. Dubacheva, Ralf P. Richter, *et al.*

MARCH 14, 2023  
ACCOUNTS OF CHEMICAL RESEARCH

READ 

Get More Suggestions >